Technische Universität München
Fakultät für Elektrotechnik und Informationstechnik

Validation of Hybrid Brain-Computer Interface Algorithms for Neuroprosthetics Control

Zied Tayeb

Vollständiger Abdruck der von der Fakultät für Elektrotechnik und Informationstechnik der Technischen Universität München zur Erlangung des akademischen Grades eines

Doktors der Ingenieurwissenschaften (Dr.-Ing.)

genehmigten Dissertation.

Vorsitzender:

Prof. Dr. Bernhard Wolfrum

Prüfer der Dissertation:

1. Prof. Gordon Cheng, Ph.D.
2. Prof. Dr. Jörg Conradt

Die Dissertation wurde am 25.03.2021 bei der Technischen Universität München eingereicht und durch die Fakultät für Elektrotechnik und Informationstechnik am 06.02.2022 angenommen.

Abstract

Brain-computer interface (BCI) is a particular human-machine interfacing system that processes users' brain activities and translates them into commands to control external assistive devices. Overall, BCI proposes a promising solution to directly connect the human brain to neuroprostheses, en route to developing a bidirectional, closed-loop interface between amputees and their prostheses. However, a good BCI system for neuroprosthetics control should allow the reliable classification of complex movements from users' intentions when interacting in real-time with their assistive devices, and more importantly should decode the human brain perception of different external sensory stimuli, ranging from gentle touch to very intense sensations.

Within this thesis, I demonstrate that one way to approach this problem is by exploiting electroencephalography (EEG) signals alongside other biosignals, such as electrooculography (EOG) and electromyography (EMG). As will be shown in this thesis, BCI represents an intriguing technology for feed-forward control, as well as for sensory substitution. When focusing on both sides of the equation, two main control methods were investigated. From a feed-forward control standpoint, the following approaches were pursued: First, Only EEG signals were used for decoding two motor imagery (MI) movements when controlling a robotic arm. For that, I validated different EEG learning models using data collected from 20 healthy subjects. Overall, the validated deep learning model outperformed the state-of-the-art machine learning techniques and showed high stability across subjects, with a mean standard deviation of less than 3.32%. The successful decoding of these two MI movements spurred the exploration of other techniques to decode more complex arm movement intentions and led to a second follow-up study. For that purpose, EOG+EMG and EEG+EMG were used to classify five and six reach-to-grasp movements, achieving an average online accuracy of 95.8% and 89.6%, respectively. For the sensory substitution part, vibrotactile stimulation was investigated, and four human subjects were able to control in real-time four gestures of a prosthetic hand, using decoded EMG signals, with an average accuracy of 86.25%, while being able to simultaneously differentiate between the stiffness of three different grasped objects with an average online accuracy of 88.46%. Thereafter, two follow-up studies were designed, where EEG was used to quantify the brain perception of electrical

and thermal sensory stimulations. First, I identified and validated Spatio-temporal features of brain activity during innocuous, moderately intense, and very intense stimulation of an amputee's phantom limb using transcutaneous nerve stimulation (TENS). Based on these identified EEG features, I classified the three stimuli with a test accuracy of 94.66%. Similarly, I reported that the unpleasant (very intense) stimulus activated the pre-motor cortex with the highest activation shown in the central cortex between 450 ms and 750 ms post-stimulation, whereas the highest activation for the moderately intense stimulation was found in the parietal lobe. Further, I localized the cortical sources and observed early strong activation of the anterior cingulate cortex (ACC) for the very intense stimulus. These results were further extended in a follow-up study, where we used EEG to identify spatial, temporal, and spectral patterns of brain responses to five different thermal stimulations. Results showed that the most intense thermal stimuli elicit a decrease in alpha power compared to intense and innocuous stimulations. Spatio-temporal analysis reveals that in the first 400 ms post-stimulus, brain activity increased in the prefrontal and central brain areas for the very intense thermal stimulations, whereas for the moderately intense stimulation, high activity of the parietal area was observed post-500 ms. Based on these EEG patterns, I classified the different thermal stimulations (average accuracy of 87%). When performing source localization, my findings reveal that the most intense thermal stimuli (very cold and very hot) were anticipated and induced early (before 400 ms) activation of the ACC. Moreover, activation of the pre-frontal cortex, somatosensory, central, and parietal areas, was observed in the first 400 ms post-stimulation for very intense thermal conditions and starting 500 ms post-stimuli for intense conditions. Overall, the results of these studies could lead to a better understanding of thermal and electrical sensations perception and processing in the human brain.

Zusammenfassung

Gehirn-Computer Schnittstellen ist ein spezielles Mensch-Maschine-Schnittstellensystem, das die Gehirnaktivitäten der Benutzer verarbeitet und in Befehle zur Steuerung externer Hilfsgeräte umsetzt. Insgesamt schlägt BCI eine vielversprechende Lösung zur direkten Verbindung des menschlichen Gehirns mit Neuroprothesen vor, auf dem Weg zur Entwicklung einer bidirektionalen, geschlossenen Schnittstelle zwischen Amputierten und ihren Prothesen. Insbesondere sollte ein gutes BCI-System für die neuroprothetische Steuerung die zuverlässige Klassifizierung komplexer Bewegungen aus den Intentionen der Anwender bei der Interaktion mit ihren Hilfsmitteln in Echtzeit ermöglichen und, was noch wichtiger ist, die Wahrnehmung verschiedener externer sensorischer Reize im menschlichen Gehirn entschlüsseln, die von sanften Berührungen bis hin zu sehr intensiven Empfindungen reichen.

Im Rahmen dieser Arbeit zeige ich, dass ein wichtiger Weg zur Lösung dieses Problems darin besteht, die Signale der Elektroenzephalographie (EEG) neben anderen Biosignalen, wie der Elektrookulographie (EOG) und der Elektromyographie (EMG), zu nutzen. Wie in dieser Arbeit gezeigt wird, stellt der BCI eine faszinierende Technologie für die Feed-Forward-Kontrolle sowie für die sensorische Substitution dar. Wenn man sich auf beide Seiten der Gleichung konzentriert, wurden zwei Hauptkontrollmethoden untersucht. Aus der Sicht der Feed-Forward-Kontrolle wurden die folgenden Ansätze verfolgt: Zunächst wurden nur EEG-Signale zur Dekodierung von zwei motorischen Bildbewegungen (MI) bei der Steuerung eines Roboterarms verwendet. Dazu validierte ich verschiedene EEG-Lernmodelle anhand von Daten, die von 20 gesunden Probanden gesammelt wurden. Insgesamt übertraf das vorgeschlagene Lernmodell die modernsten Techniken des maschinellen Lernens und zeigte eine hohe Stabilität über die Probanden hinweg, mit einer mittleren Standardabweichung von weniger als 3,32%. Die erfolgreiche Dekodierung dieser beiden MI-Bewegungen spornte die Erforschung anderer Techniken zur Dekodierung komplexerer Armbewegungsabsichten an und führte zu einer zweiten Folgestudie. Zu diesem Zweck wurden EOG+EMG und EEG+EMG verwendet, um fünf und sechs Greifbewegungen zu klassifizieren, wobei eine durchschnittliche Online-Genauigkeit von 95,8% bzw. 89,6% erreicht wurde. Für den sensorischen Ersatzteil wurde die vibrotaktile Stimulation untersucht, und vier menschliche

Versuchspersonen waren in der Lage, in Echtzeit vier Gesten einer Handprothese unter Verwendung dekodierter EMG-Signale mit einer durchschnittlichen Genauigkeit von 86,25% zu kontrollieren, während sie gleichzeitig in der Lage waren, zwischen der Steifheit von drei verschiedenen gegriffenen Objekten mit einer durchschnittlichen Online-Genauigkeit von 88,46% zu unterscheiden. Danach wurden zwei Folgestudien konzipiert, bei denen das EEG zur Quantifizierung der Gehirnwahrnehmung von elektrischen und thermischen sensorischen Stimulationen verwendet wurde. Zunächst identifizierte und validierte ich die raum-zeitlichen Merkmale der Gehirnaktivität während einer harmlosen, mäßig intensiven und sehr intensiven Stimulation der Phantomschleife eines Amputierten mittels transkutaner Nervenstimulation (TENS). Basierend auf diesen identifizierten EEG-Merkmalen klassifizierte ich die drei Stimuli mit einer Testgenauigkeit von 94,66%. In ähnlicher Weise berichtete ich, dass der unangenehme (sehr intensive) Stimulus den prämotorischen Kortex aktivierte, wobei die höchste Aktivierung im zentralen Kortex zwischen 450 ms und 750 ms nach der Stimulation gezeigt wurde, während die höchste Aktivierung für die mäßig intensive Stimulation im Parietallappen gefunden wurde. Ferner lokalisierte ich die kortikalen Quellen und beobachtete eine frühe starke Aktivierung des anterioren cingulären Kortex (ACC) für den sehr intensiven Stimulus. Diese Ergebnisse wurden in einer Folgestudie weiter vertieft, in der wir mit Hilfe des EEG räumliche, zeitliche und spektrale Muster der Gehirnreaktionen auf fünf verschiedene thermische Stimulationen. Die Ergebnisse zeigten, dass die intensivsten thermischen Stimuli eine signifikante Abnahme der Alpha-Power im Vergleich zu intensiven und harmlosen Stimulationen hervorrufen. Die räumlich-zeitliche Analyse zeigt, dass in den ersten 400 ms nach dem Stimulus die Hirnaktivität in den präfrontalen und zentralen Hirnarealen bei den sehr intensiven thermischen Stimulationen zunahm, während bei der mäßig intensiven Stimulation nach 500 ms eine hohe Aktivität des Parietalbereichs beobachtet wurde. Basierend auf diesen EEG-Mustern klassifizierte ich die verschiedenen thermischen Stimulationen (durchschnittliche Genauigkeit von 87%). Bei der Durchführung der Quellenlokalisation zeigen meine Ergebnisse, dass die intensivsten thermischen Reize (sehr kalt und sehr heiß) antizipiert und früh (vor 400 ms) zur Aktivierung des ACC induziert wurden. Darüber hinaus wurde die Aktivierung des präfrontalen Kortex, des somatosensorischen, zentralen und parietalen Bereichs in den ersten 400 ms nach der Stimulation bei sehr intensiven thermischen Bedingungen und ab 500 ms nach der Stimulation bei intensiven Bedingungen beobachtet. Insgesamt könnten die Ergebnisse dieser Studien zu einem besseren Verständnis der Verarbeitung thermischer und elektrischer Empfindungen im Gehirn führen, was einen Weg für die Entwicklung eines Echtzeit-Entzugsreaktionssystems bei der Interaktion mit Prothesen aufzeigen könnte.

Acknowledgements

A mere couple of paragraphs cannot usually be enough to give thanks, show appreciation, and express sincere gratitude to all of those who have been supporting and helping out in various ways and under different circumstances. Nonetheless, I decided to take up the challenge, so let me get started:

First and foremost, I would like to thank my dissertation advisor **Prof. Gordon Cheng**, for giving me the opportunity to join his research laboratory and carry out my doctoral research under his supervision. Particularly, I would like to thank him for giving me all the scientific independence to follow my research passion and pursue my vision. Without his unwavering dogma to wrap up my thesis, his patience, and support over the last few years, I wouldn't be able to reach this major milestone. Thank you, once again, **Prof. Gordon Cheng** for your encouragement and all the fruitful discussions about my thesis work. In a nutshell, I could not have wished for a better doctoral advisor. Additionally, I would like to chase this opportunity to thank my former supervisor **Prof. Jörg Conradt** who gave me the opportunity to join the Technical University of Munich family and to get the ball rolling in this Ph.D. journey.

My deepest gratitude goes to my mentors **Dr. Christoph Richter** and **Dr. Emmanuel Dean** who supported and coached me in various aspects. Without their constant guidance and criticism, I wouldn't be where I am today.

I would like to also thank our research collaborators **Prof. Nitish Thakor** and **Prof. Tassos Benzarios**, for their guidance and support during my 3-month research visit to their lab at the National University of Singapore. A BIG thank you goes to **Luke Osborn** and **Andrei Dragomir** who introduced me to the amazing research area of pain perception in the human brain. Moreover, I would like to thank all great and bright colleagues at the Institute for Cognitive Systems lab for these fun years. A particular thank you goes to **Constantin Uhde** for critiquing my animation videos and figures. A special thank you goes also to **Nicolas Berberich** who has been a great office mate and who usually comes up with great ideas,

such as setting up a TUM initiative to participate in the Cybathlon competition 2020.

I would like to thank **my parents** for their support and guidance. My siblings **Tesnim** and **Bacem** for believing in my skills and for their emotional support. A special thank you goes to my **loving companion** for her unconditional love and for pinpointing my weaknesses as well as my imperfections.

Last, I would like to thank my funding agency **German Academic Exchange Service (DAAD)**, which made this work possible by providing continuous financial support throughout the whole journey. Along the same lines, I want also to thank the **TUM Faculty Graduate Center for electrical and computer engineering (FGZ-EI)** for their support. Last, I would like to thank, you, **the reader**. I hope you enjoy reading this thesis and find this work relevant as much as I do.

Dedication

To my parents without whom none of my success would be possible.

List of Figures

List of Tables

List of Publications

1 Journal Articles

J6: Z. Tayeb, A. Dragomir, J. H. Lee, N. Abbassi, E. Dean, A. Bandla, R. Bose, R. Sundar, A. Bezerianos, N. Thakor, G. Cheng, Distinct spatio-temporal and spectral brain patterns for different thermal stimuli perception, Nature Scientific Reports, 2022.
DOI: https://www.nature.com/articles/s41598-022-04831-w

J5: L. E. Osborn, K. Ding, M. A. Hays, R. Bose, M. M. Iskarous, A. Dragomir, **Z. Tayeb**, G. M. Lèvay, C. L. Hunt, G. Cheng, R. S. Armiger, A. Bezerianos, M. S. Fifer, N. V. Thakor, Sensory stimulation enhances phantom limb perception and movement decoding, Journal of Neural Engineering, 2020.
DOI: https://iopscience.iop.org/article/10.1088/1741-2552/abb861

J4: Z. Tayeb, R. Bose, A. Dragomir, L. Osborn. N. Thakor, G. Cheng, Decoding of Pain Perception using EEG signals Towards a Real-Time Reflex System in Prostheses, Nature Scientific Reports - Journal, 2020.
DOI: https://www.nature.com/articles/s41598-020-62525-7

J3: Z. Tayeb, J. Fedjaev, N. Ghaboosi, C. Richter, L. Everding, X. Qu, Y. Wu, G. Cheng, J. Conradt, Validating Deep Neural Networks for Online Decoding of Motor Imagery, Sensors, 2019.
DOI: https://www.mdpi.com/1424-8220/19/1/210

J2: J. Behrenbeck, **Z. Tayeb**, C. Bhiri, C. Richter, O. Rhodes, N. Kasabov, S. Furber, G. Cheng, J. Conradt, Classification and Regression of Spatio-Temporal EMG Signals using NeuCube Spiking Neural Network and its implementation on SpiNNaker Neuromorphic Hardware, Journal of Neural Engineering, 2019.
DOI: https://iopscience.iop.org/article/10.1088/1741-2552/aafabc

J1: Z. Tayeb, N. Waniek, J. Fedjaev, L. Rychly, C. Widderich, C. Richter, J. Braun, M. Save-

riano, G. Cheng, J. Conradt, Gumpy: A Python Toolbox Suitable for Hybrid Brain-Computer Interfaces, Journal of Neural Engineering, 2018.
DOI: https://iopscience.iop.org/article/10.1088/1741-2552/aae186/meta

2 Peer-Reviewed IEEE Conference Papers

C3: B. Specht, **Z. Tayeb**, E. Dean, R. Soroushmojdehi, G. Cheng, Real-Time Robot Reach-To-Grasp Movements Control Via EOG and EMG Signals Decoding, The International Conference on Robotics and Automation (ICRA 2020), 2020.
DOI: https://ieeexplore.ieee.org/abstract/document/9197550

C2: Z. Tayeb, P. Jakovleski, Z. Chen, J. Lippert, P. L. Pradas, D. Lee, and G. Cheng, Enabling the sense of touch in EMG-controlled hand prostheses using vibro-tactile stimulation, International IEEE EMBS Conference On Neural Engineering (NER'19), San Francisco, CA-USA, 2019.
DOI: https://ieeexplore.ieee.org/document/8717124

C1: Z. Tayeb, E. Erçelik, and J. Conradt, Decoding of Motor Imagery Movements from EEG Signals using SpiNNaker Neuromorphic Hardware, 8th IEEE International Conference on Neural Engineering (IEEE EMBS), 2017.
DOI: https://ieeexplore.ieee.org/abstract/document/8008341

3 Workshop/Conference Abstracts and Poster Presentations

P3: Z. Tayeb and G. Cheng, Hybrid Brain-Computer Interfaces for Neuroprosthetics Control, Summer School on Neurorehabilitation (SSNR), 2018.

P2: Z. Tayeb, E. Erçelik, J. Conradt, Decoding of EEG Signals using Spiking Neural Networks on SpiNNaker Neuromorphic Hardware, Bernstein Conference, 2017.

P1: Z. Tayeb, J. Conradt, An embedded neuromorphic controller for a neuro-prosthetic hand, Bernstein Conference, 2016.

Contents

1 Introduction

1.1 Motivation

Brain-computer interface (BCI) [1, 2, 3, 4, 5, 6, 7, 8] is a specific human-machine interfacing system that monitors users' brain activity and translates them into actions that can be used for operating different external devices. The study by J. J. Vidal in 1973 [1] is considered the first attempt to capture electroencephalography (EEG)-evoked electrical activity of the cerebral cortex [9]. Since then, we have witnessed the rapid evolution of BCI systems to cover a wide range of applications [9], including brain fingerprinting for lie detection [10], detecting drowsiness for enhancing people working performances [11], controlling virtual reality [12] and playing video games [13], as well as controlling and steering humanoid robots [14, 15, 16]. Specifically, BCIs can be used to support people with motor disabilities and helping them interact with their surroundings [17, 18]. The main idea is that an individual can accomplish tasks only by thinking about specific actions. For instance, motor imagery describes a mental process in which a person imagines to perform a certain action, e.g., opening or closing the left or right hand and the BCI system translates this action into commands to control external assistive devices [19, 18]. Unfortunately, BCI systems based on motor imagery are still slow, inaccurate, and present several limitations [3, 20]. Hence, the hybrid approach, relying on the combination and simultaneous decoding of multiple biosignals is considered an alternative to circumvent these limitations [21, 22], in particular when decoding complex hand and arm movements (e.g. reach-to-grasp movements). For instance, electromyography (EMG)-based systems have been widely used as assistive technologies for different applications such as prosthetics control [23, 24]. Although being faster, more reliable, and less noisy, solely relying on EMG interfaces has some remaining drawbacks. Usually, the EMG interface requires extensive training, and recorded signals are sensitive to the electrode placement, they show variations when it comes to muscle fatigue, and cannot be used by everyone due to physical (e.g. spinal cord injury or amputation) and technical reasons. Combining EMG with other signals, such as EEG or electrooculography (EOG) is a good approach to compensate for some disadvantages when relying on a single input signal. Aside from this, BCI represents a good approach for the bidirectional

control of neuroprostheses. This connection between BCI and prosthetic devices has become widely acknowledged and has gained momentum over the last decades [25, 19, 18]. In this context, BCI could be used in both efferent and afferent pathways not to only improve the feedforward control of these devices, but more importantly, to understand and quantify the human brain perception of different external stimuli, en route to developing a real-time withdrawal reaction system in sensory-enabled prostheses. As was previously suggested in the study by Tombini et al. [26], closed-loop BCI control, particularly the understanding of external sensory stimuli perception dynamics and their related cortical activations, using EEG signals, can also lead to the alleviation of the phantom limb pain (PLP) syndrome [26], which is affecting more than 42% of amputee population [27].
This thesis focuses on both sides of the equation (efferent and afferent), investigating, in different ways, how BCI can be used to improve the control of prosthetic devices. On the one hand, EEG signals were decoded and combined with EOG and EMG for the real-time feedforward control of reach-to-grasp movements of two different robotic arms. The essential motivation behind this first contribution was to develop a software system that can be used for real-time control of assistive devices, particularly prosthetic hands. Such a hybrid BCI system could be of importance, specifically when other biosignals such as muscle activity cannot be decoded and/or accessed. On the other hand, the same brain signals were used to quantify and understand the brain perception and processing of two different types of sensory stimuli, ranging from innocuous sensation to very intense transcutaneous electrical nerve and thermal stimulations. Overall, analyzing and classifying neural activity evoked by external sensory stimuli when using sensory substitution was motivated by the idea of developing a real-time withdrawal reaction system when interacting with prostheses, which can increase sense of embodiment [28]. The long-term vision of this research is illustrated in Figure 1.1.

1.2 Research questions

There are a couple of research questions we set out to answer within this thesis. In fact, the design of those research questions contributed to the validation of different approaches to improve the feed-forward control of robotic prostheses, the validation of sensory substitution methods [29], as well as the investigation of the human brain perception and processing of different external sensory stimuli, induced by electrical and thermal stimulations. Within this thesis, we found out that one way to approach these central questions is to exploit EEG brain activity (alongside other biosignals (EOG, EMG)) when controlling robotic arms and perceiving the external sensory stimulation. As will be demonstrated in this thesis, the hybrid

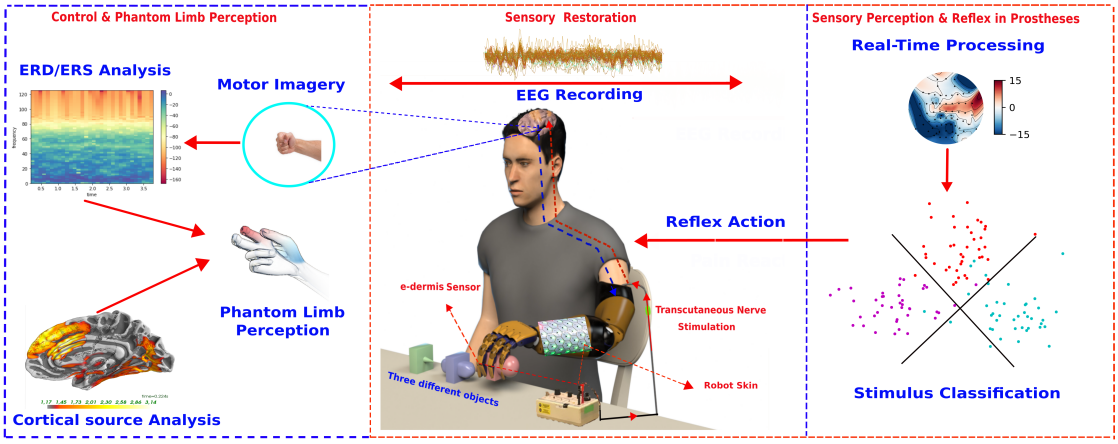

Figure 1.1: Long-term vision of the proposed research

concept presents a good approach for real-time control, as well as for the human brain perception quantification of external sensory stimuli. Figure 1.2 summarizes the different questions for both the feed-forward and the sensory/perceptual path. These questions are structured as follows:

- Would it be possible to validate a robust and real-time BCI/EEG-based control decoding system that works across different subjects?
- Would the fusion, combination, and classification of multiple biosignals allow a more accurate and real-time decoding of complex hand and arm movements?
- Would it be possible to validate and test a non-invasive vibrotactile sensory substitution modality to encode the stiffness of different objects during real-time and bidirectional control of the prosthesis?
- Would it be possible to identify specific features in EEG brain recordings and detect differences in neural activity between sensory stimulation that ranges from a light touch to a very intense tactile sensation?
- How does the brain respond to a wide range of thermal stimuli ranging from extremely cold to very hot stimulations?

1.3 Challenges

In this section, we discuss the different technical challenges encountered in this thesis. These challenges served as the basis for this work and defined its areas of focus.

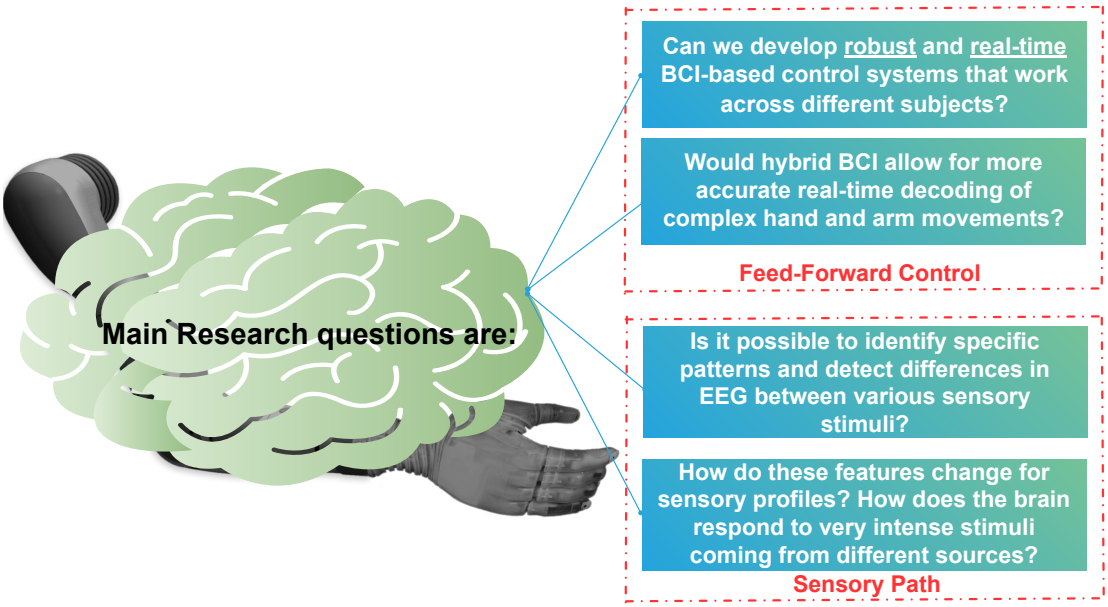

Figure 1.2: Overview of main research questions proposed in this thesis.

High non-stationarity of EEG signals when used for real-time decoding applications

Overall, when processing EEG signals, the main challenges are data collection, feature extraction, model implementation, and the design of a robust online system architecture [30, 31]. Specifically, one of the major technical challenges we faced in this work was the low signal-to-noise ratio (SNR) of EEG recordings [3, 30]. Although EEG has a good temporal resolution [3, 31], it suffers from high non-stationarity and low spatial resolution. As a result, it is often time very challenging to localize the sources and responsible regions of this brain activity. This is due to the fact that EEG signals are captured from multiple channels and from several time segments. Similarly, EEG non-invasive recordings are susceptible to many factors in the environment that are unrelated to the underlying cerebral activity, such as eye blinking and movement artifacts [32]. The fact that EEG data is vulnerable to artifacts, even in well-controlled conditions [30, 32], makes it challenging to perform real-time decoding of such a signal. Hence, these problems have resulted in difficulties to reliably decode these signals and accurately classify the users' intentions. When processing EEG data, researchers have relied on multiple de-noising approaches [3], such as independent component analysis (ICA) [33]. The problem with such de-noising algorithms is that noisy channels are usually excluded using manual visual inspection, and hence they are less suitable for real-time applications. Other research papers have focused on dimensionality

reduction techniques, such as principal component analysis (PCA) to de-noise collected EEG data [34]. However, the main issue with dimensionality reduction techniques is the high risk of losing a significant amount of information from EEG data. In different studies of this thesis, both PCA and ICA were also used for data pre-processing but they were further combined with an automatic feature selection approach [35] to select the best subset of discriminative features before being fed to the machine learning classifier. After successfully processing EEG data, extracting robust features and decoding the recorded signal are another challenging steps. For that, standard machine learning techniques have been widely investigated to classify EEG data for different purposes and applications [3, 18, 19, 36]. These previous attempts to analyze EEG signals focused on well-characterized sensorimotor data features. However, BCI seems to have stagnated in improving the reliable decoding of these signals using standard processing techniques. Along the same lines, the high dimensionality and non-stationarity of EEG data lead to the heavy computational effort, making them not suitable for real-time applications. Our validated decoding models based on deep learning (presented in **chapter 3**) achieved less inter-trial and inter-subject variability and demonstrated the possibility to be used in real-time when controlling two-state movements of a robotic arm, compared to traditional machine learning approaches. The best performing deep learning model presented in chapter 3 was thereafter used and tested in the next follow-up study, presented in chapter 4 of this thesis.

EEG's low spatial resolution hinders the decoding of complex movements

Another technical challenge when decoding EEG data is the limited spatial resolution of this signal, which hinders the decoding of complex movements when interacting with robotic arms, such as reach-to-grasp movements. Previous studies attempted to classify, by solely using EEG signals, different hand and arm movements for neuroprosthetics control [37, 38, 39]. However, all these studies reported difficulties to achieve a good decoding accuracy when solely relying on motor imagery movements, as well as many challenges when testing the EEG-based BCI system in real-time. In **chapter 4**, another approach based on by relying on multiple biosignals fusion and decoding was demonstrated in this thesis to circumvent the limitation of solely relying on EEG decoding, and the low spatial resolution problem.

High inter-variability across subjects hinders the development of robust and generalized BCI decoding models

In the feedforward control, different challenges were faced in this thesis, particularly when recording, processing, and decoding different biosignals. Sweat, slight changes in the elec-

trode's positions during recording and the difference between the participants (muscle tissues, gender, age, etc.) drastically decreased the quality of recorded signals (EEG, EMG, EOG) and resulted in deteriorated classification accuracy when decoding them. Overall, this high inter- and intra-subject variability between trials and across subjects made the problem more intricate and led to unreliable models which cannot be generalized across different human subjects. Along the same lines, data pre-processing had to be customized to each individual to reach good overall performance. These observations and challenges are not surprising, as they were extensively reported in the literature [40, 41, 42]. To overcome these challenges, subjects had to be trained to correctly and repetitively perform the different tasks, and new experimental paradigms were validated in this thesis.

Sensory substitution stimuli perception and processing in the human brain remain elusive

On the other side of the equation, a major part of this thesis focused on the general quantification of the human brain activity when perceiving and processing innocuous and very intense sensory stimuli. EEG changes induced by electrical stimulation, using brain data collected from one amputee, was studied and investigated in **Chapter 6**. Additionally, EEG changes induced by five distinct thermal stimuli, using brain data collected from three able-bodied participants, was studied in **Chapter 7**. In both studies, one of the major technical challenges was to find robust spectral, spatial, and temporal features that can be used to effectively decode and discriminate between external sensory stimuli, ranging from gentle touch to very intense stimulation conditions. This is due to the highly complex and interconnected mechanisms involved in processing intense sensory stimuli [43]. Additionally, the perception dynamics of these stimuli seem to be harbored in different brain regions, making their understanding elusive. Along the same lines, literature has been extensively relying on functional magnetic resonance (fMRI) [43] and Positron emission tomography (PET) [44] to understand and classify external sensory stimuli. To overcome this challenge, this thesis focused on advancing new EEG signal processing methods, as well as validating existing decoding models and source localization techniques, to provide an understanding of sensory perception and processing, taking, therefore, an advantage of the good EEG compromise between the level of invasiveness and the high temporal resolution [3].

1.4 Thesis overview

This dissertation primarily focuses on the field of hybrid brain-computer interface (BCI) and its application in upper-limb prostheses control. For that, two main control approaches were investigated throughout this work. For the feed-forward control, the following approaches were explored:
(1) Only EEG brain activity was used to decode in real-time two state movements for a robotic arm control. For that, we validated different real-time EEG decoding models, such as convolutional neural networks and standard machine learning classifiers. The successful decoding of two classic motor imagery movements led to a follow-up study where the decoding of reach-to-grasp movements was investigated.
(2) Additional biosignals were classified and used either alone or with EEG for real-time decoding of other arm movements (mainly reach-to-grasp movements).

For the sensory feedback and the perceptual path, the following approaches were investigated:
(3) Vibrotactile sensory substitution modality was used to encode and convey back the stiffness of different manipulated objects. This work resulted afterwards in two follow-up studies, where EEG was used to quantify brain activity when receiving external sensory stimulations.
(4) Particularly, we first shed light on the brain perception of very intense electrical stimulation in an amputee. The motivation was to first understand how does the brain perceive innocuous and very intense stimuli, encoding object's curvature and level of sharpness. This would lead to a better understanding of how we can develop a withdrawal reflex system in prostheses, mimicking the one in the nervous system.
(5) In a second study, the focus was on the decoding of the human brain's perception of five different thermal stimuli, ranging from extremely cold to extremely hot stimuli.

1.5 Thesis contribution

The work presented in this thesis utilizes emerging techniques and methods spanning from signal processing, to advanced machine learning techniques for interpreting changes in non-stationary biosignals. Figure 1.3 gives an overview of the work being presented in this thesis. Main original contributions:

- Validated different deep learning models (convolutional neural networks, recurrent neural networks) and compared them to classic machine learning approaches for controlling in real-time a robotic arm through the decoding of two motor imagery move-

ments from EEG signals. We sought to validate these deep learning models by changing and adapting their internal architectures to process and learn from complex EEG time series data.

- To circumvent the limitation of solely utilising EEG signals for control, we tested a hybrid BCI machine learning algorithm for real-time decoding of complex reach-to-grasp movements. The classic machine learning algorithm combines and processes various biosignals at the same time, which are EEG+EMG and EOG+EMG signals.

- Validated a noninvasive vibrotactile stimulation paradigm to provide artificial sensation (sensory substitution) and encode different objects' stiffness, while simultaneously controlling, using EMG signals, multiple hand poses and force levels of a prosthetic hand.

- Validated different processing and machine learning algorithms, as well as EEG source reconstruction, for brain activity interpretation and localization when perceiving different thermal and electrical sensations (encoding objects' level of sharpness and temperature).

- Investigated, using EEG signals, the question of how does the brain perceive very intense sensory stimuli (for both extreme thermal stimulation and unpleasant electrical stimulation)? This was validated using data collected from an amputee, as well as data gathered from three able-bodied subjects.

Open-source software & Datasets: Besides direct research contributions, and as part of this research work, an open-source BCI software was designed and made publicly available for researchers (https://github.com/gumpy-bci). This software has been used by different Universities across the world [46, 47, 45, 48, 49], including Technical University of Munich (TUM), University of Houston, Johns Hpokins (JHU), and the National University of Singapore (NUS). Similarly, this software has been used by a number of students at TUM in different scientific events and lectures, such as the CyberTUM; a TUM initiative to participate in the Cybathlon 2020. Aside from that, this work resulted in different datasets, which were made publicly available for download [50].

1.6 Thesis outline

This thesis is structured as follows:

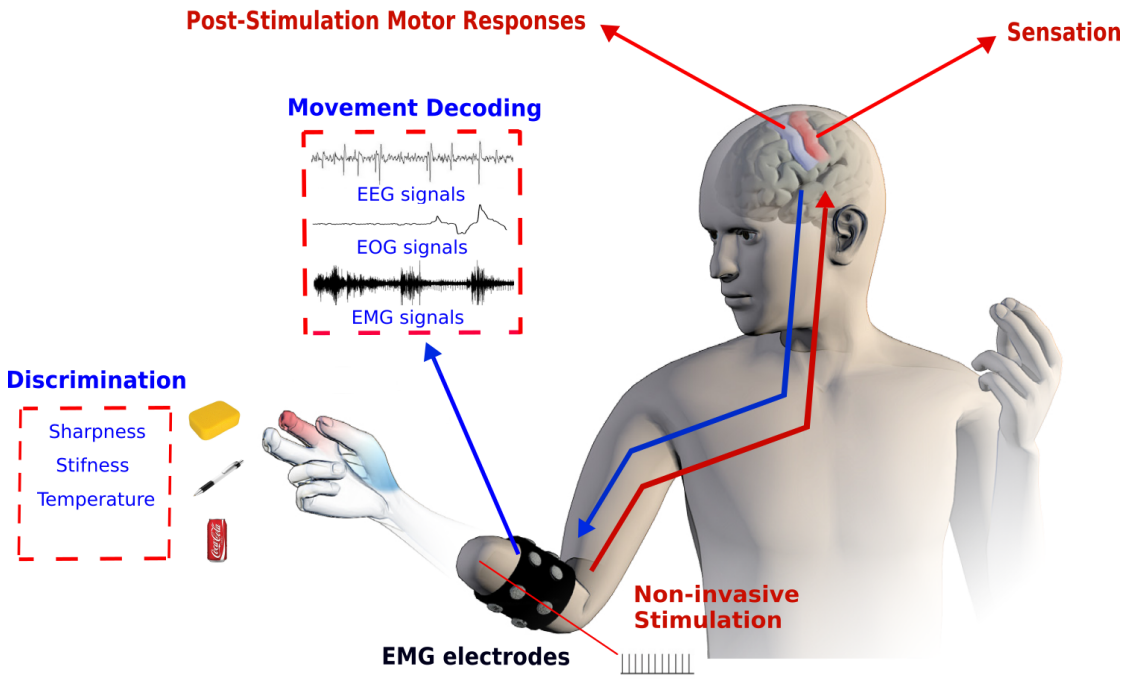

Figure 1.3: Proposed system overview. Adapted with permission from [45]

- **Chapter 2 - Background:** This chapter gives an introductory overview of EEG signals, BCI, hybrid BCI, current state of sensory feedback in prostheses, as well as somatosensory evoked potentials brain responses.
- **Chapter 3 - Investigation of real-time EEG decoding for a robotic arm feedforward control:** This chapter explores how EEG can be used to decode two motor imagery movements for a real-time robot arm control.
- **Chapter 4 - Processing and decoding of multiple biosignals for real-time human-robot interaction:** In this chapter, I describe how multi-biosignal processing and hybrid BCI can be deployed to decode complex reach-to-grasp movements, circumventing the limitation of using EEG as the single decoded input signal.
- **Chapter 5 - Investigating vibro-tactile stimulation to enable the sense of touch in sEMG-controlled hand prostheses:** In this chapter, I describe how vibrotactile sensory substitution can be used to encode different objects' stiffness and translate them into artificial sensations and sensory substitution.

- **Chapter 6 - Decoding of EEG signals when perceiving three distinct sensory stimuli induced by TENS: An amputee case study:** In this chapter, I show how EEG can be used to quantify different sensory stimuli ranging from innocuous to a very intense stimulus.
- **Chapter 7 - The development of distinct brain patterns for five thermal stimuli perception reveals an anticipatory brain activity:** This chapter shows how EEG can be used to quantify different thermal stimuli ranging extremely cold to extremely hot sensations. I also investigate brain activity at the source level, reporting new findings of the main autonomic functions of different brain regions.
- **Chapter 8 - Conclusion and Outlook:** This chapter summarizes the thesis, discusses the major ramifications and proposes future research directions and possibilities.

2 Background

This chapter lays the foundation of the different terminologies and research disciplines of relevance to this thesis. First, this background chapter introduces the general concept of brain-computer interfaces (BCI) in Section 2.1, and we particularly focus on EEG-based BCI in Section 2.1.1. Second, the concept of hybrid BCI, by relying on additional biosignals, such as surface electromyography (sEMG) and electrooculography (EOG), is described in Section 2.1.2. On the other side of the spectrum, the concept of neural sensory prostheses, and the different stimulation techniques for the afferent pathway are introduced in Section 2.2. Particularly, we focus on intense sensory stimuli in sensory-enabled prostheses and we discuss their perception and processing in the human brain in Section 2.3. Last, brain motor responses, so-called somatosensory evoked potentials, are described and reviewed in Section 2.3.2. A more in-depth literature review is also presented as related work in each individual chapter.

2.1 Brain-computer interfaces (BCI): Overview

Paralyzed people need the ability to control assistive devices such as wheelchairs, spellers, prosthetics, or exoskeletons to improve their quality of life and ensure their independence [51]. The employed control interface needs to be reliable, robust, accurate, intuitive, and safe to reduce the additional mental and physical workload for them and to make sure that users and their environment stay unharmed. Many paralyzed people have no or solely limited ability to use their bodies as well as their peripheral nervous systems. Depending on the severeness of the respective body-impairment, BCI represents a promising solution to connect the brain directly to assistive devices [52]. The BCI field is still in its infancy with most research works published in the last 20 years [8]. Broadly speaking, BCI is a specific human-machine interface (HMI) system that monitors users' brain activities and translates them into actions that can be used to operate different external devices. Such a system allows paralyzed patients to control, without directly using conventional neuromuscular pathways, arm prostheses, wheelchairs, and various robotic devices. BCIs can be used in a wide range of applications, particularly to support people with motor disabilities by interact-

ing with their surroundings. The essential idea is that an individual can accomplish tasks only by thinking about a specific action. Aside from that, BCI can also provide an additional communication channel for able-bodied people to interact with their environment by controlling external robotic devices, augmenting, thereby, their body capabilities well beyond their needs [3]. A BCI system consists of three stages (as illustrated in Figure 2.1): (1) signal acquisition by either invasively or non-invasively recording the electrophysiological signals, which are used as inputs for the second stage. (2) signal processing and feature extraction by removing signal artifacts using different filtering and machine learning techniques, in order to find thereafter a proper representation of the acquired signal, hence glean the useful information into feature vectors. (3) signal decoding by classifying the signal and translates it into real-time control commands to execute the user's desired task. Overall, brain activity can be measured using different sensing techniques [53], such as functional magnetic resonance imaging (fMRI), magnetoencephalography (MEG), electrocorticography (ECoG), local field potential (LFP), or EEG. Different possible control signals are illustrated in Figure 2.2. Depending on the sensing technique, different signals, such as electrical potentials, magnetic fields, or electrical activity, are captured. Particularly, EEG has become one of the most widely used techniques for BCIs due to its non-invasive and comparably affordable character, as well as its high temporal resolution. In general, one should distinguish between different types of BCIs: (1) Invasive BCI relies on microarrays or surgically implanted electrodes. (2) Non-invasive BCI described in Section 2.1.1 is based on recording techniques that do not require any implantation. (3) Passive BCI which is a non-invasive class that, unlike active BCI, does not rely on any voluntary or intentional control by the user and decodes spontaneous mental states without a necessary sense of awareness. (4) Unlike the passive system whose purpose is to serve the able-bodied population, the active BCI focuses more on decoding the user's voluntary or intentional control usually linked to rehabilitation and motor tasks. Overall, although BCI technology has seen significant improvements during the last years [3], it still exhibits several limitations compared to other conventional control modalities, such as keyboards or joysticks [54]. As a result, this hinders its potential to be clinically deployed [3].

2.1.1 EEG-based BCI

BCIs are being widely used to control robotic arms and prostheses [19, 18]. For closed-loop control, an additional BCI stage can be introduced, so-called the feedback stage, where brain activity is used to quantify sensory perception and processing. In this thesis, we only considered EEG signals for both efferent and afferent pathways.

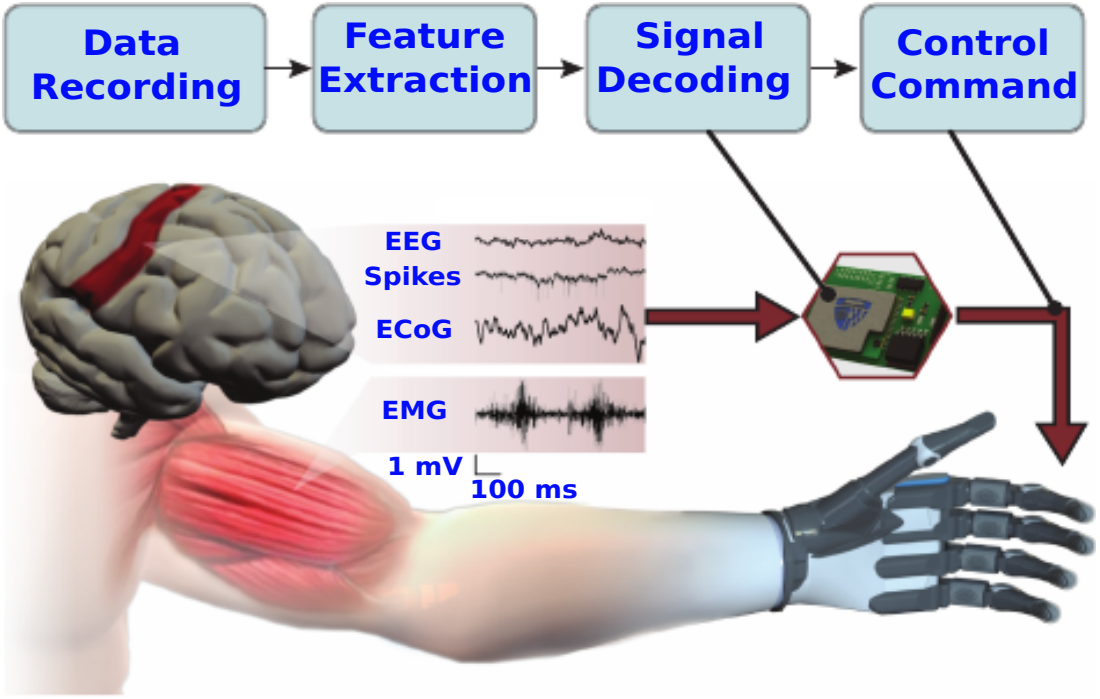

Figure 2.1: Overview of neuronal signals for arm prostheses control. Adapted with permission from [55]

2.1.1.1 Signal source and recording principle

As aforementioned, a wide range of sensing techniques has been used in BCI. The BCI system properties highly depend on the signal source, such as the temporal/spatial resolution, health risk for users, the recording device, and the signal acquisition price. Although the main focus of this thesis is on EEG, we compare and summarize the main differences between these different signals in Table 2.1. Overall, the synaptic activity within the brain induces and generates locally detected potentials, so-called, local field potential (LFP). These potentials elicit, within the nerve tissue, ionic currents that can be recorded in intra- and extra-cellular space [56]. This summed voltage propagates to the skull and results in a detectable signal on the scalp. This scalp signal (EEG) was initially discovered by Hans Berger in 1924 [57], and it captures electric fields arising from the superposed neural activation with a relatively poor spatial resolution. Both dry and wet electrodes can be used to record EEG signals, with clear advantages and drawbacks for each recording method [20]. The placement of electrodes used for EEG recording has been standardized in the international 10/20 recording system. It is worth noting that the use of ”10” and ”20” describes the actual dis-

tances between adjacent electrodes, which are either 10% or 20% of the total front-back or right-left distance of the skull (e.g. from the nasion to inion) [58]. Depending on the electrode placement and the used paradigm, different patterns can be extracted from the EEG and could be used in different BCI applications.

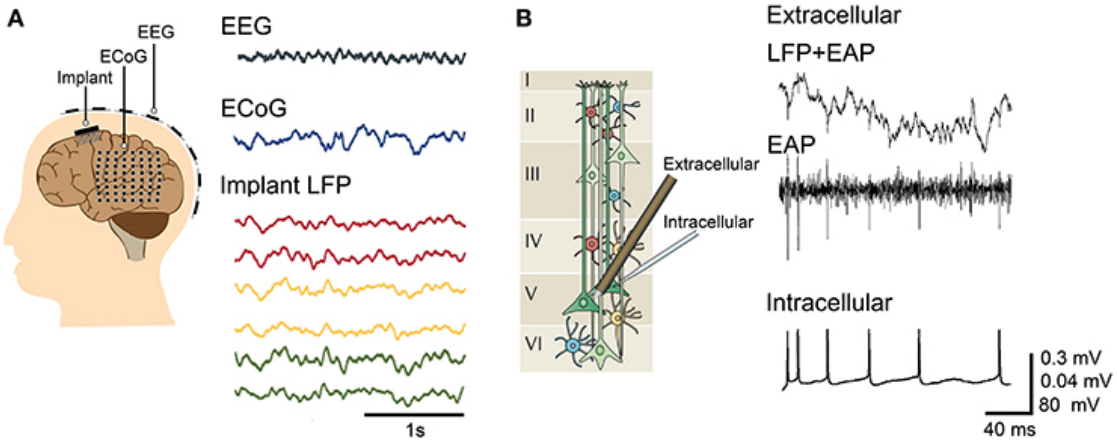

Figure 2.2: Standard electrophysiological BCI signals and recording methods. Taken with permission from [59].

Table 2.1: Qualitative comparison of different brain sensing techniques: ECoG, fMRI, and EEG [60].

Characteristics	**ECoG**	**fMRI**	**EEG**
SNR	High	High	Low
Health risk	High	Low	Low
Spatial resolution	High	High	Low
Temporal resolution	High	Low	High
Price	Low	High	Low
Manageability	compact	Bulky	compact

2.1.1.2 EEG signal processing pipeline

EEG signals are usually sampled at 256 Hz or 512 Hz [3]. First, epochs of fixed size should be extracted from initially recorded trials. All channels are first notch-filtered at 50 Hz or 60 Hz depending on where the recording sessions took place. Thereafter, EEG data is usually filtered between 2 and 60 Hz to preserve all interesting frequency bands' information.

Depending on the decoding task, a wide range of feature extraction methods have been proposed in the literature, such as the logarithmic power of a specific frequency band [61], which is often used in motor imagery decoding tasks, common spatial patterns [62], and simple time-domain statistical features for ERP decoding [3]. Different classification methods spanning from classic machine learning [36], spiking neural networks [61], to advanced deep learning techniques [63] can be used to decode EEG signals, depending on the task complexity [64].

2.1.1.3 Artifact removal

EEG signals can be easily contaminated by different noise sources, such as interference with power line, EMG signals when moving your head/neck during the recording, as well as EOG coming from blinking or eye movements. Hence, artifact removal is an important step when processing EEG data [3]. For that, we shed light in this section on the most widely method for removing EEG artifacts. Independent component analysis (ICA) is a blind-source separation technique which extracts all the different underlying signals that produced the recorded EEG data, including noise [65]. Overall, ICA attempts to unmix signals that are mutually exclusive to each other [33]. The ICA can be modelled with the equation 2.1, where **A** is the unknown mixing matrix, **x(t)** are the observed signals, and **s(t)** are the source signals. The overall objective is, therefore, to recover the original signals by only using the observed signals [65]. ICA is considered the most widely used artifact removal method for EEG signals [3].

$$x(t) = A \cdot s(t) \tag{2.1}$$

2.1.1.4 Source localization and reconstruction

To reconstruct EEG signals and analyze them at the source level, several steps are usually performed. First, cortical surface reconstruction are estimated. Second, the forward solution and the forward model are computed using the boundary-element model (BEM) [66]. Thereafter, the regularized noise-covariance matrix, which gives information about potential patterns describing uninteresting noise source, is estimated. Afterward, the singular value decomposition (SVD) of the matrix composed of both estimated noise-covariance and the source covariance matrix is computed. Overall, for EEG source localization, the standardized low-resolution brain electromagnetic tomography (sLORETA) [67] is widely used [3]. The Standardized low-resolution brain electromagnetic tomography (sLORETA) [67] computes the EEG distribution across the full brain volume. The sLORETA method offers a

smooth and good deep sources localization. It provides a unique solution to the inverse problem using a defined cost function [68] F as follows:

$$F = \|\phi - KJ - c1\|^2 + \alpha\|J\| \tag{2.2}$$

where ϕ defines the electrical potential recorded from the 64-electrode scalp EEG signal, K defines the lead field matrix, J represents the measured current density, α defines the positive regularization parameter, $c1$ is constant, and $\|.\|$ is the Euclidean norm.

2.1.1.5 Decoding methods

Both standard machine learning techniques and deep learning have been used in BCI, particularly when decoding EEG signals. Here, we focus on proposed motor imagery classification methods. Over the last two decades, support vector machine (SVM) and linear discriminant analysis (LDA) have been the most commonly used decoding methods and they achieved up to 75% accuracy when classifying three motor imagery movements [69, 70]. For a comprehensive literature review, readers are referred to this study on the state-of-the-art of EEG-based BCI classification [4]. Deep learning for EEG decoding has gained popularity and has been recently widely used in BCI. Both recurrent neural networks (RNN) and convolutional neural networks (CNN) have been investigated [63]. For instance, Stober et al. evaluated and benchamrked different methods for learning discriminating features with deep learning techniques [71] by training convolutional auto-encoders on EEG data. Alex Greaves implemented a RNN and a fully-connected NN to classify EEG that was recorded when subjects where exposed to either 2D or 3D stimuli and he achieved 72% accuracy [72], whereas Schirrmeister et al. investigated the design choices of CNN architectures for decoding motor imagery movements from raw EEG data and he reached 71% accuracy [73]. For more in-depth review on deep learning for BCI, readers are urged to check out this study [63].

2.1.1.6 Event-related potentials and motor imagery

Depending on the BCI task and paradigm, different event-related potential (ERP) patterns can be detected from EEG recordings. Here, we describe the most widely used EEG patterns in BCI applications.

- **Steady State Evoked potentials (SSVEP)**: Steady-state visually evoked potentials (SSVEP) can be detected while observing a flickering visual stimulus as shown in [46]. They show up in EEG signals as a peak in the frequency spectrum of the electrodes

over the primary visual cortex at the respective stimulus frequency. Although the frequency rate and the number of distinguishable frequencies are limited, SSVEP-based BCIs have a high SNR, information transfer rate (ITR), and require almost no user training. However, an external stimulus is required, which makes this BCI dependent on the environment and limited to synchronous control tasks [3].

- **P300**: P300 are positive brain deflections, where p stands for positive and 300 ms is the post-stimulus latency to detect these patterns. This ERP is elicited when applying the oddball paradigm and can be measured most strongly over the parietal lobe. P300-based BCIs show the same stimulus dependence as SSVEP-based BCIs and are also restricted to synchronous control tasks. Furthermore, they require extensive training of the classifier and are generally slow. This is due to the multiple recordings that must be averaged to visualize the wave deflection [74].
- **Motor Imagery (MI)**: Motor imagery (MI) BCIs use event-related desynchronization (ERD) [75] in the sensorimotor rhythm (mu band 8-12 Hz and beta band 13-30 Hz) recorded over the primary motor cortex M1 to recognize preparation, execution, or imagination of motor actions [75]. MI BCIs are self-paced and do not depend on external stimuli, which enables them to be employed in asynchronous communication tasks. They are suited for continuous control tasks, but require extensive training of the classifier as well as the user, particularly if the movements are not executed but only imagined. Furthermore, they are slow and the low spatial resolution of the EEG only allows for the recognition of coarse body movements. Studies have shown that left arm, right arm, and foot movements can be recognized and distinguished while the accuracy drops significantly when increasing the number of classes, and hence single finger movements cannot be accurately distinguished [76].

2.1.1.7 MI-based BCI limitations

BCI seems to have stagnated in improving MI movements decoding [3, 77]. In fact, the most challenging task is how to extract reliable features from noisy EEG data, which are characterized by low signal to noise ratio (SNR) and poor spatial resolution. Additionally, EEG performance and interaction speed is lower compared to other control modalities and good results usually require extensive training sessions. Another approach to control assistive devices is the use of EMG signals, another HMI technology which measures the users' muscular activity. Due to its easy usability and high SNR (signal-to-noise ratio) it has a high potential to serve as a control channel for assistive devices. However, EMG is only recordable if the user has any residual muscular activity and, even then, it is highly sensitive to

muscle fatigue which prevents long-term usage even for healthy people. Trying to overcome these problems of a single modality control has led to the development of multimodal solutions, so-called hybrid brain-computer interfaces (hBCI). An hBCI combines a conventional BCI with at least one additional control modality, which can either be another BCI signal (pure hybrid), a physiological signal such as EMG (physiological hybrid), or another device such as a keyboard or joystick (mixed hybrid) [54].

2.1.2 Hybrid approach: Combining multiple signals

This section primarily focuses on EEG, EOG, and EMG combination. In general, hBCI can be split into simultaneous and sequential systems [21]. In a simultaneous hBCI, the two input channels are classified at the same time. Either both channels are used redundantly encoding the same information which shall increase the accuracy of the overall system, or the channels are used in a complementary paradigm to increase the complexity of the control scheme. In a sequential hBCI, one system (BCI or EMG) serves as the input of the second system, usually as a switch or toggle device, to change the state of the system and thereby increase the control complexity and authority of the user over the system [22]. An example of a hybrid system, where EEG, EOG, and EMG are decoded and fused, is illustrated in Figure 2.3.

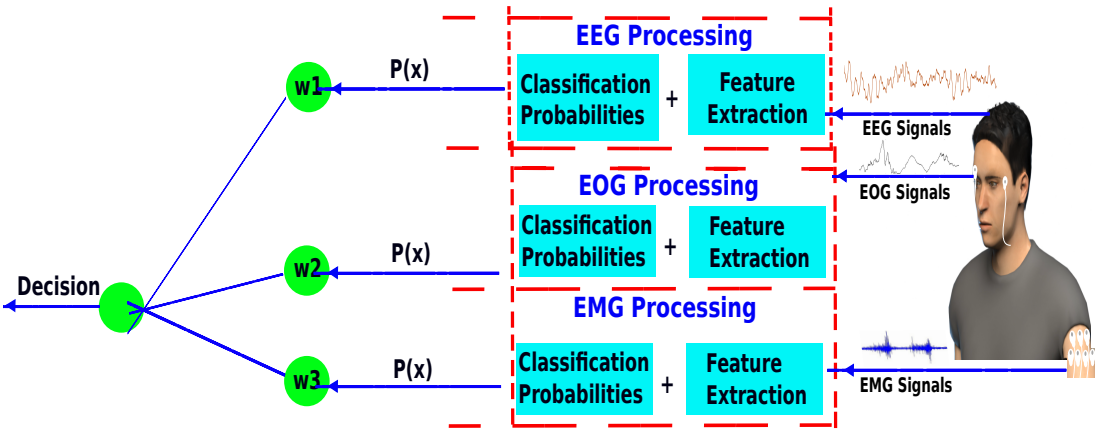

Figure 2.3: A hybrid BCI system based on EEG, EOG, and EMG decoding.

2.1.2.1 Electrooculography (EOG)

EOG is a sensing method for measuring the corneo-retinal standing electrical potential. This potential arizes from hyperpolarizations and depolarizations between the cornea and

the retina [78]. The resulting signal is called the electrooculogram. The main applications of such a signal are in ophthalmological diagnosis and in recording eye movements for BCI control [78]. EOG is relatively easy to process compared to EEG or EMG signals, thanks to its high SNR. However, one of the limitations of EOG is being more sensitive to electrodes' positions and can easily interfere with noise.

2.1.2.2 Surface electromyography (sEMG): Origin and recording principle

sEMG is recorded non-invasively with electrodes by measuring the electrical potential on the skin above a muscle, which is the end of the signal pathway in a motor command. The electrical potential is created by the sum of action potentials arriving in muscle fibers close to the electrode. Although the transmission through the skin induces noise into the signal, the SNR is comparably high and muscular activity is reliably detectable (accuracies up to 100%)[24]. Even for people with muscular dystrophy, residual muscular activity can be recognized. sEMG provides a fast, asynchronous, and reliable communication channel. However, sustaining sEMG signals for a long period imposes physical work, especially for motor-impaired people, and decreases the classification accuracy as muscle fatigue changes the amplitude and frequency spectrum of the EMG signal. There are also symptoms such as tremor and lesions which inhibit the use of sEMG data [79]. The EMG processing steps are similar to EEG signals, with the difference being that EMG is considered less noisy than non-invasive brain signals. Generally, an experimental paradigm is shown to the participant with the different hand/arm gestures to be recorded during the experiment. Pairs of liquid-gel ECG electrode (model: 50×48 mm) covering the forearm and/or upper-arm in a ring-like fashion are usually used, as illustrated in Figure 2.4.

2.1.2.3 sEMG signal decoding algorithms

This section provides a review of the different algorithms used to classify sEMG signals spanning from classic machine learning techniques to SNN approaches. In [23], the authors investigated the decoding of sEMG in the early stages of reach-to-grasp movements (pre- reach-to-grasp) for prosthetic hand control. Five different grasp types were classified, namely precision disk, tripod, thumb-2 fingers, thumb-4 fingers, and ulnar pinch. In the paper, the authors showed that an accuracy of 90% of the final grasp gesture was obtained $0.5\,$s after the movement onset. In [80], the authors used the NeuCube spiking model to classify six different hand gestures, namely hand closed, hand open, wrist flexion, wrist extension, ulnar and radial deviation. Various feature-extraction techniques were investigated (Mean-absolute value (MAV), Wavelength (WL) and combined features). Overall, a classi-

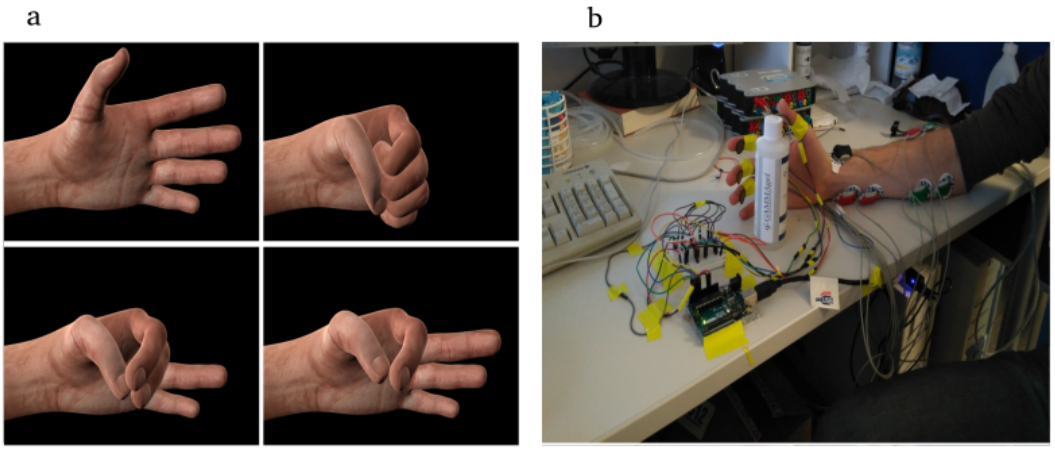

Figure 2.4: Example of sEMG recording paradigm. (a) Different hand gesture renderings prompting subjects. (b) Recording setup of sEMG signals during grasp movements [46].

fication accuracy of 95.3% was reached and the authors showed that the spiking approach outperformed classic machine learning methods when using MAV features. It should be noted, however, that an accuracy of only 68.7% was attained when classifying raw sEMG data without hand-crafted features. Table 2.2 compares different studies for sEMG classification and summarizes the obtained results. For a more comprehensive survey of sEMG classification, readers are referred to [24].

Table 2.2: Comparison of different sEMG classification studies and their achieved accuracy

Reference	Nº of classes	Extracted features	Classifier	Accuracy
[81]	7	RMS	Adaptive Fuzzy classifier (ANFIS)	86%
[82]	10	RMS and WL	Linear discriminant analysis (LDA)	98.87%
[83]	5	RMS	Support vector machine (SVM)	73%
[84]	6	MAV and WL	LDA	91.64%
[85]	3	TD	Fuzzy logic (FL)	97%
[86]	4	MAV, WL and RMS	Artificial neural networks (ANN)	89.2%
[87]	-	Time-Frequency (TF)	SVM	90%
[88]	4	TF	ANFIS	92%
[80]	6	MAV, WL	NeuCube	95.33%
[80]	6	Raw data	NeuCube	68.7%
[89]	9	spiking neurons	Neural networks	92.3%

2.1.2.4 Literature review of hybrid BCI systems: EEG and EMG data fusion as a case study

There have been several reviews on hBCI in general such as [90], with a few studies that focused on the combination of EEG and EMG [91]. The following collection shall extend

these works and add more recent approaches, as well as it focuses on motor imagery (MI) based-BCI give the interest in restoring abilities in motor-impaired patients. Similar to [92], proposed solutions are classified into simultaneous and sequential hBCI.

Sequential hBCI: sEMG as binary EEG-switch: In [92], a 16-channel MI-BCI is supplemented with a bipolar EMG in a sequential manner as a brain switch to enable split attention for the user. The MI BCI is used to send control commands (left or right) to a telepresence robot. A shared control approach is used to deal with low-level navigation tasks such as obstacle avoidance. If no turning command is recognized by the system, the robot drives straight. This mental state of intentionally sending no commands is called intentional non-control (INC) and can be mentally exhausting for subjects when performed over a longer period. Therefore, a switch was implemented using the EMG channel to start and stop the telepresence robot and simultaneously disable BCI commands. In a feasibility study, four healthy subjects drove the telepresence robot along eight predefined trajectories and paused on an audible cue using the EMG. The results were compared to the original BCI paradigm, in which the robot is stopped by the shared control and restarted by any delivered BCI command. Due to the low number of participants, no significant results could be obtained. However, the experiment showed that the use of EMG as a brain switch instead of INC could only be sustained for around 20 seconds, reduced the perceived workload of the users. There was one false positive command in the EMG signal but it could easily be reversed by the user. On average, the participants preferred the hybrid BCI version over the BCI plus INC version because they reported less effort and more authority over the robot. However, no specific measures on the accuracy, speed, or training were given in this paper.

Sequential hBCI: sEMG as multi-class toggle switch for EEG control: A progression of the binary switch control paradigm can be seen in [93] where the EMG is used as a multi-class toggle switch based on the duration of the muscle activation. In this study, the subjects are controlling a two-dimensional computer mouse cursor using a six-channel BCI with electrodes spread across the left and right rear half of the head, and a bipolar EMG on the master muscle. The BCI classifier recognizes left and right commands which are mapped to the horizontal (up or down) or vertical (left or right) dimension depending on the state of the system. The EMG is used to turn on/off the system and to turn the control direction from horizontal to vertical and vice versa. 60 subjects were used in an experiment to test the system. It is not mentioned if the subjects were healthy or impaired in any kind. The results showed accuracies of 88% for left-brain activation, 90% for right brain activation, and 100% for EMG. This study shows how a control paradigm for BCI can be extended using a multi-class toggle switch based on an additional EMG channel to allow for more complex

controls. Last, in [92], a physiological, simultaneous, hBCI was tested with respect to its general usability and the influence of muscle fatigue on the overall system accuracy.

2.2 Neural Sensory Prostheses

In humans, somatic receptors in the upper-limb are divided in cutaneous and subcutaneous mechanoreceptors, muscle and skeletal mechanoreceptors, nociceptors and thermal receptors. This complex sensory system encodes and transmits to the Central Nervous System information about four major modalities: touch, proprioception, pain, and temperature. There are several sensor options possible for integration in myoelectric hands, capable of measuring a wide range of information like: contact, force, pressure, position, slip and temperature [94]. Overall, sensory feedback seems to play a vital role in prosthetic arms acceptance and embodiment [95]. Over the last few years, researchers have shown that it is possible to complete the sensory feedback loop by either providing natural sensations back to amputees through invasive simulations of their residual nerves [96], such as directly targeting nerves with implantable electrodes, or through non-invasive artificial sensation known as sensory substitution [97], like transcutaneous electrical nerve stimulation (TENS) [98] and vibrotactile stimulation [99]. When providing sensory feedback, median, ulnar, and radial nerves are the essential ones to be targeted. The focus of the next section is solely on non-invasive methods, which are relevant to this thesis.

2.2.1 Stimulation techniques

2.2.1.1 Vibrotactile stimulation

Vibrotactile feedback allows the user to learn the association of certain vibrations at the skin surface with one of the physical properties of manipulated objects by the prosthetic hand. It typically uses small commercially available vibrators, which are usually small and lightweight. Vibration amplitude and frequency are the two main features of the stimulus, but other features like pulse duration, shape, and duty cycle can also be modulated to transmit other information [100]. The user's ability to discriminate between different amplitude thresholds depends on several parameters, including the frequency and location on the body. According to previous research results [101], the sinusoidal waveform performed the best, the bicep region was determined to be the most comfortable and achieved the highest accuracy, desensitization occurred after 66 seconds, and batteries lasted for 1-3 days. A research group also tested a system, where vibrators were placed on a sports glove on the remaining hand [99]. It leads to fast learning, but makes it difficult to use two hands

at the same time, which happens quite often. Generally, according to the current research literature, the user performs better with vibrotactile feedback rather than without it. He/She often has better control of grip force and reduces the number of errors in task execution, feels a higher sense of embodiment in their prosthetic, and needs a lower cognitive load to pick up objects compared to using visual feedback alone [102]. Using vibrotactile feedback to communicate hand velocity, point of contact and grasping force without visual feedback even provided enough information for the subjects to pick up objects without seeing them [103]. However, there are some noticeable drawbacks in vibrotactile feedback, for example, the extra delay is approximately 400 ms to start generating vibration, which can decrease the sense of embodiment [102], and hence a shorter delay must be achieved. The optimal and ideal time delay must be at most 100 ms, according to some research results [101].

2.2.1.2 Electrical stimulation: TENS

The principle of electrotactile (or electro-cutaneous) feedback is the stimulation of afferent nerve endings through a local electrical current, thus producing sensations within the skin. Multiple features can be easily and reliably controlled including the intensity, pulse width, frequency, and location of stimulation (with multiple electrodes), which leads to a higher bandwidth being available. The great advantages of electrotactile devices are being safe and comfortable to use [104], the electrodes are slim and lightweight, they consume less power and they respond faster than vibrotactile systems as there are no moving mechanical parts, thus having a better potential to improve sense of embodiment. Indeed, a study by Ismail and Shimadi [102] suggests that the feedback delay should be less than 200 ms to maximize the sense of body ownership, which gives an advantage to using electrical stimulation and may limit the effectiveness of mechanotactile systems. However, the minimum sensation threshold and pain threshold is different for each person so they must be personalized, and the placement of the electrodes can highly modify the perception of electrotactile information [105], since movements as small as 1mm have an influence [106]. Additionally, the comfort and dynamic range of electrotactile stimulation depend on skin conditions [105], which means that recalibration of thresholds is required every time electrodes are placed on the user and that the pulse width, frequency, and amplitude may need readjusting to achieve the same perception each time. Furthermore, potential problems can arise from interference between myoelectric sensors for control and electrotactile stimulation when the stimulation sites are close to the EMG electrodes [102].

2.2.1.3 Thermal stimulation

Temperature is one of the main information provided by our skin sensors and provides extra information about the environment, as well as any potential dangers or warnings that involve heat. Producing heat on the upper-arm to match and encode the temperature detected at the prosthetic hand was the only method of temperature feedback found within the literature, via a Peltier element, which drew upon a large amount of power [107]. As response times are currently very long, a prediction algorithm based upon initial measurements was developed to speed up measurements. It could however play a great role in providing a patient with a good sense of embodiment [95].

2.2.1.4 Phantom hand

Amputees can sometimes not only experience phantom limb pain, but also phantom limb sensations [108, 109]. These sensations can be exploited to transmit sensory feedback. In particular, amputees can have locations known as phantom digits that, when touched, trigger a sensation that corresponds in their brain to touching their missing finger. Those phantom digits provide a natural and efficient pathway to communicate a variety of sensations without requiring any training. The use of TENS can induce sensations in these phantom digit locations for all fingers. The feelings of pressure, pressure and vibration, vibration, tingling and numbness in the corresponding finger location were induced through TENS applied to the phantom digit location. These sensations were stable for an 11- month period for nine amputees [106]. The ideal size and spacing of TENS electrode to stimulate a phantom hand map were studied by the authors [110]. According to them, the bigger electrode, the wider range of sensations produced, but a higher current is then required and further space between electrodes is needed. So they concluded that having an electrode sizing of 5-7 mm was a good compromise based on their preliminary investigations. In terms of performance, patients with a complete phantom hand map recognised multiple sites of feedback with a higher success rate than those who had an incomplete or no phantom hand map [110]. It can also provide up to five separate somatotopicaly matched feedback pathways that feel natural to the user according to studies. However, all amputees do not present phantom digit locations, their location and size can vary [111]. Therefore, this approach cannot be applied uniformly to all patients, as it is unsuitable for those without phantom digits and individual customisation, such as customised prosthetic sockets, will also be required for those who possess them. This approach seems quite promising in terms of sense of embodiment potential for those who can profit from it, though.

2.2.1.5 Noxious stimulation

The somatosensory cortex provides exteroceptive sensations for perception and reaction to external stimuli. Different skin cells and mechanoreceptors are responsible for conveying tactile information. Among the tactile perception components, the sense of pain is an important one. Despite its undesired nature, pain is a vital mechanism to protect ourselves from damaging stimuli. When touching a harmful object, different sensations ranging from innocuous to extremely noxious can occur. Pain can be useful for various purposes and can allow amputees to interpret useful information about the surrounding environment, such as preventing damage to the fingertips or cosmesis, a skin-like covering, of a prosthetic hand. To encode the sense of pain, particular nociceptors are involved [112]. These nociceptors are dedicated sensory afferents in both glabrous and non-glabrous skin responsible for conducting tactile stimuli that we perceive as painful [112]. Overall, nociceptors, free nerve endings in the epidermal layer of the skin, act as high threshold mechanoreceptors (HTMRs) and respond to noxious stimuli through $A\delta$, $A\beta$ and C nerve fibers [113], which enables our perception of tactile pain. The importance of the sense of touch [114] has spurred research in this direction. Notwithstanding the considerable advances in developing sensory feedback methods to encode pressure [114], proprioception [115], and texture [116], temperature and pain have not been extensively investigated [117]. Similarly, investigation of perception and processing of pain in the human brain have been limited to fMRI and invasive studies [43] and have been rarely investigated in the context of prostheses [117].

2.3 Noxious sensation perception and processing in the brain

2.3.1 Noxious sensation perception and processing review

The quantification of human pain using various neuroimaging techniques have been previously investigated [118, 119]. Despite the enormous number of studies in this area [120, 121], understanding nociceptive processing in the human brain is still challenging [122]. This is due to the complex brain mechanisms and areas involved in the processing of noxious stimuli. Authors in [123] investigated perceptual, motor, and autonomic responses to short noxious heat stimuli using EEG and confirmed that pain perception is subserved by a distinct pattern of EEG responses in healthy subjects. fMRI was used in [43] to demonstrate pain-related activation of the anterior cingulate cortex (ACC) and the posterior cingulate cortex (PCC) during transcutaneous electrical nerve stimulation (TENS) in healthy participants. Additionally, authors in [124] showed the important role of the parietal lobe in pain perception and understanding. Positron emission tomography (PET) [125], and invasive record-

ings [126], were exploited to investigate exogenous pain perception and processing. In the study by [127], frequency analysis were investigated and an EEG frequency analysis was performed and event-related desynchronization (ERD) of alpha were detected during performing hand immersion into cool and extremely cold water (noxious). Readers are referred to **chapter 6 & 7** of this thesis for a more comprehensive literature review of pnoxious sensation processing studies investigating the use of EEG and other neuroimaging techniques for quantification and interpretation.

2.3.2 Somatosensory Evoked Potentials for closed-loop BCI systems

Somatosensory evoked potentials (SEPs) are EEG patterns, which have been extensively used to evaluate the somatosensory pathway in closed-loop BCI systems. Notwithstanding the advances in imaging studies, such as MRI, SEPs have gained popularity, particularly in clinical studies [128]. Overall, SEPs are time-locked potentials evoked by electric stimulation of the sensory or mixed peripheral nerves [128]. Predictable SEPs of certain values (amplitude and latency) are elicited as a result of an electric stimulation applied over the peripheral nerves.

2.3.3 Upper-limb SEPs

Median and ulnar SEPs are usually recorded in post upper extremities stimulation. They are frequently evoked by TENS applied over the skin of the chosen nerve. In Figure 2.5, Epi represents the side of stimulation, whereas EPc refers to the contralateral side. C5s refers to the fifth cervical vertebral spinous process, CPi refers to the centroparietal and ipsilateral to the side of stimulation, CPc the contralateral side of it, and AC is the noncephalic anterior cervical, just above the thyroid cartilage in the midline. As shown in Figure 2.5, there are different SEP patterns that can be subcortically detected. SEPs may be useful in predicting response to spinal cord stimulation (SCS) for the treatment of chronic neuropathic pain [128].

2.4 Summary

This chapter defines the main terminologies and concepts investigated throughout this thesis. Additionally, it provides the reader with a literature review of the main fields and subfields covered in this work, while following a chronological order of their appearances in the different studies presented in this thesis. First, the general concept of BCI was presented

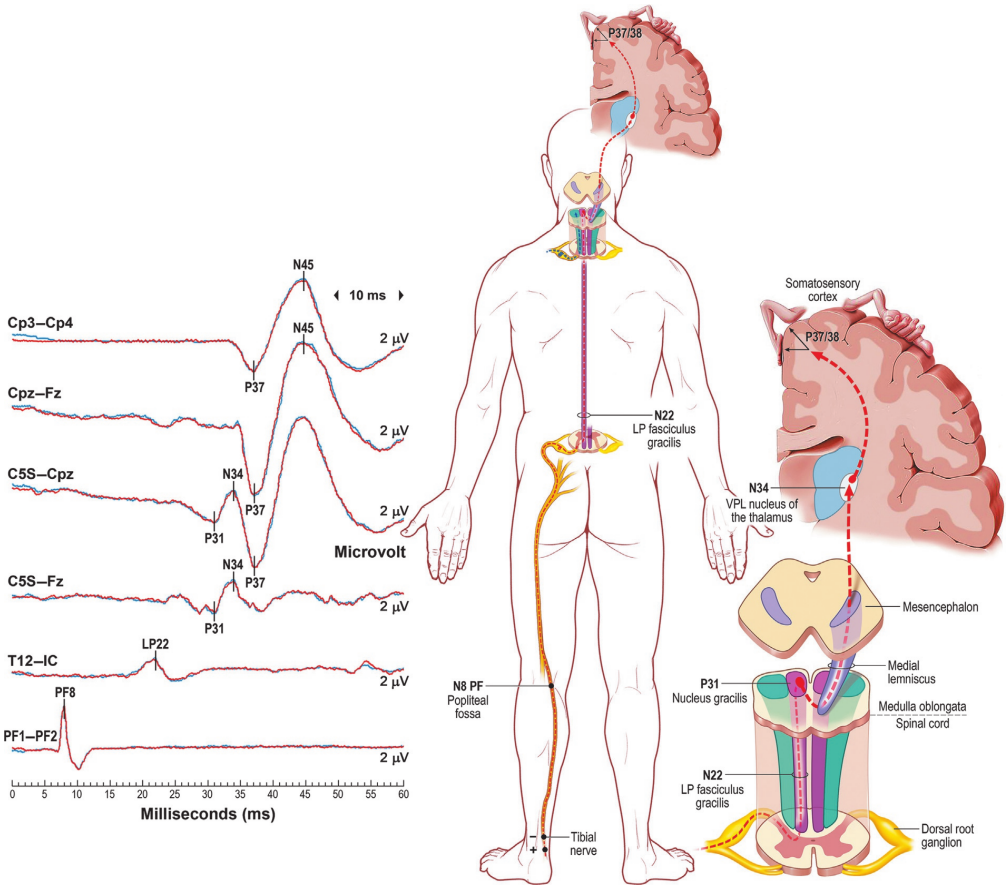

Figure 2.5: (Left) 6-Channel left tibial SEP with annotated SEP peak waveforms and their corresponding recording channels. (Middle and right) Left tibial SEP/somatosensory pathway: pathway neuroanatomy and corresponding SEP peak generators. Black arrows (on mesial postcentral gyrus) show P37 variable dipole orientation. Taken with permission from [128]

with a particular focus on non-invasive BCI and the most widely used EEG signal processing and decoding methods. This section lays the foundation of chapter 3 and introduces the reader to the main methods used in that chapter. Second, the concept of hBCI and the different investigated biosignals were presented and reviewed. hBCI is the main field that was studied and validated in Chapter 4. As this thesis investigates both sides of the equation, neural sensory prostheses alongside the different non-invasive stimulation methods were thereafter described. This neural sensory prostheses section was introduced to give the reader a notion of the field of sensory-enabled prostheses and the various stimulation techniques used in the literature to restore the sense of touch, and hence it lays the foundation of chapter 5. Last, a review of the concept of noxious sensation perception and

processing in the human brain with a literature review was presented. This section helps the reader understand all the underlying mechanisms and methods for noxious sensation processing, as well as compare this thesis' results presented in chapters 6 and 7 with the ones previously reported in the literature.

3 Investigation of real-time EEG decoding for a robotic arm feedforward control

This chapter is made up of content adapted with permissions from the manuscript Zied Tayeb, Juri Fedjaev, Nejla Ghaboosi, Christoph Richter, Lukas Everding, Xingwei Qu, Yingyu Wu, Gordon Cheng, Joerg Conradt, "Validating Deep Neural Networks for Online Decoding of Motor Imagery." Published in Sensors, 19(1), 210 (2019). DOI: https://www.mdpi.com/1424-8220/19/1/210

Author Contributions: Zied Tayeb conceptualized the idea, designed the research, and wrote the paper. Zied Tayeb and Juri Fedjaev did the recording and the processing of EEG data as well as the development and test of the different standard machine learning and deep learning models. Zied Tayeb and Xingwei Qu performed the real-time experiment. Nejla Ghaboosi, Christoph Richter, Lukas Everding, Xingwei Qu and Yingyu Wu contributed to the implementation of the different models and assisted in writing the paper. Gordon Cheng and Joerg Conradt contributed to designing the research and revised the manuscript.

Note: This research paper has been recognized as an outstanding publication by being selected as an "Editor's Choice Article" in the journal "Sensors".

3.1 Study overview

As described in the previous chapter, non-invasive, EEG-based BCI on MI movements translate the subject's motor intention into control signals through classifying the EEG patterns caused by different imagination tasks, e.g., hand movements. This type of BCI has been widely studied and used as an alternative mode of communication and environmental control for disabled patients, such as those suffering from a brainstem stroke or a spinal cord injury (SCI) [3]. Notwithstanding the success of traditional machine learning methods in classifying EEG signals, these methods still rely on hand-crafted features [3, 51, 18]. The extraction of such features is a difficult task due to the non-stationarity of EEG signals,

which is a major cause by the stagnating progress in classification performance. In this study, we validated three deep learning models: (1) A long short-term memory (LSTM); (2) a spectrogram-based convolutional neural network model (CNN); and (3) a recurrent convolutional neural network (RCNN), for decoding motor imagery movements directly from raw EEG signals without (any manual) feature engineering. We changed the internal architectures of these models to be able to process and learn from complex EEG time-series data. Overall, this study served as a survey of methods by implementing different learning algorithms for decoding MI movements from EEG, and comparing their performances with three deep learning models. Decoded movements were translated, thereafter, into commands to control the robotic arm. Results were evaluated on our own publicly available, EEG data collected from 20 subjects and on an existing dataset known as 2b EEG dataset from "BCI Competition IV". Overall, better classification performance was achieved with deep learning models compared to state-of-the art machine learning techniques. We underpin this point by demonstrating the successful real-time control of two states (left, right) of a robotic arm using our CNN based BCI. An overview of the proposed system is illustrated in Figure 3.1. To sum up, this work validates different deep neural network architectures for real-time control of a robotic arm using two decoded left and right motor imagery movements.

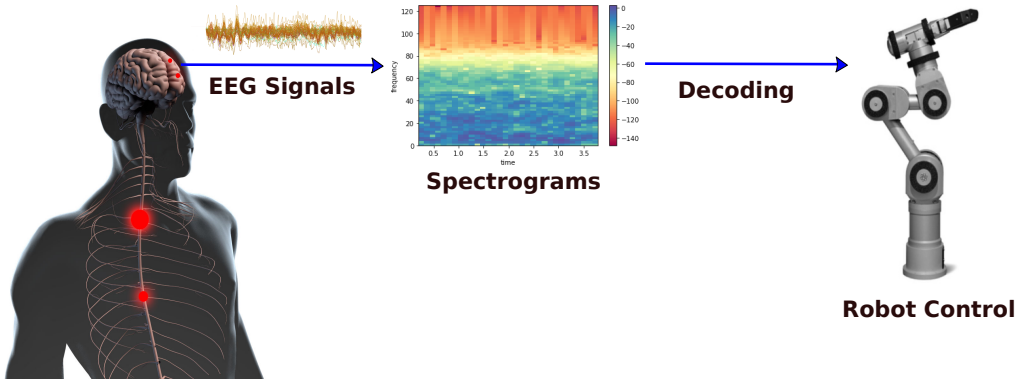

Figure 3.1: The proposed BCI system overview for real-time feed-forward control of robotic arms.

3.2 Introduction

Non-invasive BCIs are intelligent systems which enable users to communicate with external devices such as computers or neural prostheses without the involvement of peripheral nerves and muscles [3, 18]. Therefore, BCIs can be applied to a wide range of applications in order to support people with motor disabilities by interacting with their surroundings.

BCI-based MI describes a mental process in which a person solely imagines to perform a certain action, e.g., opening or closing the left or right hand without executing it. Our study demonstrates the successful and real-time decoding of two MIs, namely left-and right-hand movements. It shows the potential of using deep learning methods to classify binary MI movements in EEG signals. Three different deep learning models were investigated and tested. These models are LSTMs [129], CNNs [130], and RCNNs which have until now been rarely investigated for BCI applications [131, 64, 132, 133]. In addition, five different machine learning classifiers (Support Vector Machine (SVM), K-Nearest Neighbours (KNN), Logistic Regression (LR), Naive Bayes (NB), Quadratic Linear Discriminant Analysis (QLDA), and Decision Tree (DT)), were implemented and used for the purpose of comparison with the aforementioned deep learning methods.

3.2.1 Overview of convolutional neural networks (CNN)

In the following subsection, CNN is introduced and its basic structure is defined. Moreover, an overview of different CNN architectures, design choices, and the most widely used strategies to train them are described.

3.2.1.1 Basic CNN architecture & design choices

Overall, CNN consists of three different stages. In the first stage, known as convolutional layer, the spatial information of the input is extracted through convolution and displayed in a feature map. Therefore, the input is element-wise multiplied with a set of weights as a filter or kernel and the multiplication outputs are summed up to a single element of the feature map [130]. These weights are used in the same constellation at every position of the input, thereby each neuron is connected to only a small number of regions of the input volume and only one parameter set has to be learned. In the second stage, a non-linear activation function is applied to the obtained feature map, which increases the non-linear properties of the overall network. The most commonly used operation is the Rectified Linear Unit (ReLU) defined as $f(x) = max(0, x)$, which replaces all negative values of the feature map with zero. In the last stage, the input dimensionality is further reduced with pooling. Pooling replaces the input at a location with a summary statistic of nearby inputs. There are several types of pooling operations such as max, average or sum. Max-pooling is prevalent and partitions the input into non-overlapping sub-regions. In each sub-region, the maximum value is chosen whereas the other elements are discarded. Pooling does not only decrease the input scale but also the number of parameters but also helps control overfitting

and reduce the computation time. An additional property of pooling is that it makes the representations invariant to slight translations of the input data.

3.2.1.2 CNN training

The CNN output is produced by a fully connected layer. However, this output has to be further transformed in order to assign a specific imagined movement to the obtained feature vector. Assume the given datasets $D_i = \{(X^1, y^1), ..., (X_i^N, y_i^N)\}$ with a total number of N_i trials for subject i. X_j represents the input signals of trial j and y_j the corresponding class label from a set of K class labels L. $\forall y^j : y^j \in L = l_1, ..., l_k$, where each label l_k represents a corresponding imagined movement. In the final classification layer, the conditional probabilities of a class label l_k are computed using the softmax function

$$p(l_k \rfloor f(X^j; \theta) = \frac{exp(f_k(X^j; \theta))}{\sum_{k=1}^{K} exp(f_k(X^j; \theta))} \tag{3.1}$$

where θ are the parameters of the classifier $f_k(X^j; \theta)$. The aim is to obtain a parametric classifier f that can assign the correct label to unseen trials. Therefore, the optimization problem based on the cross-entropy loss function can be described by:

$$\theta* = \arg\min_{\theta} \sum_{j=1}^{N} loss(y_j, p(l_k \rfloor f_k(X^j; \theta))) \tag{3.2}$$

In order to train a CNN, the parameters θ are optimized by computing the gradient of the loss function via backpropagation [73, 130]. Two different methods to train a CNN are usually used. Trail-wise training is a standard strategy that uses whole trials as input and the corresponding trial labels as targets. Unlike trail-wise training, cropped training splits the trials into crops using sliding input windows within the trial. In this case, the label of a crop is identical to the label of the corresponding trial. Cropped training yields a larger number of training examples for the network. Particularly for EEG decoding, only a relatively small data set is available, and hence this strategy is an effective way to increase the training set size.

3.2.2 Overview of long-Short Term Memory (LSTM)

In the following subsection, LSTM network is introduced and its basic structure is defined. Moreover, an overview of the most widely used strategies to train LSTM networks are described.

3.2.2.1 Basic LSTM architecture & design choices

LSTM is based on the cell state which acts as a memory, and how much memory will be wiped out is controlled by the forget layer. Gates are composed of a sigmoid layer and a pointwise multiplication operation, and whose essential function is to preserve the relevant information and abandon the rest. How much old memory will be preserved and abandoned is controlled by the output of forget gates. The memory will be completely erased when the output is 0, whereas it will be fully preserved when the output value is 1. The general information flow is regulated by the "input gate layer", which has a similar function as the "forget gate layer". The previous cell state is controlled by the 'forget gate layer', while the new candidate cell state is controlled by the 'input gate layer'. The new cell state is computed based on the controlled previous cell state and controlled new candidate cell state. After that, the new output will be calculated by the new cell state and the output gates [129]. Mathematically, LSTM can be described as follows:

$$i_t = \sigma(W_{xi}x_t + W_{hi}h_{t-1} + W_{ci}c_{t-1} + b_i) \tag{3.3}$$

$$f_t = \sigma(W_{xf}x_t + W_{hf}h_{t-1} + W_{cf}c_{t-1} + b_f) \tag{3.4}$$

$$c_t = (f_t c_{t-1} + i_t \tanh(W_{xc}x_t + W_{hc}h_{t-1} + b_c) \tag{3.5}$$

$$o_t = \sigma(W_{xo}x_t + W_{ho}h_{t-1} + W_{co}c_t + b_o) \tag{3.6}$$

$$h_t = o_t \tanh(c_t) \tag{3.7}$$

where σ is the logistic sigmoid function, i, f, o, h and c denote, input gate, forget gate, output gate, hidden vectors and cell activation vectors, respectively.

3.2.2.2 LSTM training

Generally speaking, the most common training algorithm for recurrent neural network (RNN) is known as backpropagation through time (BPTT). BPTT is a gradient-based method for training RNN. Since RNN can be considered as a layered, feed-forward network with shared weights, if unfold the RNN, then obviously, the forward pass builds up a stack of the activities of all the units at each time steps. Neural network training is challenging, particularly for RNNs [134]. Two main problems may arise when training RNNs, known as exploding and vanishing gradient problems [134]. For exploding gradient, the gradient norm increase largely during the training phase and lead to an exponential growth of long-term components, whereas for vanishing gradient, the norm and long-term component converge ex-

ponentially to 0. To address both problems, several methods have been proposed in the literature. To mitigate the explosion problem, authors in [135] proposed an approach that limits the gradient to a certain threshold, so-called gradient clipping, and is mathematically described as follows:

$$\hat{g} \leftarrow \frac{\partial \epsilon}{\partial \theta} \tag{3.8}$$

if $\|\hat{g}\| \geq$ threshold then

$$\hat{g} \leftarrow \frac{threshold}{\|\hat{g}\|}\hat{g} \tag{3.9}$$

end if

Authors in [135] also proposed a regularization method to solve the gradient vanishing problem. The main concept is to use a regularization term in such a way that the back-propagated gradient neither exponentially increase nor decrease in magnitude, and hence preserves the gradient in one relevant direction.

3.2.3 Review of different deep learning approaches for EEG decoding

This section provides a review of different deep learning approaches developed for EEG decoding. In fact, recent research has shown that this type of BCI could allow both healthy and severely paralyzed people to control a robotic arm [18] or to move around in a wheelchair [91]. Notwithstanding the good results obtained by previous work focusing on the well-known MI patterns [18], the progress in BCI performance has been stagnating in the last decade. Apparently, the design of more stable classification methods is comprising formidable challenges. One of these challenges stems from the low SNR of EEG signals as well as the high variability in recordings across trials and within participants, which puts the identification of more robust and discriminative features in EEG-based BCI systems under high demand.

3.2.3.1 Elman neural network

Elman Neural Network (ENN) is a type of RNN which was proposed by Jeff Elman. In ENN with multiple stacked hidden layers, each hidden layer receives the activation of previous hidden layers per timestep. The feedback connection enables the neural network to capture the temporal patterns, which makes RNN a success in natural language and video processing. In [72], an Elman network was used to classify EEG data during a 3-D perception task where subjects were viewing either 2D or 3D images. In that paper, the authors showed that an accuracy of 58% can be achieved using ENN whereas, an accuracy of 72% was obtained on the same task using a two layer multilayer perceptron (MLP). Due to the unsatisfactory obtained performance, the authors concluded that it is not straightforward to apply

RNNs to EEG data. In [136], the authors used an ENN to classify MI mental tasks such as right hand clenching, observing a tumbling cube and silently singing a song. Three subjects participated in the study and the accuracy varied drastically across subjects from 58.8% to 93.3% reflecting a large intra-subject variability. In [137], authors used only two electrodes, namely, C3 and C4, and achieved 93% accuracy for four MI movements classification using an ENN.

3.2.3.2 Long-short term memory (LSTM)

Since ENNs share the same weight matrix at different time steps, this can cause either the gradient exploding or the gradient vanishing problem. To address that, Sepp Hochreiter and Jürgen Schmidhuber proposed the LSTM network in 1997 [129], where simple neurons are replaced by LSTM units each consisting of four main components: an input gate, a neuron with a self-recurrent connection, a forget gate and an output gate [129]. In [133], with the use of a large EEG dataset (109 subjects, 26.4 million samples) from PhysioNet eegmmidb [138], an accuracy of 95.53% was achieved for five MI movements classification problem using seven RNN layers with two LSTM layers. It is worth noting that unlike [136], the results obtained using PhysioNet dataset were stable over all subjects. However, the developed model was only tested with the large scale PhysioNet dataset and no evaluation on their own recorded dataset was performed. In [139], five different recurrent neural network architectures were tested for hand motion recognition of grasp-and-lift task from EEG signals, namely LSTM, GRU, MUT1, MUT2, and MUT3 [140]. The obtained results showed that MUT3 performs the best with an accuracy of 88.82%, whilst LSTM and GRU had an accuracy of 87.89% and 88.60%, respectively.

3.2.3.3 Convolutional neural networks (CNN)

Classifying raw EEG data without hand-crafted features is a challenging problem. Schirrmeister et al. [73] pioneered the development of a CNN capable of decoding movement-related information from raw data. Deep as well as shallow-CNNs with various design choices were introduced and compared. The first convolution of the deep-CNN (dCNN) was split into a convolution across both time and space. In the shallow-CNN (sCNN), the first two layers were split into temporal and spatial convolutions. The rest of the networks contained standard convolution-max-pooling blocks with a softmax classification layer at the end. Moreover, the results were evaluated on different frequency bands. By including recent advances from the field of deep learning, such as batch normalization and exponential linear unit activations, the authors obtained accuracies of 71.90% and 70.10% on BCI dataset IVa for

dCNN and sCNN models, respectively. We wish to mention that both dCNN and sCNN models have been reimplemented in this work for benchmarking purposes and their architectures are described in the Methods section 3.3. In [141], a generalized neural network architecture, called EEGNet, was implemented which is capable of solving different BCI tasks. EEGNet contained three layers. The first layer learns sixteen 1D convolutional kernels. In the second and third layers, four 2D convolutional kernels are learned and 2-D max-pooling is applied. Furthermore, the model iterates between convolutions along spatial dimension (layer 1 and 3) and temporal dimension (layer 2). In each layer, the Exponential Linear Unit activation function is used and Batch Normalization and Dropout are applied to improve the model robustness. An overall accuracy of 70% was achieved using EEGNet on four MI movements.

3.2.3.4 Recurrent convolutional neural networks (RCNN)

In [142], the authors proposed to construct the spectral information over the whole trial duration as a sequence of images, and used RCNN, which is a combination of RNN and CNN, for four-classes working memory task classification. The obtained results showed that deep RCNN is capable of learning robust representations from sequence of images. They also demonstrated that their proposed model outperforms the state-of-the-art traditional machine learning approaches. In addition, in [143], authors proposed an RCNN model for six-class hand motion classification problem with 94.8% accuracy. They also showed that their RCNN architecture outperforms CNN. It should be noted that this high accuracy was only obtained for hand motion tasks and was not tested with motor imagery movements.

3.2.4 Motivation & aims of this study

Overall, this study investigated the real-time decoding of EEG brain data for robot arm control. This work serves as the foundation of our feed-forward control system of robotic arms, which was further improved using the hybrid BCI system introduced in the next chapter. Using our proposed model, EEG signals could be used in real-time to control a robotic arm. The system overview is illustrated in Figure 3.1. This chapter is structured as follows: Section 3.3 describes the implementation details of the different proposed deep learning models. Section 3.4 shows the obtained results using deep neural networks as well as traditional machine learning methods on our recorded EEG data and the publicly available dataset 2b from BCI Competition IV [144]. Real-time control of a robotic arm using our trained CNN model on EEG signals is described in Section 3.4.3. Section 3.5 enumerates the strengths

and weaknesses of our proposed methods and proposes possible future improvements. Finally, Section 3.6 concludes the main findings and results of the study.

3.3 Methods

3.3.1 Study design: Experimental paradigm

For MI-EEG data recording, 20 healthy and right-handed human subjects (31 ± 5.5 years old) were recruited to perform a series of kinesthetic MI tasks across 2 sessions yielding a total of 750 trials. All recording sessions took place at our lab and were set up as shown in Figure 3.2. Each session consisted of 4 runs of 12 min separated by 10-min breaks to avoid mental fatigue. Each run consisted of several MI tasks, each 10 s long. At $t = 4.5\,\mathrm{s}$, an arrow pointing either to the left or right was displayed with an acoustic warning tone (1 kHz, 70 ms). The subject was instructed to imagine a movement according to the displayed cue (left vs right) for four seconds. The MI task was followed by a relaxation period of 1.5 s that separated two trials. During the recording, no movement execution was requested. Data were recorded and sampled at 256 Hz using a g.tec g.USBamp EEG system [145] with 32 active electrodes located according to the 10/20-system. The number of electrodes was reduced to three, namely C3, C4, and Cz, over the sensorimotor cortex. The experimental paradigm is made publicly available with the gumpy toolbox [46]. 375 trials were recorded for each MI movement (left and right) with every subject.

3.3.2 Data processing & analysis

EEG signals were processed using the gumpy.signal module in the gumpy BCI toolbox [46]. First, a notch filter at 50 Hz was applied in order to remove power line interference. Second, data were high-pass filtered with a cutoff frequency of 0.5 Hz to remove baseline drift and then band-pass filtered between 2 and 60 Hz using a 5th order zero-phase Butterworth filter. Afterwards, the EEG data were clipped to $\mu(x_i) \pm 6\sigma(x_i)$ rectifying outliers. $\mu(x_i)$ and $\sigma(x_i)$ denote, respectively, the mean and standard deviation for the EEG data of channel i. Next, the data were normalized by subtracting $\mu(x_i)$ from each channel i and then dividing by the standard deviation $\sigma(x_i)$. Furthermore, a thresholding-based method [146] to detect and remove EOG and EMG artifacts from EEG was used. For that, we removed artifacts based on the mean amplitude value and standard deviation from individual channels within single epochs. Overall, deleted portions and epochs from the data were generally characterized by high amplitude values $> 83\,\mu\mathrm{V}$. Finally, in order to reflect the partial time invariance

Figure 3.2: Experimental setup and an example of a recording session of motor imagery-electroencephalography (MI-EEG) recording.

of the data and overcome the problem of overfitting, a data augmentation method was performed: A time window of $4\,\mathrm{s}$ was used to create different crops with a stride of $125\,\mathrm{ms}$ yielding 25 new sub-trials from each individual trial. The crops were gathered starting 3 s prior to the motor imagery onset until the end of the trial. Noticeably, this augmentation method was very helpful and forced our proposed "pragmatic" CNN model to learn complex features from all the crops and therefore led to better classification performance. In total, this cropping strategy increases the training set by a factor of 25 yielding 25 new examples per trial and a total number of 18,750 trials (9375 for each class).

3.3.3 System architecture & decoding methods

A BCI's decoding stage aims to extract usually distinct user intention's commands from the complex, multidimensional EEG data stream. Different strategies and myriad methods could be applied to this problem, which is essentially a classification task. In this work we systematically compare traditional ML methods to contemporary neural ones. Within the scope of this work the categorical difference between the traditional and the neural

approach is that only the latter can perform well on raw EEG data (or a direct representation thereof), whereas the former would typically rely on “hand-crafted” features. These are discriminative data properties like, e.g., the power in specific frequency bands at specific recording electrodes. They are specific to the individual task and experimental paradigm and are commonly defined and selected by an expert—a task we term “feature hand-crafting” or “feature engineering”. The specificity and discriminative power of an individual feature would often vary among different subjects and different trials. Automatic (optimizing) feature selectors can only partly counteract this tendency. Certain neural networks, in contrast, can classify EEG data directly: RNNs can evaluate EEG time series [72]; CNNs can classify [141] (series of) spectrograms. The networks can apparently find discriminative features automatically, without user intervention, without hand-crafted features. This is beneficial, because (1) less “hand-crafting” is required to define task-specific features, (2) potentially more complex spatio-temporal features can be found, and (3) the process of selecting or weighting relevant features is more dynamic and adaptive, so inter-subject and inter-trial variability should eventually be reduced.

3.3.3.1 LSTM model

Over the last few years, recurrent neural networks, mainly LSTM has gained tremendous momentum and prevalence for a variety of applications such as sequence to sequence generation and time-series prediction. As LSTM models are capable of learning long-term dependencies in time-series data, it would be appropriate to investigate their potential in classifying MI from EEG data. Hence, we developed an LSTM network with one hidden layer containing 128 cell units followed by an additional fully-connected layer that consists of two output neurons representing the two classes “left and right hand movements”. In regard to the model’s architecture choice, it is worth mentioning that using more layers and memory cells improved the training accuracy, but led to overfitting during the test phase, due to the exponential number of parameters. Likewise, reducing the number of memory cells to less than 128 led to underfitting shown by a significant decrease in both training and validation accuracies. Moreover, a dropout layer with a deactivation rate of 0.05 was used between the LSTM layer and the output to alleviate overfitting. The network was trained using a stochastic gradient descent on mini-batches of size 256 and using categorical cross-entropy as the loss function on a NVIDIA GTX Titan X GPU, with CUDA 8.0 and cuDNN v5, using Theano 0.9 [147] and Keras library [148]. For each of the 20 participants, training has been conducted using a stratified 5-fold cross-validation. More precisely, one of the five folds was held back for testing (3750 trials) while the four remaining folds (15,000 trials) were used

for training and validation with a split of 90% and 10%, respectively, in a loop until each fold has once been used for testing. Stratified in this context means that both classes are represented equally in each fold. Finally, we point out that early stopping [149] was used to avoid overfitting. That means the model is trained until the minimum of the validation loss is found and then tested on the test data split to measure its generalization capabilities.

3.3.3.2 The Pragmatic CNN model (pCNN)

In addition to reimplementing the two aforementioned CNN models (shallow sCNN and deep dCNN) by Schirrmeister et al. [73] we have developed a third CNN which we term "the pragmatic CNN" (pCNN). In terms of complexity the pCNN is in between of sCNN and dCNN. As will be shown the model can classify MI tasks with a high accuracy, yet it is sufficiently lightweight to perform real-time control of a robotic arm. Given that EEG data have a time-series structure, it was paramount to convert them into an image-like representation by computing spectrograms using a short-time Fourier transform (STFT), which is a well-known technique in audio signal processing [150]. An example of the obtained spectrograms during left and right imagined movements is shown in Figure 3.3. Overall there is a subtle, but clear difference in the generated spectrograms between the two imaginations on the same electrode in the frequency range of 25–50 Hz. However, it remains challenging to recognize the event-related (de)synchronization (ERD) in the alpha band between 8–13 Hz and lower beta band (14–24 Hz) [151] from the generated spectrograms. Computed spectrograms in the input layer are fed into our pragmatic CNN model (pCNN), which contains three convolutional blocks. Each block contains one convolutional layer, batch normalization to minimize covariate shift and enhance the robustness of the model [152], and max-pooling layer with a downsampling factor of 2 between each layer. A rectified linear unit (ReLU) is used as the activation function. Finally, a fully connected layer with a softmax activation function is used to compute the probability of each class. Weights were learned using the Adam optimizer [153]. The network architecture is shown in Figure 3.4. Similar to LSTM, the CNN network was trained using the same procedure. Overall, Figure 3.5 shows the fast convergence of the CNN model. It should be noted that the early stopping strategy was used to efficiently find the best model. The full architecture of the pCNN model can be found in Table 3.1.
As shown in Figure 3.5, at epoch 62 the validation loss starts increasing as opposed to the continued decrease of the training loss. This indicates the overfitting problem which could be explained by the small amount of data that is used for training. Hence, the early stopping technique, as aforementioned, was chosen in order to save the best model.

Table 3.1: Pragmatic CNN (pCNN) architecture. E is the number of channels, T is the number of timesteps and K is the number of classes. Input and Output sizes are shown for cropped training with $E = 3$ (electrodes C3, C4, and Cz) and $T = 1024$ for window size of 4 seconds; binary classification with two classes for $K = 2$.

Layer	Input	Operation	Output	Parameters
1	$E \times T$	STFT	$65 \times 64 \times E$	-
2	$65 \times 64 \times E$	$24 \times$ Conv2D (12×12)	$65 \times 64 \times 24$	10,392
	$65 \times 64 \times 24$	BatchNorm	$65 \times 64 \times 24$	260
	$65 \times 64 \times 24$	MaxPool2D (2×2)	$32 \times 32 \times 24$	-
	$32 \times 32 \times 24$	ReLU	$32 \times 32 \times 24$	-
2	$32 \times 32 \times 24$	$48 \times$ Conv2D (8×8)	$32 \times 32 \times 48$	73,776
	$32 \times 32 \times 48$	BatchNorm	$32 \times 32 \times 48$	128
	$32 \times 32 \times 48$	MaxPool2D (2×2)	$16 \times 16 \times 48$	-
	$16 \times 16 \times 48$	ReLU	$16 \times 16 \times 48$	-
3	$16 \times 16 \times 48$	$96 \times$ Conv2D (4×4)	$16 \times 16 \times 96$	73,824
	$16 \times 16 \times 96$	BatchNorm	$16 \times 16 \times 96$	64
	$16 \times 16 \times 96$	MaxPool2D (2×2)	$8 \times 8 \times 96$	-
	$8 \times 8 \times 96$	ReLU	$8 \times 8 \times 96$	-
	$8 \times 8 \times 96$	Dropout (0.2)	$8 \times 8 \times 96$	-
4	$8 \times 8 \times 96$	Flatten	6144	-
	6144	Softmax	K	12,290
Total				$170,734$

3.3.3.3 RCNN model

As was shown in Figure 3.3, it remains unclear whether the computed spectrograms encode enough information from EEG signals and whether the CNN could learn high-level features from them. Additionally, it may be desirable to improve the CNN model's ability to integrate the context information, which might be of utmost importance while learning the sequence of spectrograms in EEG signals. Consequently, an RCNN model has been implemented and its capability of learning MI movements has been investigated. The key module of such a model is the recurrent convolutional layer (RCL) [154], which can be seen as a specific form of RNN. In the RCL, the feed-forward and recurrent computation both take the form of convolution. During the training and test phase, the RCL is unfolded through discrete time steps into a feedforward subnetwork. The number of time steps, namely recurrent iterations, is pre-fixed as a hyper-parameter. Overall, RCNN can be described as a stack of these RCLs. The proposed RCNN architecture is described in Table 3.2.

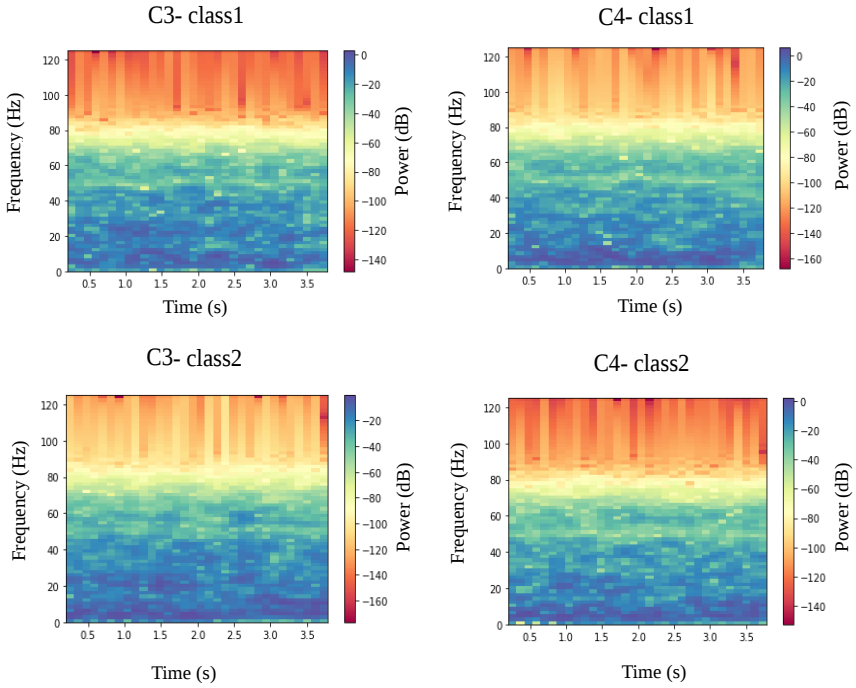

Figure 3.3: Generated spectrograms during left (class 1) and right (class 2) hand movements imagination.

3.3.3.4 Shallow-CNN (sCNN) and deep-CNN (dCNN)

To benchmark our obtained results we validated with three aforementioned models (LSTM, pCNN, RCNN), and two deep learning models (dCNN, sCNN) proposed recently by Schirrmeister et al. [73]. The dCNN model consists of four convolutional-max-pooling blocks followed by a dense softmax classification layer. Unlike previous implementations, the first convolution block is split into two parts where filters of the first one learn temporal information and the ones of the second layer learn 2D spatial information from the already learned temporal layers. On the other hand, the sCNN architecture which is inspired by the filter bank common spatial patterns (FBCSP) [62] relies essentially on band power features. For more technical details about the models' architecture, readers are referred to [73].

3.3.3.5 Traditional machine learning approaches

Aside from the deep learning techniques, we implemented and tested a range of classical machine learning approaches which are based on hand-crafted features. Five different classifiers from the gumpy.classification module [46] have been used and evaluated in order to provide a baseline for the deep learning models: KNN, DT, LR, NB, and QLDA [155]. Three

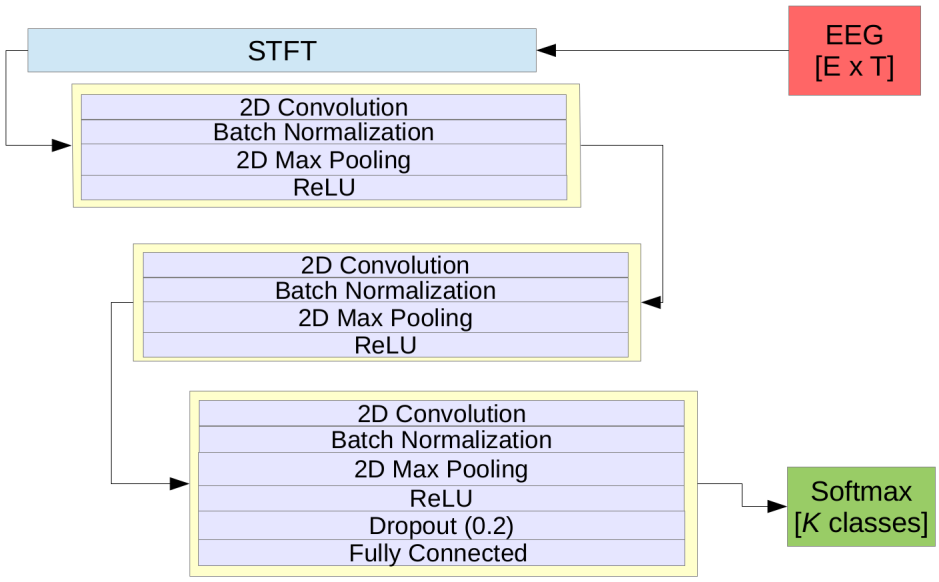

Figure 3.4: Pragmatic CNN (pCNN) architecture. E is the number of channels, T is the number of timesteps and K is the number of classes. Input and Output sizes are shown for cropped training with $E = 3$ (electrodes C3, C4, and Cz) and $T = 1024$ for window size of 4 seconds; binary classification with two classes for $K = 2$.

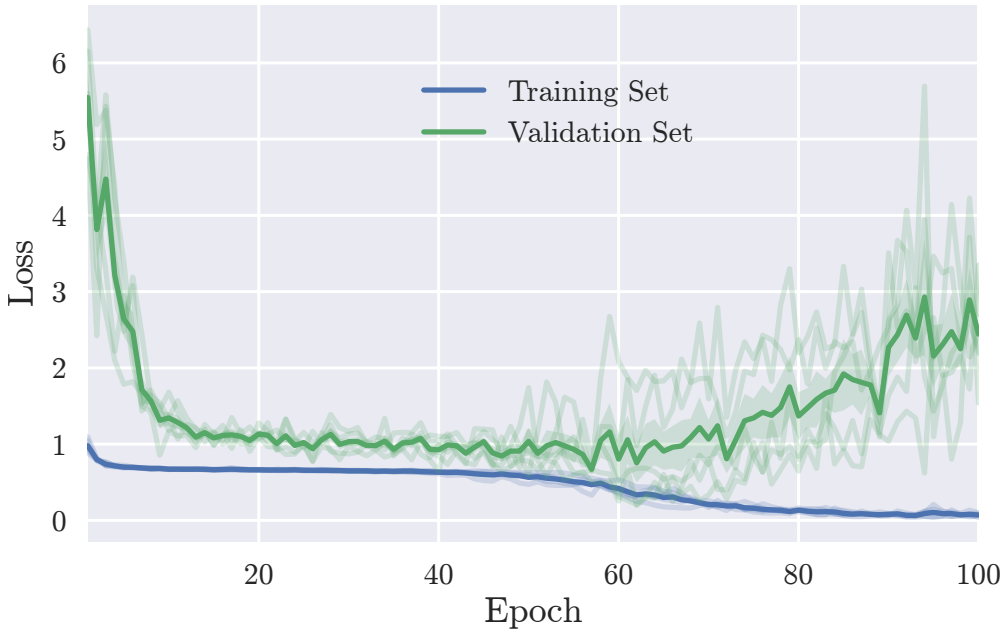

Figure 3.5: Training and validation loss of the pCNN model. The blue and green lines represent the average of the 5 folds for training and validation, respectively.

Table 3.2: The proposed recurrent convolutional neural network (RCNN) architecture

Layer Type	Size	Output Shape
Convolutional	256×9 filters	(144,1,1280,256)
Max pooling	Pool size 4, stride 4	(144,1,1280,256)
RCL	256 filters (1×1), 256 filters (1×9), three iterations	(144,1,1280,256)
Max pooling	Pool size 4, stride 4	(144,1,320,256)
RCL	256 filters (1×1) , 256 filters (1×9), three iterations	(144,1,320,256)
Max pooling	Pool size 4, stride 4	(144,1,80,256)
RCL	256 filters (1×1) , 256 filters (1×9), three iterations	(144,1,20,256)
Max pooling	Pool size 4, stride 4	(144,1,5,256)
RCL	256 filters (1×1) , 256 filters (1×9), three iterations	(144,1,20,256)
Max pooling	Pool size 4, stride 4	(144,1,5,256)
Fully connected	1280×3	(144,2)

different feature extraction methods were used, namely logarithmic band power (log-BP) [156], common spatial patterns (CSP) [157] and discrete wavelet transform [158]. For the log-BP method, we analyzed the log-power of mu rhythm (8–12 Hz) and beta (14–30 Hz). For each of the three channels (C3, C4, and Cz), log-BP features in 72 frequency bands were calculated using different overlapping narrow bands between 8 and 30 Hz yielding a total of 216 BP features. Additionally, the CSP method, which maximizes the pairwise compound variance between our two classes in the least square sense, was implemented and used for benchmarking purposes. Furthermore, statistical features (mean, root mean square (RMS) and standard deviation (SD)) were extracted from D3 and D4 wavelet coefficients. Thereafter, a feature selection algorithm [35] was used for each feature extraction method to select a subset of features. A 5-fold cross validation was performed and features were fed into the classifiers in order to discriminate between the two classes.

3.4 Main results of EEG decoding using traditional classifiers and neural models

Our motor imagery data recorded from 20 subjects were used to compare the models' performance. In order to further verify our results on independent data, we additionally used Graz dataset 2b from BCI Competition IV [144]. It should be noted that balanced accuracy

was chosen as the evaluation metric for the trained models and a stratified 5-fold cross-validation was applied during the validation phase.

3.4.1 Decoding results of our EEG recorded dataset

3.4.1.1 Traditional, Baseline classifiers

Figure 3.6a presents the results of the traditional classification algorithms. Overall, QLDA outperforms all the other classifiers with a mean accuracy over all subjects of 79.5% with CSP features and 78% with log-BP features. DT performs the worst with a mean accuracy of 67%. According to their performance with the QLDA classifier, the 20 participants could be classified into three groups: (G1) Participants S3 and S14 achieved a mean accuracy below 75%. (G2) Participants S1, S2, S4, S5, S7, S8, S9, S10, S11, S12, S13, S15, S16, S17, S19, and S20 achieved a mean accuracy between 75% to 79%. (G3) Participants S6 and S18 reached a mean accuracy of 80.52% and 82.09%, respectively. It should be noted that an average mean accuracy of 75% was obtained using the wavelet method when tested with QLDA. In Figure 3.6b, the polar bar plot shows the accuracy range (mean $\pm$ standard

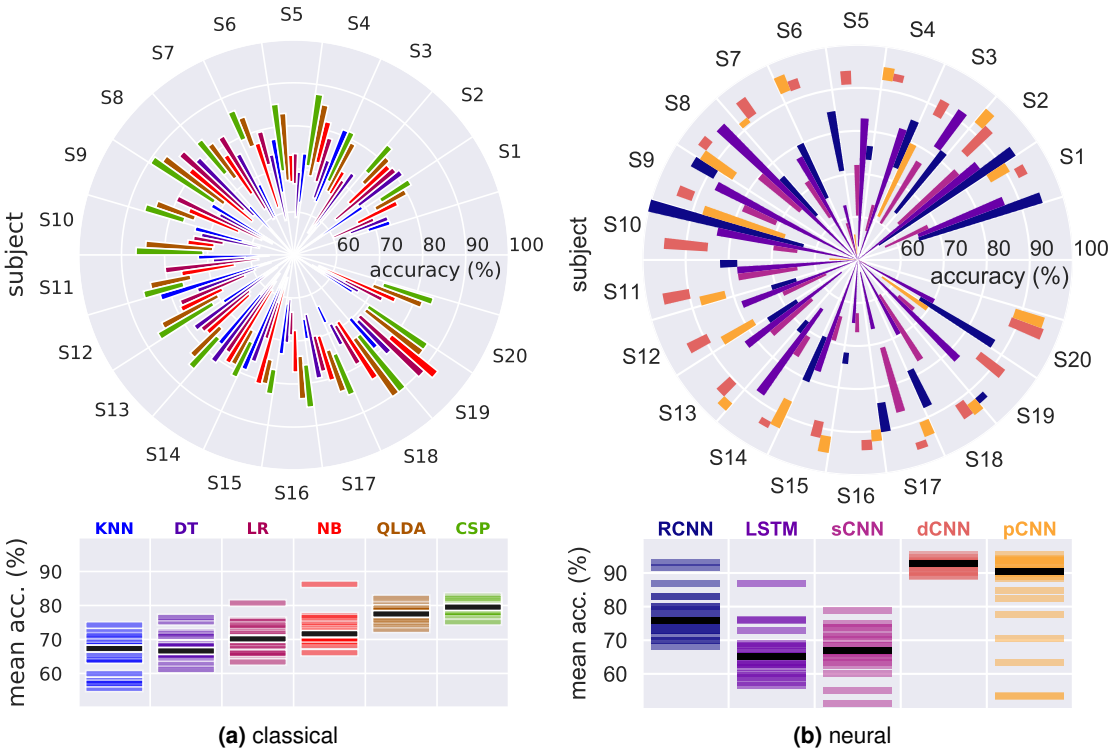

(a) classical **(b)** neural

Figure 3.6: MI classification accuracies from 20 subjects using (**a**) traditional machine learning approaches and (**b**) different neural classifiers.

deviation) achieved by the 5 models for each of the 20 subjects. The lower panel subsumes for each algorithm the 20 mean accuracies achieved, black bars indicate the median result.

3.4.1.2 Neural models

Figure 3.6b compares the classification accuracies achieved using the developed neural classifiers (RCNN, LSTM, pCNN) and two other models dCNN and sCNN proposed by Schirrmeister et al. [73]. It is worth noting that the dCNN and pCNN models outperformed all the other developed classifiers and attained higher accuracy.

LSTM model: To assess the LSTM's capability of learning discriminative features, only raw EEG signals were fed into the model. Noticeably, obtained results show a high standard deviation (SD) within subjects and across the test splits. Overall, a mean accuracy of 66.2 % ($\pm 7.21\%$) from all subjects was achieved for two classes. Interestingly, the LSTM model could perform well with some of the subjects e.g., S3 with a reached accuracy of 86.97 % ($\pm 5.18\%$). Contrary, an average accuracy of only 60 % was obtained from S6, S16, S18, and S20 which could be due to the fact that the raw data collected from these subjects were too noisy and hence the LSTM model could not learn any discriminative features. As illustrated in Figure 3.6b, the LSTM-based raw EEG data approach did not outperform any of the other developed models and the results remained slightly inferior to those obtained by state-of-the-art methods as will be shown in the next sections.

CNN models: Herein, we show the obtained results using our pCNN and two other CNN models proposed by Schirrmeister et al. [73] which have been reimplemented in this work for benchmarking purposes. Through all subjects, a mean accuracy of 84.24% ($\pm 14.69\%$) was achieved using the pCNN model. We wish to emphasize that such a high standard deviation could be easily explained by the failure of the model to classify recorded EEG signals from S5, S10, and S19 as shown in Figure 3.6b. Although reasons for that remain unclear, we could explain that some of these participants were unable to properly imagine the requested MI movements which resulted in a low signal to noise ratio of the collected data, and hence most of the developed deep learning models (except the dCNN model) failed to classify them. Overall, it is important to highlight that the pragmatic model (pCNN) shows a high stability across test splits with a mean SD of less than 3.32%. Furthermore, the achieved results with the sCNN model are also shown in Figure 3.6b The mean accuracy over all the participants is 66.97% ($\pm 6.45\%$), which is barely lower than the presented results in [73] and close to the one obtained with the LSTM model. However, it should be noted that the sCNN

shows less variance in the obtained accuracy across subjects and within different data splits compared to LSTM. Finally, a mean accuracy of 92.28% ($\pm 1.69\%$) was obtained with the dCNN model, which is better than the pCNN model. However, it should be noted that the dCNN model requires a significant amount of computation due to its extremely large number of parameters. Such a large model requires a large number of floating point operations and can run in a data center. But, for neurorehabilitation devices, the model should be small enough to be fitted into the memory. This makes the pCNN model a better choice as it requires about 50% less memory and computation compared to the dCNN.

RCNN model: A mean accuracy of 77.72% ($\pm 6.50\%$) was obtained with the RCNN model as illustrated in Figure 3.6b. Overall, RCNN model seems to provide better accuracy than the LSTM and sCNN but worse accuracy than both the pCNN and dCNN. Furthermore, we wish to highlight that the RCNN model required more epochs of training to avoid overfitting.

3.4.2 Results of EEG Graz dataset decoding using deep learning models and standard machine learning classifiers

To further evaluate the trained models' performance, we tested the pCNN architecture as well as the LSTM model on the Graz data set B from the BCI Competition 2009 [144]. The data consist of three bipolar recordings (C3, Cz, and C4) sampled at 250 Hz and two classes, namely the MI of left and right hand. Figure 3.7 shows that the pCNN model outperforms both LSTM, Naive Bayes and quadratic LDA for all nine subjects except for subject B08. For the LSTM model, better results than Naive Bayes and quadratic LDA are obtained with subjects B03, B05, B07, B08 wheareas quadratic LDA with the log-power features provided better mean accuracy results for subjects B01, B02, B04 B06, B09. Overall, models' performances are aligned with previously obtained performance on our recorded EEG data with lower variance for the pCNN model. We wish to mention that a mean accuracy of 95.72% and 78.22% was obtained through all subjects, using the dCNN and sCNN, whereas a mean accuracy of 91.63% and 78.93% was achieved using the pCNN and the LSTM models, respectively. In Figure 3.7, the polar bar plot shows the accuracy range (mean $\pm$ standard deviation) achieved by the five models for each of the nine subjects. The lower panel subsumes for each algorithm the nine mean accuracies achieved, black bars indicate the median result.

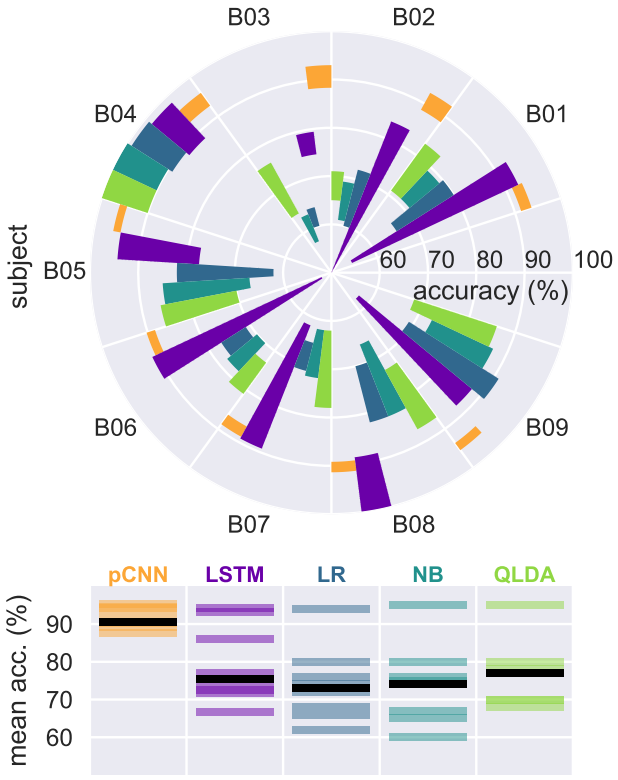

Figure 3.7: MI classification accuracies from nine subjects using five different classifiers.

3.4.3 Real-time control of a robot arm

We further tested and validated the real-time capability of the pCNN by online decoding of MI movements from streamed EEG signals for a robot arm control. Three electrodes were used to record live EEG data. First, a band-pass filter between 2–60 Hz as well as notch filter at 50 Hz were applied. All filters were implemented as Butterworth IIR filters. Second, the experimental setup shown in Figure 3.2, and the lab streaming layer (LSL) [159] were used to continuously stream the created spectrograms from live EEG data within a circular buffer that stores a predetermined number of samples up to the most recent one. The process of creating spectrograms from EEG streaming data is shown in Figure 3.8. In Figure 3.8, the top part represents filtered signal during a trial. Blue and red traces illustrate channel 1 and channel 2, respectively. Vertical lines indicate visual (orange) and acoustic cues (red). The bottom part represents the generated spectrograms from data within the grey rectangle shown above. Thereafter, live spectrograms were fed into the trained pCNN model for real-time classification and a robot arm was controlled accordingly. A Katana robotic arm was directed to either move to the left, right or stay in middle position according

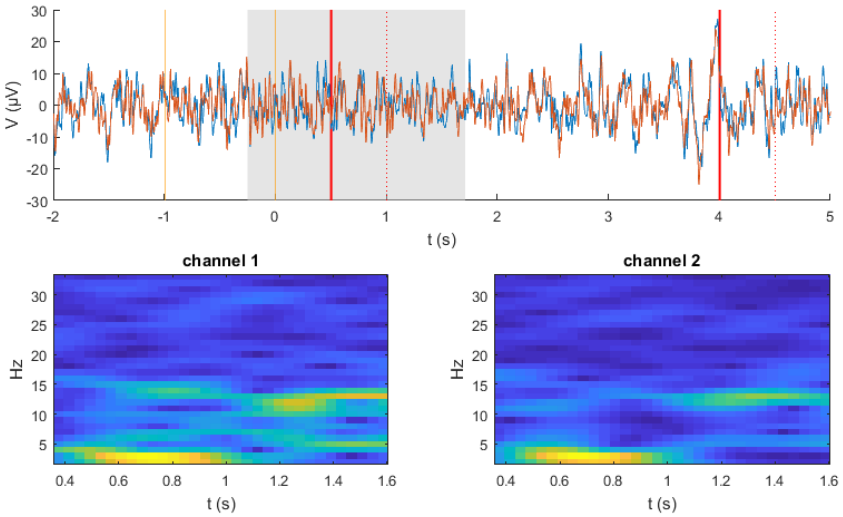

Figure 3.8: A frame of a live stream.

to the decoded movement from EEG signals. The trained model provides the probability of left and right hand movements. To detect the stay position, we defined a threshold for the classifier. That means signals with a high probability to move (left or right movements) are classified accordingly, and the remaining are categorized as no movements. The whole process is depicted in Figure 3.9. The live generation system using the trained pCNN has been tested for frame rates up to 128 Hz on a PC with a 2.8 GHz quadcore CPU. As shown in the supplementary video, a noticeable delay ($\sim$ 1.4 s) was experienced when performing the real-time experiment using the pCNN model. This delay can be attributed almost entirely to the CNN processing. A delay of $\sim$ 2.55 s is expected when using the trained dCNN model. [1]

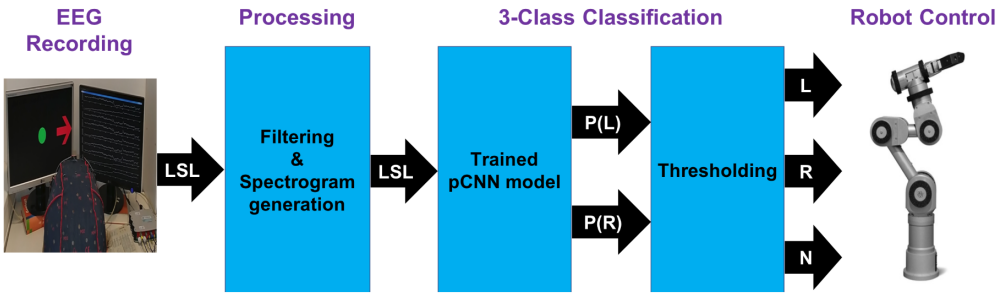

Figure 3.9: Live setup for real-time EEG signal decoding and Katana robot arm control. P(L) and P(R) represent the probability of left and right hand movements, respectively.

[1] A demo video of this work is available: `https://youtu.be/MClm6T5d5PM`

3.5 Discussion on real-time EEG decoding using the different validated approaches

This study aimed at validating various deep neural network architectures to decode human intentions from EEG signals and translate that into left and right commands to control, in real-time, a robotic arm. For that, three different deep learning models were proposed to classify the two MI movements from our recorded EEG signals: a time-series based LSTM, a pCNN, and a RCNN model. In addition, the deep- and shallow-CNN models proposed in the literature [73] were reimplemented for benchmarking purposes. Furthermore, five classic machine learning classifiers were also used for comparison. Several models for BCI-based MI have been proposed in the past. However, the present study was able to show an online decoding of motor imagery movements using the pCNN model. Overall, with a classification accuracy of $(66.2 \pm 7.21)\%$ the LSTM model performed similar to the sCNN model with $(66.97 \pm 6.45)\%$ accuracy. Despite the LSTM's capability of learning time-series sequences, the LSTM model did not outperform our pCNN, the dCNN, or even well-known machine learning classifiers that are commonly used in BCI such as SVM and quadratic LDA. As LSTM is prone to overfitting, one intuitive reason for the inferior results (with respect to [144]) could be the limited amount of training data which at the same time hindered the development of more complex LSTM models with more layers and cell units. On the other hand, our pCNN showed better performance compared to the LSTM model. The obtained performance could be due to the capability of CNNs to learn complex non-linear features as well as the fact that the time-frequency representation of the signal was used as an input to the model. Also, interestingly, the pCNN model showed higher stability in both training and validation accuracy compared to the other models despite the existence of overfitting potential due to its high number of parameters (170,734). The dCNN model showed promising results and slightly outperformed all the trained models confirming the ability of convolutional models in general to extract complex and discriminative features. Moreover, it confirmed that deeper networks could provide more accurate results. However, it should be noted that the large depth of very deep models like dCNN could result in an extremely high number of parameters (268,977), which in turn causes the model to be computationally expensive. As a "pragmatic" alternative, our pCNN provides a much better computation-accuracy trade-off and hence makes it a more attractive choice for the type of applications that we are interested in. It is also worth mentioning that unlike previous obtained results in [73], the performance of the shallow model was vastly inferior to the dCNN (66.97% vs 92.28%). Although the reasons for that remain unclear, we could explain this inferiority by a poor choice of the optimizer's hyper-parameters. These hyper-parameters

have to be carefully chosen for models like sCNN and dCNN as they do not rely on standard activation functions such as ReLu, exponential ReLu, sigmoid, and Tanh. Lastly, the RCNN model showed better performance than the developed LSTM, sCNN, and classic machine learning methods with a mean accuracy of $(77.72 \pm 6.50)\%$, but not the dCNN and pCNN models. However, RCNN could be subject to further improvement by optimizing the network architecture. Thus, a different RCNN architecture as presented by Bashivan et al. [142], that combines CNN and LSTM, could improve the achieved results. Finally, it should be noted that the amount of data used to train all of the aforementioned models were limited and low noise to signal ratio did not allow to decode more complex movements. Therefore, simultaneous multiple biosignals processing and decoding was investigated to classify more complex movements, such as reach-to-grasp, and is introduced in the next chapter.

3.6 Summary

Overall, this work is considered as a survey of different learning methods for EEG decoding, by implementing and benchmarking the performance of five machine learning algorithms with three deep learning models advanced in this study. The details of these three deep learning models (LSTM, pCNN, RCNN) for online decoding of two imagined hand movements from EEG signals were described. Additionally, the developed DNN models were compared with two other models (dCNN, sCNN) proposed in the literature. Overall, the two CNN architectures (dCNN, pCNN) showed better performance and achieved a mean accuracy higher than 84% over all the 20 participants, the RCNN model reached a mean accuracy of 77.72% and a comparable accuracy to state-of-the-art results was obtained with the LSTM model. In general, the traditional way of decoding EEG data has consisted in (1) data preprocessing, (2) feature engineering, and (3) classification. Methods for all three processing steps abound, but have to be carefully selected and linked together by experts. Neural networks can merge steps (2) and (3), and identify relevant data features automatically. Their crucial benefit is not that they require less expert knowledge, rather it is that they can automatically and dynamically adapt their selection and weighting of features to different trials, different subjects, and possibly also different tasks [160]. Our data confirm at least the two former points: Sufficiently deep convolutional neural networks achieve less inter-trial and less inter-subject variability. Overall they classify more accurately than traditional methods. This is, however, quickly becoming easier and more accessible thanks to powerful and user-friendly software frameworks like Keras [148] or EEG (and EMG) specific toolkits like gumpy [46]. Furthermore, a successful real-time control of a robot arm was achieved using the trained pCNN model. Our next study presented in the next chapter was

designed to overcome all limitations of this EEG-based approach by relying on multiple signals decoding, and hence increase system's complexity and the number of controlled DoF of the robotic system. In the next chapter, the pCNN model advanced in this work is used and combined with an EMG decoder to classify more complex reach-to-grasp movements instead of the two state decoding system presented in this study.

4 Processing and decoding of multiple biosignals for real-time human-robot interaction

Some parts of this chapter (Sub-study 1) are created based on content adapted with permissions from the manuscript Bernhard Specht*, Zied Tayeb*, Emmanuel Dean, Rahil Soroushmojdehi, Gordon Cheng, "Real-Time Robot Reach-To-Grasp Movements Control Via EOG and EMG Signals Decoding", Published in International Conference on Robotics and Automation (ICRA 2020), 2020.
*: Both authors contributed equally to the manuscript
DOI: `https://ieeexplore.ieee.org/abstract/document/9197550`
Authors Contribution: Zied Tayeb and Bernhard Specht contributed equally to this manuscript. Zied Tayeb proposed the idea, designed the experiments, prepared the protocols for data recordings, recorded EMG data, co-analyzed the data with Bernhard Specht, prepared the figures and wrote the manuscript. Bernhard Specht recorded and collected the data, co-analyzed the data by advancing and testing the developed algorithms, tested the system offline and online, and co-wrote the manuscript. Emmanuel Dean developed the software for the robotic arm control, helped with testing the system online with the robotic arm, and assisted in writing the paper, Rahil Soroushmojdehi helped with testing the experimental setup and helped with writing the manuscript. Gordon Cheng supervised the research and revised the manuscript.

4.1 Study overview

In two separate follow-up studies, a real-time human-robot interface (HRI) system based on the combination of different biosignals was proposed. In the first sub-study, EOG and EMG signals (introduced and described in chapter 2) were decoded to perform reach-to-grasp

movements, instead of solely relying on EEG data and the decoding of two-state movements (presented in the previous chapter). For that, four different eye movements (up, down, left, right) and rest were classified in real-time and translated into commands to steer an industrial robot (UR-10) to one of the four approximate target directions. Thereafter, EMG signals were decoded to perform the grasping task using an attached gripper to the UR-10 robot arm. The proposed system was tested offline on three different healthy subjects, and mean validation accuracy of 93.62% and 99.50% were obtained across the three subjects for EOG and EMG decoding, respectively. Furthermore, the system was successfully tested in real-time with one subject [1], and mean online accuracy of 91.66% and 100% were achieved for EOG and EMG decoding, respectively. Our results obtained by combining real-time decoding of EOG and EMG signals for robot control show overall the potential of this approach when being used in real-time scenarios.

In the second sub-study, the combination of EEG and EMG was investigated and led to the successful decoding also of these signals with a mean validation of 89.6%. For that, the pCNN model proposed in the previous study (chapter 3) was used for EEG decoding and was combined with a standard machine learning model (SVM) for EMG decoding, following the same sequential paradigm used for EOG and EMG decoding. This investigation of simultaneous EEG+EMG decoding was performed to classify more complex reach-to-grasp movements instead of the two-state decoding system proposed in this previous chapter. For that, two motor imagery movements (left, right) and rest were decoded and translated into commands to steer an industrial robot (KUKA-Arm), whereas three different hand movements were classified from EMG signals to control a 3-D prosthetic hand. Overall, the outcomes of these two sub-studies confirm the potential of using multiple biosignals for human-robot interaction and the decoding of more complex arm movement intentions compared to the previous study, but they also highlight challenges to overcome in order to enhance the usability of the proposed methods.

4.2 Introduction

Human-robot interaction for rehabilitation and assistance has gained momentum [161] and has continuously attracted many researchers and industrial companies [162]. Highly autonomous robots have been used in multiple industrial applications, such as disassembling tasks and robot-cranes [163]. Apart from industrial sections, robots have been utilized in different healthcare applications. For instance, nursing robots [164], robots in gait rehabilitation for patients after stroke [165] and assistive telepresence robots for elderly [166] have

[1] A demo video of this work is available: `https://youtu.be/EEsq_7e-XLQ`

been widely used. Despite the tremendous advances that have been made, various problems persist [167] and the development of human-robot interfaces (HRI) still needs further investigation of the capabilities of human-robot collaboration when designing the interface to produce desirable actions [168]. Many researchers have been working on incorporating human bio-signals, as one of the most important input signals that can be used to control assistive robots [169]. Assistive robotics using signals that are acquired from muscle activity (EMG) [170], brain activity (EEG) [171] and eye movements (EOG) [172], [173], [174], [175] have shown promising results. However, these systems still exhibit some drawbacks, such as complex and expensive experimental setups, which makes transferring this into commercial products a challenging task [176]. Along the same lines, using one unique signal for robot control limits the number of degrees of freedom (DoF) that can be controlled. In this context, many studies have been recently focusing on combining multiple bio-signals to increase the number of DoF when controlling assistive robots [177]. This has therefore spurred research in designing hybrid HRI systems [178]. In [179], authors integrated EOG, and evoked related potentials. A comparison between different modes of robot control including accelerometer data, EOG + EMG, EOG + blink and EOG + ERD/ERS + blink in [176] showed that combining EOG and EMG offers a good compromise between accuracy, ease-of-use, and number of DoFs for robot control. Recent work by Zhang et al. combined EEG/EMG/EOG-Based Multimodal Human-Machine Interface to control a soft robot-hand in real-time [180]. This work investigated the fusion and combination of different biosignals to increase the number of extracted commands from these signals when interacting with robotic arms, while maintaining a good real-time decoding accuracy. The online system was demonstrated by simultaneously processing and classifying EOG and EMG signals. The next section provides a more comprehensive review on previous studies that investigated the fusion of different biosignals, as well as their limitations and the novelty of this study.

4.2.1 Summary of previous research on hybrid BCI and simultaneous biosignals decoding

Over the last few years, there have been several literature reviews on fusing and decoding multiple biosignals, such as EMG+EEG or EMG+EOG. Overall, when combining different body signals for robot control, decoding approaches are classified into simultaneous and sequential [181]. In [92] and [182] a physiological, simultaneous, hybrid BCI was tested with respect to its general usability and the influence of muscle fatigue on the system accuracy. People with muscular dystrophy and elderly people suffer generally from muscle fatigue during the day, as the number of employable muscle fibers as well as their size and power

decrease [183]. As a result, this badly affects the frequency spectrum and amplitude of EMG signals, resulting in a poor decoding performance. The hybrid BCI system, by either adding EEG or EOG as a second decoded signal, presents another solution to maintain a good decoding performance. In [92], the study was conducted with nine healthy subjects who had to repeat the execution of left- or right-hand movements depending on the presented cue. A 16-channel EEG was recorded over the primary motor cortex and a 4-channel EMG was recorded on the flexor and extensor of each forearm. The problem of muscle fatigue was simulated by attenuation of the recorded EMG signal. Classifier accuracies were tested for four fatigue levels (100% EMG, 90% EMG, 50% EMG, 10%EMG) and compared to EMG-only and EEG-only modes. Additionally, two data fusion approaches were investigated. The first one used equally balanced weights to fuse the EMG and EEG classifier outputs processing chain, whereas in the second approach, a nave Bayesian fusion was employed using probabilities calculated from the training data. Experiments resulted in classification accuracies for EEG-only and EMG-only of 73% and 87%. In the first fusion approach (equal weights) an average accuracy of 91% (100% EMG), 90% (90% EMG), 85% (50% EMG) and 73% (10% EMG) was achieved for the different fatigue levels. In the Bayesian fusion approach an accuracy of 92% could be achieved for 100%, 90% and 50% EMG, which for the 50% case presents a significant improvement compared to the first fusion approach. Overall, this study showed that the hybrid BCI system based on the fusion of EEG and EMG led to a significant performance improvement compared to the single use of EEG-based BCI. Additionally, it was shown that the muscle fatigue had no or only a moderate negative influence on the classifier performance, increasing, therefore, the long-term reliability of such a system when used during the day. Nevertheless, one of the limitations of this study was the limited number of decoded movements (robot's control commands) given that the extracted information from both signal channels was redundant. Other studies [184, 185, 186] investigating the combination of multiple biosignals in the field of assistive technology (such as hybrid BCI speller systems) demonstrated that multimodal systems always improved the performance or complexity of the systems. Despite the number of challenges to overcome when fusing and decoding different biosignals at the same time, these previous studies have confirmed the usefulness of this hybrid approach, as well as have shown the overall motivation behind investigating this concept. Along these lines, these studies clearly demonstrated the control limitations when relying on a single input signal (EMG/EEG/EOG) for both motor-impaired and healthy human subjects. People who suffer from muscular dystrophy have difficulties to maintain EMG signals for longer periods. Additionally, even for healthy people, the continuous contraction of a muscle can lead to muscle fatigue and unease and decrease the usability of the system [183]. Like muscle fatigue, when solely

relying on MI movements from EEG, mental fatigue is considered another problem, given that maintaining mental states such as intentional non-control for a longer period can be mentally exhausting. Furthermore, it is known that some people are not able to produce or use EMG, EEG, or even EOG signals at all. Patients with tremor or other spastic symptoms tend to produce false positives in the EMG signal making this channel useless [186]. Furthermore, some paralyzed or tetraplegic people or even amputees do not even have any recordable muscle activity. Similarly, as was shown in the chapter 3 of this thesis (the previous study), the detection of ERD/ERS in EEG signals is very sensitive to users, which hinders its acquisition from a large proportion of subjects, and the number of distinguishable movements that can be accurately decoded is usually limited to two or three states. For this purpose, the hybrid system is considered a good alternative despite the challenging seamless integration of multiple modalities, as well as the overall number of movements that can be extracted. Extending upon the obtained results of these studies, this work aimed at using the hybrid concept with two different investigated approaches (EEG+EMG and EOG+EMG) to investigate the robust decoding of more complex movements, known as reach-to-grasp movements, when interacting in real-time with robotic arms. This work showed first the high accuracy that can be obtained when decoding these movements (91.66% for EOG+EMG, and 89.6% for EEG+EMG). Moreover, this study showed the possibility to use such a system in real-time when controlling reach-to-grasp movements (EOG+EMG) of a robotic arm, while maintaining a high online accuracy. Table 4.1 compares different studies that relied on more than one single decoded biosignal when interacting with robotic devices, and summarizes the main obtained results.

Table 4.1: Comparison of different hybrid BCI studies for human-robot interaction and their achieved results

Reference	Nº of Classes	Validation Mode	Decoded Signals	Accuracy
[178]	2	Online	EMG+EEG	94.4%
[181]	2	Offline	ERD+SSVEP	77%
[92]	2	Offline	EMG+EEG	92%
[180]	4	Online	EMG+EOG+EEG	93.83%
Our work	6	Online	EOG+EMG	95.83%
Our work	5	Online	EEG+EMG	89.6%

4.2.2 Motivation & aims of combining and decoding multiple biosignals for real-time human-robot interaction

The core contribution of these two sub-studies within this investigation resides in designing an HRI system based on real-time decoding of EOG+EMG and EEG+EMG for the control of different reach-to-grasp movements of two different robotic arms. Overall, the results from both proposed paradigms and sub-studies showed comparable performance. As was shown in the previous chapter, relying solely on EEG signals still exhibits many problems and limitations, such as low spatial resolution limiting the number of the control commands that can be decoded [3], as well as low SNR making them impracticable to use in daily-life scenarios. Thus, adding other biosignals is thought to offer a better solution for more robust and real-time human-robot interaction. In this work, we underpin the real-time capabilities of the proposed systems by demonstrating the successful online control of a UR-10 robot arm (universal-robots). Our EMG+EOG system (shown in Figure 4.1) can be extended to classify more complex movements. An overview of the EMG+EOG system is depicted in Figure 4.1, whereas the EEG+EMG system is illustrated in Figure 4.12.

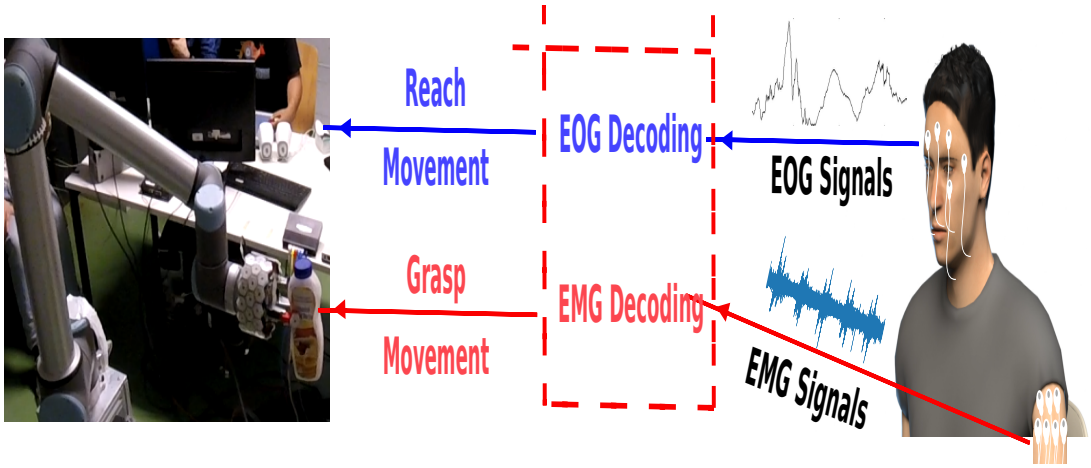

Figure 4.1: Overview of the real-time developed EOG+EMG system.

4.3 Sub-study 1 on EOG+EMG decoding for reach-to-grasp movements control

4.3.1 Methods

4.3.1.1 EOG & EMG signals recording and processing

EOG and EMG signals were recorded from three healthy subjects (two males and one female) using the g.USBamp system with a sampling frequency of 1200 Hz. Subjects were between 22 and 27 years old and claimed to have no record of neurological disorders. The three subjects were recruited to perform four different eye movements (up, down, left, and right) by following a pointing arrow on the screen during the training phase (EOG task), as well as to perform one hand movement, namely power-fist followed by a relaxation phase. The pointing arrow (cue) was randomly displayed and was selected from a discrete uniform distribution. Both experimental paradigms for EMG and EOG recording were prepared by Zied Tayeb and Bernhard Specht. EMG and EOG data collection was jointly performed by Bernhard Specht, Rahil Soroushmojdehi, and Zied Tayeb. All recording sessions took place in the lab and yielded a total of 150 and 400 trials for EOG and EMG signals, respectively. For EOG signals, 30 trials for each direction were recorded (including the rest phase/no movement) forming the total number of 150 trials. For EMG, 200 trials for each condition (power-fist vs rest) were collected yielding to the total number of 400 trials. One pair of electrodes, which cover the muscles of the forearm (flexor and extensor carpi radialis) in a ring-like fashion were used, and the reference electrode was placed on the elbow bone. The open source library mushu [187] was used for data acquisition and both EMG and EOG signals were thereafter processed using the gumpy.signal module in the gumpy BCI toolbox [46]. For that, EOG signals were band-pass filtered between 1 and 22 Hz using a 4th order zero-phase Butterworth filter, whereas EMG was band-pass filtered between 30 and 500 Hz using the same filter. Both signals were notch filtered at 50 Hz to remove the power line interference [46]. The designed experimental paradigms, electrode placement and recorded signals for EOG and EMG are shown in Figure 4.2 and Figure 4.3, respectively.

4.3.2 Main results of EOG+EMG decoding

The processing and classification algorithms described and used in this sub-study were proposed and developed by Bernhard Specht and Zied Tayeb. Thereafter, those algorithms were advanced and tested offline and online by Bernhard Specht.

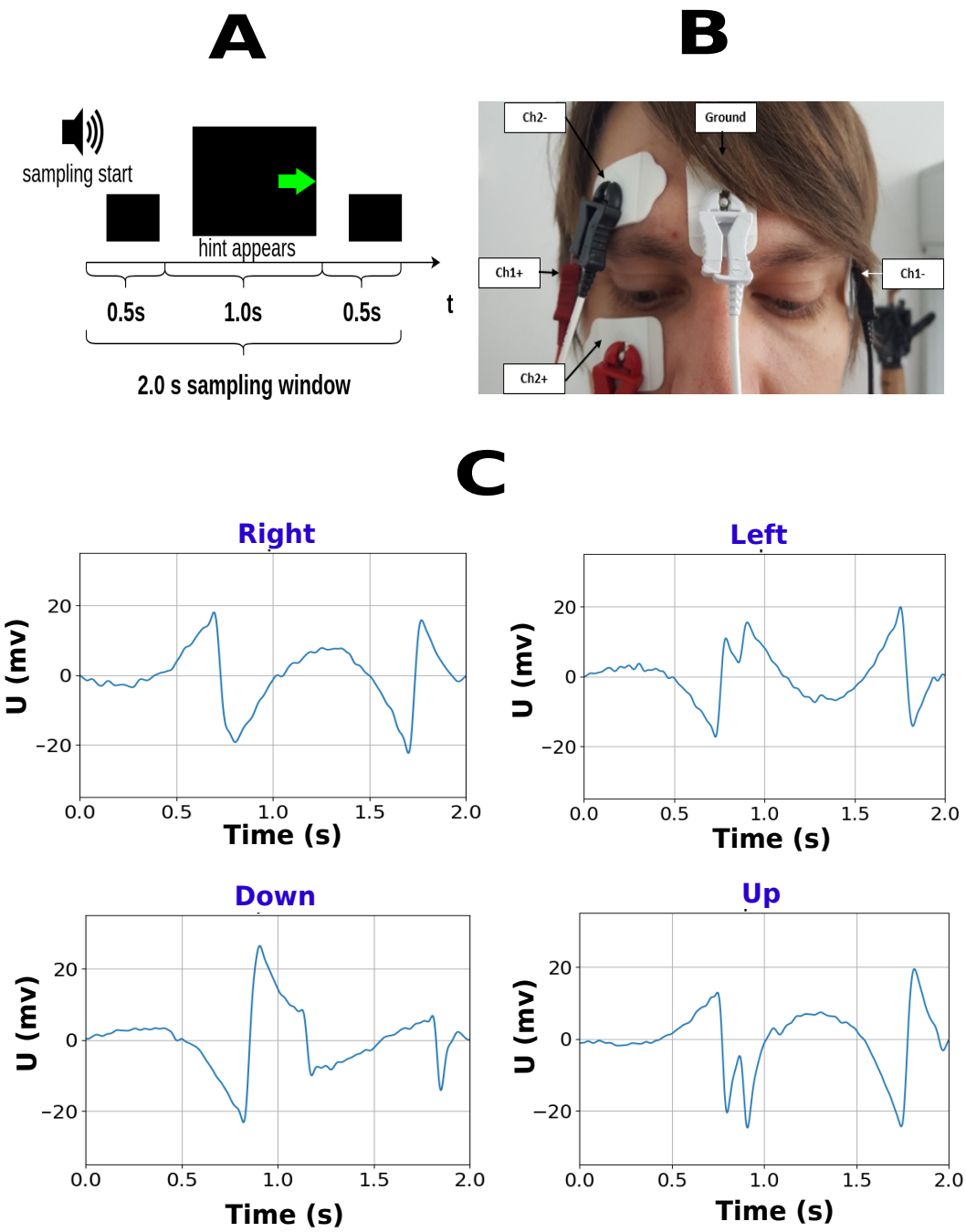

Figure 4.2: **A** shows the paradigm for recording trials used to train the EOG classifiers. For each trial, a window of two seconds is sampled. For the first half second the screen is black, then a uniformly selected cue in the form of an arrow appears at the position where the subject is expected to look at, or the screen stays empty for classification of relaxation. The cue disappears after one second and is followed by a black screen for another half of a second. A short tone marks the start of a sampling period. **B** shows the electrode placement on the subject. One ground electrode was placed in the middle of the forehead. The electrodes CH1+ and CH1- were placed on the right of the subject's right eye and left of the subject's left eye respectively. CH2+ and CH2- were placed on beneath and on top of the subject's right eye. **C** shows the filtered subtracted signals of the horizontally placed electrodes for left and right eye movements and the vertically placed electrodes for up and down eye movements.

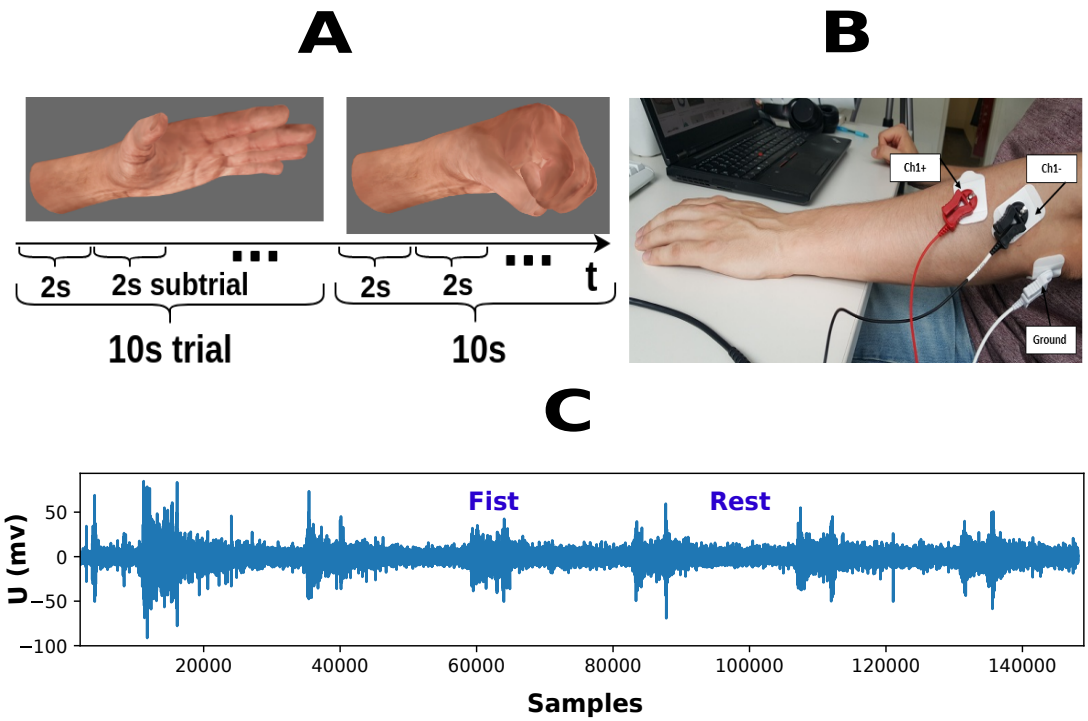

Figure 4.3: **A** shows the animations with timings of two consecutive trials showed to the subject while recording EMG signals. A trial is divided into five sub-trials, where each trial is recorded as a sampling window of two seconds. **B** shows the electrode placement for the EMG recording. The ground electrode was placed on the elbow. Two electrodes CH1+ and CH2+ were placed on top of the forearm forming a channel for bipolar recording. **C** shows recorded EMG data. When the subject forms a fist higher activity can be observed.

4.3.2.1 Offline results: EOG data classification

Filtered EOG signals were analyzed using two sliding windows (from 0.0s to 1.5s, and from 0.5s to 2s). The length of the sliding window was chosen for the purpose of allowing real-time control. For each sliding window of 1.5s, four different features, namely minimum value, maximum value, variance and threshold crossing count (crossing positive and negative threshold) were extracted and were used for training, as well as for the movement classification in real-time. A feature selection algorithm (SFSF) [188] was used and trained to select the best features (a subset of the initial features) using a 10-fold cross validation. Only the selected features were then used to train a KNN classifier. We wish to mention that two different KNN models were trained to classify EOG signals. The first one was served for detecting if there is an eye movement or not (rest vs eye movement). If an eye movement was detected, a second classifier was trained to classify the different directions of eye

movement (up, left, right, or down), and hence deciding on the robot's target direction. It is worth noting that 10-fold cross-validation was used during the validation phase to evaluate the model's performance. Figure 4.4 shows the classification results for the three different subjects. Overall, we achieved an average success rate of $97.91\% \pm 3.22\%$, $89.92\% \pm 8.66\%$ and $93.04\% \pm 7.69\%$ for the three subjects, respectively, yielding a mean accuracy of 93.62% across the three subjects, when recognizing the different eye movements. A principal component analysis (PCA) was performed (n_components=2) to visualize the different classes and results are depicted in Figure 4.5, which shows that most eye movements trials are highly separable, except the left and right which were also confused during the real-time test. It should be mentioned that the mean balanced accuracy (bACC), where the average of correct predictions for each class was computed and used.

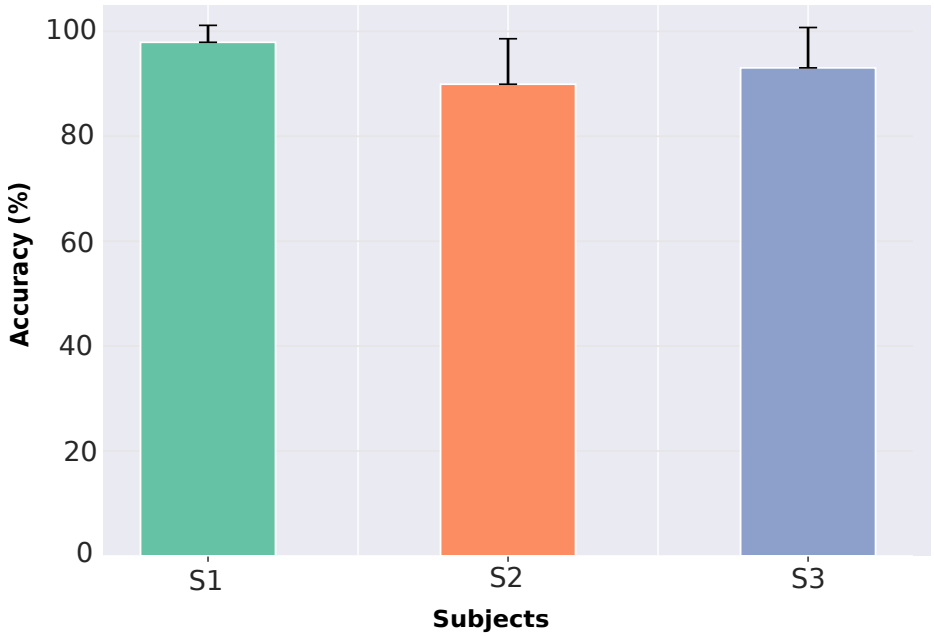

Figure 4.4: Bar plot showing the mean validation accuracy for each subject with the standard deviation.

4.3.2.2 EMG signal classification

The mean absolute value and the sum of absolute discrete differences were used to extract features from EMG signals. Those two features were extracted from different consecutive overlapping windows within a time window of two seconds. The overlapping windows had

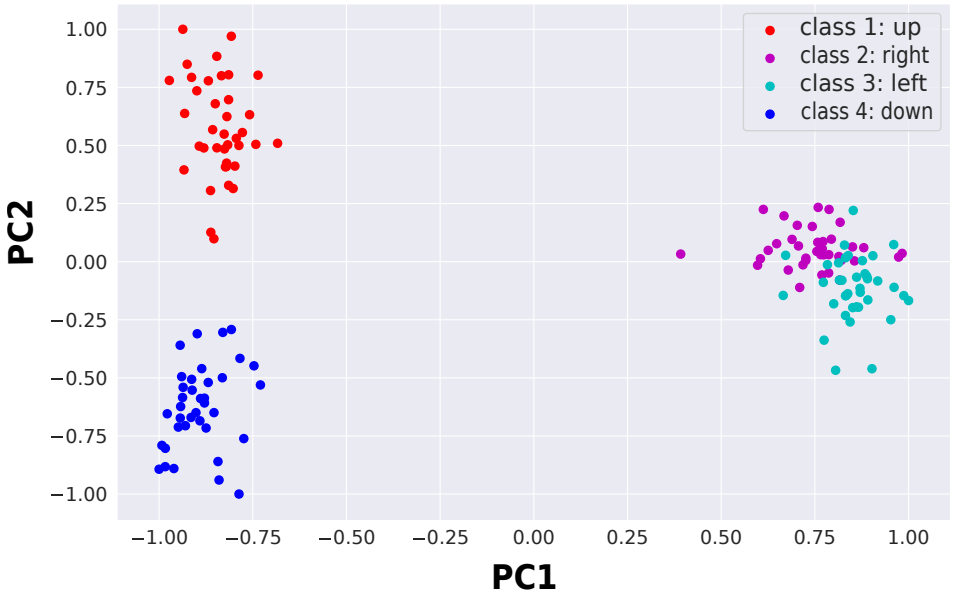

Figure 4.5: Feature space showing the different eye movement trials after performing PCA.

a size of 0.2 seconds and overlapped with their neighbors for 0.04 seconds. The same sequential feature selector algorithm was used to choose features for training a KNN classifier with 10 fold cross-validation. As this is a binary EMG classification task, signals were correctly classified during the validation as well as in the test phase with 100% accuracy.

4.3.2.3 Real-time signals decoding

After the validation of the proposed system offline, we used a UR-10 robot with an attached gripper to test the proposed system online. For that, the subject had to perform one of the four different eye movements to control the robot to perform a reach movement as described in table 4.2. EOG signals are acquired in real-time, processed, classified using the saved offline model and decoded information was thereafter translated into commands to move the UR-10 robot towards the right direction. Once the robot reaches the target object, the subject flexes his muscles, EMG signals are processed, classified in real-time using the saved EMG classifier and the attached gripper to the UR-10 robot arm performed the grasping task. Overall, an online accuracy of 91.66% and 100% were, respectively, obtained when classifying EOG and EMG signals using one single subject. The confusion matrix in Figure 4.6 shows that down and up eye movements were always correctly classified, whereas the left and right movements were sometimes confused during the test phase. For the EMG online classification, all performed fist movements were correctly classified. Table 4.2 summarizes

robot's and subject's different actions. The robot arm's action was controlled depending on the decoded subject's eye movement, whereas the gripper's action was controlled using the decoded EMG movement.

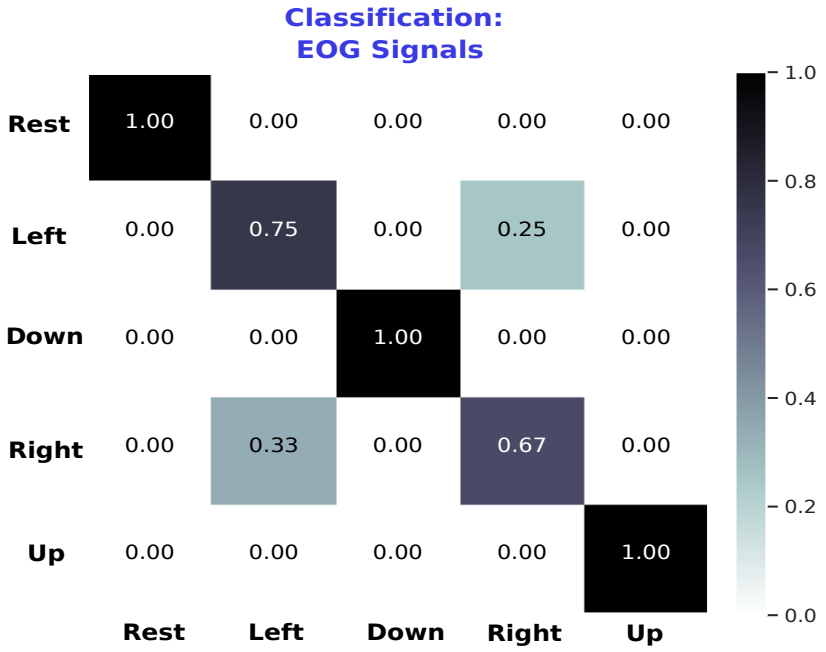

Figure 4.6: Confusion matrix for the real-time test showing that left and right were the only classes confused during the online phase.

Table 4.2: Subject action to robot action mapping

Signal	Subject's Action	Robot's Action [$P(i)\&G(j)$]
EOG	look left	move up left
	look up	move up right
	look right	move down right
	look down	move down left
	rest (idle state)	no movement
EMG	grasp	close gripper
	relax	open gripper

4.3.2.4 Robot interface

The robot interface described in this section of the thesis was developed by Emmanuel Dean and was then used for the real-time demonstration with the robotic arm. The robot interface, which was used to connect the *Decoder* with the robot controller is depicted in Figure 4.7. The *Decoder* uses two robot operating system (ros)-clients to trigger the *Robot's Actions* defined in table 4.2, namely *Reach Movements* $P(i)$and *Gripper States* $G(j)$. Herein, the ros-client communicate with the server system, and wait thereafter for a response by that server (ros-service). In the case of $G(j)$, the client triggers two possible gripper actions *open* and *close*. These actions are directly transformed into gripper commands by the *Gripper Driver*, which, in turn, are transformed into digital outputs (DI/O) running in the UR-Control Unit. For the Arm actions, the *Decoder* selects a specific *Reach Movement* $P(i)$ using the classification of the EOG signals. The selected $P(i)$ is sent to the *Arm Driver* using a ros-client. The ros-service implemented in the *Robot Interface* maps the desired $P(i)$ into a predefined end-effector state (end-effector position $x_{ef_s}(i)$). This position $x_{ef_s}(i)$ is used in a *State Machine* (SM) to trigger the different end-effector goals $x_{ef_g}(k)$. These goals are used as desired positions in a Cartesian controller. Then, the output of the Cartesian controller is transformed into joint velocity commands [189] and sent to the robot.

4.3.2.5 Cartesian control

To control the robot end-effector, we implemented a second order sliding mode controller in the Cartesian space defined as:

$$\tau = -K_d S_q + Y_r \Theta \in \mathbb{R}^n \tag{4.1}$$

where $K_{d_+} = K_{d_+}^T \in \mathbb{R}^n$ and $Y_r\Theta \in \mathbb{R}^n$ is the robot regressor. The joint error surface S_q is defined as:

$$S_q = \dot{q} - \dot{q}_r \in \mathbb{R}^n \tag{4.2}$$

where the joint velocity reference $\dot{q}_r \in \mathbb{R}^n$ is given as:

$$\dot{q}_r = J(q)^{-1}\dot{x}_r \tag{4.3}$$

and the Cartesian velocity reference $\dot{x}_r$ is given as:

$$\dot{x}_r = \dot{x}_d - K_p \Delta x + S_d - K_{i_1} \int_{t_0}^{t} S_\delta d\zeta - K_{i_2} \int_{t_0}^{t} \tanh\left(\mu S_\delta\right) d\zeta \tag{4.4}$$

with $\tanh(\mu\bullet)$ as a smooth approximation for the function $sign(\bullet)$, and $\mu > 0 \in \mathbb{R}$. $K_p, K_{i_j} > 0 \in \mathbb{R}^{6\times6}$, $j = 1, 2$. The Cartesian error manifold S_δ is

$$S_\delta = S - S_d = (\Delta\dot{x} + K_p\Delta x) - \left(S(t_0)\, e^{-\kappa t}\right) \tag{4.5}$$

with the Cartesian position error defined as:

$$\Delta x = x - x_d \in \mathbb{R}^6 \tag{4.6}$$

where $\Delta\dot{x} = \dot{x} - \dot{x}_d$ is the Cartesian velocity error, where x_d and $\dot{x}_d$ stands for the desired Cartesian pose and velocity, respectively. The desired Cartesian pose $x_d \in \mathbb{R}^6$ is composed of a desired position vector x_{ef_d} and a desired orientation vector $\theta_{ef_d} \in \mathbb{R}^3$, which is obtained using the *Euler angles* representation *Z-Y-X*. In our particular case, the goal is to keep the orientation of the end-effector constant, i.e. $\theta_{ef_d}(t) = \theta_{ef}(0)$. The position of the end-effector depends on the *Reach Movement* $P(i)$ triggered by the EOG/EMG Decoder. The discrete movement obtained from $P(i)$ is transformed into a set of end-effector goals $x_{ef_g}(k) \in \mathbb{R}^3$, where k is defined by the State Machine SM, see Figure 4.7. Then, we generate a continuous desired trajectory using a spline function for each $x_{ef_g}(k)$.

4.3.2.6 Spline End-Effector Trajectory x_{ef_d}

To generate a smooth trajectory from the initial desired Cartesian position $x_{ef_i} \in \mathbb{R}^3$ to the goal position $x_{ef_g}(k)$, we employ the following trajectory generator:

$$x_{ef_d} = a_1\bar{x}_{ef} + x_{ef_i},\ \dot{x}_{ef_d} = a_2\bar{x}_{ef} \tag{4.7}$$

where $\bar{x}_{ef} = x_{ef_g}(k) - x_{ef_g}(k-1)$, with $x_{ef_g}(0) = x_{ef_i} = x_{home}$.

The coefficients a_i are defined as: $a_1 = 10r^3 - 15r^4 + 6r^5$, $a_2 = (30r^2 - 60r^3 + 30r^4)/(t_f)$ and $a_3 = (60r - 180r^2 + 120r^3)/(t_f^2)$, where $r = t/t_f$ is a time ratio between the current time t and the desired total time t_f. This function guarantees a smooth trajectory that satisfies the constraints $x_{ef_d}(0) = x_{ef_g}(k-1)$, $x_{ef_d}(t_f) = x_{ef_g}(k)$ and $\dot{x}_{ef_d}(0) = \dot{x}_{ef_d}(t_f) = \ddot{x}_{ef_d}(0) = \ddot{x}_{ef_d}(t_f) = 0 \in \mathbb{R}^3$. The discrete movements $P(i)$ are a set of predefined Cartesian positions $x(i) \in \mathbb{R}^3$. The robot's end-effector continuous trajectory $\chi(t)$ is generated

using polynomial interpolation between two positions u and v of that set, see eq. (4.11).

$$r = \frac{t - t_0}{\Delta t} \tag{4.8}$$

$$\Delta t = t_f - t_0 \tag{4.9}$$

$$p(t) = 35r^4 - 84r^5 + 70r^6 - 20r^7 \tag{4.10}$$

$$\chi(t) = p(t)\Delta x(k) + x(v), \tag{4.11}$$

with t_0 and t_f as the initial and final time for the trajectory, and Δt defines the total time of the trajectories, in our case, it was set to $10s$. $\Delta x(k) = x(u) - x(v)$, where the indices u, v are the *target* defined by the SM, depending on the desired action. Each action takes $30s$ since the robot has to move to three different stations, namely, *home*, *reach*, and *target*.

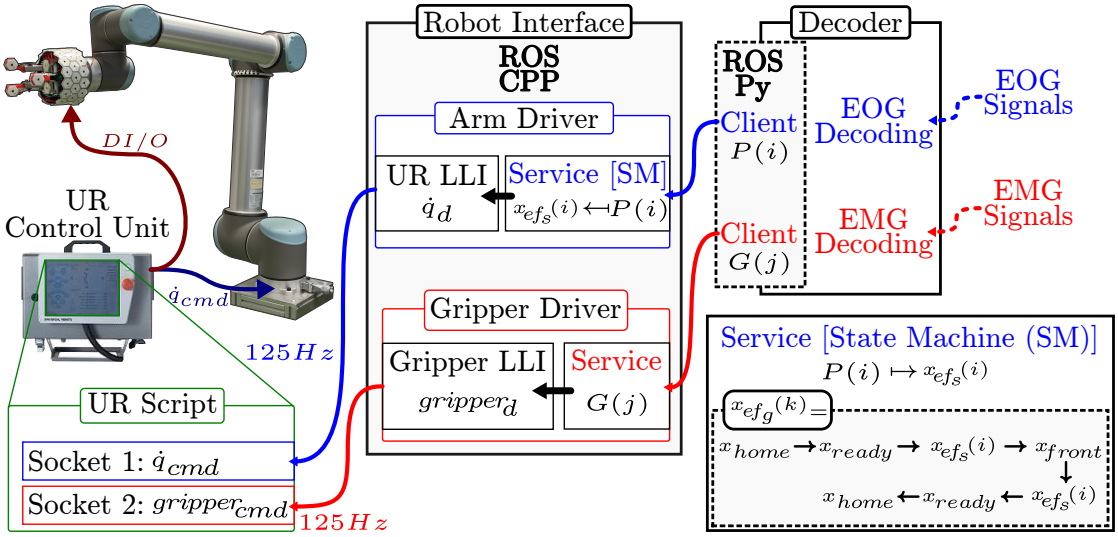

Figure 4.7: Robot Interface: The robot interface to control the robot's actions is implemented in ROS, where two ROS services have been implemented. The first one to control the arm motions, using a State Machine SM, and the second one to trigger the gripper states (open/close). The EOG decoder executes the *Reach Movements* $P(i)$, and the EMG triggers the *Gripper States* $G(j)$. The *Reach Movements* are divided into a sequence of end-effector positions ($x_{ef_g}(k)$) triggered by a *State Machine*.

4.4 Sub-study 2 on EEG+EMG decoding for reach-to-grasp movements control

In addition to the EOG+EMG interface, the pCNN model for two motor imagery (MI) movements decoding from EEG, which was described in the previous chapter, was combined with

posture classification from EMG using a classic machine learning model (SVM). For that, 2-MI movements namely left and right imagined hand movements, and three hand poses (fist, 2-finger pinch, and 3-finger pinch) were decoded. The experimental paradigms and processing classification algorithms described and used in this sub-study 2 were proposed by Zied Tayeb and were made freely available within gumpy software [50]. The robot interface for the robot control was developed by Matteo Saveriano and all the developed algorithms were thereafter advanced and jointly tested (offline and in real-time) by all the co-authors of Tayeb et al. [46].

4.4.1 Methods

4.4.1.1 EEG & EMG signals recording and processing

For EMG signal recording, an experimental paradigm using a simulated hand was designed and used to record EMG data corresponding to three-hand postures, namely fist, two-finger pinch, and three-finger pinch, as illustrated in Figure 4.8. For that, eight silver chloride solid gel electrodes were placed on the forearm, with four pairs of electrodes covering the muscles in a ring-like fashion, as shown in Figure 4.9. The reference electrode was placed on the elbow, the g.USBamp amplifier [145] was used to record data and the LSL [159] was used for data acquisition. Both EMG and EEG signals were processed using gumpy

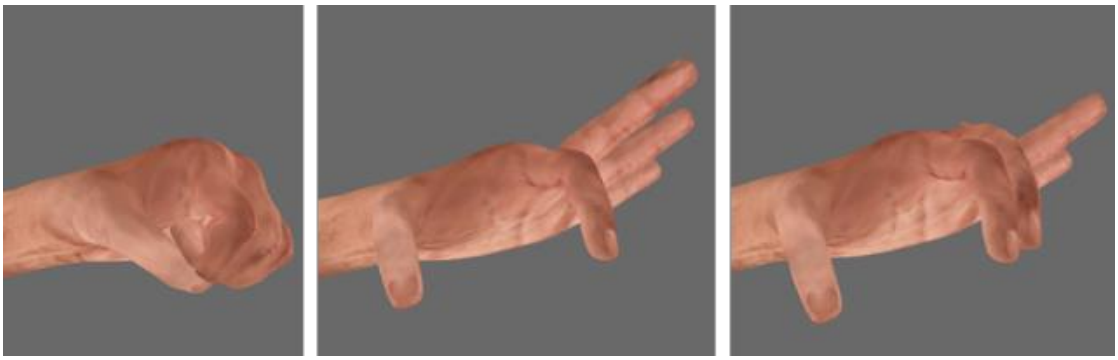

Figure 4.8: EMG recording paradigm for three hand postures.

software [46]. EMG data was first filtered using a fourth order band-pass filter with cut-off frequencies 20 Hz and 255 Hz and a notch filter with cut-off frequency 50 Hz to remove power line interference. Thereafter, the channel pairs get subtracted from each other and separate epochs from recorded trials were extracted. For this EMG classification task, the root mean square (RMS) was extracted as a feature from each EMG channel using a sliding window of 0.2 seconds and overlap factor of 0.05 seconds. Afterwards, the feature matrix

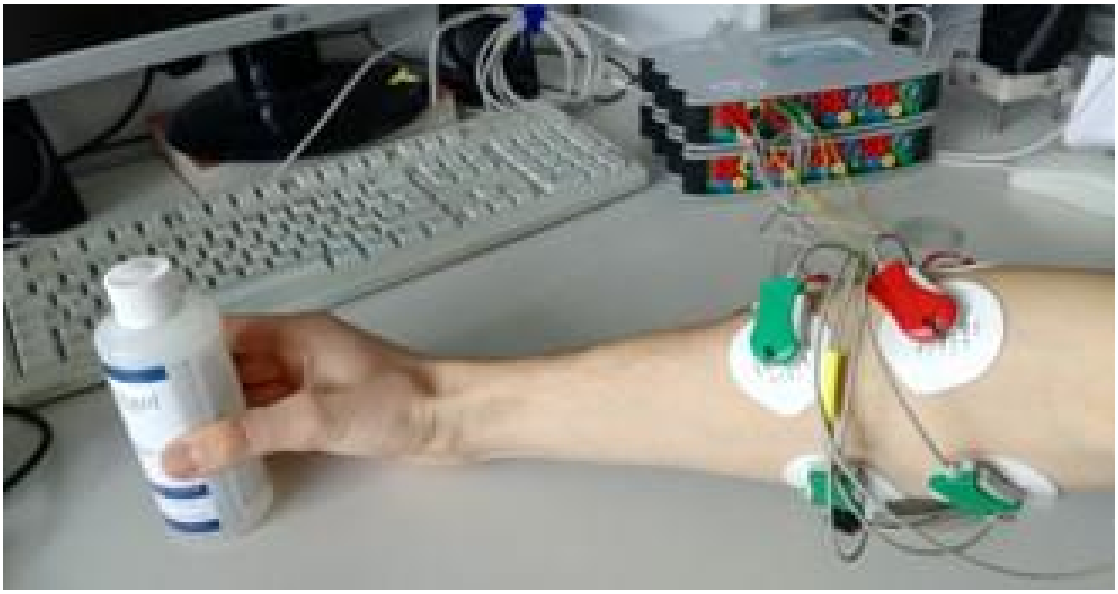

Figure 4.9: EMG electrodes' placement.

was normalized and the feature selection algorithm [35] was used to reduce the number of features into three before feeding them into the machine learning classifier. For EEG signals, the same recording paradigm as described in the previous chapter (chapter 3) was used to instruct the subject to either imagine a passive left or right hand movements. The motor imagery movement's duration was 4 seconds (as shown in Figure 4.10). Eight different electrodes over the motor cortex were used for data recording, but only three of them (Cz, C3, C4) were chosen for data analysis, given that they contain the most useful information when performing a motor imagery task [190, 3]. The same EEG processing pipeline as was presented in Chapter 3, was used in this sub-study and the pCNN model was trained using the collected EEG data.

4.4.2 Results of EEG & EMG decoding

4.4.2.1 Offline classification results

For the offline classification, five different machine learning classifiers (Support Vector Machine (SVM), K-Nearest Neighbours (KNN), Logistic Regression (LR), Naive Bayes (NB), and Quadratic Linear Discriminant Analysis (QLDA)) were validated tested offline to discriminate between the three hand postures from EMG signals. Data was split into 80% for training and 20% for test. A comparison of the five classifiers performances is available in

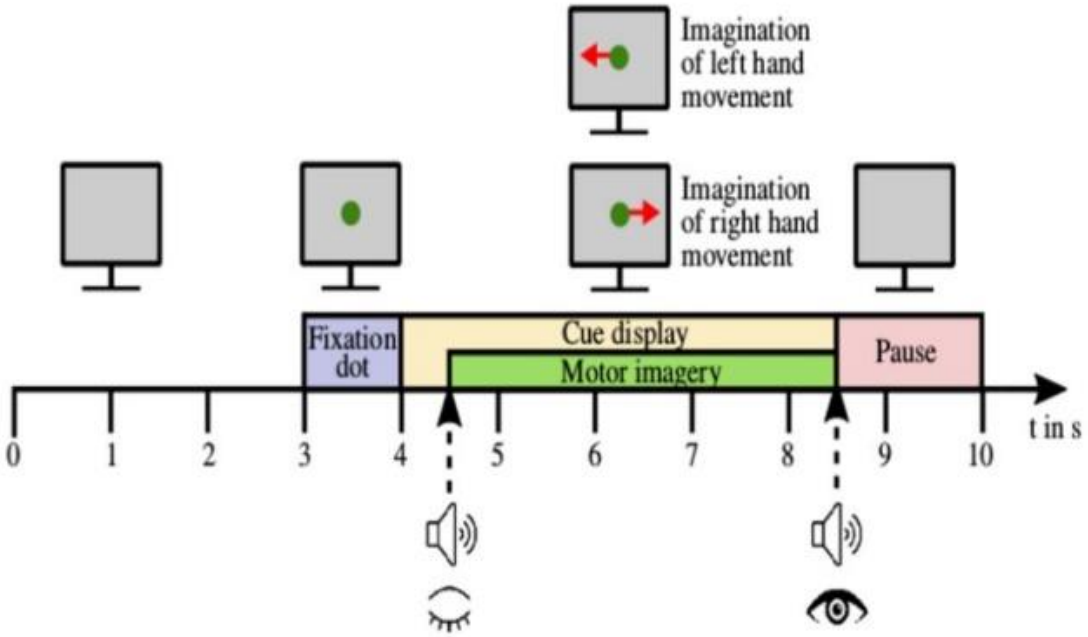

Figure 4.10: EEG experimental paradigm for motor imagery movements recording.

Figure 4.11. For EEG data, the pCNN was trained, and similar average performance as was described in chapter 3 was obtained.

4.4.2.2 Online classification results and robot control

For the online experiment, a SVM trained model for EMG signal classification was combined with the pCNN model for EEG signal decoding. In this second sub-study, the online mode was designed to perform reach-to-grasp movement decoding, where a KUKA robot arm [191] was controlled by the two decoded MI movements from EEG (reach movements), whereas the mounted prosthetic hand was controlled using EMG signals (grasp movements) during the same experiment. In this second sub-study, the LSL [159] was used to synchronize different data streams (EEG, EMG) and the temporal procedure was arranged as a state machine. During the offline recording, the program alternates between two states, which execute the tasks related to EEG and EMG experiments. The participant performed the EEG experimental paradigm first. Thereafter, the EMG experimental paradigm was performed. This procedure was repeated for a defined number of offline trials, for instance, 72 as was shown in the online EMG experiment in section A.4.2.2. After completion of the offline experiments, the program entered a state, where the model used for posture detection was trained based on the offline recorded EMG data, whereas the MI pre-trained pCNN

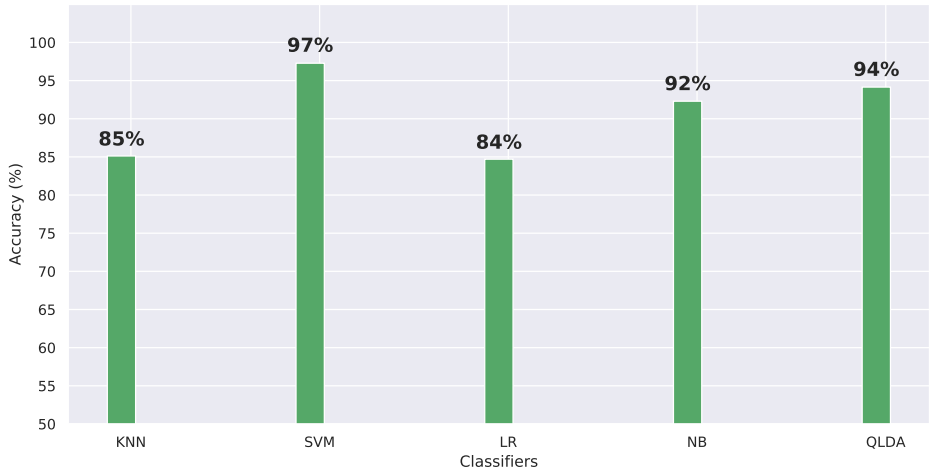

Figure 4.11: Comparison of the offline accuracy of EMG decoding obtained using five different machine learning classifiers.

model was retrained based on the offline EEG data. It should be noted that the pre-trained model can be either a CNN or also a standard machine learning classifier, depending on the end-user's configuration. Afterwards, the program entered the online phase, which consists of three states (EEG, EMG, and classification). These states were performed sequentially for a defined number of online trials. Likewise, the EEG state was first performed and was followed by the EMG state. The robotic arm was programmed to execute either a left or right reach movement (or move back to home position if no movement was decoded), depending on the decoded EEG signal and using commands sent through a user datagram protocol (UDP) socket with a module developed in Python. The prosthetic hand was programmed to execute one of the three grasping postures, depending on the decoded EMG signal. Overall, comparable performance to the EOG+EMG system was obtained, by achieving a mean accuracy of 89.6%, where the three hand poses from EMG signals were recognized with an accuracy of 95.25%, whereas reach movements from EEG motor imagery movements were recognized with an accuracy of 83.95%. After classifying both EEG and EMG signals, the KUKA-robot arm as well as the Open Bionics prosthetic hand attached to it were controlled to perform a reach-to-grasp movement as shown in Figure 4.12, reaching a validation accuracy of 89.6% when classifying the desired reach-to-grasp movement. Overall, one potential benefit offered by combining EEG and EMG [34] is the low latency provided by EEG when decoding reach movements as well as the rich spectro-temporal information that can be decoded from EMG when classifying complex grasp movements [34, 23]. Nevertheless,

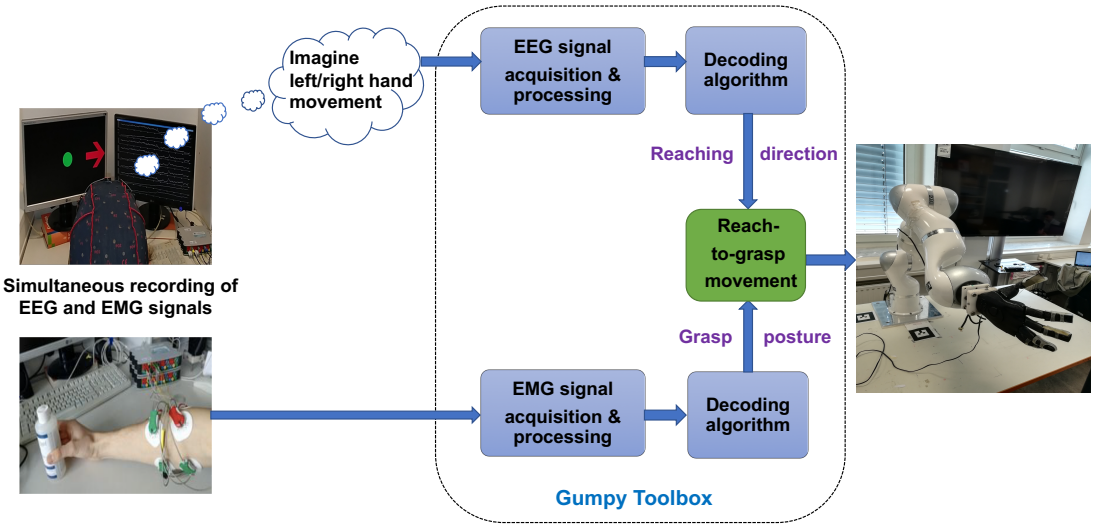

Figure 4.12: The proposed hybrid BCI experiment for reach-to-grasp movements decoding.

we observed that the accuracy of the EOG+EMG is more stable, particularly when used in real-time applications.

4.5 Discussion

In this study, we proposed a human-robot interface based on decoding and combining multiple signals to control reach-to-grasp movements of different robot arms, such as KUKA and UR-10. For that, two sub-studies were designed and investigated. An EOG+EMG experiment was designed and tested to control a UR-10 robot with an attached gripper, whereas EEG+EMG was designed and tested with a KUKA-Arm and an attached Open Bionics prosthetic hand. Overall, our results show that we could successfully classify both EMG and EOG signals with more than 90% accuracy across three different subjects and we underpin the real-time aspect by showing the successful online control of the robot arm. Additionally, reach-to-grasp movements were classified from both EEG and EMG signals with an accuracy of 89.6%. To the best of our knowledge, these two sub-studies are among the very few to demonstrate the real-time control of multiple reach-to-grasp movements of different robot arms using decoded information from different biosignals. Nonetheless, the proposed concept still has some limitations that should be addressed in future work, in order to investigate to what extent this approach could be generalized across many subjects, including

elderly and disabled people, to further verify the robustness of such a system when used in real-life scenarios, as well as to extend the proposed approach to classify more complex reach-to-grasp movements.

4.5.1 Limitations

First, the EOG+EMG experiment was solely tested on healthy subjects and no experiments with elderly or disabled people were performed. Hence, it remains questionable whether a similar performance could be obtained when testing with patients. Furthermore, we wish to mention that the subject had to be trained to correctly and repetitively perform the different eye movements prior to the recording. Therefore, generalizing the developed approach across many subjects would be a challenging task. Aside from that, we noticed that sweat or slight changes in the electrode's position during recording and the difference between muscle tissues of the participants drastically decreased the quality of the recorded EMG signal, and therefore deteriorate the classification accuracy. For example, the accuracy dropped when testing on the female participant (subject 2 in our analysis) and a validation accuracy of only 89.92% was attained compared to more than 97% and 93% for subjects 1 and 3, respectively. Similarly, for the EEG+EMG experiment, extensive training was needed to master the task and slight changes in the electrode's position resulted in a decrease of SNR for both signals, and caused a drop in the validation accuracy. For both experiments, only one side of the equation was investigated and no sensory feedback was provided to the human controller. Hence, this gave rise to focus on the other side of the equation, the afferent pathway, by investigating the use of vibrotactile stimulation to provide artificial sensation about the stiffness of the different manipulated objects, while controlling, using EMG signals, a 3D-printed prosthetic hand. This work is described in the next study presented in chapter 5.

4.6 Summary

This study proposed a human-robot interface system based on two separate studies, where the real-time decoding of EOG+EMG to control reach-to-grasp movements using an industrial UR-10 robot arm was described in the first one, and the classification of EEG+EMG to control reach-to-grasp movements using an industrial KUKA robot arm with an attached 3D prosthetic hand was described in the second sub-study. The EMG+EOG system was tested with three different healthy subjects in the validation phase and one subject during the online phase, whereas the EEG+EMG system was successfully validated with one sub-

ject. Overall, we obtained a mean validation accuracy of 93.62% and 99.50% for EOG and EMG classification, respectively, and online accuracy of 91.66% and 100% during the online phase. The EEG+EMG achieved similar performance of 89.6% as a validation accuracy. We demonstrated the real-time capability of the proposed EOG+EMG system by showing a successful control of the robot arm using decoded information from both signals.

5 Investigating vibro-tactile stimulation to enable the sense of touch in sEMG-controlled hand prostheses

This chapter is made up of content adapted from the manuscript Zied Tayeb, Philipp Jakovleski, Zhong Chen, Jannick Lippert, Pablo Lanillos, Dongheui Lee, Gordon Cheng, "Enabling the sense of touch in EMG-controlled hand prostheses using vibro-tactile stimulation." accepted for publication at the 9th International IEEE/EMBS Conference on Neural Engineering (NER). DOI: `https://ieeexplore.ieee.org/abstract/document/8717124`.

Author Contributions: Zied Tayeb designed the research, designed the experimental paradigm, developed the software for data processing, prepared the figures, and wrote the paper. Philipp Jakovleski and Zied Tayeb performed the real-time experiment. Zhong Chen and Jannick Lippert designed and prepared the hardware system used in the experiment and tested the different system parameters. Pablo Lanillos and Dongheui Lee assisted with writing the paper. Gordon Cheng supervised all experiments, data analysis, and interpretation of the results. All authors contributed in writing the paper.

5.1 Study overview

This study is disconnected from the previously described studies of this thesis and whose purpose was to investigate the other side of equation when controlling robotic arms using BCI systems. In this work, we focused on the afferent pathway by investigating the use of vibrotactile stimulation in sensory substitution. The overall goal of this study was to assess the feasibility of designing a low-cost, non-invasive sensory-enabled prosthetic hand controlled by surface electromyographic (sEMG) signals. First, four hand movements and two force levels (low, high) were successfully classified from sEMG signals with an accuracy of

86.25% for posture decoding and 100% for force recognition. Second, a real-time control of the prosthetic hand was achieved using the decoded sEMG activity. Thereafter, measured finger-tip forces were translated into vibrotactile stimulation of the muscles for feedback. With solely 10 trials per posture, an average online accuracy of 86.25% was reached across the four different human participants when classifying the different hand poses with the applied finger forces. Additionally, an average success rate of more than 88.46% was obtained, when differentiating between three different grasped objects (soft, hard, and medium) using the proposed vibrotactile feedback. Taken together, this study showed the potential of using low cost and non-invasive approaches for a bidirectional control of hand prostheses.

5.2 Introduction

The design of a prosthetic hand that can grasp and manipulate daily life objects precisely and effortlessly is undoubtedly a big challenge, which is still lacking in prostheses currently available on the market [192]. An intuitive reason for that is the absence of any kind of sensory feedback to users, which makes the control of the device frustrating, ineffective [193], and explains the high abandonment rate of available prosthetic hands [194]. Owing to that, it has become important to develop more advanced encoding and decoding algorithms. On one side of the spectrum, the decoding algorithms should be able to reliably classify different hand gestures and force levels from sEMG for a more lifelike dexterity [195]. On the other end of the spectrum, the encoding algorithms should translate the captured information from the sensorized prosthetic hand into a feedback signal to the user through different feedback modalities, such as vibrotactile [99] or electro-tactile stimulation [196], or the combination of both modalities [197]. Many non-invasive sensory substitution approaches for transradial prosthetic hands have been studied and proposed in the literature [198]. A functional non-invasive system that does not need any surgical operations and can work in real-time and closed-loop fashion has been rarely demonstrated [198]. Such a system should combine the decoding of different hand poses and force levels from sEMG with multimodality sensory substitution. This work sheds light on the real-time classification of four-hand poses with two force levels from sEMG signals. In addition, low-cost, coin-shaped vibration motors were used to provide a feedback signal by translating the measured pressure on the fingertips into a vibration in the bicep and the forearm of four different healthy subjects. With that, participants could successfully identify the stiffness of three different objects (soft, hard, and medium). This study proposed a myoelectric prosthetic hand system capable of decoding four hand poses with two force levels from sEMG signals, and providing tactile feedback by translating the measured pressure on the fingertips into a vibration in the biceps and the

forearms of users, using low-cost coin shaped vibration motors. We validated the system experimentally on four participants (online) that could successfully identify the stiffness of three different objects.

5.2.1 Previous research on non-invasive sensory substitution in prostheses using vibrotactile stimulation

Non-invasive hand prostheses have the benefit of not requiring any surgical operations, making them more practical, and increase thereby their acceptance rate by amputees [192]. Thus, they can be potentially less expensive, easy and more intuitive to use for the patient who will not have to undergo any clinical surgeries [192]. Indeed, there have been several literature reviews on the different feedback techniques and modalities for sensory-enable upper-limb prostheses [198]. Particularly, sensory substitution feedback, by either using modality mismatch to provide sensory information to the user through a channel that usually differs from the normally used (e.g. substitute touch with hearing) or through the use of the same channel but with a different modality (e.g. substitute pressure with vibration) [97], has become important [198]. Among these feedback modalities, vibrotactile and electrotactile have been the most prevalent techniques [198]. Previous studies [100] investigated how changes in the amplitude and frequency of the stimulus can convey information about the manipulated object. One study [105] tested a system, where a sports glove on the non-amputated arm, was used to provide sensory feedback. In that study, EMG was not combined with the vibrotactile system but authors only focused on the sensory substitution part. Overall, their proposed haptic feedback improved the grip force accuracy by 129% compared to when the feedback was not provided. In another study [199] that was performed on 15 healthy subjects and validated on three patients, authors showed improvement when executing a grasping task, and users reported that, overall, they would prefer to use vibrotactile compared to electrotactile feedback. It is worth noting that no EMG was used for the feedforward control of the device nor the user's applied force was decoded. One of the limitations of these studies is that the vibrotactile feedback was in most cases either tested alone or with a binary EMG classifier (open vs close) and no simultaneous decoding of different grasping movements nor of the applied force extracted from EMG were performed [198]. Extending upon these studies, this work investigated the reliable decoding (86.25%) of four different hand postures from sEMG signals, two force levels (high, low) for a real-time control of 3D-printed prosthetic hand. Simultaneously, the four participants received different vibrotactile stimulations on their forearms, encoding the stiffness of three different objects (soft, medium, hard), and they were able to recognize them with an aver-

age accuracy of more than 88.46%. Table 5.1 compares different studies that used sensory substitution for prosthetics control and summarizes the main obtained results. For more in-depth review on non-invasive sensory substitution methods for prosthetics control, readers are urged to check out this study [198].

Table 5.1: Comparison of different studies that used sensory substitution for prosthetics control and their achieved results

Reference	Modality	Feedback	Posture & Force decoding	Accuracy
[105]	Electrotactile	Force (Offline)	NO	78.8%
[199]	Hybrid	Position (Offline)	NO	Not reported
[200]	Vibrotactile	Velocity & Force	only 1 posture	74% & 33%
[201]	Vibrotactile	1 single force	NO	94%
[202]	Electrotactile	only 6 force levels	only 1 posture	94%
Our work	Vibrotactile	3 stiffness levels	4 postures & 2 force levels	88.46%

5.2.2 Motivation & aims of investigating vibro-tactile sensory substitution for upper-limb prostheses control

The overall aim of this study was to propose a real-time and non-invasive system for upper-limb prostheses bidirectional control based on sEMG decoding and vibrotactile stimulation. Such a system allowed four different healthy subjects to control four different hand movements with two force levels of a 3D-printed prosthetic hand, while receiving a sensory substitution vibratory signal about the stiffness of the manipulated object. Owning to that, subjects were able to distinguish between soft, hard, and medium objects in real-time. An overview of the proposed system is presented in Figure 5.1.

5.3 Methods

5.3.1 Experimental paradigm and data recording

5.3.1.1 Hand gesture recognition

For sEMG data recording, four healthy and right-handed human subjects (25 ± 2.5 years old) with no record of neurological disorders were recruited to perform a series of hand movements, namely a 2-digit grasp, a 3-digit grasp, a fist grasp and hand open (rest). During each trial, the subject was asked to perform one of the postures, which were selected from a discrete uniform distribution, with two levels of force (high, low). Data used in this example study as well as the experimental paradigm are made publicly available with the gumpy

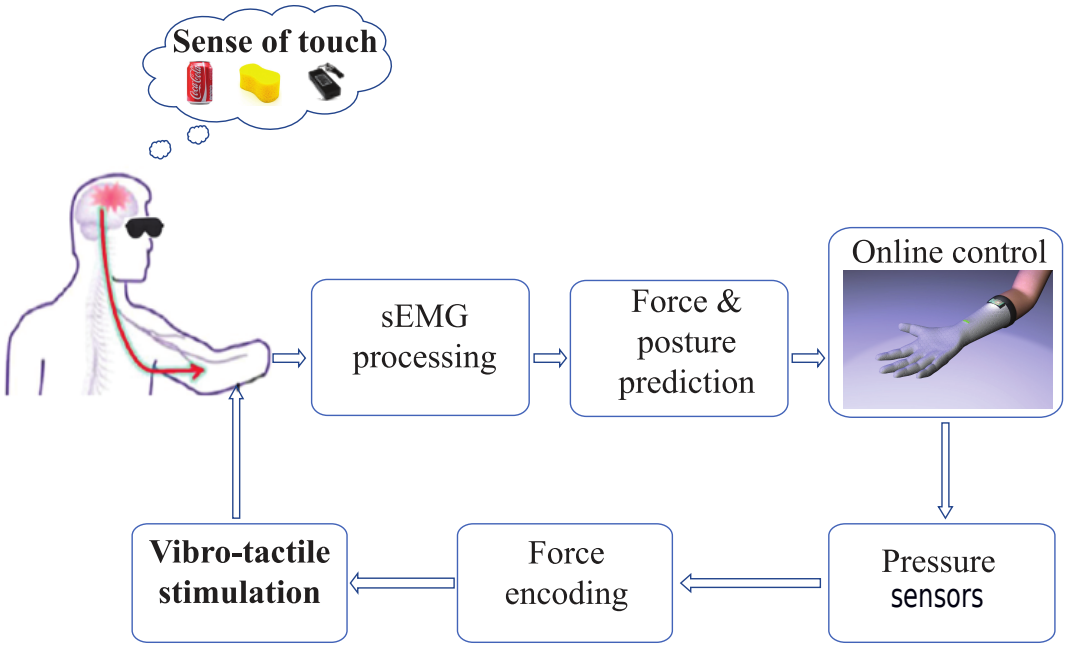

Figure 5.1: Overview of the proposed non-invasive bidirectional control system

toolbox [46]. EMG data were recorded and sampled at 200 Hz using the MYO armband wireless system [203]. Four pairs of electrodes, which cover the muscles of the forearm in a ring-like fashion were used, and the reference electrode was placed on the elbow bone.

5.3.1.2 Force encoding

To measure the applied force, force sensing resistors (FS402) were placed on the fingertips. A voltage divider circuit and an Arduino Nano were used to acquire the global force values from each individual finger. The FS402 force sensitivity range is from 0.1 to 100 N. The choice of FS402 sensors in this experiment was based on its low cost and human-like touch characteristics. The sensor can be placed in the fingertip of different prosthetic hand, and it can cover comparatively a wide area and when interacting with the environment and manipulating objects.

5.3.1.3 Prosthetic hand control

As mentioned, an open-source 3D printed prosthetic hand from Open Bionics [204] was used in this experiment. It is a body powered passive prosthetic hand that was assembled in our research laboratory. The prosthetic hand has a chestnut board to control the different movement of fingers. Each time, the prosthetic hand receives the decoded movement and force information, it activates the motor which can control each of the five different fingers, and hence the intended hand movement is performed. Beetroot v1.0 firmware from Open Bionics was used to control the chestnut board. Beetroot includes full serial control of individual fingers and grip patterns, muscle control through EMG sensors and provides a framework for adding extra functionality to the hand.

5.3.1.4 Vibro-tactile stimulation

For the vibrotactile feedback system, three coin type vibration motors were placed on the biceps and the forearm of the participants. All of the three vibrators were controlled by pulse width moderation (PWM) (as shown in Figure 5.3) sent by an Arduino Nano. The PWM signal was used to control the three vibration motors; each vibration motor was associated with one of the force sensors, where the duty cycle of the PWM signal controlling that vibration motor was set to be proportional to the measured finger pressure. For the vibrotactile feedback experiment, three different classes of objects (soft, hard and medium) were used. During the experiment, the participant learnt to associate the vibration at one specific site with the lifted object and could therefore differentiate between them according to the received feedback signal. We wish to mention that a similar experiment was proposed before in [114], despite the high level of invasiveness of their designed system.

5.3.2 Data processing & analysis

5.3.3 EMG signal processing and hand poses classification

EMG signals were processed using the gumpy.signal module in the gumpy BCI toolbox [46]. Filtered EMG signals were analyzed using 200 ms sliding time windows with 50 ms overlapping. The length of the sliding window was chosen for the purpose of allowing real-time control. For each interval, the computed mean of the signal was subtracted and divided by the standard deviation. Thereafter, the root mean square (RMS) was computed in each time window and fed into the classifier. A feature selection algorithm (SFSF) [35] was used to select a certain number of features in the k range (10, 25). Four different classifiers, namely (Naive Bayes (NB), Quadratic Discriminant Analysis (QLDA), k-nearest neighbors (KNN),

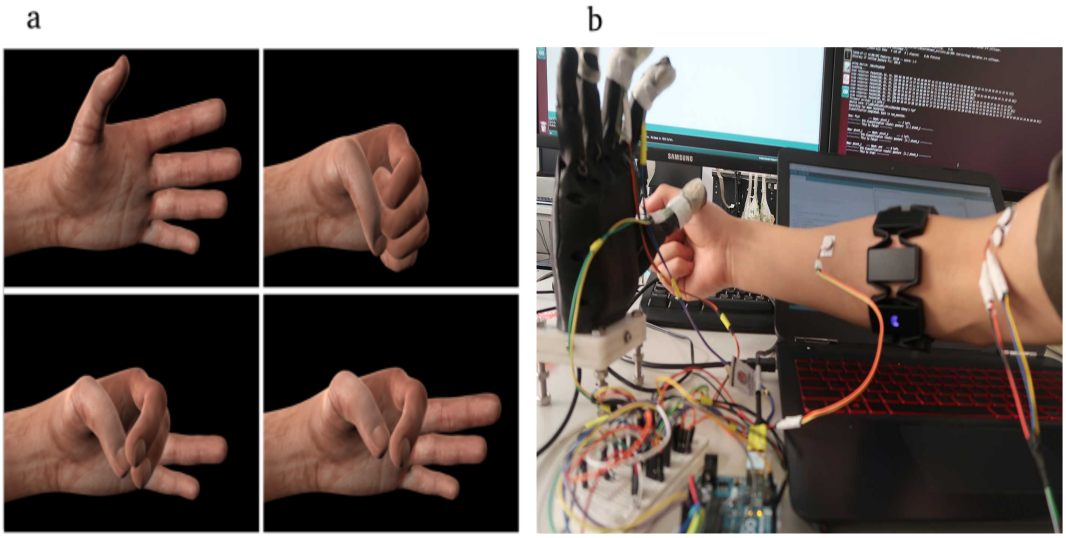

Figure 5.2: Proposed experimental paradigm for the closed-loop system. (a) Different hand gesture renderings prompting subjects. (b) Recording setup of EMG signals and fingertips pressure during grasp movements with the proposed vibrotactile feedback system.

and Support vector machine (SVM)) were tested, and a 3-fold cross validation was used to train and validate the selected (offline) model. The comparison of the different classifiers trained and tested offline is presented in Figure 5.4.

5.3.4 Force values encoding and decoding

Two force levels were simultaneously decoded from sEMG signals with the recognized hand pose and they were converted into a control signal to drive a 3D printed prosthetic hand designed by Open Bionics. It is worth noting that the same feature extraction method used for gesture recognition was chosen to classify each type of the two associated force levels (low, high). Afterwards, the measured pressure on the fingertips was translated into a vibrotactile feedback using coin type vibration motors placed on the subject's arm. Based on the received feedback signal and the elicited sensations, the blindfolded subject could identify the stiffness of three different objects.

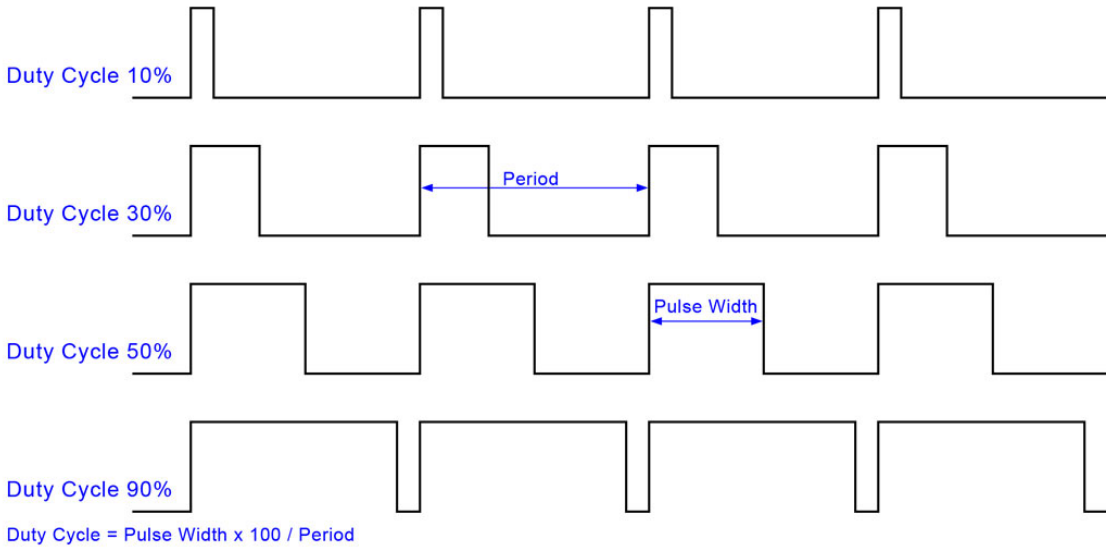

Figure 5.3: Duty cycle of pulse width moderation (PWM)

5.4 Main results of using vibro-tactile substitution and sEMG signals decoding for a 3D prosthetic hand control

5.4.1 Real-time control of a 3D prosthetic hand

A successful online decoding of four hand poses, namely a 2-digit grasp, a 3-digit grasp, a fist grasp, and rest (the no movement class) with two levels of force was performed. Interestingly, only 10 for each posture were needed from each of the four participants to train the model. Thereafter, 15 new online trials were used for online testing. The number of offline trials used for model training was reduced in retrospective analysis to evaluate the effect of the training data size on the online classification accuracy.

5.4.2 Sensory substitution results

Our experiment was conducted solely on healthy subjects. First, the proposed system was validated and tested with two subjects without the prosthetic hand. Afterwards, the proposed system was further validated and tested directly with a prosthetic hand. The experimental setup is illustrated in Figure. 5.6. **Experiment 1:** For the first experiment, two participants (P1, P2) were needed in order to perform the vibro-tactile experiment and validate the proposed system. P1 was asked to perform one of the four postures as shown on the screen with two different force levels. Force levels were chosen by the subject based on to the object that can be grasped. Recorded EMG signals were decoded and converted into a

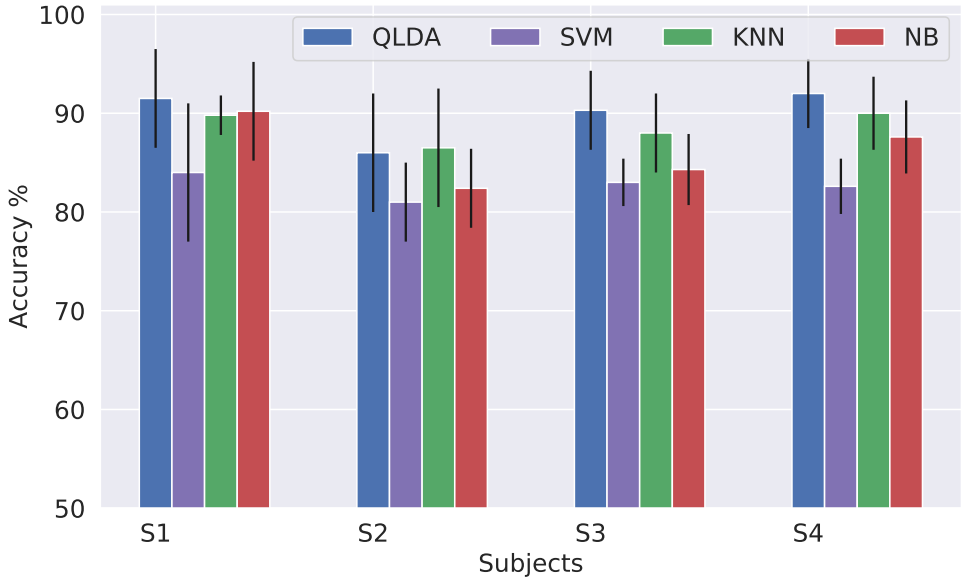

Figure 5.4: Offline classification results for sEMG decoding. This bar plot shows the validation accuracy for each subject for the 4 different tested classifiers, as well as the standard deviation of each model.

control signal of the 3D printed prosthetic hand. The measured force using the FS402 sensors placed on the fingertips, were encoded and translated into vibration-tactile stimulations on the arm of P2, who had to recognize the stiffness of the lifted object. Overall, we achieved an average success rate of more than 92%, when recognizing the stiffness of three different objects. More importantly, the four subjects needed solely one training session to learn the vibro-tactile feedback mapping. As the model performance should not be solely assessed on classification accuracy, precision and recall performance measures were also computed.

Experiment 2: After the validation of the proposed system with two human subjects, the system was tested directly with the prosthetic hand. The subject was asked to perform one of the hand gestures, which was decoded online and translated into commands to control the prosthetic hand to grasp and hold one of the three objects. Simultaneously, the same participant received a vibro-tactile and had to recognize the stiffness of the grasped object. Overall, we achieved an average success rate of 88.46%, when recognizing the stiffness of three different objects. More importantly, subjects needed only one training session to learn the vibro-tactile feedback mapping. Results are presented in Figure 5.7. The confusion matrix presented in Figure 5.7 shows that the four participants could easily distinguish between

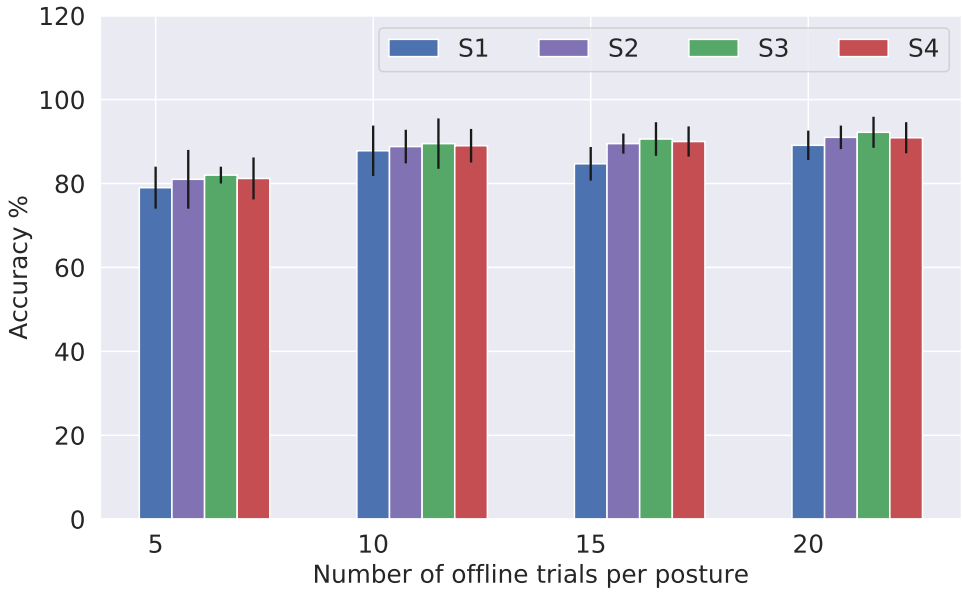

Figure 5.5: Online classification results

soft and hard objects. However, as shown in Figure 5.7, the medium object was sometimes confused with the soft and hard objects for most of the four participants. [1]

5.5 Discussion

In this study, we showed the control of a 3D printed prosthetic hand using decoded sEMG signals and a low cost vibro-tactile feedback system. Several similar systems have been proposed in the past. However, the main contribution of this work resides in proposing and testing a low-cost and bidirectional system in real-time that combines both EMG decoding and stiffness recognition through sensory substitution. Overall, this study is considered an extension upon previous studies whose focuses were either on solely validating individual parts of the closed-loop system or the use of invasive approaches when tackling the problem. Notwithstanding the good online results presented in this work, it is thought that the proposed system exhibits some limitations, which should be addressed in future work. First, the developed system was only tested on healthy subjects and no experiments with amputees were performed. Hence, it remains questionable whether similar performance could be obtained when testing with amputees and the translation of this engineering approach

[1] A demo video of this work is available: `https://youtu.be/RfcDedfgQs4`

Figure 5.6: Overview of the proposed closed-loop approach for prosthetic hand control.

into clinical trials should be investigated. Second, long-term validation of the robustness and the effectiveness of this developed system should be considered in the future. Sweat, slight changes of electrode position during recording and the difference between muscle tissues of the participants could drastically decrease the quality of the recorded sEMG signal and therefore deteriorate classification accuracy. Additionally, better classification results could be obtained when decoding simultaneously EMG signal and force levels by using more discriminative features. Aside from that, recording and training the system with more complex hand poses and individual fingers control should be addressed in future work. Last, despite the good performance of the proposed sensory substitution system (92% and 88.46% accuracy when differentiating between three different grasped objects), considerable improvements could be achieved. Using more accurate pressure sensors when providing the feedback signal could improve the performance of the system, particularly when increasing the complexity of the problem, testing with more objects, and investigating the encoding of other physical properties of manipulated objects. This study gave rise to focus on somatosensory evoked potentials (SEP) identification and analysis in our follow-up studies, in particular those associated with other sensory substitution modalities, in order to understand how the human brain perceives different sensory substitution signals. Thus, this sparked the interest to use the identified SEP patterns to quantify brain activity in response to different sensory modalities, including transcutaneous electrical nerve stimulation and thermal stim-

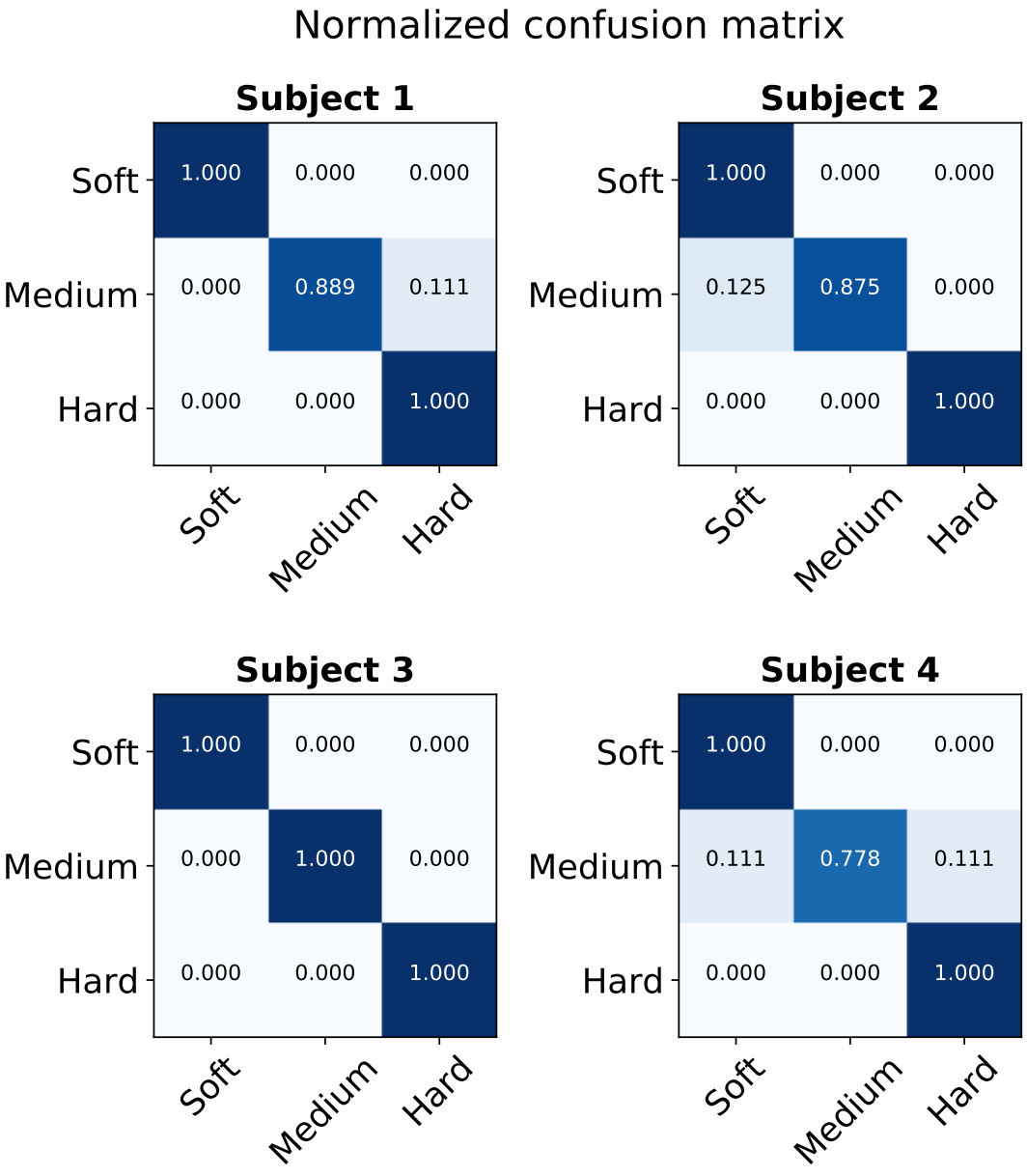

Figure 5.7: Confusion matrices for the object discrimination task tested with four participants using the proposed vibrotactile feedback system.

ulation. This was, therefore, investigated in the next two studies presented chapters 6 and 7.

5.6 Summary

This study proposed a non-invasive system for hand prostheses control that investigated the use of sensory substitution (vibrotactile stimulation) combined with multiple hand gesture decoding and force levels from sEMG signals. Four hand poses and two force levels were successfully decoded from sEMG signals with an online accuracy of 86.25% and 100%, respectively. The measured finger forces from the fingertips of a 3D printed prosthetic hand were encoded and translated into vibro-tactile stimulation. Using this feedback paradigm, all subjects were able to recognize the stiffness of three different objects with more than 88.46%.

6 Decoding of EEG signals when perceiving three distinct sensory stimuli induced by TENS: An amputee case study

This chapter is made up of content adapted with permissions from the manuscript Zied Tayeb, Rohit Bose, Andrei Dragomir, Luke E Osborn, Nitish V Thakor, Gordon Cheng, "Decoding of Pain Perception using EEG Signals for a Real-Time Reflex System in Prostheses: A Case Study." Published in Nature Scientific Reports, 10 (1), 1-11, (2020). DOI: `https://www.nature.com/articles/s41598-020-62525-7`
Author Contributions: Zied Tayeb developed the software for EEG data analysis, analyzed the data, interpreted the results, prepared the figures, and wrote the paper. Luke E Osborn collected the data and designed the experimental paradigm. Rohit Bose, Andrei Dragomir and Luke E Osborn contributed in the data analysis. Nitish V Thakor and Gordon Cheng supervised all experiments, data analysis, and interpretation of the results. All authors contributed in writing the paper.
Note: This research has been nominated for the BCI Award 2020.

6.1 Study overview

In recent times, we have witnessed a push towards restoring sensory perception to upper-limb amputees, which includes the whole spectrum from gentle touch to noxious stimuli. These are essential components for body protection as well as for restoring the sense of embodiment. Notwithstanding the considerable advances that have been made in designing suitable sensors and restoring tactile perceptions, very intense sensation perception dynamics and its decoding using effective features, are still not fully understood. In this study, using EEG recordings, we identified and validated spatio-temporal patterns of brain activity during innocuous, moderately more intense, and noxious stimulation of an amputee's phantom limb using transcutaneous nerve stimulation (TENS). Based on the spatio-temporal

EEG features, we developed a system for detecting noxious sensation perception and reaction in the brain, which classified three different stimulation conditions with a test accuracy of 94.66%, and we investigated the cortical activity in response to sensory stimuli in these conditions. Our findings suggest that the noxious stimulation activates the pre-motor cortex with the highest activation shown in the central cortex (Cz electrode) between 450 ms and 750 ms post-stimulation, whereas the highest activation for the moderately intense stimulation was found in the parietal lobe (P2, P4, and P6 electrodes). Further, we localized the cortical sources and observed early strong activation of the anterior cingulate cortex (ACC) corresponding to the noxious stimulus condition. Moreover, activation of the posterior cingulate cortex (PCC) was observed during the noxious sensation. An overview of the real-time withdrawal system is shown in Figure 6.1.

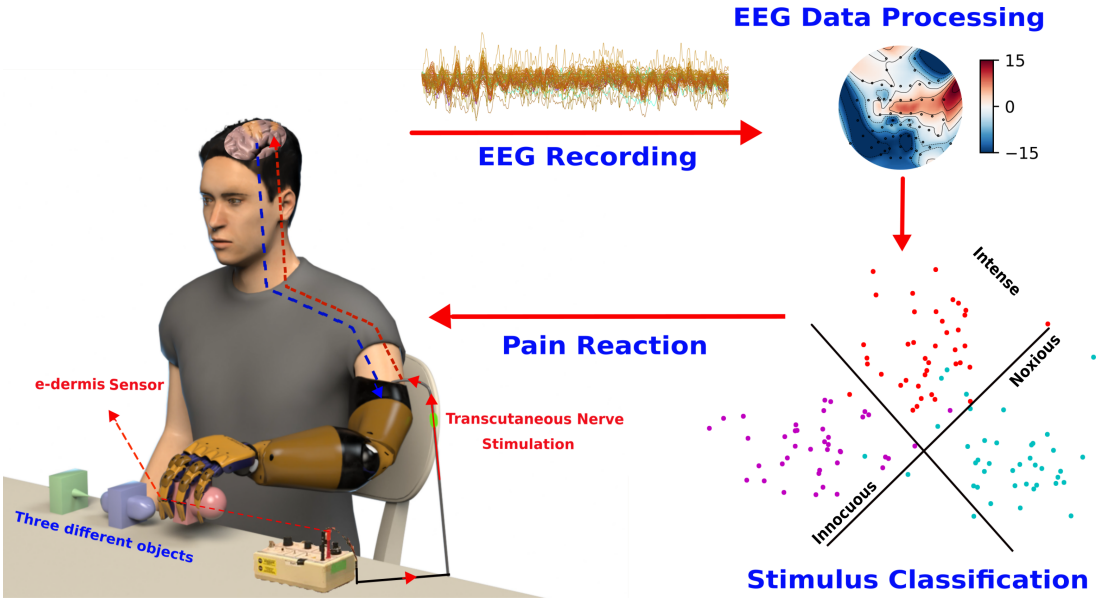

Figure 6.1: System implementation overview of a prosthetic arm that can restore the sense of touch and pain. An upper-limb amputee wears a prosthesis equipped with e-dermis sensors capable of measuring pressure and object curvature. Tactile sensations from innocuous to noxious, based on detected pressures at the fingertips, are conveyed to the user's phantom hand through TENS on the residual limb. Brain responses are analyzed and decoded to understand the tactile sensory perception, including noxious stimulus, and identify activated brain regions. Neural activity can be used to design a prosthesis that mimics natural pain withdrawal behavior in humans.

6.2 Introduction & Related Work

Nociception is commonly known as the sense of pain [112]. Specialized receptors called nociceptors that cover the skin and organs react to harmful chemical, mechanical and thermal stimuli [205]. Some of these microscopic pain receptors react to all kinds of noxious stimuli while others only react to specific pain like burning or pricking your finger on something sharp. Jolts of sudden pain activate the A-type fibers to send an electrical signal up to the spinal cord [206]. Pain signals then activate the thalamus, which relays the signal to the different brain regions[207]. Subsequently, the signal activates the somatosensory cortex which is responsible for physical sensations; the signals are then relayed to the frontal cortex where higher-order cognitive processing occurs, and finally to the limbic system, which is linked to emotions [208]. This pain processing network, along with pain reflex pathways in the spinal cord [206], are considered of the utmost importance for body protection from damaging stimuli [117]. These insights into brain networks have therefore spurred research on unraveling the processes within the body that lead to the unpleasant sensation of pain [209] and on understanding the pain perception mechanism in the brain [210]. Authors in [123] investigated perceptual, motor, and autonomic responses to short noxious heat stimuli using EEG and confirmed that pain perception is subserved by a distinct pattern of EEG responses in healthy subjects. Functional magnetic resonance imaging (fMRI) was used in [43] to demonstrate pain-related activation of the ACC and the PCC during TENS in healthy participants. A template of nociceptive brain activity that is sensitive to analgesic administration and suitable for clinical trials and research investigations was identified and validated in [211]. Furthermore, different somatosensory evoked potential (SEP) components and latency differences after stimulation of proximal and distal sites of the median nerves were studied and identified in eight healthy right-handed males [212]. Similarly, other previous studies showed that primary and secondary somatosensory cortices, insular cortex, ACC, prefrontal cortex (PFC), and thalamus are activated during experimental pain stimuli [213, 214, 215]. Authors in [124] showed the important role of the parietal lobe in pain perception and understanding. Notwithstanding the enormous number of studies on pain perception and brain responses to different painful stimuli using EEG and fMRI, most of these studies focused on studying brain responses in healthy subjects and have not investigated brain responses when perceiving the sense of pain in amputees nor in human-robot interaction settings [117]. It has, therefore, become imperative to study amputees' brain activity when integrating the sense of touch and pain in their arm prostheses [117]. The core novelty and the main contribution of this study reside in the use of non-invasive EEG activity to analyze somatosensory evoked responses recorded when receiving three different

types of stimulations. These stimulations were chosen to convey different sensation profiles, ranging from pleasant to uncomfortable sensation. For that, we identified a brain activity template during innocuous (INNO), moderately intense (MOD) and noxious (NOX) stimulation of an amputee's phantom hand delivered through TENS [98]. Based on the identified spatio-temporal brain activity patterns, we developed an offline system for detecting pain reaction in the brain which can recognize the three stimulation conditions from recorded EEG responses by using effective spatio-temporal bio-markers to identify the different brain regions involved in noxious stimuli processing as well as latency responses for each stimulation condition. The overall goal of this study was to extend upon the work performed by Osborn et.al [117], where the reflex system was implemented in the arm prosthesis and the amputee was not involved in the withdrawing reaction. This is thought to be of the utmost importance when designing a better bidirectional-control system between the human and the prosthesis, and hence increase the amputee's sense of embodiment and the sense of ownership [216, 28]. Additionally, detecting this perceived pain sensation and reaction would have an important role in protecting the prosthesis from being damaged by external stimuli [217]. To the best of our knowledge, even though the presented results are from a case study, this work is among the very few to investigate brain responses to different types of NOX and INNO stimuli and the first study to investigate and characterize spatio-temporal brain activities in amputees during a range of noxious and innocuous sensory feedback to the phantom hand. Extending upon the findings of the aforementioned studies, we also investigate attention and perceptual brain circuitry involved in the withdrawal reaction.

6.2.1 Motivation & aims of decoding EEG signals when perceiving three TENS-induced sensory stimuli

This work reports a proof-of-principle of this approach to analyze and classify neural activity when restoring sensory perception to amputees, which could chart a route ahead for designing a real-time withdrawal reaction system in upper-limb prostheses.

6.3 Methods

6.3.1 Study design: Experimental paradigm

6.3.1.1 Patient recruitment and sensory stimulation

An amputee participant (29 years old) with a bilateral amputation for more than five-year prior to the current experiments, due to tissue necrosis from septicemia, was recruited at

Johns Hopkins University in Baltimore to perform a series of an embodied prosthesis control as well as sensory feedback experiments. The participant has a transhumeral amputation of the left arm and a transradial amputation of the right arm. All sensory feedback and prosthesis experiments were performed on the participant's left arm. EEG data were collected in one session over a period of two hours. For the sensory stimulation, we performed sensory mapping of the amputee's phantom hand through transcutaneous electrical nerve stimulation (TENS) using a 1-mm beryllium copper (BeCu) probe connected to an isolated current stimulator (DS3, Digitimer Ltd., Hertfordshire, UK). An amplitude of 0.8 mA and frequency of 2 to 4Hz were used while mapping the phantom hand. The amputee identified areas of phantom activation during sensory mapping and the stimulation sites were noted using anatomical and ink markers. For the stimulation experiment, we used 5-mm disposable Ag-Ag/Cl electrodes on the residual limb sites that mapped to the thumb/pointer, pinky/ulnar, and wrist of the phantom hand [218]. The stimulation sites were the same as those used in [117]. It should be noted that sensory mapping was only performed on the left (transhumeral) residual limb because the amputee participant only wears a prosthesis on his left (transhumeral) side and not his right (transradial) side.

6.3.1.2 Research governance

This study was carried out in accordance with the Declaration of Helsinki. All experiments were approved by the Johns Hopkins Medicine Institutional Review Boards. The whole experiment and data recording were performed at Johns Hopkins University (JHU). The participant was asked to sign a written informed consent and he agreed to take part in all our experiments. Additionally, the participant consented, by signing a written informed document, to have images and recordings taken during the experiments used for online open-access publication and presentations.

6.3.1.3 EEG data recording and experiment

Brain activity correlates of transcutaneous electrical nerve stimulations were investigated by recording 64-channel EEG data from the amputee participant. Different locations on the participant's left residual limb were identified so that, when stimulated, they activate different regions of the participant's phantom hand. In this EEG experiment, the subject was seated comfortably and was looking at a black cross on a white wall. EEG recordings during various stimulations of the subject's peripheral nerve sites corresponding to the thumb/pointer finger, pinky/ulnar side of the hand, and the wrist of his phantom hand. We stimulated the subject's residual limb in regions that activated his phantom hand using transcutaneous electrical

nerve stimulation (TENS). The stimulation included three different conditions for the thumb/pointer and two conditions for the other sites. All values of stimulation were based on previous mapping and psychophysics with this subject [117]. Condition 1 (INNO stimulation): Pulse width (PW)= 1 ms, freq = 45 Hz – perceived as a light, almost pleasant touch sensation. Condition 2 (MOD stimulation): PW = 5 ms, freq = 4 Hz – perceived as a slightly more noticeable/intense touch but not uncomfortable. Condition 3 (NOX stimulation): PW = 20 ms, freq = 20 Hz – perceived as a slightly painful and uncomfortable touch sensation. All values of stimulation were based on previous mapping and psychophysics with this subject [117]. All three conditions (INNO, MOD, NOX) were applied to the thumb/pointer stimulation site and the INNO and MOD conditions were applied to the pinky/ulnar and wrist stimulation sites. Blocks of each stimulation condition were randomly presented as a five consecutive stimulation pulse trains lasting for 2 s with a delay of 4 s $\pm$ 25% jitter between each stimulation pulse train. Stimulation condition blocks were presented 4 times, yielding a total of 60 trials for the three conditions. A break up to 10 min was chosen between each block. Condition 3 (NOX) was only presented to the thumb/pointer stimulation site, whereas Conditions 1 and 2 (INNO and MOD) were presented to all stimulation locations (thumb/pointer, pinky/ulnar, and wrist). Condition 3 was only presented to the thumb/pointer location to reduce the total time the subject experience noxious sensations. EEG data were collected using a 64 channel EEG device (Neuroscan system) with a 500 Hz sampling rate. The montage was in accordance with the 5% 10/20 system. Electrode impedance was kept below 10 kOhm in at least 95% of derivations throughout the experiment. The amplitude of the transcutaneous electrical nerve stimulation was 1.6 mA for all sites of stimulation and the subject rated each condition's discomfort level using a comfort scale. To ensure that the subject is not substituting/anticipating the stimuli by sight, the EEG data was recorded without the subject wearing the prosthesis. The pulse width and the frequency of the TENS stimulation were selected based on extensive psychological experiments to quantify the perception of TENS as was reported in [117, 218].

6.3.2 Data processing & analysis

EEG data were recorded at 500 Hz. The reference electrode was chosen on the vertex and the ground electrode was located on the forehead. Data were processed with special designed Jupyter notebooks in Python using both gumpy [46] and MNE [219, 220] toolboxes. For data analysis, 60 trials in total for the three stimulation conditions were used. EEG signals were band-pass–filtered between 0.5 and 70 Hz using a fourth-order Butterworth filter and notch filtered thereafter at 60 Hz [211, 190]. All signals were extracted from the record-

ings in 1000 ms epochs, and to 100 ms time-window for further analysis. Epochs were baseline-corrected to the pre-stimulus mean [151]. Muscle artifacts were rejected by the Automatic Artifact Rejection (AAR) [221] as well as independent component analysis (ICA) were used to remove eye movement artifacts [222]. Additionally, epochs containing high-amplitude artifacts or high-frequency muscle noise (visually inspected) were rejected from the analysis using a threshold-based method [146]. EEG data collected over several trials of the same experiment were averaged together. All EEG scalp topographies were plotted using the MNE toolbox, by matching channel location with its value given the defined latency. Topographies are color encoded, where the green or yellow present null values, blue color presents negative values, and red encodes positive values; with the color intensity correlates with the channel value. Chosen time latencies in the topographic maps were chosen based on an algorithm [219] that computes and finds the highest peaks at each time point from all electrodes. For feature extraction and classifying the three conditions from EEG, we implemented and tested a wide range of classical machine learning approaches which are based on hand-crafted features. Five different classifiers from the gumpy.classification module [46] have been used and evaluated: K-Nearest Neighbor (KNN), Support vector machine (SVM), Naive Bayes (NB), Linear Discrimination Analysis (LDA) and Quadratic Linear Discrimination Analysis (QLDA). Two different feature extraction methods were used, namely the maximum amplitude value computed from each channel for a fixed 100 ms time-window, yielding a total number of 64 features (number of electrodes) as well as common spatial patterns (CSP) [62]. The CSP method yielded to slightly lower results (a mean accuracy of 85%) than the maximum amplitude value and was therefore discarded in our further analysis. Two different post processing methods were investigated and tested. First, a principal component analysis (PCA) with only two components was used for dimensionality reduction and the two components were fed thereafter to the different classifiers resulting in the presented 2D feature space (Figure 6.5). Second, we further investigated keeping all the extracted 64 features and we used a feature selection algorithm [35] to select the most discriminating subset of features (channels) as was depicted in Figure 6.6. Data were divided into 80% for training and 20% for testing. As the number of trials was small when splitting the data into validation and test sets (solely four trials remained for each condition during the test phase), a data augmentation technique [190] was performed yielding two new trials from each one of the initial 60 trials, forming a total number of 120 trials. It should be mentioned that the 120 trials (after data augmentation) were only used when preforming the PCA, splitting the data, and computing the test accuracy. Overall, a 10-fold cross validation was performed on training data to validate the model (validation accuracy) and the remaining 20% were using for the test phase. It should be noted for all analyses, balanced accuracy (bACC) was cho-

sen as an evaluation metric for the trained models. bACC is calculated as the average of the proportion corrects of each class individually, where the same number of examples in each class was used. Overall, we wish to mention that the first feature extraction method (max amplitude value) combined with PCA using SVM clearly outperformed the other investigated methods, yielding a validation accuracy of more than 95% and a test accuracy of more than 94%. It is worth noting that a grid search was performed to select the best hyper parameters of the SVM classifier for a given 10-fold cross validation.

6.3.2.1 GFP computation

The Global Field Power (GFP) is the standard deviation of the potentials at all EEG channels of an average given reference map [223]. The GFP formula is shown below in equation 6.1:

$$GFP = \frac{\sqrt{\sum_{i=0}^{\mathrm{N}}(\mu_{\mathrm{i}} - \overline{\mu}^2)}}{N} \tag{6.1}$$

where μ_{i} is the voltage of the map μ for a given electrode i, $\overline{\mu}$ is the mean voltage of all EEG electrodes of the map u and N is the number of electrodes of the map μ. High GFP wis explained by peak EEG activities as well as steep gradients. Overall, as illustrated in Figure 6.2, NOX stimulation shows higher global field power (GFP) compared to the MOD and the INNO stimulation. The GFP shows here the amount of activity at each time point in the field considering the data from all the 64 recording electrodes simultaneously [224].

6.3.2.2 Source localization

MNE toolbox [219] combined with gumpy [46] Python toolbox were used for EEG processing and for source localization. First, cortical surface reconstruction using FreeSurfer [225]. Second, the forward solution and the forward model were computed using the boundary-element model (BEM) [66]. Thereafter, the regularized noise-covariance matrix, which gives information about potential patterns describing uninteresting noise source, was computed and estimated. Afterward, we computed the singular value decomposition (SVD) of the matrix composed of both estimated noise-covariance and the source covariance matrix. Finally, dynamic statistical parametric maps (dSPM) [226] was computed and used for source localization and reconstruction. For dSPM, an anatomical linear estimation approach is applied. This assumes the sources are distributed in the cerebral cortex [227]. A linear collocation single-layer boundary-element method (BEM) [228] is used to compute the forward solution which models the generated signal pattern at each location of the cortical surface. A noise-normalized minimum norm estimate is estimated at each cortical location resulting

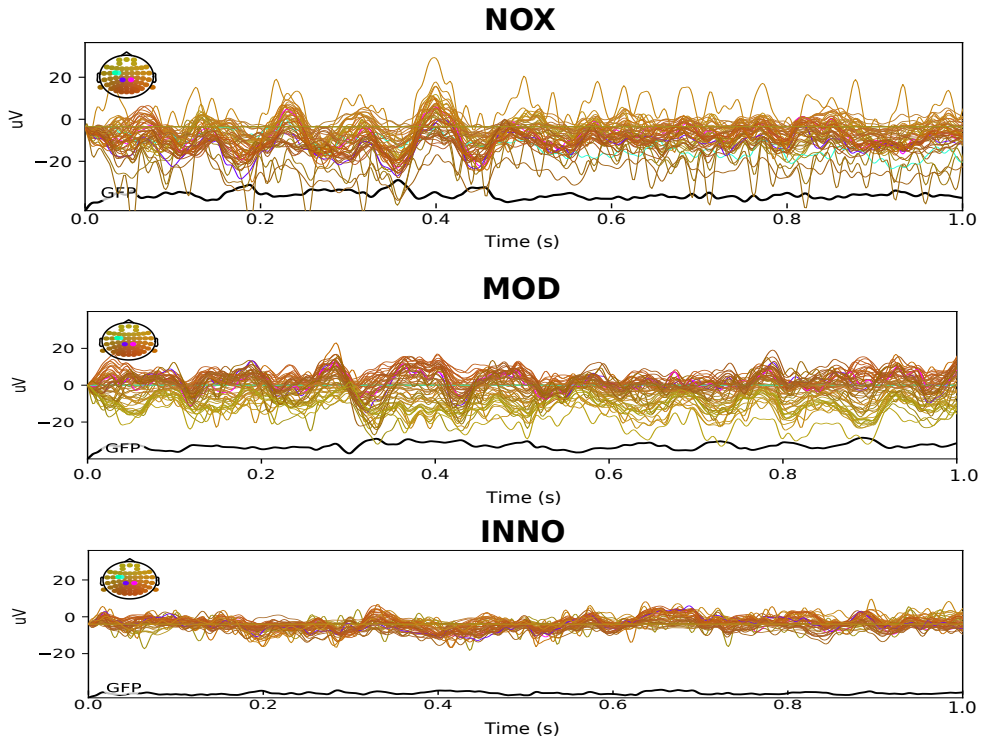

Figure 6.2: EEG activity for all 64 electrodes combined with the global field power (GPF) shown for the three different stimulation conditions. NOX stimulation shows higher GFP than the other two conditions and high activity in the somatosensory electrodes (CZ, C4, and C6). MOD shows higher GFP than the INNO and higher activity in the parietal lobe electrodes (P2, P4, and P6). Low GFP is shown during the INNO stimulation. The electrodes are color-coded as shown in the 10/20 system in the figure (up-left).

in an F-distributed estimation of the cortical current. Overall, dSPM identifies the locations of statistically increased current-dipolar strength relative to the noise level. The sLORETA method for source localization was also implemented for benchmarking purposes.

6.3.2.3 Data analysis and statistics

All relevant information about the obtained results is presented alongside their corresponding figures. For all statistical analyses, we first checked the normality as well as the independence of the data before applying the adequate statistical test. The normality of the data (the three conditions with the background activity) was checked using one-sample Kolmogorov-Smirnov test, which is a strict normality test, and as was suggested in the study by Strauss et.al [229]. Thereafter, the independence was checked using the Mann-Whitney U Test was

used (used when data is not normally distributed) and we found that the conditions are statistically independent ($p < 0.0001$). As the data was not normally distributed, we applied a Kruskal-Wallis test instead of ANOVA [229]. The Kruskal-Wallis test was combined with the post-hoc test for multiple group comparison. For all the obtained results, we considered $p < 0.05$ statistically significant to reject the null hypothesis. The software for the statistical analysis was implemented in python using the scipy and stats libraries.

6.4 Main results of EEG processing and decoding

6.4.1 All stimulation conditions activate the parietal lobe and noxious stimulation activates the central motor cortex

Sensory feedback of the three conditions (NOX, MOD, and INNO) tactile stimuli was delivered to the phantom hand using TENS on the transhumeral amputee's residual limb. Three different stimulation sites were used on the residual limb, which activated the thumb/index, wrist, and pinky of the phantom hand. The NOX stimulation was reported by the subject as uncomfortable but tolerable [117], the MOD stimulation was reported as slightly more noticeable/intense compared to the INNO stimulation. EEG was used to quantify brain activity during each stimulation and to identify the activated brain regions as well as the physiological principles underlying the perception of pain in amputees. For that, brain activity topography and time course were performed by analyzing all electrodes' activities in the first second post-stimulus period. Our analysis shows that all stimulation conditions elicit early activation of the parietal lobe (around 54 ms) which persists over time for all types of sensation. Interestingly, the MOD stimulation elicits higher activation of the parietal lobe compared to the INNO and the NOX stimulations. In contrast to both INNO and MOD stimulations, only the NOX stimulation activates the central cortex. Based on our findings, we postulate that the NOX stimulation started in the parietal (54 ms) and centro-parietal lobe, rapidly activated the perceptual mechanism in the subject's brain but moved thereafter towards the pre-motor and central cortex, which could, therefore, explain that the NOX stimulation activated the pain perception and reaction mechanism in the brain and the amputee had the intention to move away his residual limb during the stimulation. Results of brain activity topography for the three types of stimuli are illustrated in Figure 6.3. As shown in Figure 6.3, deactivations of the ipsilateral centro-parietal and the frontal lobe were observed during the NOX and the MOD stimulation, respectively, whereas a slight deactivation of the right temporal lobe was observed during the INNO stimulation. Further, 6.3 shows that there is no activation of the different brain regions when analyzing the pre-stimulus activation for the three different con-

ditions, concluding that the participant was not anticipating any of the three stimuli prior to the stimulation.

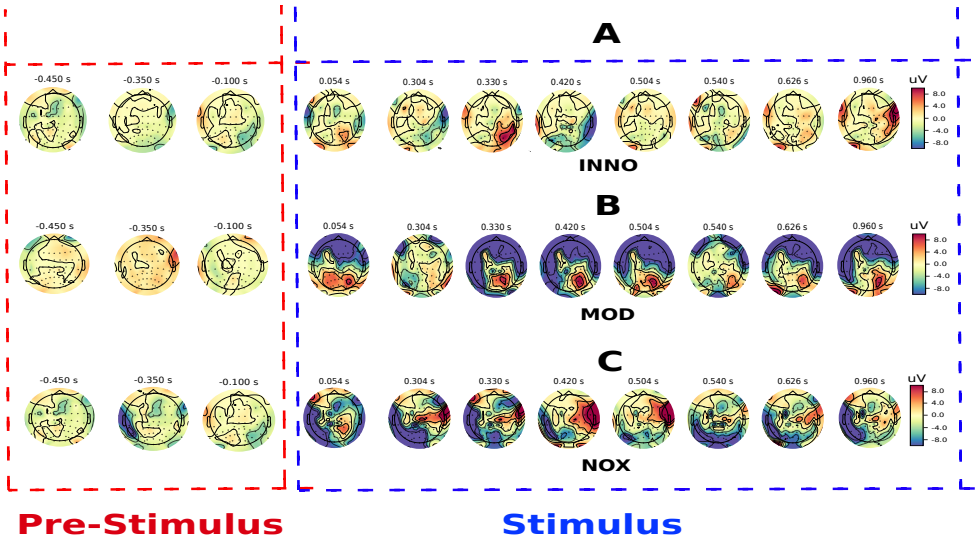

Figure 6.3: EEG topographic maps for NOX, MOD and the INNO stimulation. **A**, **B** and **C** represent topographic scalp map of the EEG amplitude response for three classes of stimuli: INNO, MOD and NOX stimulation, respectively, using the average of all trials for each condition. All topographic maps were plotted for the first second post-stimulation time window (average of across each condition's trials). The get_peak algorithm in the MNE software [219] was used to compute and detect the amplitude of the maximum EEG response (local maxima) for the noxious stimulation as well as the location (EEG channel) and latency of the detected peak amplitude. Time courses of NOX stimulation identified and found using the get_peak algorithm were used thereafter for analysis and benchmarking with the other two conditions. Early activation of the parietal lobe was found for all conditions, followed by strong activation of the central cortex during the NOX stimulation, strong continuous activation of the parietal region during the MOD stimulus and almost no activity during the INNO stimulus. For all three conditions, no activation of the different brain regions was found when analyzing the half-second pre-stimulus phase, indicating that the subject was not anticipating the applied stimulus.

6.4.2 Spatio-temporal features for noxious-evoked activity

We then extended the aforementioned analysis by seeking to identify a spatio-temporal template to distinguish between the three conditions and find the exact brain response time and spatial location. For the NOX stimulation, the highest activation was found at the central cortex in the post-stimulation time window from 450 to 750 ms when comparing it to the INNO stimulation, and the EEG background activity [$p < 0.0001$, Kruskal-Wallis test was

combined with the post-hoc (using Tukey HSD test) for multiple group comparison. Number of trials=60]. Additionally and as shown in Figure 6.4, the highest response in the amputee's brain activity during the noxious stimulation was localized at the vertex electrode in the middle of the scalp (Cz) [$p < 0.001$, when comparing to the other two conditions. Kruskal-Wallis test was combined with the post-hoc (using Tukey HSD test) for multiple group comparison. Number of trials=60] (relatively high activation was also detected in C4 and C6 electrodes). In contrast with the NOX stimulation which shows high activation of the central cortex, the MOD stimulation was found to be high at P2, P4, and P6 electrodes for the whole second of analysis as depicted in Figure 6.4 [$p < 0.05$, Kruskal-Wallis test was combined with the post-hoc (using Tukey HSD test) for multiple group comparison. Number of trials=60]. Although an activation of the parietal lobe was also found during the INNO stimulation, it should be noted that no special spatio-temporal biomarkers were observed. Based on our findings, we postulate that the intense stimulation was perceivable by the subject, which led to high and continuous activation of the parietal lobe in the brain [124] but the level of discomfort was not high to activate the central and pre-motor cortex, which is responsible for motor movements. Figure 6.4 illustrates activation of the parietal and centro-parietal cortex for the different conditions. Similarly and as was shown in Figure 6.3, no pre-stimulus activation was detected in the parietal lobe (P2, P4, and P6 electrodes) nor in the central cortex (Cz) for the three different stimulation conditions.

6.4.3 Classification of the three different stimulation conditions

We further investigated EEG based spatio-temporal biomarkers for the classification of the three different stimulation conditions. First, we studied how the classification accuracy changes in each 100 ms post-stimulation time. As shown in Figure 6.5 (A), our findings are in accordance with our aforementioned analysis results, and higher mean balanced accuracy (bACC) was found in the time window between 450 and 750 ms, with the highest bACC found between 650 and 750 ms post-stimulation [$p < 0.005$, Kruskal-Wallis test was combined with the post-hoc (using Tukey HSD test) for multiple group comparison. Number of trials=60]. We wish to emphasize that a mean accuracy of more than 90% was also observed in the time-window between 150-250 ms, which could be also further investigated and used as a time marker to design a nociceptive pain reaction system, where a minimum delay is usually required [230]. As the highest validation accuracy (validation bACC) was found in the time-window 650-750 ms, we used that time window during the test phase to classify the three different conditions and for further analysis. A mean bACC of 95% was obtained in the validation phase and more than 94% was achieved in the test phase, whereas

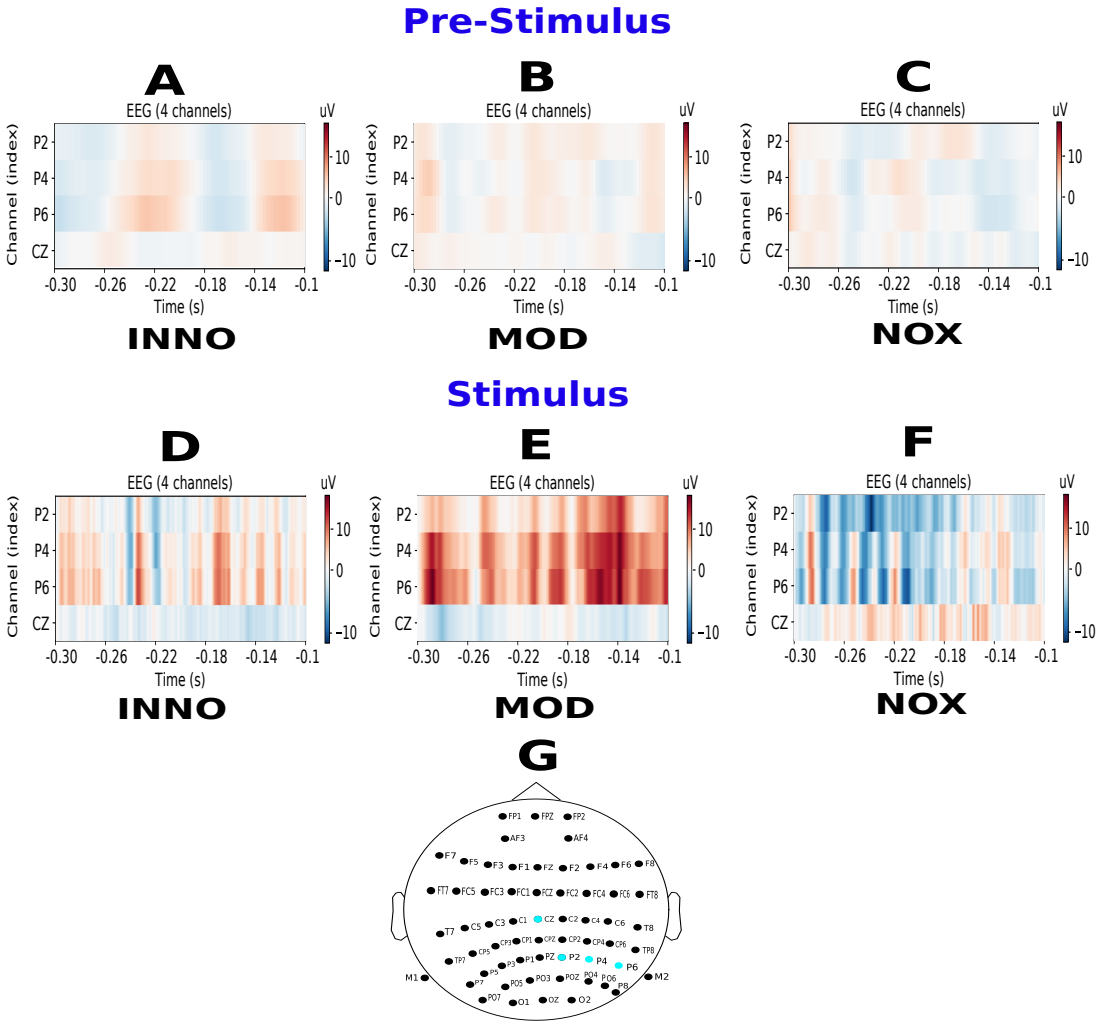

Figure 6.4: EEG activity for the parietal and central cortex electrodes. **A**, **B**, and **C** represent EEG activity in Cz, P2, P4 and P6 during the pre-stimulus phase during the INNO, MOD, and NOX stimulation, respectively. **D**, **E** and **F** represent EEG activity in four different electrodes; Cz (middle cortex) and P2, P4 and P6 electrodes in the parietal lobe during the INNO, MOD, and NOX stimulation, respectively. When comparing **D** to **E**, a parietal enhancement (red color) and a central depression (blue color) are observable. When comparing **D**, **E** to **F**, a central enhancement is observable (red color). **G**. 10-20 EEG recording system where Cz, P2, P4, and P6 electrode's positions in the 10-20 system are highlighted in blue.

the chance level for this task is 33.33%. For that, data were split into 80% and 20% where stratified 10-fold cross-validation was performed on 80% of the data (validation phase) and the saved model was used to predict correct labels on the remaining 20% of the trials in the test phase. A principal component analysis (PCA) was performed on the recorded data, which resulted in a clear separation between the three classes as shown in Figure 6.5 (B). Figure 6.5 (C) presents the obtained results in the test phase. The confusion matrix shows that both INNO and NOX stimulation were almost correctly classified, whereas the MOD stimulation was sometimes either confused with the INNO or the NOX stimulation. Last, it is important to highlight that when we kept all the features (without performing dimensionality reduction using PCA), we observed that our feature selection algorithm selected Cz, C4, C6, FT8 and CP6 as the best electrodes/features when distinguishing between the three classes. Selected electrodes are shown in Figure 6.6 and are well aligned with our aforementioned analysis, where we showed that central and the centro-parietal cortex electrodes exhibited different activities depending on the stimulation condition, and hence of the utmost importance when differentiating between the different types of stimulation. It is worth noting that the computed features are simply the maximum amplitude value of each electrode, which led to a feature matrix of 64 dimensions.

6.4.4 Stimulus-related activation within the medial wall of the cerebral cortex

To extend our findings, we sought to study brain activity at the source level in response to NOX, MOD, and INNO stimulations, and gain more insights into how the noxious reaction mechanism is achieved in the brain and what are the different brain regions involved in this pain reaction circuitry. We identify activated brain sources, en route to developing a complete real-time pain sensation detection system. We focus our analysis mainly on the NOX stimulation, which triggers the reaction mechanism in the brain. Here, we investigate if scalp EEG can detect and localize signals originating from different brain areas during the three different conditions. Overall, our analysis confirms the evidence that scalp EEG could be used to detect and correctly localize the source of the recorded signals [231]. For that, we reconstructed EEG source dynamics using distributed source modeling [232, 233] based on realistic head models [234] derived from individual MRI scans [231]. As illustrated in Figure 6.7, we found using the reconstructed EEG sources that NOX sensation elicits activation of the centro-parietal lobe, activation of the ACC, the somatosensory motor cortex, and the PCC. Overall and as shown in Figure 6.7, the activation of the ACC presents direct evidence that it plays a role in activating the attention circuitry in the brain as well as an important role in external sensory stimuli perception [235, 236]. Moreover, our study

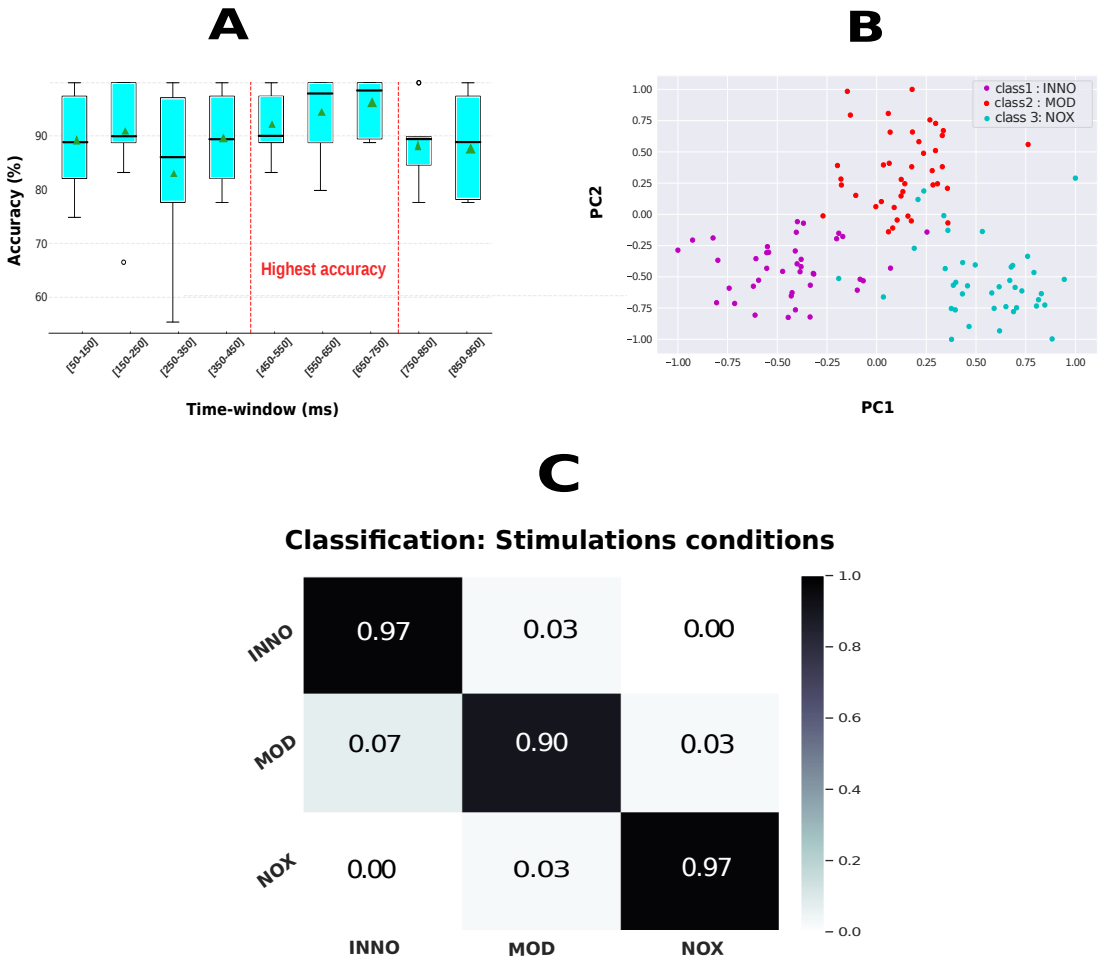

Figure 6.5: Classification results of the three stimulation conditions. **A**. Validation accuracy in different time-windows between 50 and 1000 ms after stimulation represented in a boxplot, and showing that the highest validation accuracy was obtained in the time-window 650-750 ms. The green triangle represents the mean accuracy value for each time window whereas the black line represents the median value for the same time window. **B**. 2D feature space after performing PCA, highlighting a clear separation between the three conditions. PC1 and PC2 represent the first two components after performing PCA. **C**. As the highest accuracy was obtained between 650-750 ms (shown in **A**), the confusion matrix was computed in that time-window when classifying the three stimulation conditions in the test phase.

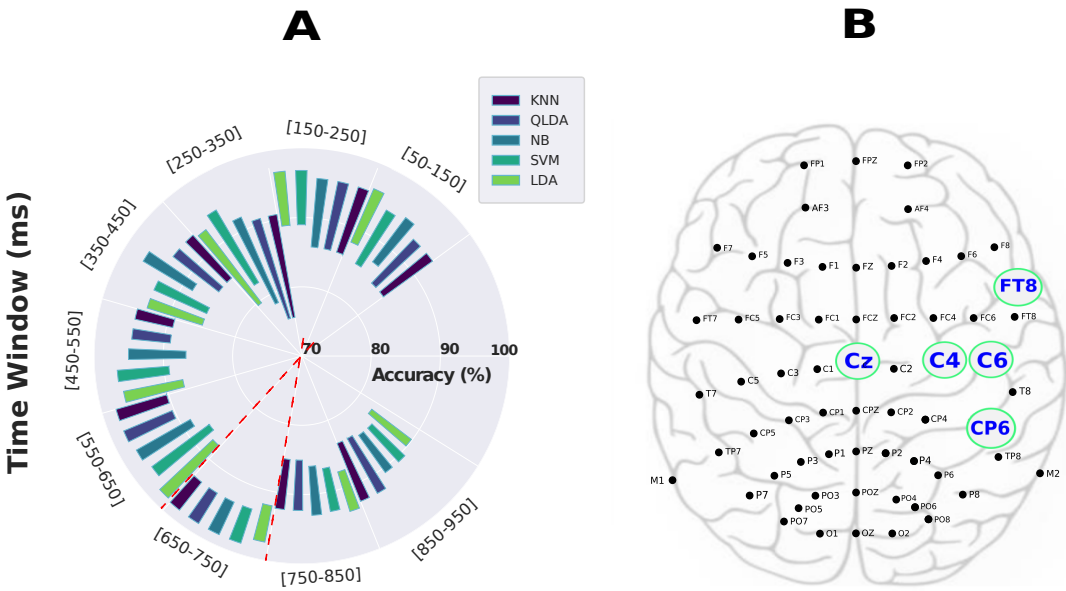

Figure 6.6: Validation results of the classification of the three stimulation conditions in each time-window using five different classifiers (KNN, QLDA, NB, SVM, LDA:Linear Discriminant Analysis) as well as the selected electrodes using the feature sequential algorithm. **A**. Validation accuracy in different time-windows between 50 and 1000 ms after stimulation using five different classifiers and represented with a polar bar plot. The polar bar plot shows the accuracy range (mean ± standard deviation) achieved by the five models for each time-window. The highest accuracy was obtained in the time-window [650-750] and is highlighted in the figure in red. **B**. The 10/20 system used for EEG data recording. A feature selection algorithm selected five different features (Cz, C4, C6, CP6, and FT8 electrodes) when classifying the three different conditions. Their positions in the brain, according to the 10/20 system, are highlighted in **B**.

reveals that the NOX stimulation activates the PCC, which seems to be in accordance with a similar study using another sensory feedback modality [43]. As shown in Figure 1 in the supplementary materials, the source localisation results for the MOD and INNO conditions show also activation of the parietal lobe at around 54 ms, which is aligned with topographic maps illustrated in Figure 6.3.

6.4.4.1 Standardized LORETA (sLORETA) benchmarking method

To benchmark our results, the standardized low-resolution brain electromagnetic tomography (sLORETA) [67] was investigated. The Standardized low-resolution brain electromagnetic tomography (sLORETA) [67] computes the EEG distribution across the full brain volume. The sLORETA method provides a smooth and good deep sources localization.

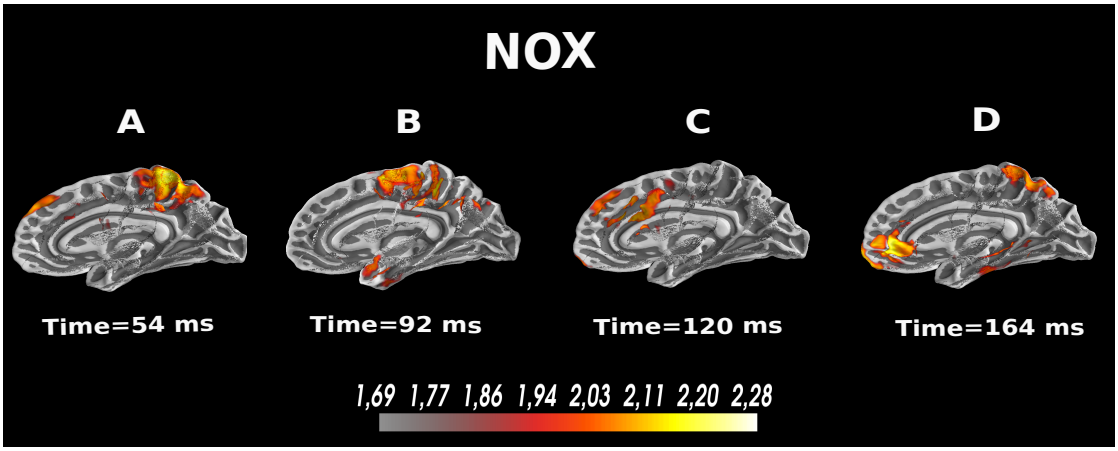

Figure 6.7: EEG analysis at the source level for the noxious evoked activity in the first 200 ms. The dynamic statistical parametric maps (dSPM) [226] is used to compute the reconstructed sources. The used scale represents the EEG amplitude activity in uV. **A**. High EEG activity in the centro-parietal lobe after 54 ms of stimulation. **B**. High EEG activity in the central cortex after 92 ms. **C**. Activation of the PCC after 120 ms. **D**. Activation of the ACC and the parietal lobe after 164 ms.

sLORETA provides a unique solution to the inverse problem using a defined cost function [68] F as follows:

$$F = \|\phi - KJ - c1\|^2 + \alpha\|J\| \tag{6.2}$$

where ϕ defines the electrical potential recorded from the 64-electrode scalp EEG signal, K defines the lead field matrix, J represents the measured current density, α defines the positive regularization parameter, $c1$ is constant, and $\|.\|$ is the Euclidean norm. For benchmarking purposes, the sLORETA was also implemented and used for EEG source localisation. As illustrated in Figure 6.8 and was previously reported in [237], results obtained by the sLORETA method are similar and match the obtained results by the dSPM method with a slightly lower values. [1]

6.5 Discussion on the identified spatio-temporal features and classification results

Here, a spatio-temporal template of brain activity during three different phantom limb stimulation conditions (INNO, MOD and NOX) has been identified and characterized in an amputee based on EEG signals. Unlike fMRI or intracranial signals, EEG allows continuous

[1] A demo video of this work is available: `https://youtu.be/Su1HAKpK9J8`

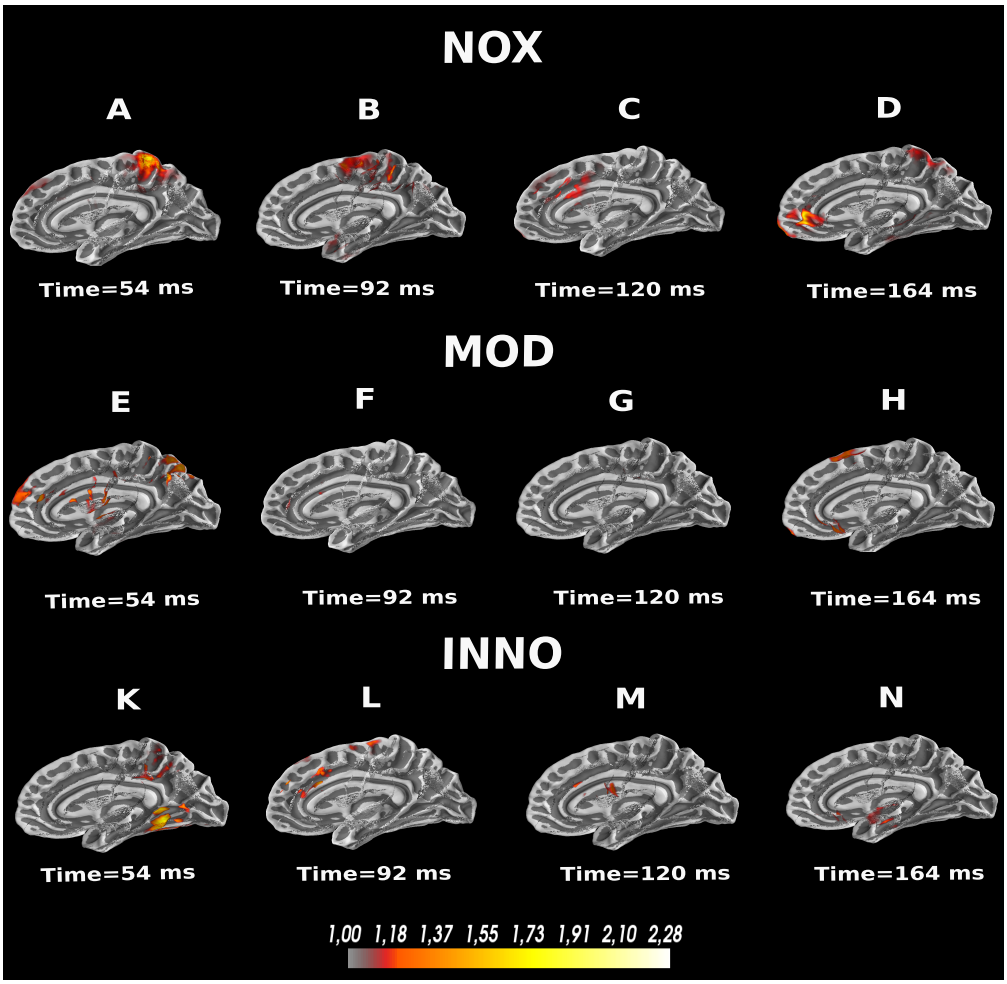

Figure 6.8: EEG analysis at the source level for the different conditions in the first 200 ms using sLORETA. The sLORETA method was computed and used for benchmarking with the dSPM method. Results from both methods are similar with lower values were found for sLORETA. The used scale represents the EEG amplitude activity in uV. **A**. High EEG activity in the centro-parietal lobe after 54 ms of stimulation. **B**. High EEG activity in the central cortex after 92 ms. **C**. Activation of the PCC after 120 ms. **D**. Activation of the ACC and the parietal lobe after 164 ms. **E**. EEG activity in the centro-parietal lobe after 54 ms of stimulation. **F**. No high EEG activity was detected after 92 ms of stimulation. **G**. No high EEG activity was detected after 120 ms of stimulation. **H**. No high EEG activity was detected after 164 ms of stimulation. **K**. EEG activity in the centro-parietal lobe after 54 ms of stimulation. **L**. No significant EEG activity was detected after 92 ms of stimulation. **M**. No significant EEG activity was detected after 120 ms of stimulation. **N**. No significant EEG activity was detected after 164 ms of stimulation.

and real-time recording with a good compromise between level of invasiveness and temporal resolution [3], which could be therefore used when developing real-time systems based on neural response to sensory stimulation. The findings in this study confirm and extend previous findings in non-amputee related studies on the high activation of the somatosensory and motor cortex during the NOX stimulation. Specifically, the highest activation was detected in Cz electrode site and its neighboring electrodes C4, C6 and CP6. Additionally, we also show early activation of the centro-parietal lobe for all the three conditions with the highest activity observed when perceiving and processing the MOD stimulation. Further, we identified a spatial template of noxious-evoked activity and we investigated different activated regions at the source level using EEG signals. This has overall confirmed the important role of the ACC to trigger the attention mechanism in the brain [43, 238], as well as the role of PCC for noxious stimulation processing [43]. Our study is extending upon Osborn et al. study [117], where a pain reflex mechanism was implemented at the level of the prosthesis. Our study suggests that such a withdrawal/pain reaction system could be implemented by harnessing the neural response to painful stimuli. The withdrawal reaction could be activated when the prosthesis touches sharp objects, and hence protect it from being damaged. Along the same lines, this can help better monitor the user's perception of what is happening to create more natural prostheses and provide the amputee more intuitive control over his prosthesis as well as increase the sense of embodiment and ownership.

6.5.1 Spatio-temporal template interpretation

Noxious-evoked activation generated high activity around Cz electrode between 450 ms-750 ms with the highest activity detected at Cz. We also investigate the relation between brain responses and three types of sensations. Based on that, we could distinguish between the three different conditions with more than 94% accuracy using an identified spatio-temporal template based on a subset of electrodes and the temporal markers. Similarly, we studied the temporal latency for each condition as well as the spatial distribution of the activity across other electrode sites. Even though exact mechanisms responsible for the delay remain to be investigated, we postulate that the early activation of the parietal lobe during all conditions makes strong evidence on its role in early processing of relevant somatosensory stimuli and its heavy connection with the ACC in painful and intense stimuli processing forming a complete circuitry for somatosensory stimuli detection and perception. We also hypothesize that only the NOX stimulation triggers the pain reaction mechanism in the brain, reflecting one's intention to escape the potential source of pain, which relies on the motor cortex. However, the processing of the other two conditions remain at the parietal lobe level and

did not activate any motor reaction. The important role of the ACC, PCC, and the premotor cortex in noxious sensation perception in amputees was also investigated during the noxious sensation. Thereafter, we observe activation of the motor cortex, the ACC, and the PCC, which is thought to be along the descending pathway to the spinal cord. Overall, our source localization results present new evidence on the similarity of the reflex system in amputees and healthy subjects. Further, our study reveals a high correlation between the stimulation condition and the activation magnitude of the ACC, which is aligned with previous studies for other purposes. Interestingly, all conditions activated the anterior portion of the ACC, which is known to be engaged in different attention networks in the brain as well as sensory stimuli processing. Further, high activation of the PCC was observed during the NOX stimulation. Overall, it has previously been shown that the PCC is part of motor responses with a wide interaction with the parietal lobe. In fact, PCC is adjacent to the supplementary motor cortex (SMA), which could explain why SMA activation was only shown during the noxious stimulation.

6.6 Summary

In this study, we were able to use EEG recordings to quantify brain activity during innocuous, moderately more intense, and noxious stimulation of an amputee's phantom limb using TENS. Based on the extracted spatio-temporal EEG features, a system for detecting pain perception and reaction in the brain was developed. This system was able to successfully classify the three different stimulation conditions with a test accuracy of 94.66%. Along the same lines, the cortical activity in response to sensory stimuli in these conditions was investigated. To further validate our findings, investigation of brain activity using a different sensory feedback modality and comparing similarities between able-bodied participants and amputees was needed. This gave, therefore, rise to focus on this in our next follow-up study.

7 The development of distinct brain patterns for five thermal stimuli perception reveals an anticipatory brain activity

This chapter is made up of content from the manuscript Zied Tayeb, Andrei Dragomir, Jin Ho Lee, Nida Itrat Abbasi, Emannual Dean, Aishwarya Bandla, Rohit Bose, Raghav Sundar, Anastasios Bezerianos, Nitish V Thakor, Gordon Cheng , "The development of distinct brain patterns for five thermal stimuli perception reveals an anticipatory brain activity" which is now under preparation for submission to the Nature Communications Journal.

Author Contributions: Zied Tayeb designed the research, developed the software for EEG data analysis and wrote the paper. Zied Tayeb, Nida Abbasi, Aishwarya Bandla collected the data and designed the experimental paradigm. Rohit Bose, and Andrei Dragomir contributed in the data analysis interpretation. Emmanuel Dean, Jin Ho Lee, and Zied Tayeb developed and performed the robotic experiment. Raghav Sundar, Anastasios Bezerianos, Nitish V Thakor. and Gordon Cheng supervised all experiments, data analysis, and interpretation of the results. All authors contributed in writing the paper.

7.1 Study overview

Understanding brain perception of different thermal sensations has sparked the interest of many neuroscientists. The identification of distinct brain patterns when processing thermal stimuli has different clinical applications, such as phantom-limb pain prediction, as well as increasing the sense of embodiment when interacting with neurorehabilitation devices. Notwithstanding the remarkable number of studies that have touched upon this research topic, understanding how the human brain processes different thermal stimuli has remained elusive. More importantly, thermal stimuli perception dynamics, their related cortical acti-

vations, as well as their decoding using effective features are still not fully understood. In this study, using electroencephalography (EEG) recorded from three healthy human subjects, we identified spatial, temporal, and spectral patterns of brain responses to different thermal stimulations ranging from extremely cold and hot stimuli (very intense/unpleasant), moderately cold and hot stimuli (intense), to a warm stimulus (innocuous). The classification of these five stimuli into three categories was determined using the average of the three subjects' perception and rating of each one of them. Our results show that very intense thermal stimuli elicit a decrease in alpha power compared to intense and innocuous stimulations. Spatio-temporal analysis reveals that in the first 400 ms post-stimulus, brain activity increases in the prefrontal and central brain areas for the very intense stimulations, whereas for intense stimulation, high activity of the parietal area was observed post-500 ms. Based on these EEG patterns, we developed a system for detecting thermal sensations perception in the brain, which successfully classified the different thermal stimuli with an average test accuracy of 87% across all subjects. En route to understanding the underlying cortical activity, we source localized the EEG signal for each of the five thermal stimuli conditions. Our findings reveal that (very cold and very hot) stimuli were anticipated and induced early (before 400 ms) activation of the anterior cingulate cortex (ACC). Moreover, activation of the pre-frontal cortex, somatosensory, central, and parietal areas, was observed in the first 400 ms post-stimulation for very intense thermal conditions and starting 500 ms post-stimuli for intense conditions. Overall, despite the small sample size, this work presents a novel approach to explore, analyze, and classify EEG-brain activity changes evoked by five different thermal stimuli, which could lead to a better understanding of thermal stimuli processing in the brain.

7.2 Introduction

7.2.1 Related work on nociceptive stimuli perception

The quantification of human pain using neuroimaging techniques has been widely studied and investigated [118, 119]. Despite the number of studies in this context [239], understanding nociceptive processing in the human brain is still very challenging [240, 122]. This is due to the complex mechanisms involved in processing noxious stimuli. Similarly, human nociceptive thermal stimuli perception and processing are likely to be harbored in different regions in the brain [241]. En route to analyzing and unraveling the underlying processes within the human body that can lead to the unpleasant stimulus perception, understanding nociceptive thermal sensation in particular has recently gained momentum [242, 243].

Neuroscientists have been relying on various neuroimaging techniques, including functional magnetic resonance imaging (fMRI) [43], Positron emission tomography (PET) [125], and invasive recordings [126], to investigate exogenous pain processing. Kwan et al. [43] investigated in their study using fMRI the anterior cingulate cortex's (ACC) role in sensory, motor and cognitive functions when perceiving four thermal stimuli categorized into innocuous (cool, warm) and noxious conditions (cold, hot). However, the correlation between EEG evoked changes and different nociceptive thermal stimuli have been minimally studied [244]. Overall, EEG offers a better temporal resolution and has not been extensively studied in this context. In a tonic pain stimulation [127], authors analyzed EEG power spectra changes and reported an increase in alpha [8 - 12 Hz] and beta [13 - 25 Hz] power [127]. Along the same lines, authors in [123] investigated the different early temporal event-related waves, as well as frequency responses in the Gamma band [25 - 140 Hz]. Interestingly, they [127] reported a difference between painful and non-painful stimulations, which was detected in both parietal and frontal areas. Thus, this could be explained by motor withdrawal responses. In the same study [127], an EEG frequency analysis was performed and event-related desynchronization (ERD) of alpha was detected when performing hand immersion into cool and extremely cold water. This initial decrease of alpha band was followed by an increase in bilateral frontal and posterior regions. Similarly, in Chen et al. [245], a pronounced decrease of alpha magnitude in the central areas was detected in EEG recordings during an experimental ice-cube cold pressor test. In a different study, Hu et al. [246] studied the relationship between EEG brain responses and $A\delta$- and C-fibre skin nociceptors. By investigating $A\delta$- and C-fiber laser evoked potentials, authors could provide quantitative analysis about latency responses of these fibers and the underlying perception-response functions depending on the stimulus as well as the exact stimulated area. In this study, we fill the gap by identifying spatial, spectral, and temporal brain patterns that can be used to distinguish a wider spectrum of thermal stimulations (five thermal stimuli) ranging from very cold to very hot stimuli. Additionally, we developed an offline system for classifying the different conditions from recorded EEG responses.

7.2.2 Motivation & aims of this study

Unlike previous studies, EEG is also used to quantify brain changes for each of the five thermal stimulations. For that, brain activity is investigated at the source level, reporting new findings of the main autonomic functions of ACC and frontal areas in thermal stimuli processing, the brain anticipatory activity of such stimuli, and their connections to internal fear emotion induced by unpleasant stimuli, as well as motor withdrawal preparation. Despite

the limited number of subjects, this work is the first study to provide such an analysis and take benefit of the EEG's temporal resolution to investigate brain responses to a wide range of thermal stimuli, as well as to accurately (87%) classify them based on the identified brain patterns. The far-reaching goal of this study is to use these patterns to develop a real-time withdrawal reaction system when interacting with neurorehabilitation devices. An overview of the proposed system and the motivation behind it is illustrated in Figure 7.1.

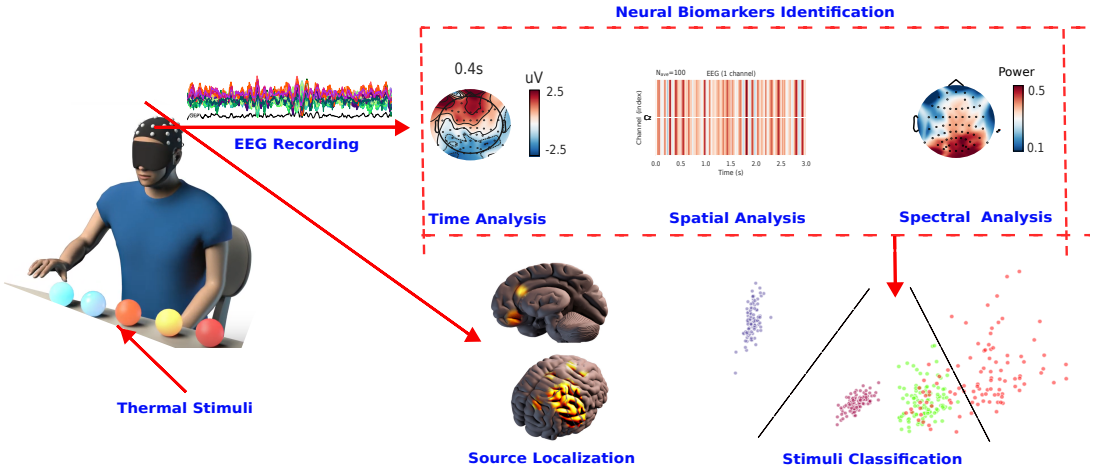

Figure 7.1: Nociceptive sensory processing system overview and analysis pipeline.

7.3 Methods

7.3.1 Subject recruitment and sensory stimulation

EEG data were recorded from three healthy volunteers (males) aged $29.66 \pm 10.27\ mean \pm SD$. All five thermal stimuli, including nociceptive cold and heat stimuli, were delivered using customized thermal stimulators. Participants were asked to score the sensation intensity on a well-validated thermal sensation scale- the visual analog scale [247] ranging from 0 to 9 (9 being least tolerable). The average thermal sensation scoring across all subjects for the five thermal stimuli is depicted in Figure 7.2 (b). All participants were right-handed, and hence all sensory stimulations were performed on their right arms. Temperature range for each stimulation condition is as follows: $[10 \sim 14.99], [16 \sim 24.99], [25 \sim 33], [35 \sim 40], [40.99 \sim 44.99]\,℃$, for very cold, cold, warm, hot, and very hot, respectively, as illustrated in Figure 7.2 (d).

7.3.2 Research governance

This study was carried out in accordance with the Declaration of Helsinki. All experimental protocols were approved by the Institutional Review Board of the National Health Group, Singapore. All subjects were informed orally and in writing about the aims of the study, and written consent for participation was sought and documented.

7.3.3 EEG data recording and experiment

The study of brain activity evoked changes by five thermal stimuli was investigated using 64-channel EEG recorded data. To make sure that the subject was not substituting/anticipating the stimuli by sight, all subjects were blindfolded during the recordings. All recording sessions took place at the lab and were set up as shown in Figure 7.2 (a). For each subject, two recording sessions were performed on two different days when each of the two NOX stimuli (very cold and very hot) were delivered on a separate day. Each session consisted of 30 runs yielding a total number of 30 trials. Each trial consisted of three stages: baseline, stimulation, and recovery. It had a total duration of 40 seconds (10 seconds baseline and 30 seconds stimulation) where subjects were exposed to one of the five thermal stimulations separated by 2-min recovery breaks. Before each run, the surface temperature of the subject's hand, as well as the thermal stimulator, were measured using an infrared thermometer. A Python script was used to display an automated visual cue informing the experimenter which thermal stimulus must be delivered. Each time, cues were pseudorandomized and were chosen from a discrete uniform distribution. An auditory warning beep preceded the cue display and was delivered five seconds before the commencement of the trial. Participants were asked to score the stimulus intensity during the recovery break at a scale from 0 to 9, as shown in Figure 7.2 (c). During the experiment, participants were seated in a comfortable chair in a silent, temperature-controlled room and were instructed to not execute any movements. EEG data were collected using a 64 channel EEG device (Neuroscan system) with a 512 Hz sampling rate. The montage was in accordance with the 5% 10/20 system. Electrode impedance was kept below 10 kΩ in at least 95% of derivations throughout the experiment. The experimental paradigm is made publicly available with the gumpy software toolbox [46]. An animation video demonstrating the whole experiment and the main results in available in the appendix.

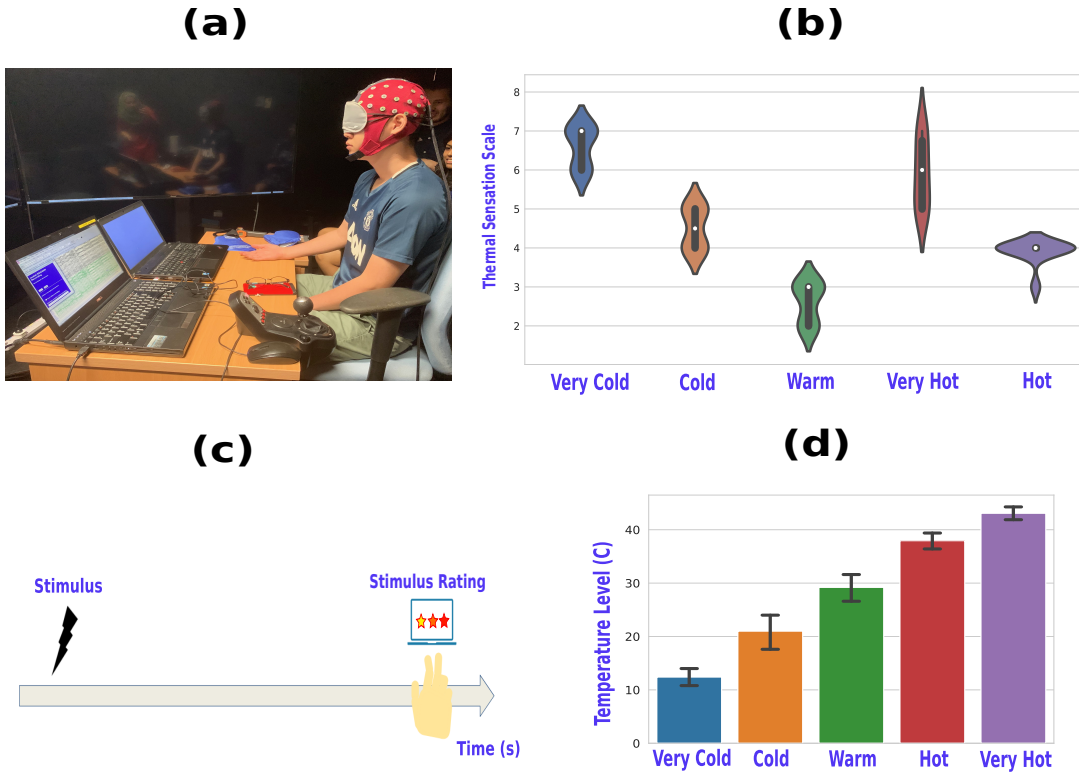

Figure 7.2: **(a)**: An example of a recording session of EEG during the thermal stimulation task. **(b)**: A violin-plot presenting the average thermal sensation scoring of the five thermal stimuli across all the three subjects. **(c)**: Experimental recording session starting with stimulus and concluded by a thermal sensation rating task during the recovery inter-trial break period. **(d)**: A bar plot describing the mean and the standard deviation of the used temperature interval for each of the five thermal stimuli.

7.3.4 EEG signal processing and classification

The reference electrode was chosen on the vertex and the ground electrode was located on the forehead. Data were processed with custom designed Jupyter notebooks in Python using both gumpy [46] and MNE [219, 220] toolboxes. For data analysis, 50 trials in total for the five stimulation conditions were used. EEG signals were band-pass–filtered between 0.5 and 70 Hz using a fourth-order Butterworth filter and notch filtered thereafter at 50 Hz. All signals were extracted from the recordings in 3000 ms epochs and used for further analysis. Epochs were baseline-corrected to the pre-stimulus mean [151]. Muscle artifacts were rejected by the Automatic Artifact Rejection (AAR) [221], as well as independent component analysis (ICA), was used to remove eye movement artifacts [222]. Additionally, epochs containing high-amplitude artifacts or high-frequency muscle noise (visually inspected) were

rejected from the analysis using a threshold-based method [146]. EEG data collected over several trials of the same experiment were averaged together. All EEG scalp topographies were plotted using the MNE toolbox, by matching channel location with its value given the defined latency. Topographies are color encoded, where the green or yellow present null values, blue color presents negative values, and red encodes positive values; with the color intensity correlating with the channel value. Chosen time latencies in the topographic maps were based on an algorithm [219] that computes and finds the highest peaks at each time point from all electrodes. For feature extraction and classifying the five conditions clustered in different binary groups from EEG, we implemented and tested a wide range of classical machine-learning approaches that are based on hand-crafted features. The common spatial patterns (CSP) [62] was used as a feature extraction method. Linear Discrimination Analysis (LDA) was selected to classify the extracted features from EEG data. A principal component analysis (PCA) with only two components was used for dimensionality reduction, and the two components were fed thereafter to the different classifiers resulting in the presented 2D feature space (Figure 7.6). During the test phase, data were divided into 80% for training and 20% for testing. As the total number of 50 trials was small when splitting the data into validation and test sets (solely few trials remained for each condition during the test phase), a data augmentation was performed [190]. This yielded 10 separate trials from each one of the initial 50 trials (by using the whole 30 seconds and splitting them into a 3-sec trial length), thus forming a total number of 500 trials. It should be mentioned that the 500 trials (after data augmentation) were only used when performing the PCA, splitting the data, computing the test accuracy, as well as when doing the spectra analysis. Overall, 10-fold cross-validation was performed on training data to validate the model (validation accuracy) and the remaining 20% were using for the test phase. It should be noted for all analyses, balanced accuracy (bACC) was chosen as an evaluation metric for the trained models. bACC is calculated as the average of the proportion corrects of each class individually, where the same number of examples in each class was used.

7.3.5 GFP computation

The computed Global Field Power (GFP) shown in Figure 7.4 is the standard deviation of the potentials at all EEG channels of an average given reference map [223]. The GFP formula is shown below in equation 7.1:

$$GFP = \frac{\sqrt{\sum_{i=0}^{\mathrm{N}}(\mu_{\mathrm{i}} - \overline{\mu}^2)}}{N} \tag{7.1}$$

where μ_i is the voltage of the map μ for a given electrode i, $\overline{\mu}$ is the mean voltage of all EEG electrodes of the map u and N is the number of electrodes of the map μ. High GFP wis explained by peak EEG activities as well as steep gradients. In Figure 7.4, GFP shows the amount of activity at each time point in the field considering the data from all the 64 recording electrodes simultaneously [224].

7.3.6 Source localization

MNE toolbox [219] combined with gumpy [46] Python toolbox were used for EEG processing and for source localization. First, cortical surface reconstruction using FreeSurfer [225]. Second, the forward solution and the forward model were computed using the boundary-element model (BEM) [66]. Thereafter, the regularized noise-covariance matrix, which gives information about potential patterns describing uninteresting noise source, was computed and estimated. Afterward, we computed the singular value decomposition (SVD) of the matrix composed of both estimated noise-covariance and the source covariance matrix. Finally, dynamic statistical parametric maps (dSPM) [226] was computed and used for source localization and reconstruction. For dSPM, an anatomical linear estimation approach is applied. This assumes the sources are distributed in the cerebral cortex [227]. A linear collocation single-layer boundary-element method (BEM) [228] is used to compute the forward solution which models the generated signal pattern at each location of the cortical surface. A noise-normalized minimum norm estimate is estimated at each cortical location resulting in an F-distributed estimation of the cortical current. Overall, dSPM identifies the locations of statistically increased current-dipolar strength relative to the noise level.

7.3.7 Data analysis and statistics

All relevant information related to the obtained results is presented alongside their corresponding figures. For all statistical analyses, a normality check was first performed as well as data independence before choosing the adequate statistical test. The data normality (for the five thermal stimulation conditions) was checked using one-sample Kolmogorov-Smirnov test, which is a strict normality test, and as was suggested in the study by Strauss et.al [229]. Afterwards, the independence was checked using the Mann-Whitney U Test was used (frequently used when data is not normally distributed) and we found that the conditions are statistically independent ($p < 0.001$). As two conditions were not normally distributed, we applied a Kruskal-Wallis test instead of ANOVA [229]. The Kruskal-Wallis test was combined with the post-hoc test for multiple group (pairwise) comparison. The software for the statistical analysis was implemented in python using the scipy and stats libraries.

The Kruskal-Wallis H statistic was assumed to have a chi square distribution. No Tukey-Kramer correction for multi-group comparison was applied. For all the obtained results, we considered $p < 0.05$ statistically significant to reject the null hypothesis.

7.4 Main results of EEG analysis for the five thermal stimuli

7.4.1 Thermal stimuli elicit a decrease in EEG alpha power

Five thermal stimuli (very cold, cold, very hot, hot, and warm) were delivered to three healthy subjects' right hands using a customized thermal stimulator. Based on the collected behavioral data, these five conditions were clustered into three categories: very intense conditions denoted by NOX (very cold and very hot stimuli), moderately intense conditions denoted by MOD (cold and hot stimuli), and innocuous stimulus denoted by INNO (warm stimulus). Throughout the experiment, a thermal sensation scale was used. The NOX stimulations were reported by all the three participants as uncomfortable, the MOD stimulations were reported as slightly less noticeable/intense compared to the NOX stimulation, and the INNO was reported as pleasant. The $mean \pm SD$ subjective responsivity of very cold, very hot, cold, hot, and warm was 6.6 ± 0.48 , 5.9 ± 0.83, 4.5 ± 0.5, 3.9 ± 0.3, 2.6 ± 0.48, respectively, on a thermal sensation scale from 0 to 9, with 9 being an intolerable thermal sensation. EEG signal was used to quantify brain activity during each thermal stimulation and to understand oscillatory neural responses en route to identifying specific brain patterns of nociceptive thermal stimuli processing in the brain. For that, averaged EEG alpha power (8-12 Hz) across all trials was analyzed. Our results reveal a suppression of alpha oscillatory activities characterized by a decrease in the alpha frequency band power [$p < 0.001$, Kruskal-Wallis test was combined with the post-hoc (Tukey HSD tests)]. It should be noted that this power decrease is detected ipsilaterally and contralaterally but is dominantly observed at contralateral-central electrodes (as presented in Figure 7.3). Our analysis reveals negative correlations between alpha power and the stimulation condition's discomfort level at contralateral-central electrodes (left side of the brain) ($p < 0.05$). Thus, the more intense the condition is, the higher and more visible the decrease is (as shown in Figure 7.3).

7.4.2 Spatial-temporal patterns for thermal stimuli brain processing

The aforementioned alpha power topography analysis was extended by aiming to identify distinct brain patterns distinguishing between the five thermal stimuli and investigate spatial and temporal brain responses for each stimulation condition. For both NOX stimulations, we find out, as shown in Figure 7.4 ((d) and (e)) that the highest brain activation is detected at

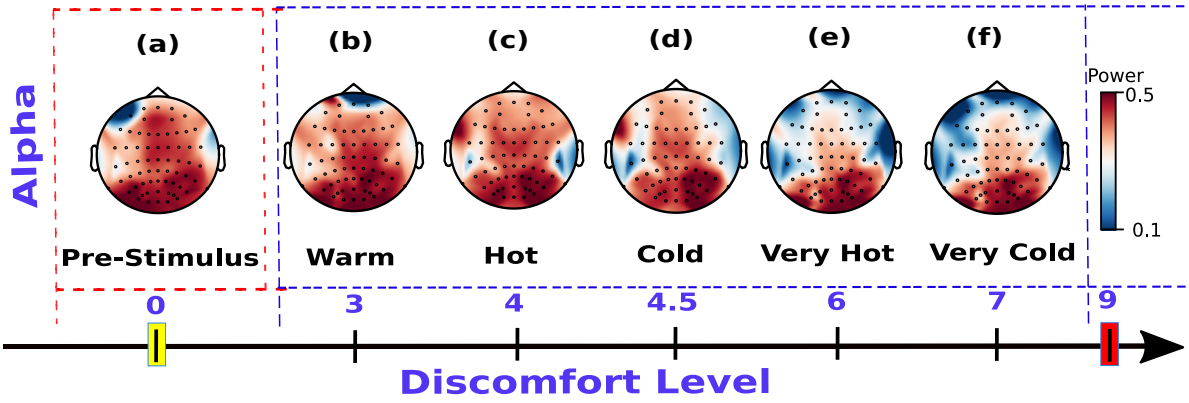

Figure 7.3: EEG alpha power topographic maps. **(a)**, **(b)**, **(c)**, **(d)**, **(e)**, and **(f)** represent topographic scalp maps of the EEG alpha power for pre-stimulus, INNO (warm), MOD (hot and cold), and NOX (very hot and very cold) stimuli, respectively, using the average of all trials for each condition and across all three subjects. Suppression of alpha oscillatory activities was found in MOD and NOX conditions ((c), (d), (e), (f)), whereas no decrease in alpha power was detected for the pre-stimulus and INNO conditions ((a), (b)). The discomfort level represents the average of all subjects' rating of each condition on a thermal sensation scale from 0 to 9 is also presented.

the pre-fontal cortex, contralateral somatosensory area, and the central cortex compared to the other three thermal stimulations. For MOD conditions (cold and hot stimuli), the highest brain response is observed in the parietal area, mainly on the right parietal electrodes, with a central and frontal deactivation compared to NOX conditions (Figure 7.4) ((b) and (c)) [$p < 0.001$, Kruskal-Wallis test was combined with the post-hoc (using Tukey HSD test) for multiple group comparison]. No significant activation is detected for the warm condition, which was reported as a pleasant sensation. Additionally, as depicted in Figure 7.5 ((d) and (e)), the highest activation for NOX conditions is localized at the vertex electrode in the middle of the scalp (Cz) when comparing it to MOD and warm stimuli (Figure 7.5 ((a), (b) and (c))) with relatively high activation also being detected in C3 and C5 electrodes. Thus, a positive correlation between Cz activity and the condition's discomfort level is observed and the highest Cz activity is detected for the very cold stimulus. Our results reveal that the highest activation for NOX conditions was detected in the first 450 ms (Figure 7.4 ((d) and (e))) post stimulation, whereas the highest activation for the other two groups is observed with a delay of 500 ms post stimulation as presented in Figure 7.4 ((b) and (c))). Based on our findings, we postulate that the NOX stimulations lead to high and continuous activation of the central lobe in the brain, which is responsible for motor movement planning.

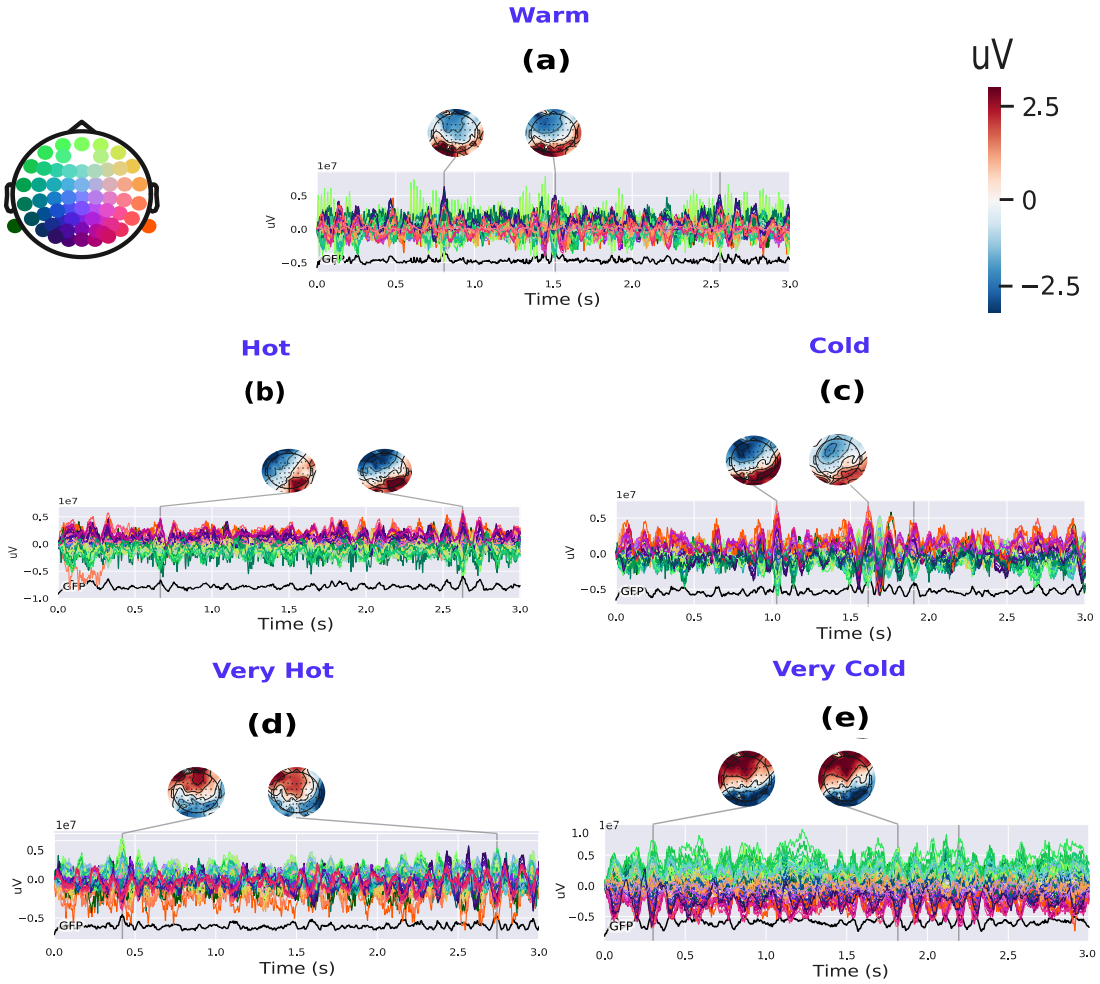

Figure 7.4: Spatial-temporal EEG features for all five thermal conditions. **(a)**, **(b)**, **(c)**, **(d)**, **(e)**, and **(f)** represent topographic scalp map of the EEG amplitude response for warm, hot, cold, very hot, and very cold stimuli, respectively, using the average of all trials for each condition and across all subjects. All topographic maps are plotted for the first three-second post-stimulation time window (average of across each condition's trials). The get_peak algorithm in the MNE software [219] is used to compute and detect the amplitude of the maximum EEG response (local maxima) for the very intense stimulation as well as the location (EEG channel) and latency of the detected peak amplitude. Time courses of NOX stimulation identified and found using the get_peak algorithm is used thereafter for analysis and benchmarking with the other two conditions. The global field power (GPF) is plotted for each stimulation condition.

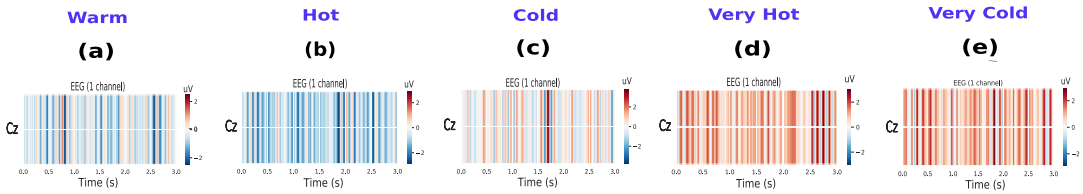

Figure 7.5: Cz activity for all five thermal conditions. **(a)**, **(b) (c)**, **(d)**, and **(e)** represent EEG activity in Cz for warm, hot, cold, very hot, and very cold stimulus, respectively.

7.4.3 Classification of the five different thermal stimulation conditions

After investigating spectral, and spatio-temporal patterns for the five different stimuli, we sought to classify them. Unlike previous studies [248, 244] where the focus was on either on classifying hot and cold stimuli or distinguishing between innocuous and intense stimuli, the novelty of this study resides in the ability to distinguish between five different temperature levels. We wish to mention that the focus of this study was not to do a multi-class classification task but rather to distinguish between specific pairs of thermal stimuli which are difficult to classify and have not been addressed before in the literature. In the present study, we are able to achieve a mean balanced accuracy (bACC) of $86.89\,\% \pm 3\,\%$, $78.16\,\% \pm 6.66\,\%$, $84.53\,\% \pm 3\,\%$, and $100\,\%$, when classifying very hot and hot, very cold and cold, warm and cold, and very hot and very cold stimuli, respectively, yielding an average validation accuracy of 87.4% within all classified conditions and across the three subjects. Classification results are summarized in Figure 7.6. A mean bACC of 87% is obtained in the test phase within all sub-classes and across all the three subjects. For that, data were split into 80% and 20% where stratified 10-fold cross-validation was performed on 80% of the data (validation phase) and the saved model was used to predict correct labels on the remaining 20% of the trials in the test phase. A principal component analysis (PCA) was performed on the extracted features, which resulted in a clear separation between the different classes as shown in Figure 7.6. Figure 7.6 shows that very hot and very cold are easily classified, whereas very cold and cold are hardly distinguishable. By analyzing each individual subject's performance, we observe a high variability between the three subjects. The third subject (S3) clearly outperforms the others (Figure 7.6 (e)) with an average accuracy of 90.75% for all the four classification tasks, whereas S2 and S1 reach an average validation accuracy of 89.675% and 81.275%, respectively.

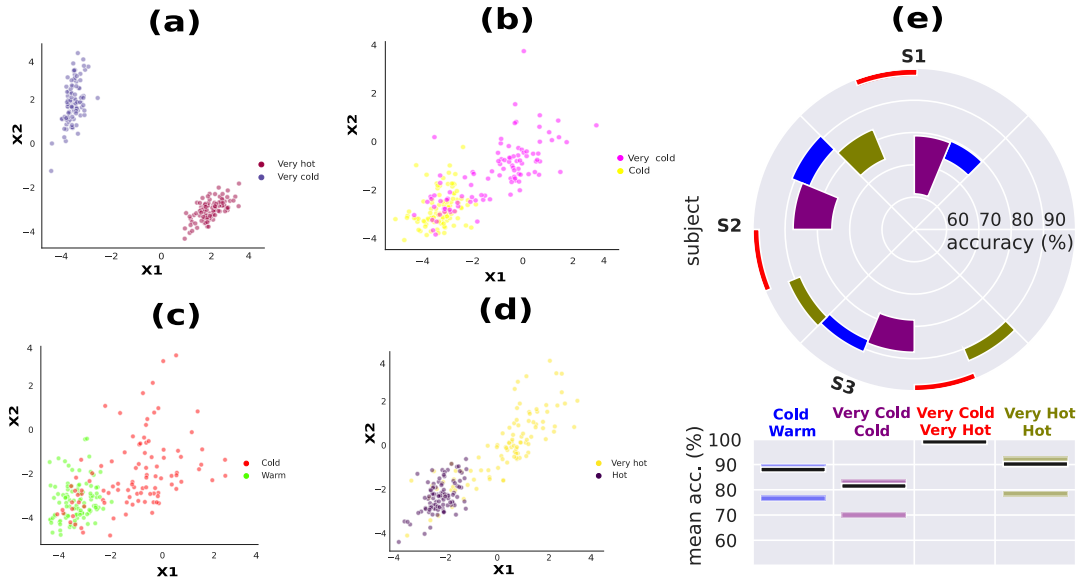

Figure 7.6: 2D feature space after performing PCA highlighting a clear separation between the different sub-classes. x1 and x2 represent the first two components after performing PCA. **(a)**, **(b)**, **(c)**, and **(d)** represent the feature space when classifying (very hot, very cold), (very cold, cold), (cold, warm), and (very hot, hot), respectively. **(e)** shows the validation accuracy for the three subjects (S1, S2, S3) and for the four classification tasks using a polar bar plot. This circular plot shows the accuracy range $mean \pm SD$ achieved by the three different subjects. The three horizontal bars represent the min, median (black bar), and max accuracy values.

7.4.4 Very intense stimuli induce high and early activation of the ACC

To extend our findings and analysis, we studied brain activity at the source level for the five stimulation conditions, grouped into the three classes: NOX, MOD, and INNO. Localized sources using EEG signals were used to gain insights into thermal stimulus processing in the brain and what are the different activated regions involved in the perception of each of the three groups. All five conditions were investigated as shown in Figure 7.7. For that purpose, we reconstructed EEG source dynamics using distributed source modeling [232, 233] based on realistic head models [234, 231]. As illustrated in Figure 7.7, only NOX conditions shows activation of the ACC. Interestingly, this activation does not persist over time and was only detectable in the 100 ms post-stimulus. Particularly, very cold stimulus elicits an early response of the ACC at 29 ms and is followed by stronger activation at 53 ms post-stimulus, which diminishes over time. Similarly, as shown in Figure 7.7, the very hot stimulus, which was rated less intense than very cold, elicits activation of the ACC at around 29 ms post-stimulus and solely persisted for the first 50 ms. For the remaining conditions,

no ACC activity is detected and a parietal activity was clearly visible in the first 100ms post stimulation. Although the latencies of activations are not compatible with conduction velocities of nociceptive and thermal nerve fibers, we interpret this by an anticipatory brain behavior, given that the subject knew in advance (with the sound beep displayed 5 seconds prior to the actual stimulation) that he might be exposed to a thermal stimulus. Overall, this positive correlation between the condition's discomfort level and the ACC activation and time response presents direct evidence of ACC's role in activating the brain's autonomic functions and attention circuitry, as well as an important role in external sensory stimuli perception [235, 236]. Overall, this is in accordance with previous studies using different types of noxious stimuli. As the highest and earliest ACC activation is found for the most NOX condition (very cold), the time snippets for it are used as a reference when analyzing the other conditions.

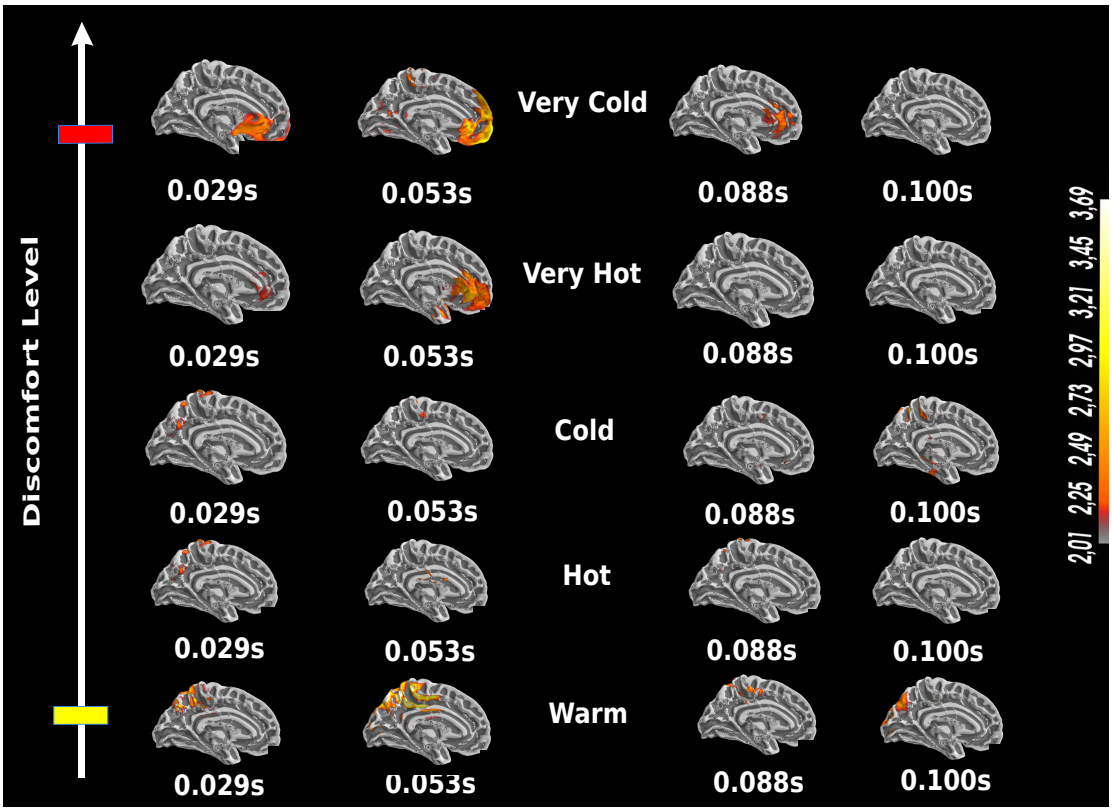

Figure 7.7: ACC-EEG activity analysis for the NOX stimuli (very cold and very hot), as well as for INNO (warm) stimulus in the first 100 ms (medial view). The dynamic statistical parametric maps (dSPM) technique [226] is used to compute the reconstructed sources. The used scale represents the EEG amplitude activity in uV. Continuous and high EEG activity in the ACC starting 20 ms post-stimulus for NOX stimuli which is only detected for the first 100ms. MOD and INNO conditions elicit an activation of the parietal lobe.

7.4.5 EEG analysis when stimulating both hands

In a separate investigation, the three subjects were exposed to both very cold and very hot stimuli at the same time. Very cold stimulus was delivered on the left hand, whereas very hot was delivered on the right hand. The very cold stimulus was rated as more intense (scored 7 in average at a scale from 0 to 9) than the very hot stimulus (rated 4 in average using the scoring scale). Interestingly, as illustrated in Figure 7.8 (a), the very cold showed higher contralateral decrease in alpha power (right side) than the very hot (left side). Similarly, higher frontal and central activity were detected for very cold (contralateral side to to the stimulation) compared to very high hot. These results confirm the main findings of the study, where a pronounced decrease of alpha power for both conditions but the most intense condition dominated the less intense one. This decrease was interpreted by an ERD resulting from a motor movement imagination. The high fronto-central activation for both NOX conditions is in accordance with our main findings, revealing, therefore, the importance of the the regions in very intense thermal stimulus perception and processing. Investigations of the brain reaction when stimulating both hands with two different NOX stimuli should be considered in future studies.

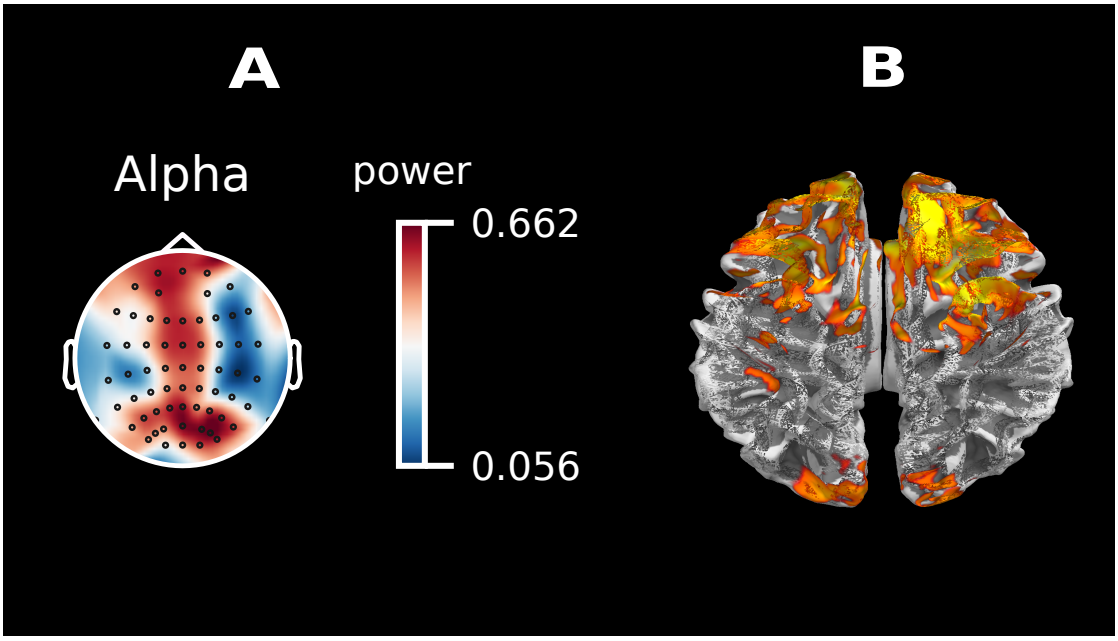

Figure 7.8: Thermal sensation rating for very cold and very hot stimuli

7.4.6 Very intense stimuli elicit high activation of the pre-frontal, frontal and central cortex, somatosensory areas, as well as the parietal lobe

Next, we attempted to characterize changes in cortical activities during perception of five different thermal stimuli. For our extended source localization analysis, we solely focused on the most NOX condition (very cold) en route to understanding the brain circuitry involved in thermal sensation processing. Overall, we observe that brain activity associated with NOX condition activates more brain regions when comparing it to MOD and INNO stimulations. Our results reveal that NOX sensations elicit high activation of the pre-frontal, frontal and central cortex, somatosensory areas, as well as the right parietal cortex. Similarly, we observe that, for NOX conditions, contralateral activity is higher than the ipsilateral one, which is aligned with the literature [127]. These activated regions seem to form a complex interconnected circuitry for noxious stimulus perception and processing as was reported in the literature [127]. Figure 7.9 (left) summarizes the main activated brain regions for NOX conditions using EEG localized sources, whereas the right side of Figure 7.9 highlights the time response of those activated regions. Overall, as shown in the figure, the most NOX stimulus induces activation of the parietal areas, which is followed by an activation of both frontal (23 and 242 ms) and central area (76 and 292 ms). Despite the incompatibility with conduction velocities of nociceptive and thermal nerve fibers, these early activations are explained by an anticipatory brain component.

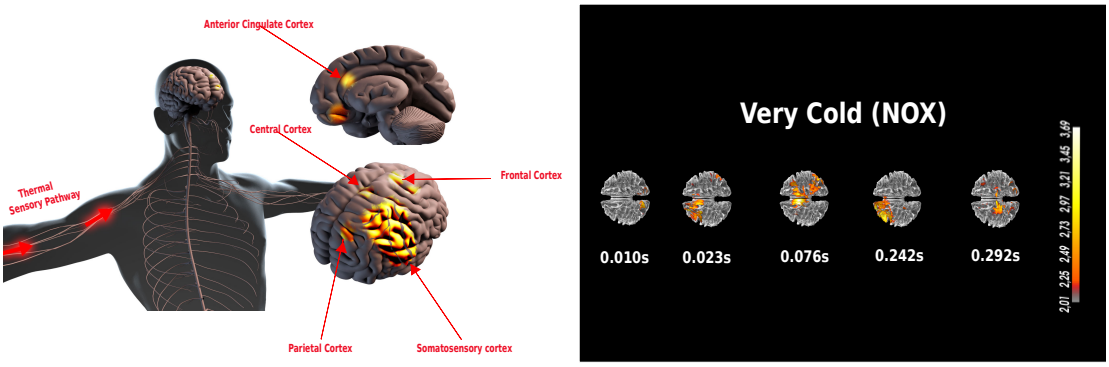

Figure 7.9: Main activated region for the very intense stimuli after performing EEG source localization. ACC, central cortex, pre-frontal and parietal areas are the main activated brain regions for NOX conditions (left). NOX condition localized sources with brain time responses in the first 300 ms window of post stimulation

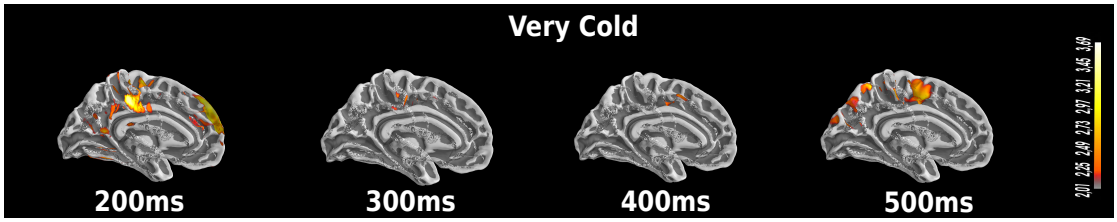

Figure 7.10: Source localization for the very cold condition in the time window [200 - 500] ms.

7.5 Discussion on thermal stimuli responses in the human brain using EEG

In this study, temporal, spatial, and spectral EEG changes for five different thermal stimuli were characterized using brain signals collected from three healthy subjects. The choice of using EEG to quantify brain changes and to develop distinct patterns for different thermal stimuli was motivated by its good compromise between the level of invasiveness and high temporal resolution [3, 51, 18].

7.5.1 Neural patterns of thermal stimuli-evoked activity

As shown in Figure 7.9, EEG-alpha power was found to be negatively correlated with stimulus intensities. Overall, a pronounced decrease of alpha power in the central areas was identified for NOX conditions. Although this decrease was detected contralaterally and ipsilaterally, it was higher on the contralateral side of the stimulation. We postulate that this power difference is explained by an event-related desynchronization (ERD) [151, 190], which is usually evoked by phasic endogenous or exogenous stimulation, frequently applied in visual, auditory, and movement experimental paradigms [249]. As this decrease was mainly detected in central electrodes, overlapping with somatosensory regions, we hypothesize that for NOX conditions, subjects had the intention to move their limbs away from the very intense/unpleasant stimulus, which potentially resulted in a motor imagery movement [250, 3] and led to a clear ERD pattern similar to the one widely used in brain-computer interfaces. Overall, our results concur with most previous studies investigating the relationship between EEG-alpha power and noxious stimuli [251, 127], as well as further extend upon these studies by analyzing five distinct thermal conditions. In [127] where only two conditions (painful cold and cool water) were investigated, authors reported an initial decrease in alpha power in the first minute post-stimulus, which was thereafter followed by an alpha power increase in bilateral frontal and posterior electrodes. Similarly, they reported that cool (warm) stimulation produced less alpha power change than the cold painful condition. Along the same

lines, the pronounced decrease of Alpha amplitude in the central areas was also detected in [245], where subjects participated in an ice-cube cold pressor experiment. It should be noted, however, that in some previous studies painful stimulations were rather associated with an increase in alpha activities [252]. This discrepancy between our results and some of the previously reported ones is likely to be explained by the chosen stimulation type or subject's age difference, as reported in the study [252], where transcutaneous electrical nerve stimulation (TENS) was used to elicit painful sensations and was tested for both young and elderly people. It is worth noting that no statistical significance was found when analyzing theta (4-7Hz), beta (13-30Hz) and gamma (25-140Hz) frequency bands, and hence they were excluded from further analysis. As depicted in Figure 7.4, our results reveal that that NOX conditions (very cold, very hot) generated high activity around Cz central electrode compared to MOD (hot, cold), and INNO (warm) conditions. Additionally, as shown in Figure 7.4, very intense thermal stimuli generated higher brain activity in the first 450 ms post-stimulus, whereas MOD and warm conditions showed higher brain activity starting 500 ms post-stimulus. We hypothesize that only the NOX conditions trigger the withdrawal mechanism in the brain, reflecting the subjects' intention to escape the potential source of noxious sensation, which heavily involves central brain areas, and hence explains the higher activation of Cz electrode for NOX stimuli compared to the other stimulation conditions. This result is in accordance with previous studies where high activation Cz was also reported when using different NOX stimuli with amputees [253] and infants [211].

7.5.2 Neuronal responses to varying thermal stimulus tolerability: Relation with $A\delta$- skin nociceptors

Even though the interpretation of the exact mechanisms responsible for the detected latency difference when responding to different tolerable and intolerable thermal sensations remains unclear, we postulate that there seems to be a strong correlation with the $A\delta$- skin nociceptors' time responses. Noticeably, the brain time response for the very intense thermal stimuli (as shown in Figure 7.4) matches the response time of $A\delta$, whereas time response for MOD and INNO conditions match the one of C-fibres, as reported in this previous study [246]. $A\delta$-fibres, which are 'fast' myelinated nociceptive nerve fibres that respond to noxious thermal stimuli by carrying rapid nervous messages from the skin to the brain [254] and play an important role in the ascending pain-control pathway [255], were shown in the study by Hu. et.al [246] to have a strong brain response in the first 400 ms after noxious stimulation. Thus, this could present evidence of their involvement in processing NOX conditions and explain the observed latency when processing the two NOX stimuli.

7.5.3 ACC's strong and early activation reveals its role in thermal sensation anticipation and focal attention

The role of ACC in thermal stimulus processing and its related cognitive functions has been widely investigated in the literature [251, 256, 43]. Overall, its role is believed to be associated with pain perception, as well as prediction and avoidance of nociceptive stimuli, with a particularly significant response when processing heat stimuli [257, 43, 258]. In the present study, we observe strong and early activation of the ACC for the very intense thermal stimuli in the first 100 ms post-stimulation (Figure 7.7). Noticeably, this activation does not seem to persist after 100 ms. Unlike the very cold and very hot conditions, this early high ACC activation was not detected when processing the other thermal conditions. Our results reveal the important role of the ACC in the central processing of noxious stimuli [259] and during the experience of pain [125]. It is worth noting that during the experiment a warning beep was used before each trial (fixed time) so the subjects knew that the stimulation would happen in a few seconds. Hence, this could explain the anticipatory pattern, as the identified latencies of brain responses are not compatible with thermal/nociceptive fibers. Additionally, recordings were performed in two different sessions, when the subjects were exposed to one of the two NOX stimuli (either very hot of very cold), which was randomized with the MOD and INNO stimuli. As a result, we hypothesize that the subjects had expectations preceding the stimuli and this triggered activation of certain brain regions even before the stimulus occurrence, so-called "anticipation". This seems to provide an explanation to this early ACC activation (29 ms) shown in Figure 6.7, further demonstrating its role in perceptual-anticipation of NOX stimuli, and presenting evidence that this stimulus anticipation triggered the salience network [260]. This network pre-activates particular brain regions [261] in which ACC is one of the central nodes. Our findings are also in accordance with the literature, where other studies showed, using invasive neuroimaging techniques, an ACC activation prior to the stimulus [261]. Interestingly, as our results reveal that this ACC activation was generally associated with high fronto-central activity, As this activation persists for the 100 ms post-stimulus and solely for NOX conditions, this highlights its role not only in anticipation but also in the second phase of sensory processing and focal attention to NOX stimuli. Hence, this clear ACC activity (at 53 and 88 ms) shown in Figure 6.7 could be linked to the subjects' inhibitory intention and withdrawal behavior when being exposed to NOX conditions [262]. One intuitive reason why this activation was only present for NOX conditions is that the other stimuli (cold, hot, warm) did not present any potential risk and were not considered by the subjects as harmful or damaging stimuli. Additionally, as this activation was only detected for NOX conditions, we postulate that this could be explained

by an internal brain model that is anticipating these stimuli and only reacting to the most intense ones. Overall, using a high-temporal resolution neuroimaging technique, our results solidify and extend upon previous findings on the essential role of the ACC as an early warning system to alert humans about potential risks, and could further explain its involvement in autonomic functions.

7.5.4 Interpretation of central role of prefrontal, parietal, central, and somatosensory areas in thermal stimuli processing

In this study, we report strong brain activation of pre-frontal, frontal, somatosensory, and central areas for NOX conditions [$p < 0.0001$], whereas high activation of the right parietal cortex was found for MOD and INNO conditions [$p < 0.001$] as was illustrated in Figure 7.7 and 7.5. Overall, the involvement of these cortical areas in pain perception and processing has been previously confirmed in different neurophysiological studies [127]. Particularly, Pardo et al. [119] showed, using PET techniques, the specific role of the right posterior parietal cortex in focal attention and processing of sensory input, regardless of whether it is painful or not. It is also proven that the parietal area is part of a larger network of sensory stimuli processing, which involves attentional allocation, orientation and preparedness for withdrawal reactions. This could provide an explanation of the observed right posterior parietal activity when processing MOD and INNO stimuli. Interestingly, this seems to involve more regions when perceiving NOX sensory stimuli, mainly bilateral prefrontal, medial frontal, pre-motor cortex and the ACC, forming, therefore, a complex attention circuitry [119]. The activation of the frontal area reflects ”vigilance” [125], focal attention, and action planning [44]. Similarly, it could be also linked to its connection to the basal ganglia which has different roles in pain processing, including sensory discrimination, information gating, and provide warning input to different motor areas [263, 264]. We postulate that this could reveal the subjects' intention to either move their arms when being exposed to pain (a motor imagery function) or an internal suppression and inhibition of NOX sensations, given that they were strictly instructed not to move during the recordings. As the frontal area is heavily connected to the ACC, their observed simultaneous co-activation for NOX stimuli could be further interpreted by a stimulus evoked attention which may lead to motor initiation or suppression, and hence activate the pre-motor cortex.

7.6 Summary

In this study, EEG recordings from three healthy human subjects were used to identify spatial, temporal, and spectral patterns of brain activity during five different thermal stimulations ranging from extremely cold and hot stimuli (very intense), moderately cold and hot stimuli (intense), to a warm stimulus (innocuous). Our main findings reported a decrease in alpha power and induced high activation of the prefrontal, somatosensory, and central brain areas with the highest activation shown in the central area (Cz electrode) in the first 400 ms post-stimulus, whereas intense stimuli (cold and hot) induce high activation of the parietal area starting 500 ms post-stimulation. Localized sources were performed and revealed strong and early activation of the ACC. Based on these extracted features, a system for classifying the different thermal stimuli perception and reaction in the brain was validated. Overall, this study proposed new approaches to quantify non-invasive brain activity changes evoked by five different thermal stimuli.

8 Conclusions and Outlook

Conclusions

The development of algorithms for reliable BCI systems can greatly enhance the bidirectional control of upper-limb prostheses. Overall, such a development is a multidisciplinary endeavor that involves various disciplines, such as robotics, software engineering, cognitive science, neurophysiology, psychology, and it requires the utilization of different emerging techniques and methods spanning from signal processing to advanced machine learning techniques for interpreting changes in non-stationary biosignals. Previous studies in the literature have shown different limitations of existing BCI algorithms, particularly when used in the context of sensory-enabled prostheses control. In this thesis, two main control approaches on both sides of the equation (efferent and afferent) were investigated. From a feed-forward control standpoint, EEG brain activity was used alongside other biosignals to decode in real-time participants' intention to control reach-to-grasp robotic arms movements. For the sensory substitution and the perceptual path, EEG was used to quantify brain activity during electrotactile, and thermal stimulations, with a particular focus on very intense stimuli perception and processing in the human brain.

Deep neural networks improve the real-time decoding of two motor imagery movements from EEG signals for a robotic arm control

The first study presented in chapter 3 demonstrated the main benefit of using deep neural network to decode two classic motor imagery movements from EEG signals and use them for a real-time control a robotic arm. In this study, one observation was that traditional machine learning methods still rely on hand-crafted features [3, 51, 18], which are difficult to extract and are task/subject-dependent. Our obtained results by changing and adapting the internal architectures of three different deep learning models achieved better classification performance compared to state-of-the art machine learning techniques. Our proposed model (pCNN), which relies on extracted spectrograms from EEG time series data, was evaluated and validated on our recorded data from 20 healthy subjects, as well as on the Graz data set B from the BCI Competition 2009 [144]. This study was able to underpin

the real-time capability of the proposed model by showing the successful real-time control of two states (left, right) of a robotic arm. Although several models for BCI-based MI have been proposed in the literature, the study presented in chapter 3 showed the reliable online decoding of two motor imagery movements using the pCNN model. Overall, the pCNN model achieved a mean accuracy of 84.24% ($\pm 14.69\%$) across 20 different subjects. Another result was the high stability of the pCNN model's accuracy within trials and across the 20 subjects, which was evaluated in both the training and the validation phases. The model showed a high stability across test splits with a mean SD of less than 3.32%. This was surprising, given the existence of overfitting potential due to the high number of parameters (170,734) used to train the model. Overall, this work was only a validation study of different deep neural network architectures for real-time control of a robotic arm using two decoded left and right motor imagery movements. Thus, some future considerations and improvements still need to be further investigated to further assess the robustness of such a system when used in daily life scenarios, as well as its scalability to decode more complex movements (see Outlook below).

Combining multiple biosignals (EOG, EMG, EEG) allows the real-time decoding of more complex reach-to-grasp movements when interacting with robotic systems

The next follow-up study (Chapter 4) demonstrated the feasibility to decode from complex movements by investigating the combination of different biosignals. For that, two different approaches and experiments were performed and tested. For that, we validated a real-time human-robot interface system based on the combination of EOG and EMG decoding to control, in real-time, reach-to-grasp movements, circumventing, therefore, the limitation of the number of the possibly decoded movements from EEG presented in the first study (Chapter 3). 5 different reach movements were decoded from EOG to steer an industrial robotic arm in real-time, with a mean validation and online accuracy of 93.62% and 91.66%, respectively. EMG signals were decoded in parallel to perform the grasping movement using an attached gripper with an online accuracy of 99.50%. This experiment was a demonstration of such approach to decode more complex movements, compared to a single signal decoding. In another investigation, both EEG and EMG signals were also successfully combined and classified with a mean validation of 89.6%, when performing the same reach-to-grasp with another industrial robotic arm with an attached 3D-prosthetic hand. The decoding of EEG signals was performed using the pCNN model proposed in first study (chapter 3), whereas the EMG decoding was performed using a classic machine learning model (SVM).

Decoding of EEG signals when perceiving three distinct sensory stimuli induced by TENS: An amputee case study

Beyond proposing and using different BCI algorithms to improve the feedforward control of different robotic arm movements presented in chapter 3 and 4, EEG signals were used to quantify the human brain perception of different sensory stimuli, ranging from gentle touch (innocuous) to very intense sensations. One observation when investigating this other side of the equation was that most of the previously presented studies either focused on healthy subjects with a very limited number of encoded sensory stimuli or investigated fMRI and invasive signals to analyse brain responses. The study presented in Chapter 6 demonstrated the ability to use non-invasive EEG data to analyze somatosensory evoked responses recorded when receiving three different types of sensations profiles, ranging from pleasant to uncomfortable sensation. These signals were encoding the level of sharpness of different objects manipulated by an embodied prosthesis. The study presented spatial and temporal features to identify, analyze, and accurately decode the three sensations, namely innocuous (INNO), moderately intense (MOD) and noxious (NOX) stimulation of an amputee's phantom hand delivered through TENS [117]. The main findings of the study show that the NOX stimulation activates the pre-motor cortex with the highest activation detected in the central cortex (Cz electrode) between 450 ms and 750 ms post-stimulation, whereas the highest activation for the MOD stimulation was detected in the parietal lobe (P2, P4, and P6 electrodes). Additionally, brain regions were source localized for NOX condition, and an early strong activation of the anterior cingulate cortex (ACC) was found. Similarly, the posterior cingulate cortex (PCC) was found to be strongly activated for the NOX condition. By relying on these identified biomarkers, an offline system was developed to recognize the three sensory stimuli perception in the brain, achieving a test accuracy of 94.66% when distinguishing between them using the recorded EEG data. The scope of this study to complement the work performed by Osborn et.al [117], where they relied on the internal reflex system of the prosthesis to protect it from any damaging stimuli. Our motivation behind using EEG data to develop this reflex system was to involve the amputee in the withdrawal reaction, to increase their sense of embodiment and the sense of ownership, as well as to reduce the latency thanks to the EEG high temporal resolution and hence the intuitiveness of the control of these devices. Our source localization results, particularly the ACC responses, consolidate the previous findings about the attention and perceptual brain circuitry involved in the withdrawal reaction. Despite being a single case study, highlighting therefore some limitations of this work (See Outlook below), this study was among the very few to

present a novel approach to analyze and classify neural activity when perceiving external noxious sensations in an amputee's phantom limb.

The development of distinct brain patterns for five thermal stimuli perception reveals an anticipatory brain activity

In a follow-up study described in chapter 7, we presented effective spatial, temporal and spectral patterns from EEG signals when analysing and decoding nociceptive thermal stimuli in three healthy subjects. This further investigation of noxious stimuli perception and processing in the human brain was motivated by:
In the previous study (chapter 6), only TENS-based stimulation was analyzed and no other sensory stimuli were studied. Second, the previous study was performed in an amputee with en embodied prosthesis but did not include any healthy participants. For that, we tested a new experimental paradigm to study thermal sensation perception dynamics, its related cortical activations, as well as its decoding using effective features, which are still elusive. For that, we identified spatial, temporal, and spectral signatures of brain response to several distinct stimulation conditions ranging from extremely cold and hot stimuli, moderately cold and hot stimuli, to a warm stimulus. We first show that very intense thermal stimuli elicit a decrease in alpha power compared to moderately intense and innocuous stimulations. Second, our spatio-temporal analysis indicates that an increase of brain activity in the prefrontal and central brain areas for very intense stimulation was observed in the first 400 ms following the noxious stimulation (very cold, very hot), whereas high activity of the parietal area was observed post-500 ms following the intense stimulation (cold, hot), and no particular activity was detected for the innocuous stimulus. Similar to the previous study, the same strategy was followed by relying on those identified features to develop an offline system for detecting thermal sensation perception in the brain. This system was able to classify the five different thermal stimulation conditions with an average test accuracy of 87% across all the three participants. Furthermore, we analyzed brain data at the source level or each of the five thermal stimuli conditions, reporting an anticipatory component in the ACC (before 400 ms) following the noxious stimulation. Additionally, an activation of the pre-frontal cortex, somatosensory, central, and parietal areas, was observed in the first 400 ms post-stimulation for noxious conditions and starting 500 ms post-stimuli for intense conditions.

Outlook

Beyond the work developed in this thesis, further future investigations and validations are required. These investigations should be mainly touching upon the topics of:

(1) Further validating the robustness and reliability of both developed BCI systems, presented in chapters 3 and 4, when used with severely paralyzed people as well as with amputees. Along these lines, calibration time, variability across different patients, and the ability to be used ”off-the-shelf” should be proven.

(2) Integration of the different sensory feedback modalities and include them in real-time.

(3) The ultimate goal of the studies presented in chapters 6 and 7 is to develop a real-time withdrawal reaction when amputees interact with their prostheses, which can first protect the prosthesis from damaging stimuli, but particularly, increase the sense of agency, the intuitiveness of control, and more importantly, reduce the withdrawal reaction time using the identified effective features from EEG signals.

(4) The investigation of attention and perceptual brain circuitry involved in the withdrawal reaction in both healthy subjects and amputees could lead to the prediction of unpleasant sensation. A prediction of noxious sensation has clinical applications, such as chronic pain treatment, and the mitigation of the PLP problem. Therefore, future work should be performed in investigating the use of our proposed algorithms and findings for clinical applications.

Bibliography

[1] J. J. Vidal. Toward direct brain-computer communication. *Annual Review of Biophysics and Bioengineering*, 2(1):157–180, 1973.

[2] L.A. Farwell and E. Donchin. Talking off the top of your head: toward a mental prosthesis utilizing event-related brain potentials. *Electroencephalography and Clinical Neurophysiology*, 70(6):510 – 523, 1988.

[3] M. A. Lebedev and M. A. L. Nicolelis. Brain-machine interfaces: From basic science to neuroprostheses and neurorehabilitation. *Physiol Rev*, 97(2):767–837, 2017.

[4] L. Luis and J. Gomez-Gil. Brain computer interfaces, a review. *Sensors (Basel, Switzerland)*, 12(2):1211–1279, 2012.

[5] A. N. Belkacem, N. Jamil, J. A. Palmer, S. Ouhbi, and C. Chen. Brain computer interfaces for improving the quality of life of older adults and elderly patients. *Frontiers in Neuroscience*, 14:692, 2020.

[6] U. Chaudhary, N. Birbaumer, and A. Ramos-Murguialday. Brain–computer interfaces for communication and rehabilitation. *Nature Reviews Neurology*, 12:513–525, 2016.

[7] J. Koegel, J. Schmid, R. Jox, and O. Friedrich. Using brain-computer interfaces: A scoping review of studies employing social research methods. *BMC Medical Ethics*, 20:18, 2019.

[8] C. Brunner, N. Birbaumer, B. Blankertz, C. Guger, A. Kübler, D. Mattia, J. del R. Millan, F. Miralles, A. Nijholt, E. Opisso, N. Ramsey, P. Salomon, and G. Müller-Putz. BNCI horizon 2020: towards a roadmap for the BCI community. *Brain-Computer Interfaces*, 2(1):1–10, 2015.

[9] S. Simanto, A. Al. M. Khondaker, I. A. Khawza, M. Raqibul, R. N. Ganesh, K. Ahsan, D. Sam, and B. Mathias. Progress in brain computer interfaces: Challenges and trends. *CoRR*, abs/1901.03442, 2019.

[10] L. Farwell, D. Richardson, and G. Richardson. Brain fingerprinting classification concealed information test detects us navy military medical information with P300. *Frontiers in neuroscience*, 8(410), 2014.

[11] G. Dornhege, J. del R. Millán, T. Hinterberger, D. J. McFarland, and K. R. Müller. *Improving Human Performance in a Real Operating Environment through Real-Time Mental Workload Detection*, pages 409–422. 2007.

[12] D. Friedman. *Brain-Computer Interfacing and Virtual Reality*, pages 151–171. Springer Singapore, 2017.

[13] E. Loup-Escande, F. Lotte, G. Loup, and A. Lécuyer. *User-Centered BCI Videogame Design*, pages 225–250. Springer Singapore, 2017.

[14] C. J. Bell, P. Shenoy, R. Chalodhorn, and R. P. N. Rao. Control of a humanoid robot by a noninvasive brain–computer interface in humans. *Journal of Neural Engineering*, 5(2):214–220, 2008.

[15] B. Choi and S. Jo. A low-cost EEG system-based hybrid brain-computer interface for humanoid robot navigation and recognition. *PLOS ONE*, 8(9), 2013.

[16] T. O. Zander, C. Kothe, S. Welke, and M. Roetting. Utilizing secondary input from passive brain-computer interfaces for enhancing human-machine interaction. In *Foundations of Augmented Cognition. Neuroergonomics and Operational Neuroscience*, pages 759–771. Springer Berlin Heidelberg, 2009.

[17] L. Hochberg, D. Bacher, B. Jarosiewicz, N. Masse, J.D. Simeral, J. Vogel, S. Haddadin, J. Liu, S. Cash, P. van der Smagt, and J. Donoghue. Reach and grasp by people with tetraplegia using a neurally controlled robotic arm. *Nature*, 485:372–5, 2012.

[18] M. Jianjun, S. Zhang, A. Bekyo, J. Olsoe, B. Baxter, and B. He. Noninvasive electroencephalogram based control of a robotic arm for reach and grasp tasks. *Scientific Reports*, 6:38565, 2016.

[19] S. Bandara, J. Arata, and K. Kiguchi. Towards control of a transhumeral prosthesis with EEG signals. *Bioengineering*, 5(2):26, 2018.

[20] H. Hinrichs, M. Scholz, Anne Baum, J. Kam, R. Knight, and H. Heinze. Comparison between a wireless dry electrode EEG system with a conventional wired wet electrode EEG system for clinical applications. *Scientific Reports*, 10:5218, 2020.

[21] S. Amiri, R. Fazel-Rezai, and V. Asadpour. A review of hybrid brain-computer interface systems. *Advances in Human-Computer Interaction*, 5:147, 2013.

[22] K. Hong and M. J. Khan. Hybrid brain–computer interface techniques for improved classification accuracy and increased number of commands: A review. *Frontiers in Neurorobotics*, 11:35, 2017.

[23] I. Batzianoulis, S. El-Khoury, E. Pirondini, M. Coscia, S. Micera, and A. Billard. EMG-based decoding of grasp gestures in reaching-to-grasping motions. *Robotics and Autonomous Systems*, 91:59–70, 2017.

[24] N. Nazmi, MA. Abdul Rahman, S-I. Yamamoto, SA. Ahmad, H. Zamzuri, and SA. Mazlan. A review of classification techniques of EMG signals during isotonic and isometric contractions. *Sensors*, 16(8):1304, 2016.

[25] E. D'Anna, G. Valle, A. Mazzoni, I. Strauss, F. Iberite, J. Patton, F. M. Petrini, S. Raspopovic, G. Granata, R. Di Iorio, M. Controzzi, C. Cipriani, T. Stieglitz, P. M. Rossini, and S. Micera. A closed-loop hand prosthesis with simultaneous intraneural tactile and position feedback. *Science Robotics*, 4(27), 2019.

[26] M. Tombini, J. Rigosa, F. Zappasodi, C. Porcaro, L. Citi, J. Carpaneto, P. Rossini, and S. Micera. Combined analysis of cortical (EEG) and nerve stump signals improves robotic hand control. *Neurorehabilitation and neural repair*, 26:275–81, 2011.

[27] A. Kaur and Y. Guan. Phantom limb pain: A literature review. *Chinese Journal of Traumatology*, 21(6), 2018.

[28] D. M. Page, J. A. George, D. T. Kluger, C. Duncan, S. Wendelken, T. Davis, D. T. Hutchinson, and G. A. Clark. Motor control and sensory feedback enhance prosthesis embodiment and reduce phantom pain after long-term hand amputation. *Frontiers in Human Neuroscience*, 12:352, 2018.

[29] P. Bach y Rita and S. W. Kercel. Sensory substitution and the human–machine interface. *Trends in Cognitive Sciences*, 7(12):541 – 546, 2003.

[30] X. Hu, J. Chen, F. Wang, and D. Zhang. Ten challenges for eeg-based affective computing. *Brain Science Advances*, 1(5):1–20, 2019.

[31] M. Rashid, N. Sulaiman, A. P. P. Abdul Majeed, R. M. Musa, A. F. Ab. Nasir, B. S. Bari, and S. Khatun. Current status, challenges, and possible solutions of eeg-based brain-computer interface: A comprehensive review. *Frontiers in Neurorobotics*, 14:25, 2020.

[32] X. Jiang, G. Bian, and Z. Tian. Removal of artifacts from EEG signals: A review. *Sensors*, 19(5):987, 2019.

[33] 2.14 - independent component analysis. In S. D. Brown, R. Tauler, and B. Walczak, editors, *Comprehensive Chemometrics*, pages 227 – 248. Elsevier, Oxford, 2009.

[34] F. Artoni, A. Delorme, and S. Makeig. Applying dimension reduction to eeg data by principal component analysis reduces the quality of its subsequent independent component decomposition. *NeuroImage*, 175:176 – 187, 2018.

[35] P. Pudil, J. Novovicova, and J. Kittler. Floating search methods in feature selection. *Pattern Recognition Lett*, 15(11):1119–1125, 1994.

[36] R. Leeb, F. Lee, C. Keinrath, R. Scherer, H. Bischof, and G. Pfurtscheller. Brain-computer communication: Motivation, aim, and impact of exploring a virtual apartment. *IEEE Transactions on Neural Systems and Rehabilitation Engineering*, 15(4):473–482, 2007.

[37] P. Ofner, A. Schwarz, J. Pereira, and G. R. Müller-Putz. Upper limb movements can be decoded from the time-domain of low-frequency EEG. *PLOS ONE*, 12:1–24, 2017.

[38] J. Kim, F. BieBmann, and S. Lee. Decoding three-dimensional trajectory of executed and imagined arm movements from electroencephalogram signals. *IEEE Transactions on Neural Systems and Rehabilitation Engineering*, 23(5), 2014.

[39] T. Li, T. Xue, B. Wang, and J. Zhang. Decoding voluntary movement of single hand based on analysis of brain connectivity by using EEG signals. *Frontiers in Human Neuroscience*, 12:381, 2018.

[40] R. G. Lupu, F. Ungureanu, and C. Cimpanu. Brain-computer interface: Challenges and research perspectives. In *2019 22nd International Conference on Control Systems and Computer Science (CSCS)*, pages 387–394, 2019.

[41] E. Vaadia and N. Birbaumer. Grand challenges of brain computer interfaces in the years to come. *Frontiers in Neuroscience*, 3:15, 2009.

[42] M. D. Murphy, D. J. Guggenmos, D. T. Bundy, and R. J. Nudo. Current challenges facing the translation of brain computer interfaces from preclinical trials to use in human patients. *Frontiers in Cellular Neuroscience*, 9:497, 2016.

[43] C. Kwan, A. Crawley, D. Mikulis, and K. Davis. An fMRI study of the anterior cingulate cortex and surrounding medial wall activations evoked by noxious cutaneous heat and cold stimuli. *Pain*, 85(3):359–74, 2000.

[44] S. Derbyshire, A. Jones, P. Devani, K. Friston, C. Feinmann, M. Harris, S. Pearce, J.D.G. Watson, and R. Frackowiak. Cerebral responses to pain in patients with atypical facial pain measured by positron emission tomography. *Journal of neurology, neurosurgery, and psychiatry*, 57(10):1166–72, 1994.

[45] L. E Osborn, K. Ding, M. A. Hays, R. Bose, M. M. Iskarous, A. Dragomir, Z. Tayeb, G. M. Lèvay, C. L. Hunt, G. Cheng, R. S. Armiger, A. Bezerianos, M. S. Fifer, and N. V Thakor. Sensory stimulation enhances phantom limb perception and movement decoding. *medRxiv*, 2020.

[46] Z. Tayeb, N. Waniek, J. Fedjaev, N. Ghaboosi, L. Rychly, C. Widderich, C. Richter, J. Braun, M. Saveriano, G. Cheng, and J. Conradt. Gumpy: a python toolbox suitable for hybrid brain–computer interfaces. *Journal of Neural Engineering*, 15(6):065003, 2018.

[47] A. Ojeda, N. Buscher, P. Balasubramani, V. Maric, D. Ramanathan, and J. Mishra. SimBSI: An open-source simulink library for developing closed-loop brain signal interfaces in animals and humans. *Biomedical Physics & Engineering Express*, 6(3):035023, 2020.

[48] P. Stegman, C. S. Crawford, M. Andujar, A. Nijholt, and J. E. Gilbert. Brain–computer interface software: A review and discussion. *IEEE Transactions on Human-Machine Systems*, 50(2):101–115, 2020.

[49] J. F. Braun, G. Díez-Valencia, S. K. Ehrlich, P. Lanillos, and G. Cheng. A prototype of a P300 based brain-robot interface to enable multi-modal interaction for patients with limited mobility. In *2019 IEEE International Conference on Cyborg and Bionic Systems (CBS)*, pages 78–84, 2019.

[50] Gumpy software available: http://gumpy.org/. [Online; accessed 2019-07-11].

[51] D. J. Mcfarland and J. R. Wolpaw. Chapter 4 - brain–computer interfaces for the operation of robotic and prosthetic devices. *Elsevier*, 79:169 – 187, 2010.

[52] J. Long, Y. Li, H. Wang, T. Yu, J. Pan, and F. Li. A hybrid brain computer interface to control the direction and speed of a simulated or real wheelchair. *IEEE Transactions on Neural Systems and Rehabilitation Engineering*, 20(5):720–729, 2012.

[53] B. Morshed and A. Khan. A brief review of brain signal monitoring technologies for BCI applications: Challenges and prospects. *Journal of Bioengineering Biomedical Science*, 04, 2014.

[54] A. Kreilinger, V. Kaiser, C. Breitwieser, J. Williamson, C. Neuper, and G. Müller-Putz. Switching between manual control and brain-computer interface using long term and short term quality measures. *Frontiers in neuroscience*, 5:147, 2011.

[55] L. E. Osborn, J. L. Betthauser, and N. V. Thakor. *Neural Prostheses*, pages 1–20. American Cancer Society, 2019.

[56] G. E Solomon. Electroencephalography: Basic principles, clinical applications and related fields. *Annals of Neurology*, 14(1):96–96, 1983.

[57] M. Tudor, L. Tudor Car, and K. Tudor. Hans berger (1873-1941) - the history of electroencephalography. *Acta medica Croatica : casopis Hravatske akademije medicinskih znanosti*, 59(4):307–13, 2005.

[58] K. Böcker, J. Avermaete, and M. Berg-Lenssen. The international 10–20 system revisited: Cartesian and spherical co-ordinates. *Brain topography*, 6(3):231–5, 1994.

[59] M. E. Obien, K. Deligkaris, T. Bullmann, D. Bakkum, and U. Frey. Revealing neuronal function through microelectrode array recordings. *Frontiers in Neuroscience*, 8:423, 2015.

[60] G. Schalk and J. Mellinger. *A Practical Guide to Brain-Computer Interfacing with BCI2000*. 2010.

[61] Z. Tayeb, E. Erçelik, and J. Conradt. Decoding of motor imagery movements from EEG signals using spinnaker neuromorphic hardware. In *8th International IEEE/EMBS Conference on Neural Engineering (NER)*, pages 263–266, 2017.

[62] M. Grosse-Wentrup and M. Buss. Multiclass common spatial patterns and information theoretic feature extraction. *IEEE Transactions on Biomedical Engineering*, 8(8):1991–2000, 2008.

[63] Ç. Uyulan, T. Erguzel, and K. Tarhan. *A Review on EEG Controlled BCI: Deep Learning Approach*, pages 1–36. 2019.

[64] J. Thomas, T. Maszczyk, N. Sinha, T. Kluge, and J. Dauwels. Deep learning-based classification for brain-computer interfaces. In *2017 IEEE International Conference on Systems, Man, and Cybernetics (SMC)*, pages 234–239, 2017.

[65] Ganesh Naik and Dinesh Kumar. An overview of independent component analysis and its applications. *Informatica*, 35:63–81, 2011.

[66] J. Kybic, M. Clerc, O. Faugeras, R. Keriven, and T. Papadopoulo. Generalized head models for MEG/EEG: boundary element method beyond nested volumes. *Physics in Medicine and Biology*, 51(5):1333–1346, 2006.

[67] R.D. Pascual-Marqui. Standardized low resolution brain electromagnetic tomography (SLORETA): Technical details. *Methods and findings in experimental and clinical pharmacology*, 24 Suppl D:5–12, 2002.

[68] M. Jatoi, N. Kamel, A. Malik, and I. Faye. EEG based brain source localization comparison of sLORETA and eLORETA. *Australasian Physical Engineering Sciences in Medicine*, 4:13–21, 2014.

[69] H. Yang, S. Sakhavi, K. K. Ang, and C. Guan. On the use of convolutional neural networks and augmented CSP features for multi-class motor imagery of EEG signals classification. In *2015 37th Annual International Conference of the IEEE Engineering in Medicine and Biology Society (EMBC)*, pages 2620–2623, 2015.

[70] Y. Wang, b. Hong, X. Gao, and S. Gao. Implementation of a brain-computer interface based on three states of motor imagery. *IEEE Engineering in Medicine and Biology Society. Conference*, 2007:5059–62, 2007.

[71] S. Stober, A. Sternin, A. M. Owen, and J. A. Grahn. Deep feature learning for EEG recordings. *CoRR*, abs/1511.04306, 2015.

[72] A. Graves. Generating sequences with recurrent neural networks. *CoRR*, abs/1308.0850, 2013.

[73] R. T. Schirrmeister, J. T. Springenberg, L. D. J. Fiederer, M. Glasstetter, K. Eggensperger, M. Tangermann, F. Hutter, W. Burgard, and T. Ball. Deep learning with convolutional neural networks for EEG decoding and visualization. *Human Brain Mapping*, 38(11):5391–5420, 2017.

[74] M. Arvaneh, I. H. Robertson, and T. E. Ward. A P300-based brain-computer interface for improving attention. *Frontiers in Human Neuroscience*, 12:524, 2019.

[75] G. Pfurtscheller, C. Brunner, A. Schlögl, and F.H. Lopes da Silva. Mu rhythm (de)synchronization and EEG single-trial classification of different motor imagery tasks. *NeuroImage*, 31(1):153 – 159, 2006.

[76] K. Liao, R. Xiao, J. Gonzalez, and L. Ding. Decoding individual finger movements from one hand using human EEG signals. *PLOS ONE*, 9(1):1–12, 2014.

[77] Q. Li, D. Ding, and M. Conti. Brain-computer interface applications: Security and privacy challenges. pages 663–666, 2015.

[78] R. Barea Navarro, L. Boquete Vázquez, and E. López Guillén. Chapter 16 - EOG-based wheelchair control. In *Smart Wheelchairs and Brain-Computer Interfaces*, pages 381 – 403. Academic Press, 2018.

[79] E. Rocon, J. Gallego, L. Barrios, A. Victoria, J. Ibáñez, D. Farina, F. Negro, J. Dideriksen, S. Conforto, T. D'Alessio, G. Severini, J. M. Belda Lois, L. Maneski, G. Grimaldi, M. Manto, and J. Pons. Multimodal BCI-mediated FES suppression of pathological tremor. pages 3337–3340, 2010.

[80] L. Peng, Z. Hou, N. Kasabov, G. Bian, L. Vladareanu, and H. Yu. Feasibility of neucube spiking neural network architecture for EMG pattern recognition. In *2015 International Conference on Advanced Mechatronic Systems (ICAMechS)*, pages 365–369, 2015.

[81] A. Balbinot and G. A. Favieiro. A neuro-fuzzy system for characterization of arm movements. *Sensors*, 13(2):2613–2630, 2013.

[82] A. Phinyomark, F. Quaine, S. Charbonnier, C. Serviere, F. Tarpin-Bernard, and Y. Laurillau. EMG feature evaluation for improving myoelectric pattern recognition robustness. *Expert Systems with Applications*, 40(12):4832–4840, 2013.

[83] T. Matsubara and J. Morimoto. Bilinear modeling of EMG signals to extract user-independent features for multi-user myoelectric interface. *IEEE transactions on biomedical engineering*, 60:2205–13, 2013.

[84] A. Phinyomark, P. Phukpattaranont, and C. Limsakul. Feature reduction and selection for EMG signal classification. *Expert Systems with Applications*, 39(8):7420 – 7431, 2012.

[85] Siti A. Moving approximate entropy and its application to the electromyographic control of an artificial hand. *Doctoral Thesis*, 2009.

[86] Md. R. Ahsan, M. Ibrahimy, and O. Khalifa. *Neural Network Classifier for Hand Motion Detection from EMG Signal*, volume 35, pages 536–541. 2011.

[87] A. Tsai, T. Hsieh, J. Luh, and T. Lin. A comparison of upper-limb motion pattern recognition using EMG signals during dynamic and isometric muscle contractions. *Biomedical Signal Processing and Control*, 11:17–26, 2014.

[88] K. Englehart, B. Hudgins, P.A. Parker, and M. Stevenson. Classification of the myoelectric signal using time-frequency based representations. *Medical Engineering Physics*, 21(6):431 – 438, 1999.

[89] S. Lobov, V. Mironov, I. Kastalskiy, and V. Kazantsev. A spiking neural network in sEMG feature extraction. *Sensors (Basel, Switzerland)*, 15(11):27894–27904, 2015.

[90] B. Allison, R. Leeb, C Brunner, G. Müller-Putz, G. Bauernfeind, J. Kelly, and C. Neuper. Toward smarter BCIs: Extending BCIs through hybridization and intelligent control. *Journal of neural engineering*, 9(1):013001, 2011.

[91] T. Carlson, L. Tonin, S. Perdikis, R. Leeb, and J. del. R. Millan. A hybrid BCI for enhanced control of a telepresence robot. *Annual International Conference of the IEEE Engineering in Medicine and Biology Society*, pages 3097–100, 2013.

[92] R. Leeb, H. Sagha, R. Chavarriaga, and J. del. R. Millan. Multimodal fusion of muscle and brain signals for a hybrid-BCI. volume 2010, pages 4343–4346, 2010.

[93] B. Chang and B. Seo. Development of new brain computer interface based on EEG and EMG. In *2008 IEEE International Conference on Robotics and Biomimetics*, pages 1665 – 1670, 2009.

[94] P. Chappell. Making sense of artificial hands. *Journal of medical engineering technology*, 35:1–18, 2011.

[95] C. Hartmann, J. Linde, S. Dosen, D. Farina, L. Seminara, L. Pinna, M. Valle, and M. Capurro. Towards prosthetic systems providing comprehensive tactile feedback for utility and embodiment. In *2014 IEEE Biomedical Circuits and Systems Conference (BioCAS) Proceedings*, pages 620–623, 2014.

[96] G. Valle, A. Mazzoni, F. Iberite, E. D'Anna, I. Strauss, G. Granata, M. Controzzi, F. Clemente, G. Rognini, C. Cipriani, T. Stieglitz, F. Petrini, P. Rossini, and S. Micera. Biomimetic intraneural sensory feedback enhances sensation naturalness, tactile sensitivity, and manual dexterity in a bidirectional prosthesis. *Neuron*, 100(1), 2018.

[97] K. A. Kaczmarek, J. G. Webster, P. Bach-y-Rita, and W. J. Tompkins. Electrotactile and vibrotactile displays for sensory substitution systems. *IEEE Transactions on Biomedical Engineering*, 38(1):1–16, 1991.

[98] L. Osborn, M. Fifer, C. Moran, J. Betthauser, R. Armiger, R. Kaliki, and N. Thakor. Targeted transcutaneous electrical nerve stimulation for phantom limb sensory feedback. In *2017 IEEE Biomedical Circuits and Systems Conference (BioCAS), Torino, Italy*, pages 1–4, 2017.

[99] T. Chou, W. Daly, R. Austin, P. Chaubey, and D. A. Boone. Development and real world use of a vibratory haptic feedback system for upper-limb prosthetic users. pages 136–144, 2016.

[100] C. Cipriani, M. D'Alonzo, and M. C. Carrozza. A miniature vibrotactile sensory substitution device for multifingered hand prosthetics. *IEEE transactions on bio-medical engineering*, 59(02):400–408, 2012.

[101] N. Franck, C. Farrer, N. Georgieff, M. Marie-Cardine, J. Daléry, T. d'Amato, and M. Jeannerod. Defective recognition of one's own actions in schizophrenic patients. (03):454–9, 2001.

[102] M. Arif F. Ismail and S. Shimada. 'robot' hand illusion under delayed visual feedback: Relationship between the senses of ownership and agency. *PLOS ONE*, 11(07):1–9, 2016.

[103] P. Bach y Rita. Nonsynaptic diffusion neurotransmission and brain plasticity. *The Neuroscientist*, 2(5):260–261, 1996.

[104] C. Antfolk, M. D'Alonzo, B. Rosén, G. Lundborg, F. Sebelius, and C. Cipriani. Sensory feedback in upper limb prosthetics. *Expert review of medical devices*, 10(01):45–54, 2013.

[105] K. Choi, P. Kim, and S. Kim. Two-channel electrotactile stimulation for sensory feedback of fingers of prosthesis. Number 10, pages 1133–1138, 2016.

[106] G. Chai, S. Li, X. Sui, Z. Mei, L.W. He, C.L. Zhong, J.W. Wang, D. Zhang, X. Zhu, and N. Lan. Phantom finger perception evoked with transcutaneous electrical stimulation for sensory feedback of prosthetic hand. pages 271–274, 2013.

[107] Y. Ueda and C. Ishii. Feedback device of temperature sensation for a myoelectric prosthetic hand. *Advances in Science, Technology and Engineering Systems Journal*, 2:488–493, 2017.

[108] C. Antfolk, A. Björkman, S. Frank, F. Sebelius, G. Lundborg, and B. Rosén. Sensory feedback from a prosthetic hand based on airmediate d pressure from the hand to

the forearm skin. *Journal of rehabilitation medicine : official journal of the UEMS European Board of Physical and Rehabilitation Medicine*, 44(8):702–7, 2012.

[109] P. Li, G. Chai, K. Zhu, N. Lan, and X. Sui. Effects of electrode size and spacing on sensory modalities in the phantom thumb perception area for the forearm amputees. volume 2015, pages 3383–6, 2015.

[110] A. Y. J. Szeto and F. A. Saunders. Electrocutaneous stimulation for sensory communication in rehabilitation engineering. *IEEE Transactions on Biomedical Engineering*, BME-29(4):300–308, 1982.

[111] B. Stephens-Fripp, G. Alici, and R. Mutlu. A review of non-invasive sensory feedback methods for transradial prosthetic hands. *IEEE Access*, 6:6878–6899, 2018.

[112] E. Smith and G. Lewin. Nociceptors: A phylogenetic view. *Journal of comparative physiology. A, Neuroethology, sensory, neural, and behavioral physiology*, 195(12):1089–1106, 2009.

[113] Victoria E. A. and D. D. Ginty. The sensory neurons of touch. *Neuron*, 79(4):618 – 639, 2013.

[114] S. Raspopovic, M. Capogrosso, F. M. Petrini, M. Bonizzato, J. Rigosa, G. Di Pino, J. Carpaneto, M. Controzzi, T. Boretius, E. Fernandez, G. Granata, C. M. Oddo, L. Citi, A. L. Ciancio, C. Cipriani, M. C. Carrozza, W. Jensen, E. Guglielmelli, T. Stieglitz, P. M. Rossini, and S. Micera. Restoring natural sensory feedback in real-time bidirectional hand prostheses. *Science Translational Medicine*, 6(222):222ra19–222ra19, 2014.

[115] S. Wendelken, D. Page, T. Davis, H. Wark, D. Kluger, C. Duncan, D. Warren, D. Hutchinson, and G. Clark. Restoration of motor control and proprioceptive and cutaneous sensation in humans with prior upper-limb amputation via multiple utah slanted electrode arrays (USEAs) implanted in residual peripheral arm nerves. *Journal of NeuroEngineering and Rehabilitation*, 14:121–1, 2017.

[116] C. M. Oddo, S. Raspopovic, F. Artoni, A. Mazzoni, G. Spigler, F. Petrini, F. Giambattistelli, F. Vecchio, F. Miraglia, L. Zollo, G. Di Pino, D. Camboni, M. C. Carrozza, E. Guglielmelli, P. M. Rossini, Ug. Faraguna, and S. Micera. Intraneural stimulation elicits discrimination of textural features by artificial fingertip in intact and amputee humans. 5:e09148, 2016.

[117] L. E. Osborn, A. Dragomir, J. L. Betthauser, C. L. Hunt, H. H. Nguyen, R. R. Kaliki, and N. V. Thakor. Prosthesis with neuromorphic multilayered e-dermis perceives touch and pain. *Science Robotics*, 3(19), 2018.

[118] S. Bunk, S. Lautenbacher, J. Rüsseler, K. Müller, J. Schultz, and M. Kunz. Does EEG activity during painful stimulation mirror more closely the noxious stimulus intensity or the subjective pain sensation? 35(3-4):192–198, 2018.

[119] J. Pardo, P. Fox, and M. Raichle. Localization of a human system for sustained attention by positron emission tomography. *Nature*, 349(6304):61–4, 1991.

[120] M. Ploner, C. Sorg, and J. Gross. Brain rhythms of pain. *Trends in cognitive sciences*, 21(2):100–110, 2016.

[121] E. Schulz, E. May, M. Postorino, L. Tiemann, M. Nickel, V. Witkovský, P. Schmidt, J. Gross, and M. Ploner. Prefrontal gamma oscillations encode tonic pain in humans. *Cerebral Cortex*, 25(11):4407–14, 2015.

[122] J. Lisman. The challenge of understanding the brain: Where we stand in 2015. *Neuron*, 86(4):864–882, 2015.

[123] L. Tiemann, D. V. Hohn, S. T. Dinh, S. E. May, M. M. Nickel, J. Gross, and M. PLoner. Distinct patterns of brain activity mediate perceptual and motor and autonomic responses to noxious stimuli. *Nature Communications*, 9(1), 2018.

[124] F. Benuzzi, F. Lui, D. Duzzi, Paolo F. N., and C. A. Porro. Does it look painful or disgusting? ask your parietal and cingulate cortex. *Journal of Neuroscience*, 28(4):923–931, 2008.

[125] S. W.G Derbyshire, A. K.P Jones, F. Gyulai, S. Clark, D. Townsend, and L. L. Firestone. Pain processing during three levels of noxious stimulation produces differential patterns of central activity. *Pain*, 73(3):431 – 445, 1997.

[126] A. Walter, G. Naros, A. Roth, W. Rosenstiel, A. Gharabaghi, and M. Bogdan. A brain-computer interface for chronic pain patients using epidural ECoG and visual feedback. In *2012 IEEE 12th International Conference on Bioinformatics Bioengineering (BIBE)*, pages 380–385, 2012.

[127] M. Backonja, E. W. Howland, J. Wang, J. Smith, M. Salinsky, and C. S. Cleeland. Tonic changes in alpha power during immersion of the hand in cold water. *Electroencephalography and Clinical Neurophysiology*, 79(3):192 – 203, 1991.

[128] Somatosensory evoked potentials. In Michael J. Aminoff and Robert B. Daroff, editors, *Encyclopedia of the Neurological Sciences (Second Edition)*, pages 230 – 238. Academic Press, Oxford, second edition edition, 2014.

[129] S. Hochreiter and J. Schmidhuber. Long short-term memory. *Neural computation*, 9(8):1735–1780, 1997.

[130] Y. Lecun, Y. Bengio, and G. Hinton. Deep learning. *Nature*, 521(7553):436–444, 2015.

[131] Y. R. Tabar and U. Halici. A novel deep learning approach for classification of EEG motor imagery signals. *Journal of Neural Engineering*, 14(1):016003, 2017.

[132] S. Sakhavi, C. Guan, and S. Yan. Learning temporal information for brain-computer interface using convolutional neural networks. *IEEE Transactions on Neural Networks and Learning Systems*, 29(11):5619–5629, 2018.

[133] J. Zhang, C. Yan, and X. Gong. Deep convolutional neural network for decoding motor imagery based brain computer interface. In *2017 IEEE International Conference on Signal Processing, Communications and Computing (ICSPCC)*, pages 1–5, 2017.

[134] Y. Bengio, P. Simard, and P. Frasconi. Learning long-term dependencies with gradient descent is difficult. *IEEE Transactions on Neural Networks*, 5(2):157–166, 1994.

[135] R. Pascanu, T. Mikolov, and Y. Bengio. On the difficulty of training recurrent neural networks. *30th International Conference on Machine Learning, ICML 2013*, 2012.

[136] E. M. Forney and C. W. Anderson. Classification of EEG during imagined mental tasks by forecasting with elman recurrent neural networks. In *The 2011 International Joint Conference on Neural Networks*, pages 2749–2755, 2011.

[137] C. R. Hema, M. P. Paulraj, S. Yaacob, A. H. Adom, and R. Nagarajan. Recognition of motor imagery of hand movements for a BMI using PCA features. In *2008 International Conference on Electronic Design*, pages 1–4, 2008.

[138] Amaral L. Glass L. Hausdorff J. Ivanov P. C. Mark R. ... Stanley H. E. Goldberger, A. Physiobank, physiotoolkit, and physionet: Components of a new research resource for complex physiologic signals. *Circulation [Online]*, 101(23):e215–e220, 2000.

[139] J. An and S. Cho. Hand motion identification of grasp-and-lift task from electroencephalography recordings using recurrent neural networks. In *2016 International Con-*

ference on Big Data and Smart Computing (BigComp), number 3, pages 427–429, 2016.

[140] K. Cho, B. V. Merrienboer, D. Bahdanau, and Y. Bengio. On the properties of neural machine translation: Encoder-decoder approaches. *arXiv preprint arXiv:1409.1259*, abs/1409.1259, 2014.

[141] V. J. Lawhern, A. J. Solon, N. R. Waytowich, C. P. Hung S. M. Gordon, and B. J. Lance. Eegnet: A compact convolutional network for EEG-based brain-computer interfaces. *arXiv preprint arXiv:1611.08024*, abs/1611.08024, 2016.

[142] P. Bashivan, I. Rish, M. Yeasin, and N. Codella. Learning representations from EEG with deep recurrent-convolutional neural networks. *arXiv preprint arXiv:1511.06448*, 2015.

[143] E. Popov and S. Fomenkov. Classification of hand motions in eeg signals using recurrent neural networks. In *2016 2nd International Conference on Industrial Engineering, Applications and Manufacturing (ICIEAM)*, pages 1–4, 2016.

[144] R. Leeb, C. Brunner, G. Mueller-Put, A. Schloegl, and G. Pfurtscheller. BCI competition 2008-graz data set b. *Graz University of Technology, Austria*, 2008.

[145] Guger technologies, 2017. `Available:http://www.gtec.at/`.

[146] H. Nolan, R. Whelan, and R.B. Reilly. Faster: Fully automated statistical thresholding for EEG artifact rejection. *Journal of Neuroscience Methods*, 192(1):152 – 162, 2010.

[147] The Theano Development Team. Theano: A python framework for fast computation of mathematical expressions. *arXiv preprint*, 2016.

[148] F.Chollet. keras, 2015. `https://github.com/fchollet/keras`.

[149] D. Erhan, Y. Bengio, A. Courville, P. A. Manzagol, P. Vincent, and S. Bengio. Why does unsupervised pre-training help deep learning? *Journal of Machine Learning*, 11:625–660, 2010.

[150] D. L. Sun and J. O. Smith III. Estimating a signal from a magnitude spectrogram via convex optimization. *arXiv preprint*, 2012.

[151] G. Pfurtscheller and F. H. Lopes da Silva. Event-related EEG/MEG synchronization and desynchronization:basic principles. *Clinical neurophysiology*, 110(11):1842–1857, 1999.

[152] S. Ioffe and C. Szegedy. Batch normalization: Accelerating deep network training by reducing internal covariate shift. *arXiv preprint arXiv:1502.03167*, abs/1502.03167, 2015.

[153] S. Ioffe and C. Szegedy. Adam: A method for stochastic optimization. *arXiv preprint arXiv:1412.6980*, 2014.

[154] M. Liang and X. Hu. Recurrent convolutional neural network for object recognition. In *2015 IEEE Conference on Computer Vision and Pattern Recognition (CVPR)*, pages 3367–3375, 2015.

[155] S. Aditya and D.N. Tibarewala. Comparing ANN, LDA, QDA, KNN and SVM algorithms in classifying relaxed and stressful mental state from two-channel prefrontal EEG data. *International Journal of Artificial Intelligence and Soft Computing*, 3:143–164, 2012.

[156] N. Brodu, F. Lotte, and A. Lecuyer. Comparative study of band-power extraction techniques for motor imagery classification. In *2011 IEEE Symposium on Computational Intelligence, Cognitive Algorithms, Mind, and Brain (CCMB)*, pages 1–6, 2011.

[157] J. M. Gerking, G. Pfurtscheller, and H. Flyvbjerg. Designing optimal spatial filters for single-trial EEG classification in a movement task. *Clinical Neurophysiology*, 110(5):787 – 798, 1999.

[158] F. Sherwani, S. Shanta, B. S. K. K. Ibrahim, and M. S. Huq. Wavelet based feature extraction for classification of motor imagery signals. In *2016 IEEE EMBS Conference on Biomedical Engineering and Sciences (IECBES)*, pages 360–364, 2016.

[159] Lab streaming layer available:https://github.com/sccn/labstreaminglayer (LSL). [Online; accessed 2017-06-06].

[160] M. Hessel, H. Soyer, L. Espeholt, W. Czarnecki, S. Schmitt, and H. van Hasselt. Multi-task deep reinforcement learning with popart. *arXiv preprint arXiv:1809.04474*, abs/1809.04474, 2018.

[161] P. Beckerle, G. Salvietti, R. Unal, D. Prattichizzo, S. Rossi, C. Castellini, S. Hirche, S. Endo, H. Ben Amor, M. Ciocarlie, et al. A human–robot interaction perspective on assistive and rehabilitation robotics. *Frontiers in neurorobotics*, 11, 2017.

[162] T. Meneweger, D. Wurhofer, V. Fuchsberger, and M. Tscheligi. Working together with industrial robots: Experiencing robots in a production environment. In *2015 24th*

IEEE International Symposium on Robot and Human Interactive Communication (RO-MAN), pages 833–838. IEEE, 2015.

[163] A. Tellaeche, I. Maurtua, and A. Ibarguren. Human robot interaction in industrial robotics. examples from research centers to industry. In *2015 IEEE 20th Conference on Emerging Technologies & Factory Automation (ETFA)*, pages 1–6. IEEE, 2015.

[164] T. Tanioka, K. Osaka, R. Locsin, Y. Yasuhara, and H. Ito. Recommended design and direction of development for humanoid nursing robots perspective from nursing researchers. *Intelligent Control and Automation*, 8(02):96–110, 2017.

[165] Dennis R Louie and Janice J Eng. Powered robotic exoskeletons in post-stroke rehabilitation of gait: a scoping review. *Journal of neuroengineering and rehabilitation*, 13(53), 2016.

[166] S. Koceski and N. Koceska. Evaluation of an assistive telepresence robot for elderly healthcare. *Journal of medical systems*, 40(121), 2016.

[167] T. B. Sheridan. Human–robot interaction: status and challenges. *Human factors*, 58(4):525–532, 2016.

[168] M. A Goodrich, A. C Schultz, et al. Human–robot interaction: a survey. *Foundations and Trends® in Human–Computer Interaction*, 1(3):203–275, 2008.

[169] S. Goto, O. Yano, Y. Matsuda, T. Sugi, and N. Egashira. Development of hands-free remote operation system for a mobile robot using EOG and EMG. *Electronics and Communications in Japan*, 100(10):38–47, 2017.

[170] L. Liao, Y. Tseng, H. Chiang, and W. Wang. EMG-based control scheme with SVM classifier for assistive robot arm. In *2018 International Automatic Control Conference (CACS)*, pages 1–5. IEEE, 2018.

[171] N. M. Krishnan, M. Mariappan, K. Muthukaruppan, M. H. Ah. Hijazi, and W. W. Kitt. Electroencephalography (EEG) based control in assistive mobile robots: A review. In *IOP Conference Series: Materials Science and Engineering*, volume 121, page 012017. IOP Publishing, 2016.

[172] Q. Huang, Y. Chen, Z. Zhang, S. He, R. Zhang, J. Liu, Y. Zhang, M. Shao, and Y. Li. An EOG-based wheelchair robotic arm system for assisting patients with severe spinal cord injuries. *Journal of neural engineering*, 16(2):026021, 2019.

[173] X. Guo, W. Pei, Y. Wang, Y. Chen, H. Zhang, X. Wu, X. Yang, H. Chen, Y. Liu, and R. Liu. A human-machine interface based on single channel EOG and patchable sensor. *Biomedical Signal Processing and Control*, 30:98–105, 2016.

[174] A. Bulling, D. Roggen, and G. Tröster. Wearable EOG goggles: Seamless sensing and context-awareness in everyday environments. *Journal of Ambient Intelligence and Smart Environments*, 1(2):157–171, 2009.

[175] Q. Huang, S. He, Q. Wang, Z. Gu, N. Peng, K. Li, Y. Zhang, M. Shao, and Y. Li. An EOG-based human–machine interface for wheelchair control. *IEEE Transactions on Biomedical Engineering*, 65(9):2023–2032, 2017.

[176] L. Minati, N. Yoshimura, and Y. Koike. Hybrid control of a vision-guided robot arm by EOG, EMG, EEG biosignals and head movement acquired via a consumer-grade wearable device. *Ieee Access*, 4:9528–9541, 2016.

[177] Y. Nam, B. Koo, A. Cichocki, and S. Choi. GOM-face: GKP, EOG, and EMG-based multimodal interface with application to humanoid robot control. *IEEE Transactions on Biomedical Engineering*, 61(2):453–462, 2013.

[178] et al. DelPreto, J. Plug-and-play supervisory control using muscle and brain signals for real-time gesture and error detection. In *Robotics: Science and Systems XIV, Robotics: Science and Systems Foundation*, volume 44, page 1303–1322, 2020.

[179] J. Ma, Y. Zhang, A. Cichocki, and F. Matsuno. A novel EOG/EEG hybrid human–machine interface adopting eye movements and erps: Application to robot control. *IEEE Transactions on Biomedical Engineering*, 62(3):876–889, 2014.

[180] J. Zhang, B. Wang, C. Zhang, Y. Xiao, and M. Y. Wang. An EEG/EMG/EOG-based multimodal human-machine interface to real-time control of a soft robot hand. *Frontiers in neurorobotics*, 13(7), 2019.

[181] G. Pfurtscheller, B. Allison, G. Bauernfeind, C. Brunner, T. Solis Escalante, R. Scherer, T. Zander, G. Mueller-Putz, C. Neuper, and N. Birbaumer. The hybrid BCI. *Frontiers in Neuroscience*, 4:3, 2010.

[182] R. Leeb, H. Sagha, R. Chavarriaga, and J. d. R. Millán. A hybrid BCI based on the fusion of EEG and EMG activities. *Journal of Neural Engineering*, 8:225–229, 2011.

[183] M. Cifrek, V. Medved, S. Tonković, and S. Ostojic. Surface EMG based muscle fatigue evaluation in biomechanics. *Clinical Biomechanics*, 24(4):327 – 340, 2009.

[184] K. Lin, X. Chen, X. Huang, Q. Ding, and X. Gao. A hybrid BCI speller based on the combination of EMG envelopes and SSVEP. *Applied Informatics*, 2:1–12, 2015.

[185] A. Riccio, E. M. Holz, P. Arico, F. Leotta, F. Aloise, L. Desideri, M. Rimondini, A. Kubler, D. Mattia, and F. Cincotti. Hybrid P300-based brain-computer interface to improve usability for people with severe motor disability: Electromyographic signals for error correction during a spelling task. *Archives of Physical Medicine and Rehabilitation*, 96(3, Supplement):S54 – S61, 2015.

[186] S. Perdikis, R. Leeb, J. Williamson, A. Ramsay, M. Tavella, L. Desideri, E. J. Hoogerwerf, A. Al-Khodairy, R. Murray-Smith, and J. del R. Millan. Clinical evaluation of BrainTree, a motor imagery hybrid BCI speller. *Journal of neural engineering*, 11(3):036003, 2014.

[187] B. Venthur and B. Blankertz. Mushu, a free- and open source BCI signal acquisition, written in python. In *Engineering in Medicine and Biology Society (EMBC), 2012 Annual International Conference of the IEEE*, pages 1786–1788. IEEE, Aug 2012.

[188] S. Aungsakul, A. Phinyomark, P. Phukpattaranont, and C. Limsakul. Evaluating feature extraction methods of electrooculography (EOG) signal for human-computer interface. *Procedia Engineering*, 32:246–252, 2012.

[189] E. Dean-Leon, F. Bergner, K. Ramirez-Amaro, and G. Cheng. From multi-modal tactile signals to a compliant control. In *2016 IEEE-RAS 16th International Conference on Humanoid Robots (Humanoids)*, pages 892–898, 2016.

[190] Z. Tayeb, Fedjaev J, Ghaboosi N, Richter C, Everding L, Qu X, Wu Y, Cheng G, and Conradt J. Validating deep neural networks for online decoding of motor imagery movements from EEG signals. *Sensors*, 19(1), 2019.

[191] R. Bischoff, J. Kurth, G. Schreiber, R. Koeppe, A. Albu-Schaeffer, A. Beyer, O. Eiberger, S. Haddadin, A. Stemmer, G. Grunwald, and G. Hirzinger. The KUKA-DLR lightweight robot arm -a new reference platform for robotics research and manufacturing. In *ISR 2010 (41st International Symposium on Robotics) and ROBOTIK 2010 (6th German Conference on Robotics)*, pages 1–8, 2010.

[192] F. Cordella, A. L. Ciancio, R. Sacchetti, A. Davalli, A. G. Cutti, E. Guglielmelli, and L. Zollo. Literature review on needs of upper limb prosthesis users. In *Front. Neurosci.*, volume 10, page 209, 2016.

[193] G. Rognini, F. M. Petrini, S. Raspopovic, G. Valle, G. Granata, I. Strauss, M. Solcà, J. Bello-Ruiz, B. Herbelin, R. Mange, E. D'Anna, R. Di Iorio, G. Di Pino, D. Andreu, D. Guiraud, T. Stieglitz, P. M. Rossini, A. Serino, S. Micera, and O. Blanke. Multisensory bionic limb to achieve prosthesis embodiment and reduce distorted phantom limb perceptions. *Journal of Neurology, Neurosurgery & Psychiatry*, 90:833–836, 2018.

[194] E. A. Biddiss and T. T. Chau. Upper limb prosthesis use and abandonment: A survey of the last 25 years. *Prosthetics and Orthotics International*, 31(3):236–257, 2007.

[195] A. Gailey, P. Artemiadis, and M. Santello. Proof of concept of an online EMG-based decoding of hand postures and individual digit forces for prosthetic hand control. *Frontiers in Neurology*, 8:7, 2017.

[196] S. Dosen, M. Schaeffer, and D. Farina. Time-division multiplexing for myoelectric closed-loop control using electrotactile feedback. *Journal of NeuroEngineering and Rehabilitation*, 11(1):138, 2014.

[197] M. D'Alonzo, S. Dosen, C. Cipriani, and D. Farina. HyVE: Hybrid vibro-electrotactile stimulation for sensory feedback and substitution in rehabilitation. *IEEE Transactions on Neural Systems and Rehabilitation Engineering*, 22(2):290–301, 2014.

[198] Pamela S., Ulrika W., Anders B., and Christian A. A review of invasive and non-invasive sensory feedback in upper limb prostheses. *Expert Review of Medical Devices*, 14(6):439–447, 2017.

[199] H. J. B. Witteveen, E. A. Droog, J. S. Rietman, and P. H. Veltink. Vibro- and electrotactile user feedback on hand opening for myoelectric forearm prostheses. *IEEE Transactions on Biomedical Engineering*, 59(8):2219–2226, 2012.

[200] A. Ninu, S. Dosen, S. Muceli, F. Rattay, H. Dietl, and D. Farina. Closed-loop control of grasping with a myoelectric hand prosthesis: Which are the relevant feedback variables for force control? *IEEE Transactions on Neural Systems and Rehabilitation Engineering*, 22(5):1041–1052, 2014.

[201] M. Nabeel, K. Aqeel, M. N. Ashraf, M. I. Awan, and M. Khurram. Vibrotactile stimulation for 3d printed prosthetic hand. In *2016 2nd International Conference on Robotics and Artificial Intelligence (ICRAI)*, pages 202–207, 2016.

[202] M. Isaković, M. Belić, M. Štrbac, I. Popović, S. Dosen, D. Farina, and T. Keller. Electrotactile feedback improves performance and facilitates learning in the routine grasping task. *European Journal of Translational Myology*, 26, 2016.

[203] Available: https://www.myo.com/, Myo, 2018.

[204] Available: http://www.openbionics.org/, OpenBionics, 2018.

[205] A. E. Dubin and A. Patapoutian. Nociceptors: the sensors of the pain pathway. *The Journal of clinical investigation*, 120(11), 2010.

[206] V. Skljarevski and N. M. Ramadan. The nociceptive flexion reflex in humans—review article. *Pain*, 96:3–8, 2002.

[207] C. Aziz and A. Ahmad. The role of the thalamus in modulating pain. *Malays J Med Sci*, 13(2):11–18, 2006.

[208] E. T. Rolls. Limbic systems for emotion and for memory, but no single limbic system. *Cortex*, 62, 2013.

[209] C. E. Steeds. The anatomy and physiology of pain. *Surgery (Oxford)*, 34(2), 2016.

[210] E. R. Perl. Myelinated afferent fibres innervating the primate skin and their response to noxious stimuli. *J. Physiol.*, 197(3), 1968.

[211] C. Hartley, E. P. Duff, G. Green, G. Mellado A. Schmidt, R. Worley, R. , and S. Rebeccah. Nociceptive brain activity as a measure of analgesic efficacy in infants. *Science Translational Medicine*, 9(388), 2017.

[212] Y. Hada. Latency differences of N20, P40/N60, P100/N140 SEP components after stimulation of proximal and distal sites of the median nerve. *Clin EEG Neurosci*, 37(1), 2006.

[213] W. Y. Ong, C. S. StohlerDeron, and R. H. Deron. Role of the prefrontal cortex in pain processing. *Molecular Neurobiology*, 2(56), 2019.

[214] R. D. Treede J. K. Zubieta A. V. Apkarian, M. C. Bushnell. Human brain mechanisms of pain perception and regulation in health and disease. *Pain*, 9(4), 2005.

[215] Y. Oshiro, A.S. Quevedo, J.G. McHaffie, and R.A. Kraft R.C. Coghill. Brain mechanisms supporting discrimination of sensory features of pain: a new model. *J. Neurosci*, 29(47), 2009.

[216] A. Gouzien, F. de Vignemont, A. Touillet, N. Martinet, J. Graaf, N. Jarrasse, and A. Roby-Brami. Reachability and the sense of embodiment in amputees using prostheses. *Scientific Reports*, 7:4999, 2017.

[217] P. R. Troyk and S. F. Cogan. *Sensory Neural Prostheses*, pages 1–48. Springer US, Boston, MA, 2005.

[218] H. Nguyen, L. Osborn, M. Iskarous, C. Shallal, C. Hunt, J. Betthauser, and N.V Thakor. Dynamic texture decoding using a neuromorphic multilayer tactile sensor. pages 1–4, 2018.

[219] A. Gramfort, M. Luessi, E. Larson, D. Engemann, D. Strohmeier, C. Brodbeck, L. Parkkonen, and M. Hämäläinen. MNE software for processing MEG and EEG data. *NeuroImage*, 86, 2014.

[220] A. Gramfort, M. Luessi, E. Larson, D. Engemann, D. Strohmeier, C. Brodbeck, R. Goj, M. Jas, T. Brooks, L. Parkkonen, and M. Hämäläinen. MEG and EEG data analysis with MNE-Python. *Frontiers in Neuroscience*, 7, 2013.

[221] L. Pion-Tonachini, S. Hsu, C. Chang, T. Jung, and S. Makeig. Online automatic artifact rejection using the real-time EEG source-mapping toolbox (REST). In *2018 40th Annual International Conference of the IEEE Engineering in Medicine and Biology Society (EMBC)*, pages 106–109, 2018.

[222] T. Radüntz, J. Scouten, O. Hochmuth, and B. Meffert. EEG artifact elimination by extraction of ICA-component features using image processing algorithms. *Journal of Neuroscience Methods*, 243:84 – 93, 2015.

[223] D. Brunet, M. Murray, and C. Michel. Spatiotemporal analysis of multichannel EEG: Cartool. *Computational intelligence and neuroscience*, 2011:813870, 2011.

[224] W. Skrandies. Global field power and topographic similarity. *Brain Topogr*, 3(1):137–41, 1990.

[225] Fischl W, B. D.H. Salat, E. Busa, M. Dieterich M. Albert, C. Haselgrove, A. van der Kouwe, R. Killiany, D. Kennedy, S. Klaveness, A. Montillo, N. Makris, B. Rosen, and A.M. Dale. hole brain segmentation: Automated labeling of neuroanatomical structures in the human brain. *Neuron*, 97(33), 2002.

[226] A. M. Dale, A. K. Liu, B. R. Fischl, R. L. Buckner, J. W. Belliveau, J. D. Lewine, and E. Halgren. Dynamic statistical parametric mapping: Combining fMRI and MEG for high-resolution imaging of cortical activity. *Neuron*, 26(1):55 – 67, 2000.

[227] Anders M. D., Bruce F., and M. I. Sereno. Cortical surface-based analysis: I. segmentation and surface reconstruction. *NeuroImage*, 9(2):179 – 194, 1999.

[228] J. T. Nenonen, M. S. Hämäläinen, and R. J. Ilmoniemi. Minimum-norm estimation in a boundary-element torso model. *Medical and Biological Engineering and Computing*, 32(1):43–48, 1994.

[229] I. Strauss, G. Valle, F. Artoni, E. D'Anna, G. Granata, R. Iorio, D. Guiraud, Stieglitz, P Rossini, Stanisa Raspopovic, Francesco Petrini, and Silvestro Micera. Characterization of multi-channel intraneural stimulation in transradial amputees. *Scientific Reports*, 9:19258, 2019.

[230] O. K. A. Nanna, B. F. Erika, G. S. Troels, and S. J. Nielsen. Expansion of nociceptive withdrawal reflex receptive fields in spinal cord injured humans. *Clinical Neurophysiology*, 115(12):2798–2810, 2004.

[231] M. Seeber, L. M. Cantonas, M. Hoevels, T. Sesia, V. V. Vandewalle, and C. M. Michel. Subcortical electrophysiological activity is detectable with high-density EEG source imaging. *Nature Communications*, 10(753), 2019.

[232] C. M. Michel and M. M. Murray. Towards the utilization of EEG as a brain imaging tool. *Neuroimage*, 61(753), 2012.

[233] C. M. et al. Michel. EEG source imaging. *Neurophysiol*, 10(753), 2004.

[234] G. et al. Birot. Head model and electrical source imaging: A study of 38 epileptic patients. *NeuroImage: Clin*, 5, 2014.

[235] C. E. Chapman, M. C. Bushnell, D. Miron, G. H. Duncan, and J. P. Lund. Sensory perception during movement in man. *Experimental Brain Research*, 68(3):516–524, 1987.

[236] R. Peyron, L. G. L., M. C. Grégoire, N. Costes, P. Convers, F. Lavenne, F. Mauguière, D. Michel, and B. Laurent. Haemodynamic brain responses to acute pain in humans: Sensory and attentional networks. *Brain*, 122(9):1765–1780, 1999.

[237] O. Hauk, D. Wakeman, and R. Henson. Comparison of noise-normalized minimum norm estimates for MEG analysis using multiple resolution metrics. *NeuroImage*, 54(3):1966–1974, 2010.

[238] F. Wei and M. Zhuo. Potentiation of synaptic responses in the anterior cingulate cortex following digital amputation in rat. *The Journal of physiology*, 532:823–833, 2001.

[239] A. Mouraux, G. D. Iannetti, E. Colon, S. Nozaradan, V. Legrain, and L. Plaghki. Nociceptive steady-state evoked potentials elicited by rapid periodic thermal stimulation of cutaneous nociceptors. *Journal of Neuroscience*, 31(16):6079–6087, 2011.

[240] E. Colon, V. Legrain, and A. Mouraux. EEG frequency tagging to dissociate the cortical responses to nociceptive and nonnociceptive stimuli. *Journal of cognitive neuroscience*, 26(10):2262–2274, 2014.

[241] Bianca A. S., Cornelius T. G., and Johannes G. The neural circuits of innate fear: detection, integration, action, and memorization. *Learning memory*, 23(10):544–555, 2016.

[242] C. Woo, L. Schmidt, A. Krishnan, M. Jepma, Mathieu Roy, M. Lindquist, L. Atlas, and T. Wager. Quantifying cerebral contributions to pain beyond nociception. *Nature Communications*, 8:14211, 2017.

[243] A. K. Bräscher, S. Becker, M. E. Hoeppli, and P. Schweinhardt. Different brain circuitries mediating controllable and uncontrollable pain. *Journal of Neuroscience*, 36(18):5013–5025, 2016.

[244] G. Misra, W. E. Wang, D. Archer, A. Roy, and S. Coombes. Automated classification of pain perception using high density electroencephalography data. *Journal of neurophysiology*, 117(2):786–795, 2016.

[245] A. Chen and P. Rappelsberger. Brain and human pain: Topographic EEG amplitude and coherence mapping. *Brain Topography*, 7(2):129–140, 2005.

[246] L. Hu, M. Cai, P. Xiao, F. Luo, and G. Iannetti. Human brain responses to concomitant stimulation of a and c nociceptors. *The Journal of Neuroscience*, 34(34):11439–11451, 2014.

[247] A. Bandla, R. Sundar, L. D. Liao, S. Tan, S. C. Lee, N. Thakor, and E. Wilder-Smith. Hypothermia for preventing chemotherapy-induced neuropathy - a pilot study on safety and tolerability in healthy controls. *Acta oncologica (Stockholm, Sweden)*, 55(4):1–7, 2015.

[248] J. Lancaster, H. Mano, D. Callan, M. Kawato, and B. Seymour. Decoding acute pain with combined EEG and physiological data. pages 521–524, 2017.

[249] Peng F. C., Lars A.N., and A. C.N Chen. Dynamic changes and spatial correlation of EEG activities during cold pressor test in man. *Brain Research Bulletin*, 57(5):667 – 675, 2002.

[250] S. Marchesotti, M. Bassolino, A. Serino, H. Bleuler, and O. Blanke. Quantifying the role of motor imagery in brain-machine interfaces. *Scientific Reports*, 6:24076, 2016.

[251] V. van Veen, J. D. Cohen, M. M. Botvinick, V. A. Stenger, and C. S. Carter. Anterior cingulate cortex, conflict monitoring, and levels of processing. *NeuroImage*, 14(6):1302 – 1308, 2001.

[252] E. Yildirim, B. Güntekin, L. Hanoglu, and C. Algun. EEG alpha activity increased in response to transcutaneous electrical nervous stimulation in young healthy subjects but not in the healthy elderly. *PeerJ*, 8:e8330, 2020.

[253] Z. Tayeb, R. Bose, A. Dragomir, L. Osborn, N.V. Thakor, and G. Cheng. Decoding of pain perception using EEG signals for a real-time reflex system in prostheses: A case study. *Scientific Reports*, 10:5606, 2020.

[254] A. I. Basbaum. Chapter 3 - basic mechanisms. In Charles E. A. and Gary M., editors, *Pain Management Secrets (Third Edition)*, pages 19 – 26. Mosby, Philadelphia, third edition edition, 2009.

[255] M. Yam, L. Yean Chun, C. S. Tan, S. K. Adam, N. Manan, and R. Basir. General pathways of pain sensation and the major neurotransmitters involved in pain regulation. *International Journal of Molecular Sciences*, 19(8):2164, 2018.

[256] A. F. et al. DaSilva. Colocalized structural and functional changes in the cortex of patients with trigeminal neuropathic pain. *PloS one*, 3(10):e3396, 2008.

[257] A. Craig, E. Reiman, A. Evans, and M. Bushnell. Functional imaging of an illusion of pain. *Nature*, 384(6606):258–260, 1996.

[258] B. Vogt, S. Derbyshire, and A. Jones. Pain processing in four regions of human cingulate cortex localized with co-registered PET and mr imaging. *The European journal of neuroscience*, 8(7):1461–1473, 1996.

[259] D. Le Pera, P. Svensson, M. Valeriani, I. Watanabe, L. A.Nielsen, and A. C.N Chen. Long-lasting effect evoked by tonic muscle pain on parietal EEG activity in humans. *Clinical Neurophysiology*, 111(12):2130 – 2137, 2000.

[260] W. W. Seeley. The salience network: A neural system for perceiving and responding to homeostatic demands. 39(50):9878–9882, 2019.

[261] Yasunori K., Y. Ohgami, N. Yoshida, S. Kiryu, and Y. Inoue. Anticipation process of the human brain measured by stimulus-preceding negativity (SPN). *The Journal of Physical Fitness and Sports Medicine*, 6(1):7–14, 2017.

[262] K. Carlsson, P. Petrovic, S. Skare, K. Magnus Petersson, and M. Ingvar. Tickling expectations: Neural processing in anticipation of a sensory stimulus. *Journal of cognitive neuroscience*, 12(4):691–703, 2000.

[263] I. Tracey, L. Becerra, I. Chang, H. Breiter, L. Jenkins, D. Borsook, and R.G. González. Noxious hot and cold stimulation produce common patterns of brain activation in humans: A functional magnetic resonance imaging study. *Neuroscience letters*, 288(2):159–162, 2000.

[264] W. Y. Ong, C. Stohler, and D. Herr. Role of the prefrontal cortex in pain processing. *Molecular Neurobiology*, 56(2), 2018.

[265] Y. Li, J. Pan, F. Wang, and Z. Yu. A hybrid BCI system combining P300 and SSVEP and its application to wheelchair control. *IEEE Transactions on Biomedical Engineering*, 60(11):3156–3166, 2013.

[266] D. J. McFarland, W. A. Sarnacki, and J. R. Wolpaw. Electroencephalographic (EEG) control of three-dimensional movement. *Journal of Neural Engineering*, 7(3):036007, 2010.

[267] F. Lotte, L. Bougrain, A. Cichocki, M. Clerc, M. Congedo, A. Rakotomamonjy, and F. Yger. A review of classification algorithms for EEG-based brain-computer interfaces: a 10 year update. *Journal of Neural Engineering*, 15(3):031005, 2018.

[268] Y. Rezaei Tabar and U. Halici. A novel deep learning approach for classification of EEG motor imagery signals. *Journal of Neural Engineering*, 14(1):016003, 2017.

[269] R. Ramadan and A. Vasilakos. Brain-computer interface: Control signals review. 223, 2016.

[270] C. A. Kothe and S. Makeig. BCILAB: a platform for brain-computer interface development. *Journal of Neural Engineering*, 10(5):056014, 2013.

[271] A. Delorme and S. Makeig. EEGLAB: an open source toolbox for analysis of single-trial EEG dynamics. *Journal of Neuroscience Methods*, 134(1):9–21, 2004.

[272] G. Schalk, D. J. McFarland, T. Hinterberger, N. Birbaumer, and J. R. Wolpaw. BCI2000: a general-purpose brain-computer interface (BCI) system. *IEEE Transactions on Biomedical Engineering*, 51(6):1034–1043, 2004.

[273] S. V. Walt, S. C. Colbert, and G. Varoquaux. The NumPy array: A structure for efficient numerical computation. *Computing in Science Engineering*, 13(2):20–23, 2011.

[274] E. Jones, T. Oliphant, P. Peterson, et al. SciPy: Open source scientific tools for Python, 2001–. [Online; accessed: 2017-08-03].

[275] F. Pedregosa, G. Varoquaux, A. Gramfort, V. Michel, B. Thirion, M. Blondel O. Grisel, P. Prettenhofer, V. Dubourg R. Weiss, A. Passos J. Vanderplas, D. Cournapeau, M. Brucher, M. Perrot, and Édouard Duchesnay. Scikit-learn: Machine learning in Python. *Journal of Machine Learning Research*, 12:2825–2830, 2011.

[276] V. Bastian, D. Sven, H. Johannes, H. Hendrik, and B. Benjamin. Wyrm: A brain-computer interface toolbox in Python. *Neuroinformatics*, 13(4):471–486, 2015.

[277] B. Venthur, S. Scholler, J. Williamson, S. Dahne, M. Treder, M. Kramarek, K. Múller, and B. Blankertz. Pyff—a pythonic framework for feedback applications and stimulus presentation in neuroscience. *Frontiers in Neuroscience*, 4:179, 2010.

[278] Y. Renard, F. Lotte, G. Gibert, M. Congedo, E. Maby, V. Delannoy, O. Bertrand, and A. Lécuyer. OpenViBE: An open-source software platform to design, test, and use brain-computer interfaces in real and virtual environments. *Presence*, 19(1):35–53, 2010.

[279] J. Sauvan, A. Lécuyer, F. Lotte, and G. Casiez. A performance model of selection techniques for P300-based brain-computer interfaces. pages 2205–2208, 2009.

[280] Y. Li, J. Long, T. Yu, Z. Yu, C. Wang, H. Zhang, and C. Guan. An EEG-based BCI system for 2-d cursor control by combining Mu/Beta rhythm and P300 potential. *IEEE Transactions on Biomedical Engineering*, 57(10):2495–2505, 2010.

[281] Y. Wang, X. Gao, B. Hong, C. Jia, and S. Gao. Brain-computer interfaces based on visual evoked potentials. *IEEE Engineering in Medicine and Biology Magazine*, 27(5):64–71, 2008.

[282] Pygame, [Online; accessed 2017-05-05]. `Available:https://www.pygame.org/`.

[283] K. K. Ang, Z. Y. Chin, H. Zhang, and C. Guan. Filter bank common spatial pattern (FBCSP) in brain-computer interface. In *Neural Networks, 2008. IJCNN 2008.(IEEE World Congress on Computational Intelligence). IEEE International Joint Conference on*, pages 2390–2397. IEEE, 2008.

[284] M. Li, M. Zhang, X. Luo, and J. Yang. Combined long short-term memory based network employing wavelet coefficients for MI-EEG recognition. In *2016 IEEE International Conference on Mechatronics and Automation*, pages 1971–1976, 2016.

[285] E. Biddiss and T. Chau. The roles of predisposing characteristics, established need and enabling resources on upper extremity prosthesis use and abandonment. *Disability and Rehabilitation: Assistive Technology*, pages 71–84, 2009.

A Gumpy software technology for Hybrid brain-computer interfaces

This appendix chapter is made up of content adapted with permissions from the manuscript Zied Tayeb, Nicolai Waniek, Juri Fedjaev, Nejla Ghaboosi, Leonard Rychly, Christian Widderich, Christoph Richter, Jonas Braun, Matteo Saveriano, Gordon Cheng, Joerg Conradt, "Gumpy: A Python toolbox suitable for hybrid brain–computer interfaces" Published in Journal of Neural Engineering, 15 (6), (2018). DOI: `https://iopscience.iop.org/article/10.1088/1741-2552/aae186/meta`

My main contributions as first author: designed and implemented the majority of gumpy modules, prepared the figures and wrote the manuscript. Nicolai Waniek revised the software and improved its main functions and features, as well as co-wrote the paper. Juri Fedjaev, Nejla Ghaboosi, Leonard Rychly, and Christian Widderich assisted in developing the software code for the deep learning module. Jonas Braun and Matteo Saveriano assisted in developing the software code for the hybrid experiment. Christoph Richter, Gordon Cheng, and Jörg Conradt supervised this work and assisted in writing the manuscript.

A.1 Overview

Objective. The objective of this work is to present *gumpy*, a new free and open source Python toolbox designed for hybrid brain-computer interface (BCI). **Approach**. Gumpy provides state-of-the-art algorithms and includes a rich selection of signal processing methods that have been employed by the BCI community over the last 20 years. In addition, a wide range of classification methods that span from classical machine learning algorithms to deep neural network models are provided. Gumpy can be used for both EEG and EMG biosignal analysis, visualization, real-time streaming and decoding. **Results**. The usage of the toolbox was demonstrated through two different offline example studies, namely movement

prediction from EEG motor imagery, and the decoding of natural grasp movements with the applied finger forces from surface EMG (sEMG) signals. Additionally, *gumpy* was used for real-time control of a robot arm using steady-state visually evoked potentials (SSVEP) as well as for real-time prosthetic hand control using sEMG. Overall, obtained results with the *gumpy* toolbox are comparable or better than previously reported results on the same datasets. **Significance**. Gumpy is a free and open source software, which allows end-users to perform online hybrid BCIs and provides different techniques for processing and decoding of EEG and EMG signals. More importantly, the achieved results reveal that *gumpy*'s deep learning toolbox can match or outperform the state-of-the-art in terms of accuracy. This can therefore enable BCI researchers to develop more robust decoding algorithms using novel techniques and hence chart a route ahead for new BCI improvements.

A.2 Introduction

Paralyzed people wish to control assistive devices such as wheelchairs, spellers, prosthetics, or exoskeletons in order to improve their quality of life and ensure their independence [192]. One way to infer their desired actions is to measure their cortical activity, for instance by functional magnetic resonance imaging (fMRI), magnetoencephalography (MEG), electrocorticography (ECoG), or electroencephalography (EEG) and subsequently decode the intended movement from the measurements. Of these methods, EEG has become the most frequently used technique for BCIs, because it is non-invasive and comparably inexpensive. Although BCI technology has seen improvements over the last few years [3, 18], it still lacks reliability and accuracy. Hybrid BCIs in general [265], and particularly those which combine EEG and EMG signals are promising improvements [182]. Despite the successful multi-dimensional EEG-based BCI control achieved using simple classifiers [266, 18], reliable decoding of complex movements from brain signals is still challenging and requires advanced algorithms [267]. Recent developed techniques such as deep neural networks [268] could represent a promising solution to develop more robust decoding algorithms [267]. In order to make such algorithms readily available to a wide BCI community we developed *gumpy*, a Python library along with well documented application examples that we introduce in this paper. Gumpy is an easy-to-use, robust, and powerful software package for EEG and EMG signal analysis and decoding that tightly incorporates different recording paradigms, essential signal processing techniques, and state-of-the-art machine learning algorithms. Gumpy can be used for offline as well as for online processing of electrophysiological signals. Several similar BCI software packages exist and are widely used by the community [269]. Gumpy is free of charge, permissively licensed and written in Python, an open source

programming language that is not only backed by an extensive standard library, but also by vast scientific computing libraries. Moreover, it is widely used by many machine learning experts, engineers and neuroscientists. Gumpy offers users the opportunity to reproduce achieved results previously by other BCI researchers through implementing a wide range of signal processing and classification methods for time series signal analysis. Furthermore, the toolbox features several deep learning models such as deep convolutional neural networks (CNN) [130], recurrent convolutional neural networks (RCNN) and Long Short-Term Memory (LSTM) [129]. Those approaches have hitherto been rarely investigated by BCI researchers [73] and to the best of our knowledge no existing BCI software integrates similar techniques. This paper introduces the basic concept of *gumpy*, its main features and three successful BCI applications.

A.2.1 Related work on software frameworks for BCI

This section provides an overview of the most widely-used open source BCI platforms for research and highlights the distinctive features of gumpy with respect to them. Table 1 summarizes their main functions and limitations. References [269, 8] provide a more comprehensive survey. The discussion focuses on a particular feature set that we deem essential for the successful development of future hybrid BCI systems.

A.2.1.1 BCILAB

BCILAB [270] is among the earliest publicly available BCI software packages for research purposes. It is a free, open source toolbox developed in Matlab. BCILAB is built to emulate the plugin concept where various components can be added ”on the fly” during the runtime. BCILAB was designed as an extension of EEGLAB [271] to support both offline and online analysis of electrophysiological signals. Besides various feature extraction methods and experimental paradigms supported by the toolbox, an end-user can choose between three different classifiers (Linear Discriminant Analysis (LDA), Quadratic Discriminant Analysis (QDA) and Support Vector Machine (SVM)). In addition, BCILAB obliges users to design their scripts in Matlab [270].

A.2.1.2 BCI2000

BCI2000 [272] is an open source and free of charge BCI software package developed in 2000 to advance real-time BCI systems. It includes different modules such as data acquisition, signal processing and stimulus presentation. The toolbox is written in C++ and does

not directly support other programming languages such as Matlab or Python, so in this regard it is difficult to extend and integrate with other toolboxes. Furthermore, some important processing methods such as discrete wavelet transform and some classification techniques such as deep learning are not included [272].

A.2.1.3 MNE

MNE is an open source python package for MEG/EEG data analysis. MNE implements a wide range of functions for time-frequency analysis and connectivity estimation as well as simple decoding algorithms [220]. Similar to *gumpy*, it is built on top of widely used scientific computing libraries such as Numpy [273], Scipy [274], pandas and Scikit-learn [275]. Moreover, MNE offers functions for neuroimaging data interpretation such as fMRI analysis. Despite recent developments, the toolbox still lacks some important functions and methods, such as common spatial pattern algorithm (CSP) [62] and various popular machine learning classifiers.

A.2.1.4 Wyrm

Wyrm [276] is an open source BCI package written in Python. The toolbox implements several functions for processing and visualization of electrophysiological data such as EEG and ECoG signals. Moreover, Wyrm is suitable for both offline processing and real-time applications. Furthermore, the toolbox integrates Mushu [187] a free software for signals acquisition, and Pyff [277], which is a framework for BCI feedback applications.

A.2.1.5 OpenViBE

OpenViBE [278], another open source BCI platform, is designed in a modular fashion and incorporates an elegant graphical user interface for novice users. Moreover, it provides a wide range of signal processing techniques and supports many acquisition and BCI paradigms such as P300 [279, 280] and SSVEP [281]. One of OpenViBE's advantages with respect to the previously mentioned toolboxes is that it can be scripted using both LUA and Python. In addition, it offers a direct interface to Matlab. OpenViBE currently provides three classifiers: LDA, SVM as well as a combined classifier for a multi-class problem classification.

A.2.2 Distinctive features of *gumpy*

Despite the tremendous number of features that current BCI toolboxes offer, they still exhibit some limitations [8] such as lack of important processing and classification methods,

Table A.1: General Overview of Existing BCI toolboxes.

Software platform	Programming language	Features
BCILAB Well-designed GUI	Matlab	Wide range of algorithms
BCI2000 Wide usage by BCI community Modular programming	C++	Simple and Robust
MNE Good documentation	Python	EEG, MEG and fMRI data analysis
Wyrm Real-time capabilities Integration with other platforms	Python	EEG and ECoG signals
OpenViBE Supports many acquisition devices	LUA, Python	Modular API
Gumpy Real-time capabilities Offline and online analyses Deep learning toolbox	Python	Hybrid BCI

limited real-time performance, lack of recording experimental paradigms to conduct online BCI experiments and more importantly, none of the existing packages combine classic machine learning algorithms and deep learning techniques for signals decoding. However, *gumpy* covers a wide range of classification methods including several machine learning classifiers, voting classifiers, feature selection algorithms and different deep learning architectures such as LSTM, CNN and RCNN. Additionally, we provide many showcase examples of the usage of *gumpy* for EEG and EMG signals decoding, thereby facilitating the design of hybrid BCI systems. Furthermore, *gumpy* integrates different experimental paradigms for motor imagery, EMG, SSVEP, EEG reach-to-grasp movements recording and for the hybrid BCI, which they can be easily used and extended by end-users. Importantly, *gumpy* supports offline analysis as well as online BCI applications. With the lab streaming layer (LSL) [159] for data acquisition, the provided experimental paradigms for biosignals recording and *gumpy* package for EEG and EMG data processing and decoding, we envision *gumpy* to be a suitable toolkit for conducting online hybrid BCI experiments.

A.3 Gumpy toolbox: design, main functions and features

A.3.1 General overview of *gumpy*'s modules

Gumpy comprises six modules for plotting, processing and classification of EEG and EMG signals. Moreover, *gumpy* incorporates different deep learning models and experimental recording paradigms. This section provides a condensed overview of *gumpy*'s modules

and its main functionality which are summarized in Figure A.1. Some of the modules are described in more details in the following section on exemplary use-cases. Particularly, section 3.3 covers the available deep learning classifiers. Where possible, *gumpy* leverages existing and well established scientific and numerical libraries such as numpy [273], scipy [274] and scikit-learn [275] to compute the classification results or to perform signal analysis. For instance, *gumpy*'s SVM classifier utilizes scikit-learn. However, *gumpy* preconfigures its classifiers with default parameters that were found to be suitable in typical BCI applications. In addition, *gumpy* can perform a grid search to tune their settings. One of *gumpy*'s core design principles is to allow users to easily extend its functionality, thereby facilitating usability, customizability and collaborative development. The latter is further enabled using our public git repository at https://github.com/gumpy-hybridBCI through which we solicit the community to contribute feedback and code. In addition, the website http://gumpy.org/ provides an API reference and usage examples in the form of Jupyter notebooks.

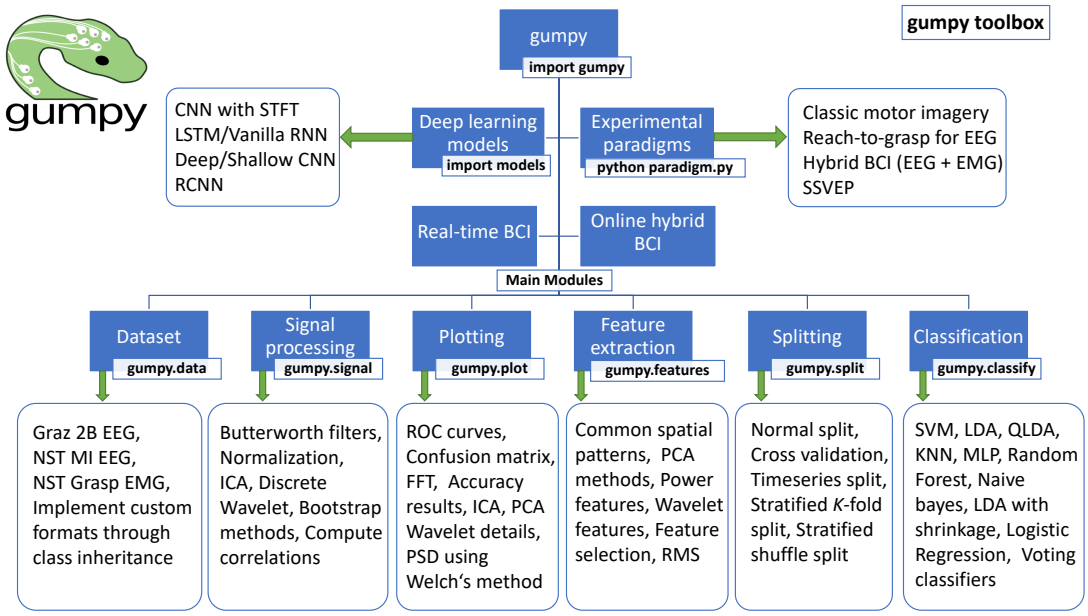

Figure A.1: Overview of *gumpy* toolbox modules and functions.

A.3.2 Gumpy's experimental paradigms

A.3.2.1 Classic motor imagery movements

Gumpy provides a cue-based screening paradigm to record classic motor imagery; namely

the imagination of the movement of left hand, right hand or both hands. At predefined times, a cue in the form of an arrow pointing is displayed on the screen either on the left, right or on both sides (both hands) and the participant has to perform a hand movement imagination as the cue was displayed.

A.3.2.2 Reach-to-grasp motor imagery movements

Gumpy incorporates a paradigm to record EEG reach-to-grasp movements imagination of six different objects placed on a shelf with fixed positions as shown in Figure A.2. The subject is asked to imagine reach movement by bringing the cursor (square) toward one of the six center-out target locations (up-left, up-right, center-left, center-right, down-left, down-right). Once the square hits the target, it turns red which triggers the participant to now imagine performing a grasping movement on that specific target.

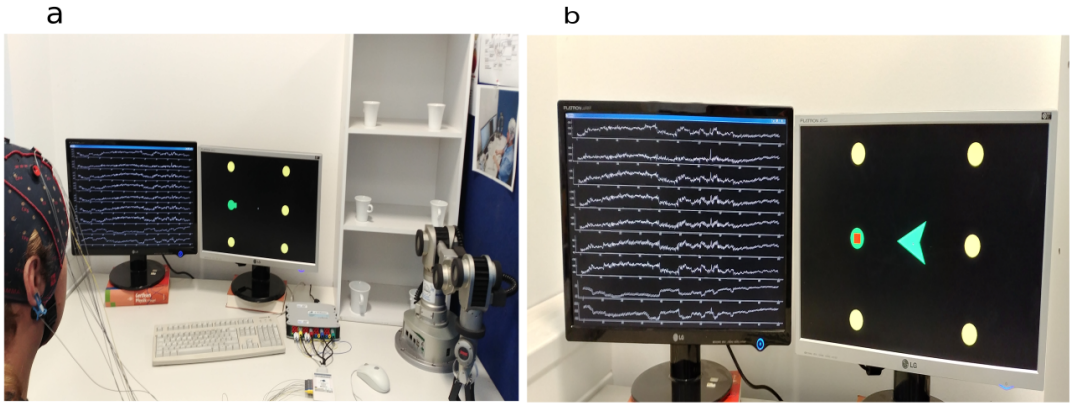

Figure A.2: Illustration of recording paradigm for reach-to-grasp movements. (a) Display requests subject to imaginatively reach for the mid-left cup in the shelf. (b) Subject is requested to imagine grasping the center-right cup.

A.3.2.3 Grasp poses and related finger forces from surface EMG signals

A special experimental paradigm was designed to record sEMG signals from the forearm during four different hand movements (2-digit grasp, 3-digit grasp, fist, hand open) as shown in Figure A.2 with two possible force levels (high, low). Strain gauge sensors placed on the fingertips measured the applied grasping force [195].

A.3.2.4 Gumpy-SSVEP paradigm

The SSVEP paradigm consists of four flickering checkerboards blinking at different frequencies (13, 15, 17 and 19 Hz), as shown in Figure A.3. The subject has to focus on one of the flickering checkerboards in order to evoke an SSVEP response. Simultaneously, EEG signals recording from O1, OZ and O2 electrodes were performed. The paradigm was implemented using PyGame [282], a gaming-oriented Python library for graphical user interfaces.

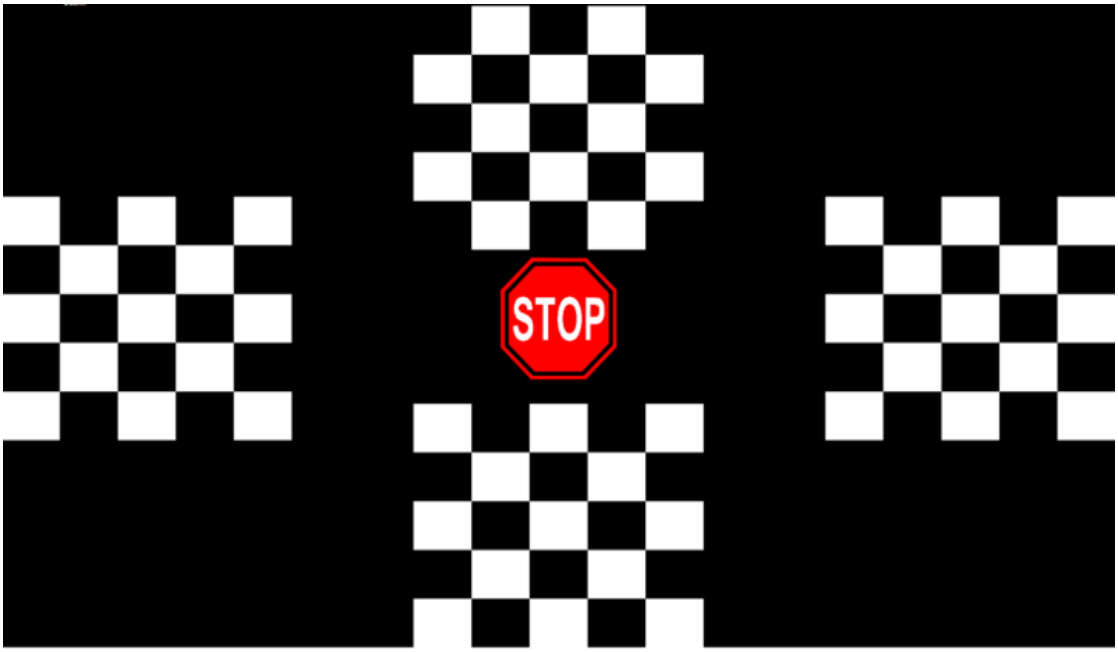

Figure A.3: Illustration of the recording paradigm for SSVEP.

A.3.2.5 Gumpy's experimental paradigm for real-time hybrid BCI

The hybrid BCI paradigm allows end users to perform online hybrid BCI experiments. For instance, this paradigm was used to perform a sequential hybrid BCI task, where the subject was asked to imagine left or right hand movement imagination and execute thereafter the same imagined movement. For that, a simultaneous recording of EEG and sEMG signals was performed using two synchronized g.USBamp devices. Signals were sampled at 512 Hz and the LSL was used for data acquisition in a master-slave communication fashion. It should be noted that the developed paradigm could be used to simultaneously collect

data from other devices (e.g. Myo armband [203] and the g.USBamp) and could be easily modified to acquire other types of biosignals. A detailed documentation of the hybrid paradigm as well as the developed code are made publicly available withing *gumpy* under https://github.com/gumpy-hybridBCI/hybrid-BCI.

A.3.3 Gumpy's deep learning module

Despite the numerous successful applications of deep neural networks [130], the development of deep learning methods in the BCI field is still quite rare [73]. The toolbox has a deep learning module, which is based on Theano [147] and Keras [148], as well as different implemented and available network architectures.

A.4 Case studies

In this section, we show how to use *gumpy* to perform offline analysis of EEG/EMG data as well as how to conduct online BCI experiments. As a result, researchers can easily reproduce the obtained results using our provided *gumpy*'s Jupyter notebooks, our freely available EEG/EMG recorded data or the EEG dataset 2b from BCI competition [144] as well as *gumpy*'s available experimental paradigms.

A.4.1 Offline analysis

A.4.1.1 Decoding of two motor imagery movements from EEG signals using Graz 2b dataset

We used *gumpy*'s signal and classification developed modules to process and classify an existing EEG dataset known as 2b EEG dataset from "BCI Competition IV" [144]. The source code utilized in these offline examples are freely available as Jupyter notebooks document under http://gumpy.org/.

a) **First approach: Standard Machine learning techniques with band power features**
In this section, three feature extraction methods, i.e. logarithmic band power (BP) [156], common spatial patterns (CSP) [157, 283] and discrete wavelet transform [284], have been investigated and tested. In general, CSP features maximize the pairwise compound variance between two or more classes in the least square sense, whereas wavelet features provide an effective time-frequency representation of non-stationary signals [158]. We wish to emphasize that those feature extraction methods have been advocated by BCI researchers in [267]. After extracting discriminative features, `gumpy.features.sequential_feature_selector`

was used to automatically select a subset of features in the feature space using the sequential feature selection algorithm (SFSF) [35]. The `gumpy.split` module provides several methods for splitting data. Herein, we used the hold-out strategy by splitting the dataset into 80% for training and 20% for test using the `gumpy.split` module. A 10-fold cross validation was performed on the training set to select the best features using six different classifiers from the `gumpy.classification` module. Afterwards, the new generated subsets based on the selected features were fed into each classifier and new predictions were made on the testing dataset. Furthermore, we wish to mention that the classification module incorporates a voting classifier, which employs an ensemble of classifiers to "vote" using their respective results. Finally, it should be noted that `gumpy.classification` can also perform a grid search to select the best hyper parameters for SVM and random forest classifiers for a given k-fold cross validation. Noticeably, BP slightly outperforms the other two feature extraction methods and provides overall better results across the different nine subjects. The obtained classification results with the BP feature extraction method with six different algorithms including the voting classifier are shown below in Figure A.4. Overall, the obtained results from

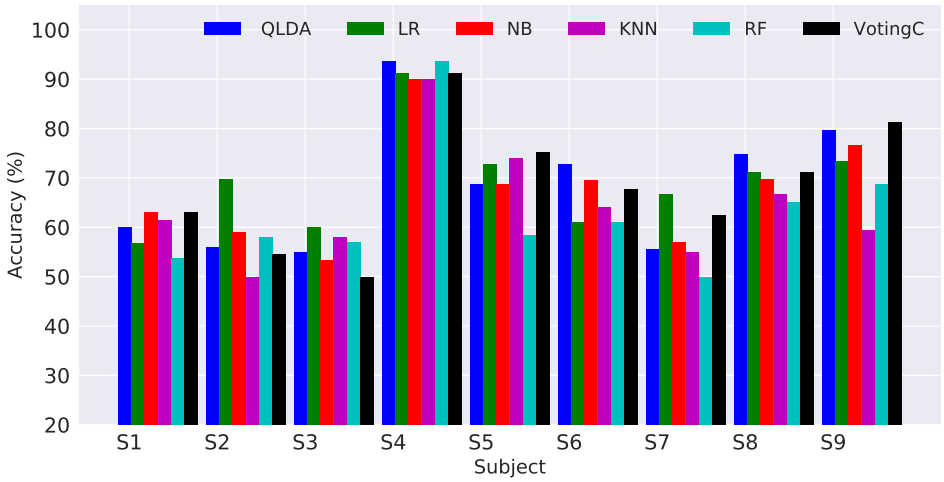

Figure A.4: Accuracy results obtained for individual participants using the BP features and six different machine learning classifiers, namely quadratic LDA (QLDA), logistic regression (LR), naive bayes (NB), k-nearest neighbors (KNN), random forest (RF) and the voting classifier (VotingC).

individual subjects show inter- and intra-subject variability. According to their performance, the nine participants could be classified into three categories: Bad participants are S1, S2, S3 and S7 with a classification accuracy between 60 to 70%, good participants are S5, S6, S8 and S9 with a classification accuracy between 70 to 82%, and an excellent participant

S4 with an average classification accuracy of 93.75%. It is worth noting that a comparable performance was obtained with the CSP features. A Jupyter notebook showing how to use the three different feature extraction methods with the different available classifiers, is made publicly available under https://github.com/gumpy-hybridBCI.

A.4.1.2 Decoding of natural grasps from surface EMG signals

Making a prosthetic hand grasp an object precisely and effortlessly is a crucial step in prostheses design [285]. Additionally, dexterous grasping of objects with different shapes and sizes seems to be a big challenge in today's prostheses. In this section, we demonstrate the usage of *gumpy* to classify four movements (Fist grasp, 2-digit grasp, 3-digit grasp, hand open) with two different force levels (low, high). Data used in this example study were recorded at our lab and are made publicly available at *gumpy*'s website. Different steps for EMG processing using *gumpy* are described below. **Filtering:** EMG signals were band-pass filtered between 20 and 255 Hz and notch filtered at 50 Hz using the `gumpy.signal` module. Feature extraction and normalization: Filtered EMG signals were analyzed using 200 ms sliding time windows with 50 ms overlapping [23]. The length of the sliding window was chosen for the purpose of allowing real-time control. For each interval, the computed mean of the signal was subtracted and divided by the standard deviation. Besides, the resulting EMG signals were normalized by the maximum voluntary isometric contraction (MVIC) magnitude. Thereafter, the root mean square (RMS) was computed in each time window and fed into the classifier. We wish to stress that we used the same feature extraction method to classify each type of the associated force level (low, high). **Feature selection:** Herein, the SFFS algorithm was used to select a certain number of features in the k range (10, 25). **Classification:** Different classifiers were used to predict one of four possible hand poses and one of the two force levels. Offline results using SVM with 3-fold stratified cross validation are illustrated in Figure A.5. Obtained prediction results during the real-time test, are presented in the next section. The validation accuracy for three different subjects were 82% ($\pm 4\%$) for posture classification and 96% ($\pm 3\%$) for force classification. It should be noted that those results were obtained after performing three-fold cross validation using *gumpy*'s validation module.

A.4.2 Gumpy for real-time brain-computer interfacing

Aside of the offline capabilities, *gumpy* can be used in an online fashion to perform real-time experiments such as robot arm control using SSVEP, online EMG decoding and real-time

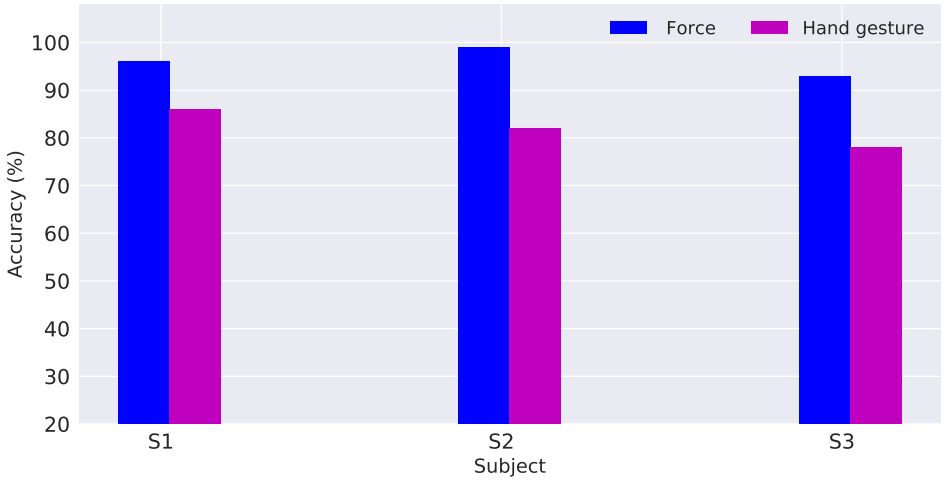

Figure A.5: Obtained results for hand posture and force classification with 3-fold cross-validation.

control of robot control using EEG signals. All the real-time *gumpy* case studies as well as the developed real-time experimental paradigms are made available under https://github.com/gumpy-hybridBCI/gumpy-Realtime. Importantly, these case studies can be easily modified or extended by *gumpy* end-users to suit their specific applications.

A.4.2.1 Real-time Robot Arm Control using SSVEP-based BCI

In this section, we further test and validate *gumpy*'s real-time capabilities by online detection and classification of SSVEP signals for a robot arm control. SSVEP are brain events measured after a visual flickering stimulation of a frequency between 3.5 Hz and 75 Hz. They appear as a peak in the frequency spectrum of the EEG signals recorded over the primary visual cortex at the respective stimulus frequency [281]. The *gumpy* SSVEP paradigm described previously in section A.3.2.4 was used for data recording. During the live experiment, the subject had to focus on one of the four displayed checkerboards flickering at different frequencies. Power spectral density (PSD) features from the electrodes (O1, O2 and Oz) over the occipital lobe were extracted, normalized and a principal component analysis (PCA) was performed to reduce the dimensionality. A random forest classifier was trained offline on recorded data collected from four different subjects (3 males, 1 female). A 5-fold stratified cross validation was performed to evaluate model performance and to tune hyper-parameters. Afterwards, the trained random forest classifier was used in the testing

phase to perform an online classification, where new predictions on the test data were performed. Thereafter, a command was sent to move a six degrees of freedom (6-DoF) robot arm in four different directions according to the position of the detected flickering object. A flowchart of this SSVEP project is shown in Figure A.6.

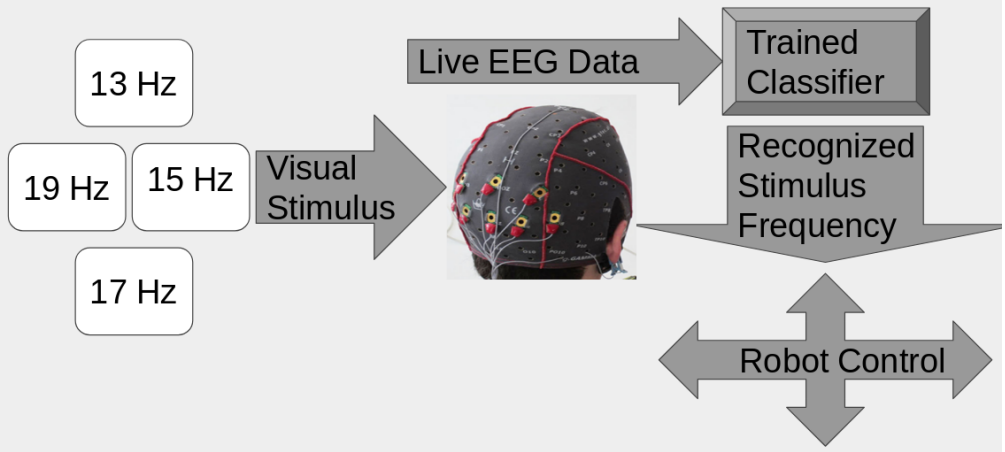

Figure A.6: SSVEP project flowchart.

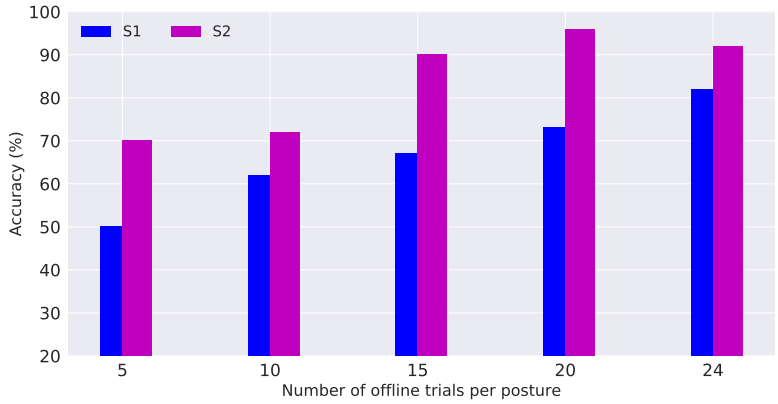

Figure A.7: Online Accuracy of EMG classification without force.

A.4.2.2 Real-time prosthetic hand using surface EMG signals

Herein, we describe the online decoding of three grasp poses, namely fist grasp, 2-digit grasp and 3-digit grasp. The offline analysis and processing described previously in section

A.4.1.2 were used. The developed algorithm was tested on two healthy subjects. 72 trials (24 for each posture) were first acquired to train the model. Thereafter, new 30 online trials (10 per posture) were used for online testing. The number of offline trials used for model training has been reduced in retrospective analysis to evaluate the effect of the training data size on the online classification accuracy as shown in Figure A.7. It should be noted that a 3-fold cross validation was used to train the (offline) model in the first place. Figure A.7 shows that with 72 offline trials, an accuracy of 82% and 92% was reached for S1 and S2, respectively. Overall, it is clear that the accuracy could be even further improved by increasing the number of training trials. However, by using 24 trials for each posture, a good compromise between duration of training time and accuracy of training was found.

B Copyright permissions

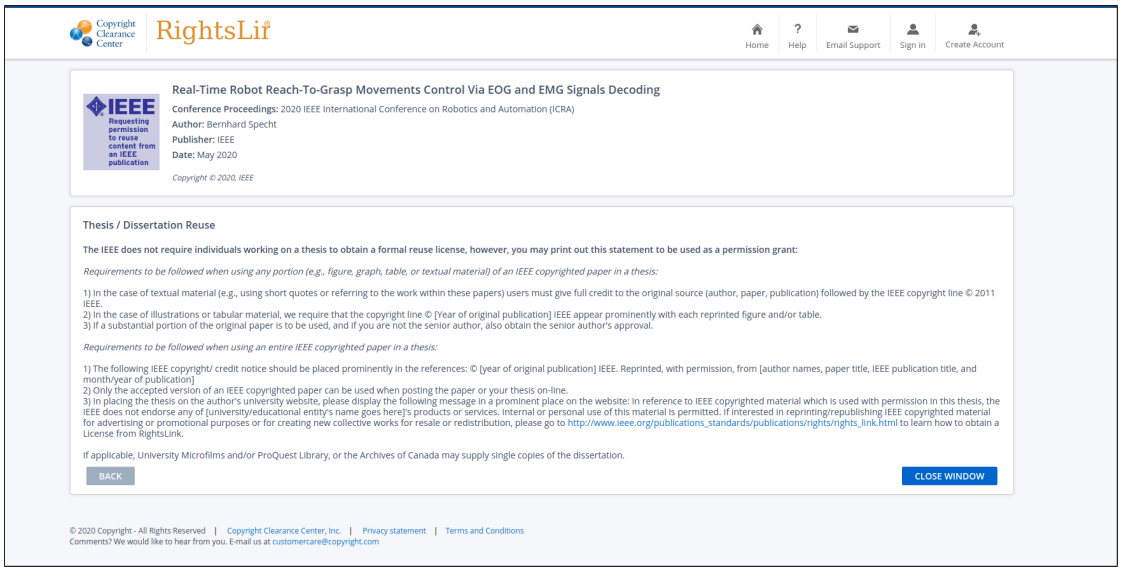

Figure B.1: Copyright permission for the content presented in chapter 4

Figure B.2: Co-author permission for use of the content presented in chapter 4

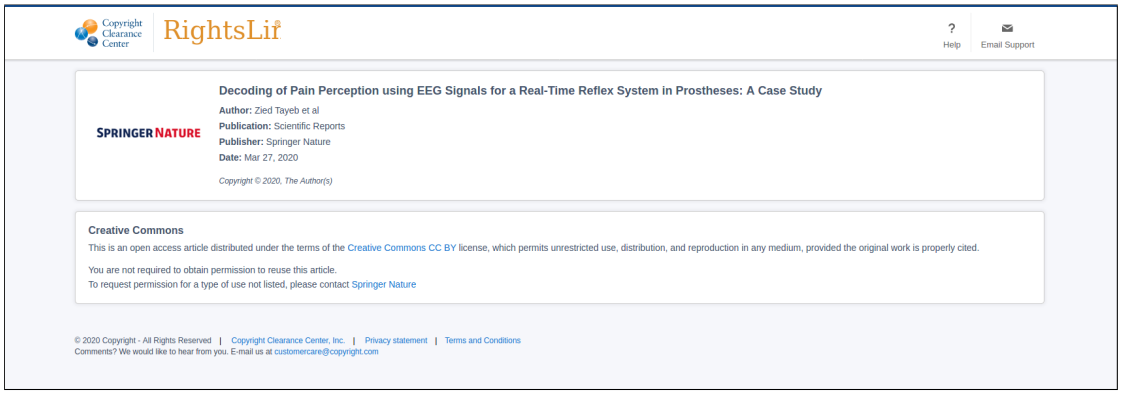

Copyright Clearance Center | RightsLink®

Help | Email Support

SPRINGER NATURE

Decoding of Pain Perception using EEG Signals for a Real-Time Reflex System in Prostheses: A Case Study

Author: Zied Tayeb et al
Publication: Scientific Reports
Publisher: Springer Nature
Date: Mar 27, 2020

Copyright © 2020, The Author(s)

Creative Commons

This is an open access article distributed under the terms of the Creative Commons CC BY license, which permits unrestricted use, distribution, and reproduction in any medium, provided the original work is properly cited.

You are not required to obtain permission to reuse this article.
To request permission for a type of use not listed, please contact Springer Nature

Figure B.3: Copyright permission for the content presented in chapter 6

Copyright Clearance Center | Marketplace™

IOP Publishing, Ltd - License Terms and Conditions

This is a License Agreement between ZIED TAYEB ("You") and IOP Publishing, Ltd ("Publisher") provided by Copyright Clearance Center ("CCC"). The license consists of your order details, the terms and conditions provided by IOP Publishing, Ltd, and the CCC terms and conditions.

All payments must be made in full to CCC.

Order Date	04-Nov-2020	**Type of Use**	Republish in a thesis/dissertation
Order license ID	1075005-1	**Publisher**	IOP Publishing
ISSN	1741-2552	**Portion**	Chapter/article

LICENSED CONTENT

Publication Title	Journal of Neural Engineering	**Country**	United Kingdom of Great Britain and Northern Ireland
Author/Editor	Institute of Physics (Great Britain)	**Rightsholder**	IOP Publishing, Ltd
Date	01/01/2004	**Publication Type**	e-journal
Language	English	**URL**	http://www.iop.org/EJ/journal/JNE

REQUEST DETAILS

Portion Type	Chapter/article	**Rights Requested**	Main product
Page range(s)	20	**Distribution**	Worldwide
Total number of pages	20	**Translation**	Original language of publication
Format (select all that apply)	Print, Electronic	**Copies for the disabled?**	No
Who will republish the content?	Publisher, not-for-profit	**Minor editing privileges?**	No
Duration of Use	Current edition and up to 5 years	**Incidental promotional use?**	No
Lifetime Unit Quantity	Up to 499	**Currency**	EUR

NEW WORK DETAILS

Title	Mr. Zied Tayeb	**Institution name**	Technical University of Munich
Instructor name	Technical University of Munich	**Expected presentation date**	2020-11-12

ADDITIONAL DETAILS

Order reference number	N/A	**The requesting person / organization to appear on the license**	ZIED TAYEB

REUSE CONTENT DETAILS

Title, description or numeric reference of the portion(s)	Classification and regression of spatio-temporal signals using NeuCube and its realization on SpiNNaker neuromorphic hardware	**Title of the article/chapter the portion is from**	Classification and regression of spatio-temporal signals using NeuCube and its realization on SpiNNaker neuromorphic hardware
Editor of portion(s)	Journal of Neural Engineering	**Author of portion(s)**	Journal of Neural Engineering
Volume of serial or monograph	16	**Issue, if republishing an article from a serial**	N/A
Page or page range of portion	whole article	**Publication date of portion**	2020-12-15

Figure B.4: Copyright permission for part of the content presented in chapter 2

Copyright Clearance Center | Marketplace™

IOP Publishing, Ltd - License Terms and Conditions

This is a License Agreement between ZIED TAYEB ("You") and IOP Publishing, Ltd ("Publisher") provided by Copyright Clearance Center ("CCC"). The license consists of your order details, the terms and conditions provided by IOP Publishing, Ltd, and the CCC terms and conditions.

All payments must be made in full to CCC.

Order Date	04-Nov-2020	**Type of Use**	Republish in a thesis/dissertation
Order license ID	1075003-1	**Publisher**	IOP Publishing
ISSN	1741-2552	**Portion**	Chapter/article

LICENSED CONTENT

Publication Title	Journal of Neural Engineering	**Country**	United Kingdom of Great Britain and Northern Ireland
Author/Editor	Institute of Physics (Great Britain)	**Rightsholder**	IOP Publishing, Ltd
Date	01/01/2004	**Publication Type**	e-Journal
Language	English	**URL**	http://www.iop.org/EJ/journal/JNE

REQUEST DETAILS

Portion Type	Chapter/article	**Rights Requested**	Main product
Page range(s)	15-20	**Distribution**	Worldwide
Total number of pages	20	**Translation**	Original language of publication
Format (select all that apply)	Print, Electronic	**Copies for the disabled?**	No
Who will republish the content?	Author of requested content	**Minor editing privileges?**	No
Duration of Use	Current edition and up to 5 years	**Incidental promotional use?**	No
Lifetime Unit Quantity	Up to 499	**Currency**	EUR

NEW WORK DETAILS

Title	Mr.	**Institution name**	Zied Tayeb (Technical University of Munich)
Instructor name	Technical University of Munich	**Expected presentation date**	2020-11-12

ADDITIONAL DETAILS

Order reference number	N/A	**The requesting person / organization to appear on the license**	ZIED TAYEB

REUSE CONTENT DETAILS

Title, description or numeric reference of the portion(s)	Gumpy: a Python toolbox suitable for hybrid brain–computer interfaces	**Title of the article/chapter the portion is from**	Gumpy: a Python toolbox suitable for hybrid brain–computer interfaces
Editor of portion(s)	IOP Publishing	**Author of portion(s)**	Zied Tayeb
Volume of serial or monograph	15 (6)	**Issue, if republishing an article from a serial**	N/A
Page or page range of portion	the whole article	**Publication date of portion**	2020-12-17

PUBLISHER TERMS AND CONDITIONS

Figure B.5: Copyright permission for the content presented in the appendix

Permission for figures use

Robert Daroff <robert.daroff@case.edu>
Mon 05/10, 22:25

Yes, this is fine.
•••

Tayeb, Zied
Mon 05/10, 15:58
robert.daroff@case.edu

Reply all

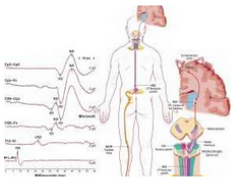

Download

Dear Dr. Daroff,
I am writing to kindly ask for your permission to use the attached figure in my Ph.D. thesis with a proper citation of the publication it was taken from. I adapted both figures according to my needs but I want to first ask for your permission to include it in my dissertation. Thank you.

Best regards,
Zied

Figure B.6: Author's permission for the use of figure 2.5 of chapter 2

[EXT] Permission for figures use

Osborn, Luke E. <Luke.Osborn@jhuapl.edu>
Fri 25/09, 12:27

Hi Zied,

Yes of course, please feel free to use them! They look great!

Hope all is going well!

Luke
•••

Figure B.7: Author's permission for the use of figure 2.1 of chapter 2

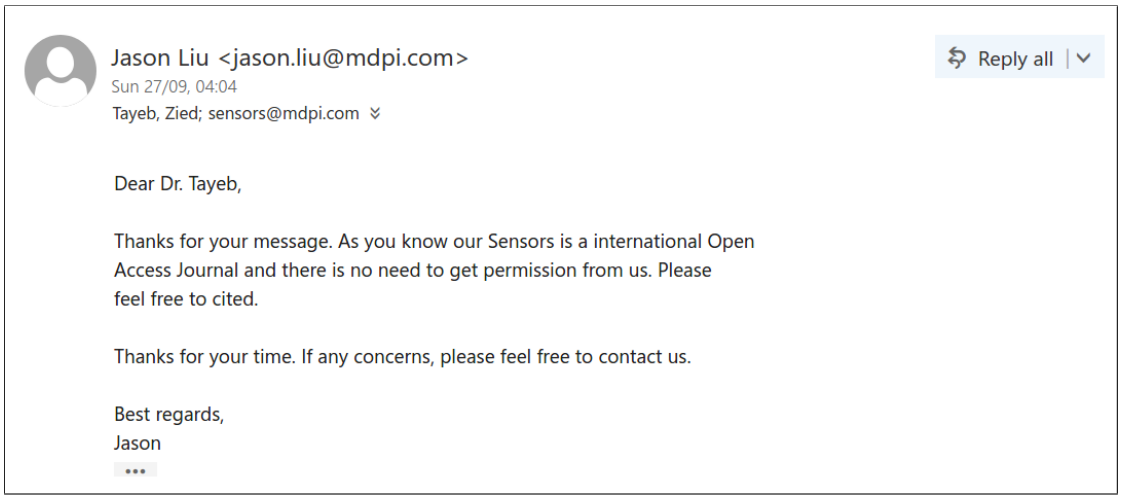

Jason Liu <jason.liu@mdpi.com>
Sun 27/09, 04:04
Tayeb, Zied; sensors@mdpi.com

Reply all

Dear Dr. Tayeb,

Thanks for your message. As you know our Sensors is a international Open Access Journal and there is no need to get permission from us. Please feel free to cited.

Thanks for your time. If any concerns, please feel free to contact us.

Best regards,
Jason

Figure B.8: Editor's permission for the use of the content presented in chapter 3

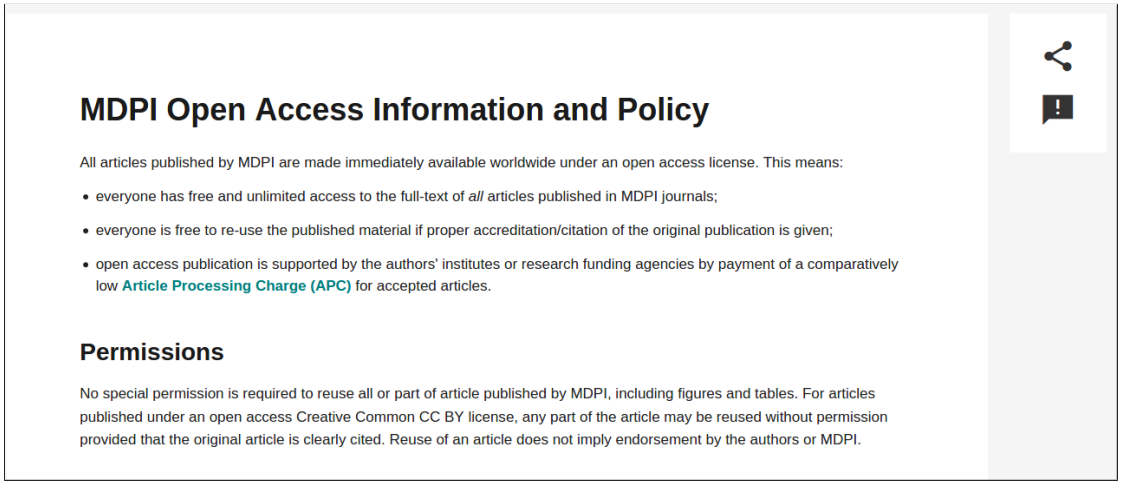

MDPI Open Access Information and Policy

All articles published by MDPI are made immediately available worldwide under an open access license. This means:

- everyone has free and unlimited access to the full-text of *all* articles published in MDPI journals;
- everyone is free to re-use the published material if proper accreditation/citation of the original publication is given;
- open access publication is supported by the authors' institutes or research funding agencies by payment of a comparatively low **Article Processing Charge (APC)** for accepted articles.

Permissions

No special permission is required to reuse all or part of article published by MDPI, including figures and tables. For articles published under an open access Creative Common CC BY license, any part of the article may be reused without permission provided that the original article is clearly cited. Reuse of an article does not imply endorsement by the authors or MDPI.

Figure B.9: Copyright permission for the content presented in chapter 3

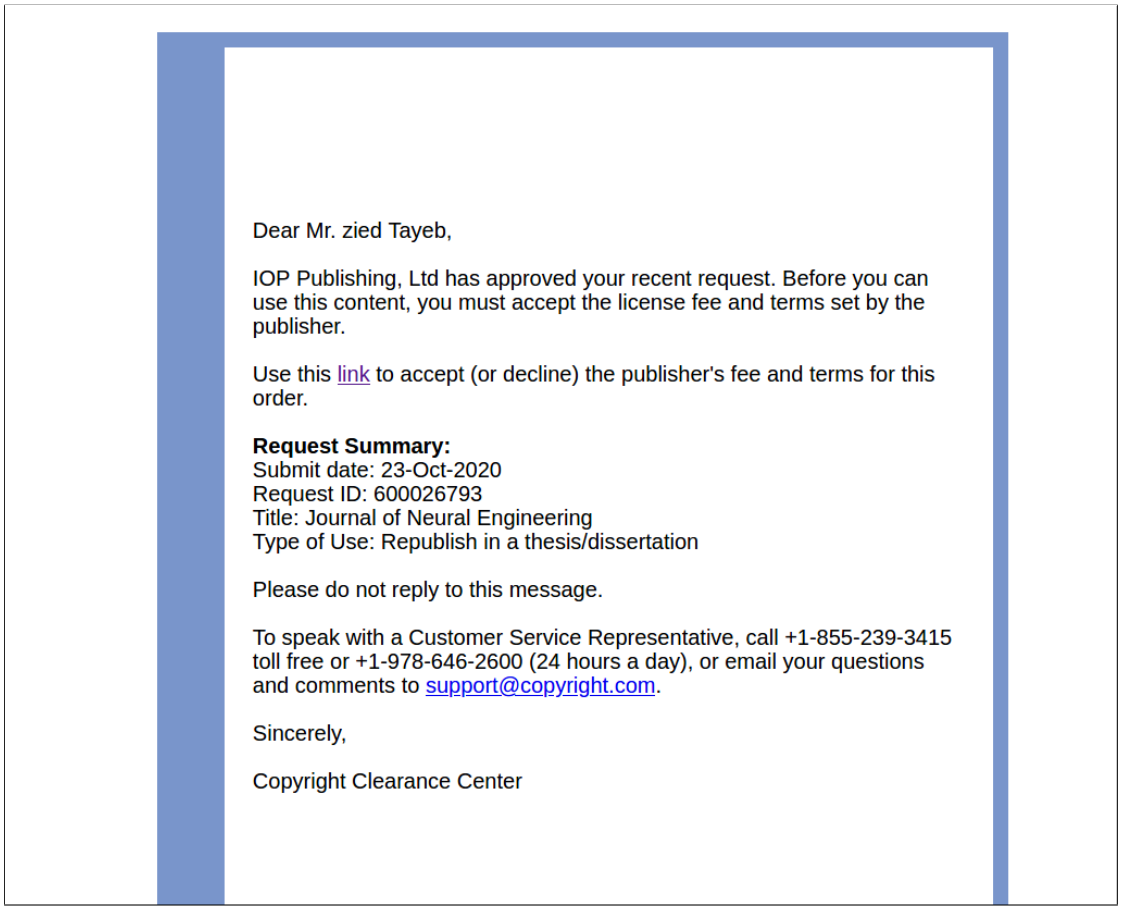

Dear Mr. zied Tayeb,

IOP Publishing, Ltd has approved your recent request. Before you can use this content, you must accept the license fee and terms set by the publisher.

Use this link to accept (or decline) the publisher's fee and terms for this order.

Request Summary:
Submit date: 23-Oct-2020
Request ID: 600026793
Title: Journal of Neural Engineering
Type of Use: Republish in a thesis/dissertation

Please do not reply to this message.

To speak with a Customer Service Representative, call +1-855-239-3415 toll free or +1-978-646-2600 (24 hours a day), or email your questions and comments to support@copyright.com.

Sincerely,

Copyright Clearance Center

Figure B.10: Copyright permission for the content presented in the appendix